

# **ANION AND SOLVENT INFLUENCES ON THE SELF-ASSEMBLY OF COPPER(I) COORDINATION SOLIDS**

---

A Dissertation  
presented to  
The Faculty of the Graduate School  
University of Missouri-Columbia

---

In Partial Fulfillment  
Of the Requirements for the Degree  
Doctor of Philosophy

---

by  
DOUGLAS A. KNIGHT  
Dr. Steven W. Keller, Dissertation Advisor

DECEMBER 2005

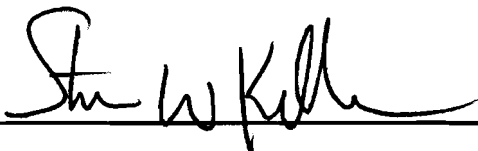
The undersigned, appointed by the Dean of the Graduate School have examined the dissertation titled

**ANION AND SOLVENT INFLUENCES  
ON THE SELF-ASSEMBLY OF  
COPPER(I) COORDINATION SOLIDS**

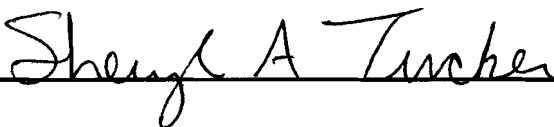
Presented by Douglas A. Knight

A candidate for the degree of Doctor of Philosophy

And herby certify that in their opinion it is worthy of acceptance.

 \_\_\_\_\_ (Chair)

 \_\_\_\_\_

 \_\_\_\_\_

 \_\_\_\_\_

 \_\_\_\_\_

To my beloved wife, Hilda.

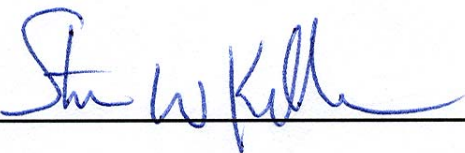
The undersigned, appointed by the Dean of the Graduate School have examined the dissertation titled

**ANION AND SOLVENT INFLUENCES  
ON THE SELF-ASSEMBLY OF  
COPPER(I) COORDINATION SOLIDS**

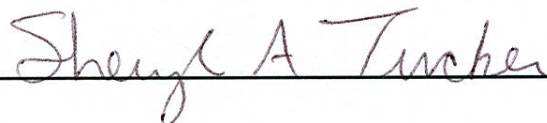
Presented by Douglas A. Knight

A candidate for the degree of Doctor of Philosophy


and hereby certify that in their opinion it is worthy of acceptance.

 \_\_\_\_\_ (Chair)

 \_\_\_\_\_

 \_\_\_\_\_

 \_\_\_\_\_

 \_\_\_\_\_

## **ACKNOWLEDGMENTS**

I would like to extend my thanks to the entire chemistry department for making my studies at MU an exciting and rewarding endeavor. I would especially like to thank my advisor, Steven W. Keller for his invaluable advice and support. Steve's demand for excellence in my work undoubtedly helped push me to achieve much more than was required, helping to prepare me for the challenges ahead of me as a chemistry researcher. I would also like to thank Chuck Barnes for his guidance in X-ray crystallography, and thank Wei Wycoff for her continued assistance with the NMR studies. Finally, I would like to thank those several unnamed souls who brought me from the brink of despair, welcomed me into their group with open arms, and placed me on the path leading to this point of triumph and hope. May my success fuel your efforts to go forth and help those still suffering.

# **ANION AND SOLVENT INFLUENCES ON THE SELF-ASSEMBLY OF COPPER(I) COORDINATION SOLIDS**

Douglas A. Knight  
Steven W. Keller, Dissertation Supervisor

## **ABSTRACT**

The investigation of solvent and anion influences on the self-assembly of copper(I) coordination solids are presented. As these extended solids vary in structural design as reactions conditions are varied, both those particular structural variances and the reaction conditions involved will be discussed.

This presentation will be divided into four major sections. The first section covers an in-depth look at those structural variances found among the copper(I) coordination solids synthesized using 4,4'-bipyridine with refined synthesis and related structures. This entire system is thoroughly examined in order to identify all possible structural variances resulting from the implementation of a specific set of reaction variables, specifically the identity of both anion and reaction solvent used.

The second and third parts will look closer at the self-assembly reaction mechanism as synthetic intermediate structures are presented and analyzed in relation to the above-mentioned structures. Each structure presented offers information in regards to the role the anion or solvent play in the self-assembly reactions

The final section deals with similar reactions using the pyrimidine ligand. Several structures presented here suggests that anion templation plays a major role in the extended solids formation. This section concludes with a practical application of these materials as a study of selective anion exchange with a large cavity Cu(I) coordination solid is presented.

## TABLE OF CONTENTS

ACKNOWLEDGMENTS.....	iii
ABSTRACT.....	iv
LIST OF TABLES.....	x
LIST OF ILLUSTRATIONS.....	xii

### Chapter 1. SUPRAMOLECULAR CHEMISTRY AND POROUS FUNCTIONAL SOLIDS

1.1 Introduction.....	1
1.2 Supramolecular Chemistry: Definitions and Design.....	2
1.3 Natural Porous Solids: Zeolites and Clays.....	12
1.4 Supramolecular Zeolite and Clay Mimics.....	19
1.5 Supramolecular Isomerism in Porous Coordination Solids.....	34
1.6 Dissertation Overview.....	40

### Chapter 2. MATERIAL SYNTHESIS AND CHARACTERIZATION

2.1 Introduction.....	49
2.2 General Experimental Section.....	49
2.2.1 Materials.....	49
2.2.2 Starting Material Synthesis.....	50
2.2.3 Synthesis of the Cu(I) Coordination Clay and Zeolite Analog..	53
2.3 Material Characterization and X-ray Crystallography.....	57
2.3.1 General Methods.....	57
2.3.2 Crystallography and X-ray Diffraction.....	60
2.3.2.1 Crystallography.....	60
2.3.2.2 X-ray Diffraction.....	72

## Chapter 3. ANION AND SOLVENT DEPENDENCE OF THE CLAY ANALOG

3.1	Introduction.....	94
3.2	Experimental Section.....	99
3.2.1	General Methods.....	99
3.2.2	Synthesis.....	99
3.2.3	Single Crystal X-Ray Diffraction.....	103
3.2.4	Powder X-Ray Diffraction and NMR Instrument Details....	104
3.3	Results and Discussion.....	108
3.3.1	Reactions With the $\text{BF}_4^-$ Anion.....	108
3.3.2	Reactions With the $\text{PF}_6^-$ Anion.....	116
3.3.3	Reactions With the $\text{ClO}_4^-$ Anion.....	122
3.3.4	Reactions With the $\text{CF}_3\text{SO}_3^-$ Anion.....	128
3.3.5	Reactions With the $\text{HSO}_4^-$ Anion.....	131
3.3.6	Examining the Distances and Angles: What it takes to make a square, pentagon, or hexagon network.....	134
3.3.7	Conclusion.....	139
Chapter 4. ANION AND SOLVENT INTERACTIONS.....		143
4.1	Introduction.....	143
4.2	Experimental.....	144
4.2.1	General Methods.....	144
4.2.2	Synthesis.....	144
4.2.3	Single Crystal X-Ray Diffraction.....	147
4.2.4	Thermogravimetric Analysis.....	148
4.3	Results and Discussion.....	151



4.3.1	The Triflate Starting Material.....	151
4.3.2	Triflate and THF Coordination.....	153
4.3.3	Perchlorate Coordination.....	159
4.3.4	The Hydrogen Sulfate Anion.....	162
4.3.5	Reactions of <b>17</b> in THF.....	165
4.3.6	Thermogravimetric Analysis.....	172
4.4	Conclusion.....	176
Chapter 5. SELF-ASSEMBLY INTERMEDIATES		
5.1	Introduction.....	180
5.2	Experimental.....	183
5.2.1	General Methods.....	183
5.2.2	Synthesis.....	184
5.2.3	Single Crystal X-Ray Diffraction.....	185
5.3	Results and Discussion	
5.3.1	The Triflate 1-D Chain.....	187
5.3.2	The Perchlorate 1-D Chain and Dimer.....	189
5.3.3	The Tetrafluoroborate (THF Coordinated) Chain.....	193
5.3.4	Coordination Spheres of the Intermediate Structures.....	195
5.4	Conclusion.....	201
Chapter 6. Cu(I)/Pyrimidine Discrete, One-, Two-, and Three-dimensional Solids		
6.1	Introduction.....	204
6.2	Discrete Cu(I) Coordinated Oligomers.....	205
6.2.1	Experimental Section.....	206

6.2.1.1	General Methods.....	206
6.2.1.2	Synthesis.....	206
6.2.1.3	Single Crystal X-Ray Diffraction .....	208
6.2.2	Results and Discussion.....	210
6.2.2.1	The Cu(I) Tetramer.....	210
6.2.2.2	The Cu(I/II) Tetramer Dimer.....	216
6.2.2.3	Anion Templatation of a Discrete Hexagon.....	218
6.3	One-Dimensional Chains.....	220
6.3.1	Experimental Section.....	220
6.3.1.1	General Methods.....	220
6.3.1.2	Synthesis.....	221
6.3.1.3	Single Crystal X-Ray Diffraction .....	221
6.3.2	Results and Discussion.....	224
6.3.2.1	An Anion Templated One-Dimensional Chain.....	224
6.3.2.2	The 1-D Chain of [Cu(pyrim) <sub>3</sub> ]ClO <sub>4</sub> .....	227
6.4	Two-Dimensional Bilayered Extended Solids.....	230
6.4.1	Experimental Section.....	230
6.4.1.1	General Methods.....	230
6.4.1.2	Synthesis.....	231
6.4.1.3	Single Crystal X-Ray Diffraction .....	231
6.4.2	Results and Discussion.....	234
6.5	Three-Dimensional Extended Solids.....	240
6.5.1	Experimental Section.....	240

6.5.1.1	General Methods.....	240
6.5.1.2	Synthesis.....	240
6.5.1.3	Single Crystal X-Ray Diffraction .....	242
6.5.2	Results and Discussion.....	244
6.5.2.1	Three-Dimensional Extended Solids With the $\text{ClO}_4^-$ and $\text{BF}_4^-$ Anions.....	244
6.5.2.2	Three-Dimensional Extended Solid With the $\text{PF}_6^-$ Anion.....	250
6.7	Conclusion.....	253
Chapter 7. Anion Exchange Using a Large Cavity, Functional Porous Solid		
7.1	Introduction.....	257
7.2	Experimental.....	259
7.2.1	General Methods.....	259
7.2.2	Instrumentation Details.....	259
7.2.3	Synthesis.....	261
7.2.4	Single Crystal X-Ray Diffraction .....	261
7.3	Results and Discussion.....	264
7.3.1	Crystal Structure of <b>37</b> and <b>38</b> .....	264
7.3.2	$\text{BF}_4^-$ and $\text{PF}_6^-$ Anion Exchange.....	271
7.3.3	Competition Exchange Study With $\text{ReO}_4^-$ .....	272
7.4	Conclusion.....	275
Chapter 8. CONCLUSION.....		
VITA.....		
		280

## LIST OF TABLES

Table		Page
1.1	A few of the metal cations and the counter anions used by others along with the various metal coordination geometries available.....	23
2.1	The Seven Crystal Systems and Fourteen Bravais Lattices.....	63
2.2	Symmetry operations and symmetry elements.....	64
2.3	The 32 Crystallographic Point Groups.....	67
2.4	The 230 Space Groups.....	70
3.1	Crystallographic Details for <b>1 – 4</b> .....	105
3.2	Crystallographic Details for <b>5 – 8</b> .....	106
3.3	Crystallographic Details for <b>9 – 11</b> .....	107
3.4	Reactions with $\text{BF}_4^-$ .....	108
3.5	Angles and Distances of the Ladder Chain for Structures <b>2</b> and <b>6</b> .....	112
3.6	Reactions with $\text{PF}_6^-$ .....	116
3.7	Unit Cells for <b>1</b> & <b>5</b> .....	116
3.8	Angles and Distances of the 1-D Chain for Structures <b>1</b> and <b>5</b> .....	118
3.9	Reactions with $\text{ClO}_4^-$ .....	123
3.10	The angles found around the pairs of hexagons found in structures <b>8</b> and <b>11</b> . Structures shown as ball and stick representations with the hydrogen atoms removed for clarity.....	132
3.11	Selected Bond Lengths and Angles for Structures <b>1, 2, 3, 5, and 6</b> .....	137
3.12	Selected Bond Lengths and Angles for Structures <b>4, 8, and 11</b> .....	138
4.1	Crystallographic Details for <b>12 – 16</b> .....	149
4.2	Crystallographic Details for <b>17 – 20</b> .....	150
4.3	Selected bond lengths (Å) and angles (deg) for <b>12</b> .....	152
4.4	Selected bond lengths (Å) and angles (deg) for <b>13 &amp; 14</b> .....	156

4.5	Selected bond lengths (Å) and angles (deg) for <b>15</b> .....	157
4.6	Selected bond lengths (Å) and angles (deg) for <b>16</b> .....	161
4.7	Unit cell dimensions for [Cu(MeCN) <sub>2</sub> (PPh <sub>3</sub> ) <sub>2</sub> ]X (X = ClO <sub>4</sub> <sup>-</sup> , BF <sub>4</sub> <sup>-</sup> , PF <sub>6</sub> <sup>-</sup> , and HSO <sub>4</sub> <sup>-</sup> ), SM6-8 and <b>17</b> .....	163
4.8	Selected bond lengths (Å) and angles (deg) <b>17</b> and <b>SM6</b> .....	164
4.9	Selected bond lengths (Å) and angles (deg) for <b>18</b> .....	166
4.10	Selected bond lengths (Å) and angles (deg) for <b>19</b> .....	169
4.11	Selected bond lengths (Å) and angles (deg) for <b>19</b> cont.....	170
4.12	Selected bond lengths (Å) and angles (deg) for <b>20</b> .....	172
5.1	Crystallographic Details for <b>21 – 24</b> .....	186
5.2	Selected Bond Lengths (Å) and Angles (deg.) for Structures <b>21, 22, 23,</b> and <b>24</b> .....	197
6.1	Crystallographic Details for <b>25 – 28</b> .....	209
6.2	Unit cells of the tetramers found in <b>24</b> and with the PF <sub>6</sub> <sup>-</sup> anion.....	211
6.3	Crystallographic Details for <b>29</b> and <b>30</b> .....	223
6.4	Selected bond lengths (Å) and angles (deg) for <b>29</b> .....	226
6.5	Selected bond lengths (Å) and angles (deg) for <b>30</b> .....	228
6.6	Crystallographic Details for <b>31</b> and <b>32</b> .....	233
6.7	Selected bond lengths (Å) and angles (deg) for <b>31</b> and <b>32</b> .....	237
6.8	Crystallographic Details for <b>33 – 36</b> .....	243
6.9	Selected bond lengths (Å) and angles (deg) for <b>34</b> and <b>35</b> .....	246
6.10	Selected Donor Numbers [kcal. mol <sup>-1</sup> ].....	250
7.1	Crystallographic Details for <b>37</b> and <b>38</b> .....	263
7.2	Selected bond lengths (Å) and angles (deg) for <b>37 &amp; 38</b> .....	265

## LIST OF ILLUSTRATIONS

Figure	Page
1.1	Molecular chemistry is responsible for making the molecular building blocks that are brought together to form the supramolecular complex..... 3
1.2	Crystal structure of the macrotricyclic receptor with the guest iodide anion in the center. Carbon atoms are gray, nitrogen atoms blue and labeled, and the iodide atom is green and labeled..... 4
1.3	Two methanol molecules showing directional H-bonding with each other..... 5
1.4	A schematic of the $K^+$ -benzene cation – $\pi$ interaction showing (left) the cation positioning over benzene along the 6-fold axis and (right) a space-fill model showing the $K^+$ -benzene complex at its optimized geometry..... 6
1.5	(a) Face-to-face $\pi$ -stacking showing the offset positioning of the rings. (b) Edge-to-face $\pi$ -stacking..... 6
1.6	The X-ray crystal structure showing the [ <i>p-tert</i> -butylmethoxycalix[4]arene-sodium-toluene] <sup>+</sup> cation inclusion complex..... 8
1.7	The hydrophobic effect brings a guest and host together..... 9
1.8	The lock and key principle illustrating how the molecular forces of a host are complimentary to those of its guest in a supramolecular complex..... 10
1.9	(a) A few examples of synthons and how they fit together forming the supramolecular complexes. (b) Synthons allow barbituric acid <b>1</b> and 2,4,6-triaminopyrimidine <b>2</b> to fit together forming a macrocycle <b>3</b> ..... 11
1.10	(a) The addition of the t-BuNH <sub>3</sub> <sup>+</sup> cation helps to organize a hemispherand complex. (b) Both the Fe <sup>2+</sup> cations and the Cl <sup>-</sup> anion act as templates to form this pentanuclear circular helicate..... 12
1.11	(a) The SiO <sub>4</sub> and AlO <sub>4</sub> <sup>-</sup> tetrahedra as they form the <i>Secondary Building Unit</i> (SBN). (b) The SBN are linked together via oxygen bonds to form the larger $\alpha$ -cavity as in Zeolite A..... 14
1.12	The four appendages of the positively charged tetraalkylammonium anion can act as a template around which silicate and aluminate ions link together to form the walls of the zeolite's cavity. The alkyl chain appendages were varied from 3 to 7 carbons long to produce different size pores..... 15
1.13	<i>Kaolinite</i> is an example of the 1:1 type and <i>Montmorillonite</i> 2:1 type clay..... 17

1.14	(a) The anthrazene – bis(resorcinol) tetraol building block for the host network. (b) Benzophenone – the guest molecule. (c) A single enclosure formed by the hydrogen bonded bis(resorcinol) tetraol (black) with two guest benzophenones (blue and red). Hydrogen atoms have been omitted for clarity. (d) Four overlapping host enclosures (black) with the benzophenone guests (blue and red). Hydrogen atoms have been omitted for clarity.....	20
1.15	(a) Tetrahedral tectons made by Jim Wuest and his colleagues that can form (b) diamondoid networks that tend to interpenetrate with each other.....	22
1.16	An assortment of organic bridging ligands; both neutral and charged.....	24
1.17	(a) The 4,4',4'',4'''– tetracyanotetraphenylmethane (tctpm) tecton and (b) as it coordinates to copper in the unit cell. The diamondoid extended network shown in (c) with its large, channeling cavities in view. Copper atoms are shown as green balls, while carbon and nitrogen atoms are gray and blue stick, respectively. Hydrogen atoms and both the anion and solvent were not included in the original crystal structure data because of unusually high crystallographic disorder.....	25
1.18	Line representations of a few examples of metal – 4,4'bipyridine (M – BPY) porous extended networks. The lines represent BPY, except for the vertical lines in (c) and the horizontal lines in (d), which, respectively, indicate Ag – Ag and Cu – Cu. The chemical formula, dimensionality of the M – BPY network, number of interpenetrating networks, and pore aperture size are listed, respectively, beneath each representation.....	26
1.19	The $\mu_2$ -chloro-bridged Cu(I) dinuclear building-block found in [Cu(bpy)Cl]. Non-hydrogen atoms are represented by 50% thermal ellipsoids. ....	27
1.20	A portion of the infinite porous sheet formed by the organization of the building-block unit, [Cu(bpy)Cl] <sub>4</sub> . Hydrogen atoms have been omitted for clarity. Dark spheres, Cu; Large grey spheres, Cl; small white spheres, C and N.....	26
1.21	(a) Line representation of the 2-D network of [Cd(bpy) <sub>2</sub> (NO <sub>3</sub> ) <sub>2</sub> ·2(C <sub>6</sub> H <sub>4</sub> Br <sub>2</sub> )]. Each line represents a bpy connecting rod. (b) A single square unit of the clathrate complex. Hydrogen atoms and nitrate anions were omitted for clarity. Carbon atoms are gray while all other atoms shown are labeled.....	29
1.22	(a) [Cu(pyrimidine) <sub>2</sub> ] <sup>+</sup> , (b) silicate, and (c) tetrapyridylsilane tecton showing the similar angled coordination, covalent, and hydrogen bonding, respectively.....	31
1.23	(a) Crystal structure of the network unit cell of [Cu(pyrimidine) <sub>2</sub> ]BF <sub>4</sub> (view down the c axis). Cu atoms: green, N atoms: blue, C atoms: grey, hydrogen atoms and anion are omitted for clarity. (b) (I) The polyhedral packing diagram of [Cu(pyrimidine) <sub>2</sub> ]BF <sub>4</sub> . The centroids of the pyrimidine ligand are defined by the sides of the polyhedra. The Cu(I) cations (located at the center of the tetrahedra) are	

	omitted, as are the anions, for clarity. (II) Schematic view of the feldspar structure viewed down the <i>a</i> axis.....	31
1.24	(a) A general formula diagram of the modified Cu(I) tetrahedra and (b) a single tetrahedron from crystal data of a typical $[\text{Cu}(\text{bpy})_{1.5}(\text{PPh}_3)]^+$ layered network, each capped by the terminal phosphine ligand.....	32
1.25	(a) The single layer of the cationic network found with $[\text{Cu}(\text{bpy})_{1.5}(\text{PPh}_3)]\text{BF}_4 \cdot (\text{THF})_{1.33} \cdot (\text{CHCl}_3)_{0.33}$ . The phosphines are yellow (with the phenyl rings removed for clarity), the nitrogen atoms blue, carbon atoms gray, and copper is green (but mostly obscured by the phosphine and carbon atoms). The hydrogen atoms have been omitted for clarity. (b) Also shown in comparison is the polyhedral packing of nekoite.....	33
1.26	A single hexagonal motif derived from the crystal structure of (a) $[\text{Cu}(\text{pyrim})_{2.3}]\text{ClO}_4$ and of (b) $[\text{Cu}(\text{pyrim})_{2.3}(\text{MeCN})_{0.33}]\text{PF}_6$ . One of the terminal pyrimidine and acetonitrile ligands on each, respectively, has been circled. Cu: green; N: blue; C: gray; O: red; F: blue; Cl and P: yellow. The hydrogen atoms and all but the centrally located anion in each structure have been omitted for clarity...	35
1.27	A close-up showing the (a) $\text{ClO}_4^-$ and (b) $\text{PF}_6^-$ anions trapped inside a cage made up of eight Cu(I) tetrahedra.....	37
1.28	(a) A space-fill representation of a single layer of $[\text{Cu}(\text{bipy})_{1.5}(\text{PPh}_3)]\text{BF}_4 \cdot (\text{toluene}) \cdot (\text{CHCl}_3)_{1.5}$ structure's cationic network and (b) two layers as they interpenetrate each other. C: gray; P: yellow; N: blue; Cu: green. The second interpenetrated network in (b) is shown as all blue except for the phosphines. Phenyl rings from the phosphines and all hydrogen atoms have been omitted for clarity.....	38
1.29	A single hexagon showing the toluene $\pi$ -stacking that occurs in $[\text{Cu}(\text{bipy})_{1.5}(\text{PPh}_3)]\text{BF}_4 \cdot (\text{toluene}) \cdot (\text{CHCl}_3)_{1.5}$ between the toluene and the bpy ligands.....	38
1.30	Space-filling representation of the ladder-like network found in the $[\text{Cu}(\text{bpy})_{1.5}(\text{PPh}_3)]\text{PF}_6 \cdot (\text{CHCl}_3)_{1.5}$ structure. Cu: green; C: gray, N: blue, P: yellow. Phenyl rings on the phosphines and all hydrogen atoms have been omitted for clarity.....	39
2.1	A typical Cu(I)/bpy reaction which produce the layered clay-analog structures.....	54
2.2	A typical vapor diffusion reaction used in the Cu(I)/pyrimidine reactions that produce the zeolite-analogs.....	55
2.3	The thermal decomposition of Lopez's clay-analog showing the systematic loss of the ligands.....	59



2.4	(a) A pictorial representation of the lattice points in two-dimensional net. (b) A different selection of lattice points simply shifts the positioning of the 2-D net.....	61
2.5	The Unit Cell showing the $a$ , $b$ and $c$ sides as well as the corresponding $\alpha$ , $\beta$ , and $\gamma$ angles.....	62
2.6	Determination of Point groups.....	66
2.7	Light being diffracted by a grating with distance $a$ .....	73
2.8	As an X-ray beam reflects off a set of planes, Braggs law states that constructive interference only occurs when $n\lambda = 2d\sin\theta$ .....	75
2.9	Drawings of two types of diffractometers with the (left) earlier <i>four-circle</i> design and (right) the more modern <i>area detector</i> design.....	76
2.10	Photos of the Siemen SMART single crystal X-ray diffractometer shown (left) in its operation cabinet and (right) a close-up showing the basic components. Shown are <b>1</b> . CCD detector, <b>2</b> . goniometer and crystal mounting, <b>3</b> . nitrogen cryogenic port, <b>4</b> . X-ray gun, <b>5</b> . X-ray generator, <b>6</b> . centering microscope.....	77
2.11	A CCD area detector (left) showing an X-ray converting to visible light, which is transmitted by fiber optics to the CCD chip. The electrical impulse from the CCD is read by the computer to generate a snap-shot like image (right) of the X-ray diffraction pattern.....	78
2.12	Diffraction patterns of (a) a single crystal, (b) the four crystals, and (c) a polycrystalline sample.....	88
2.13	(a) A drawing of a typical electronic powder X-ray diffractometer design and (b) a real-life example of powder X-ray diffraction data as collected from 5 to $\sim 35$ $2\theta$ ..	90
3.1	The ladder chain structures of (top) <b>2</b> looking down the $c$ -axis and (bottom) <b>6</b> looking down the $b$ -axis. In each structure, the anions are shown in space fill while the rest of the structure is shown in stick representation. The solvated THF in <b>2</b> is shown in black and the solvated $\text{CHCl}_3$ in both is shown in yellow. The phenyl rings on the phosphine groups and the hydrogen atoms have been omitted for clarity.....	110
3.2	A view of the stacked chains in (top) <b>2</b> as seen down the $b$ -axis and also in (bottom) <b>5</b> viewing along a diagonal. Carbons are grey, nitrogen blue, copper green and phosphorous yellow. The anions, solvent molecules, and hydrogen atoms have been omitted for clarity.....	111
3.3	A comparison of (left) the theoretical powder pattern for <b>3</b> with (right) an actual XRPD data of the precipitate that forms from the reaction if the $\text{BF}_4^-$ starting material with bpy in THF.....	114

3.4	The 1-D chains found in structures (top) <b>1</b> and (bottom) <b>5</b> shown in stick representation. The hydrogen atoms and CHCl <sub>3</sub> molecules have been omitted for clarity. The chains in <b>1</b> progress along the <i>ab</i> diagonal while the chains in <b>5</b> progress along the <i>ac</i> diagonal.....	117
3.5	The two copper centers of (left) <b>1</b> and (right) <b>5</b> showing the anion positioning and close H – F interactions in each.....	118
3.6	A stick representation of two bpy bridged Cu tetrahedra of <b>5</b> showing the bending of the ligand at the Cu – N bond. The anion shown in isotropic spheres is shown in position with the three, weak H-bonds in place. Phenyl rings on the phosphines and CHCl <sub>3</sub> molecules have been omitted.....	119
3.7	Two spectra of XRPD data for precipitates generated from the reaction of bpy with the starting materials with (top) the BF <sub>4</sub> <sup>-</sup> and (bottom) the PF <sub>6</sub> <sup>-</sup> anions. The matching peaks of the two spectra are numbered.....	121
3.8	The layered, honeycomb structure of [Cu(C <sub>10</sub> H <sub>8</sub> N <sub>2</sub> ) <sub>1.5</sub> (PPh <sub>3</sub> )]ClO <sub>4</sub> ·(CHCl <sub>3</sub> ) <sub>2</sub> <b>8</b> showing a space fill representation of (a) a single layer and (b) two overlapping layers. (c) A side view of the layers in stick representation (phosphines shown as space fill) shows they stack together and the positioning of the anion and included solvent (both as ball and stick). Phenyl rings on the phosphines and hydrogen atoms are omitted for clarity.....	124
3.9	Two spectra of XRPD data for precipitates generated from the reaction of bpy with the starting materials with (top) the BF <sub>4</sub> <sup>-</sup> , (center) the ClO <sub>4</sub> <sup>-</sup> anions, and the theoretical pattern found for <b>5</b> . The matching peaks of the two spectra are numbered.....	126
3.10	Powder patterns of the precipitate with the triflate in THF reaction solvent with a comparison to the BF <sub>4</sub> <sup>-</sup> precipitates powder pattern showing several matches as with the other samples. We find no matches with the triflate's precipitate in the reactions performed in the CHCl <sub>3</sub> :toluene solvent mixture.....	130
3.11	The spectra of XRPD data for (top) precipitate generated from the reaction of bpy with the starting materials with the BF <sub>4</sub> <sup>-</sup> and (bottom) the theoretical powder pattern for <b>11</b> . The matching peaks of the two spectra are numbered.....	134
3.12	Four tetrahedra shown in 50% thermal ellipsoids as they are bridged together in <b>4</b> . The extreme bowing of a bpy ligand Cu – L bond at N(3), while the N(2) – N(2) bpy ligand is relatively planar. The hydrogen atoms, toluene molecules, and anion are.....	139

4.1	The three cation coordination spheres that comprise the asymmetric unit in <b>12</b> showing the eclipse conformation of the PPh <sub>3</sub> ligands. Hydrogen atoms have been omitted and all other atoms are represented as 50% ellipsoids.....	151
4.2	Asymmetric units of the highly symmetric (a) <b>14</b> and somewhat less symmetric (b) <b>13</b> with the ~30° rotated THF ligand. Both show the staggered conformation of the PPh <sub>3</sub> ligands. The hydrogen atoms have been omitted and the other atoms are represented as 50% thermal ellipsoids.....	154
4.3	(a) The two coordination spheres that comprise the asymmetric unit in <b>15</b> . (b) With the Phenyl groups removed, shifting of the triflate and MeCN ligands is shown for the two unique copper centers in <b>15</b> . Hydrogen atoms have been omitted and all other atoms are represented as 50% ellipsoids.....	155
4.4	Two units of <b>14</b> lock together with ligand-to-coordinated anion association. Hydrogen atoms have been omitted on the phenyl rings.....	157
4.5	PPh <sub>3</sub> ligands also contribute to lock crystalline solid together as they (shown for <b>13</b> ) lock the in a series of edge-to-face $\pi$ - $\pi$ stacking.....	158
4.6	The H-bonding in <b>15</b> between the MeCN ligands and the oxygen atom on the triflate anion.....	159
4.7	The Cu(I) molecule of <b>16</b> with the terminally coordinated perchlorate anion (only THF molecule is shown in the THF/MeCN ligand overlap position). Hydrogen atoms have been omitted and all other atoms are represented as 50% ellipsoids....	159
4.8	(a) The dimer formed by the bridging perchlorate anion along with the third, non-coordinated perchlorate anion. Although both metal centers are from the same Cu(2) unit seen over a two-fold axis, one unit is shown with the THF ligand in place (left) and the other is shown with the MeCN ligand (right) to illustrate how these two ligands occupy the same position. (b) The complete 180° rotational disorder for the bridging perchlorate is shown (looking down the Cl – O(7) axis. All carbon and hydrogen atoms omitted).....	160
4.9	Stick representations of the two <i>almost</i> identical packing arrangements for (a) structure <b>17</b> and (b) the perchlorate salt starting material [Cu(MeCN) <sub>2</sub> (PPh <sub>3</sub> ) <sub>2</sub> ]ClO <sub>4</sub> . Color scheme: Cu green, P yellow, S purple, N blue, O red, C gray. The hydrogen atoms have been omitted for clarity.....	163
4.10	The water coordinated Cu(I) complex found in the asymmetric unit of <b>18</b> shown in 50% thermal ellipsoids. Hydrogen atoms on the phenyl rings and THF were omitted for clarity.....	165
4.11	A stick representation of the H – bonded dimer found in <b>18</b> . The hydrogen atoms on the phenyl rings and the THF have been omitted for clarity.....	167

4.12	Two hydrogen-bonded Cu(I) complexes in <b>19</b> shown as 50% thermal ellipsoids. The THF, shown as isotropic spheres, find a place in the cleft formed by the Cu(I) dimer. The two H-bonds located at O(20) and O(22) are colored in light blue. All unmarked carbon atoms are gray and hydrogen atoms, with the exception of those on the anion, have been omitted for clarity.....	168
4.13	The HSO <sub>4</sub> <sup>-</sup> bridged dimer of <b>20</b> with all atoms except the phenyl rings shown as 50% thermal ellipsoids. The hydrogen bonds between the anions are shown as red dashed lines. The phenyl ring's hydrogen atoms have been removed for clarity.....	171
4.14	Thermogravimetric analysis for <b>12</b> , <b>13</b> , and <b>14</b> .....	173
4.15	Thermogravimetric analysis for <b>17</b> , <b>18</b> , <b>19</b> , and <b>20</b> .....	174
5.1	The two tetrahedra of the asymmetric unit of <b>21</b> shown in 50% thermal ellipsoids. The hydrogen atoms have been omitted for clarity.....	188
5.2	The two unique chains developed from the bpy coordination of both Cu(1) and Cu(2) in <b>21</b> shown in stick representation as is seen looking down the c-axis of the unit cell. The most apparent interaction between these chains are the edge-to- $\pi$ stacking between the phosphine phenyl rings and the bpy ligands. Hydrogen atoms have been omitted for clarity.....	189
5.3	Stick representation of <b>22</b> showing the reversed positioning (with respect to <b>21</b> ) of the anion and phosphine ligands. The phenyl rings on the phosphine and hydrogen atoms have been omitted for clarity.....	190
5.4	Stick representations of (top) <b>21</b> and (bottom) <b>22</b> showing how the anions and phosphines have switched positions relative to each other. The phenyl rings and hydrogen atoms have been omitted for clarity.....	191
5.5	The dimer found in the structure of <b>23</b> shown in 50% thermal ellipsoids. Each of the two tetrahedra shown are crystallographically identical, with only one found in the asymmetric unit. The hydrogen atoms and solvated THF have been omitted for clarity.....	192
5.6	A view in stick representation of the extended packing of the dimers in <b>23</b> showing as looking down the a-axis. The cavities shown here contain the 3.5 THF molecules per Cu (not shown) solvated in the structure. Hydrogen atoms are also omitted for clarity.....	193
5.7	The asymmetric unit of <b>24</b> shown in 50% thermal ellipsoids. The hydrogen atoms have been omitted for clarity.....	194

5.8	Two chains from <b>24</b> shown in stick representation as viewed (left) lengthwise and a view (right) from the ends of the same two chains. Note how THF is always on one side and the phosphine ligands are more straight up and down other than tilted to the side as in <b>21</b> and <b>22</b> . The anions and hydrogen atoms have been omitted for clarity.....	194
5.9	A ball and stick representation of $[\{C_5H_3(SiMe_3)_2\}HfMe_2(\eta^6\text{-toluene})][Bme(C_6F_5)_3]$ showing toluene coordination to Hf.....	200
6.1	A single tetramer as seen in <b>25</b> with the non-hydrogen atoms shown in 50% thermal ellipsoids. Both the (left) face-on view and (right) side view illustrates how a square molecular unit can be constructed from tetrahedral building blocks. The $BF_4^-$ anions have been omitted.....	210
6.2	Two tetramers of <b>25</b> in stick representation showing the anions (seen as isotropic spheres) in their positions along the c axis. The hydrogen atoms have been omitted for clarity.....	211
6.3	Powder Patterns of Selected Tetramer Reactions and Theoretical Comparison.....	215
6.4	The Cu(I/II) dimer shown in stick representation. Unmarked atoms are gray for carbon, red for oxygen and yellow for chlorine. All the hydrogen atoms except on the hydroxides have been omitted.....	217
6.5	A side view of <b>26</b> showing the anion and THF positioning. The hydrogen atoms are omitted for clarity.....	217
6.6	The discrete hexagon found in <b>28</b> shown as 50% thermal ellipsoid, with the anion and THF (center) shown in stick representation. Each of the O(13) and O(7) labeled indicates a weak H-bond location. Carbon are gray and Mo are blue.....	219
6.7	A side view of <b>28</b> showing the 12 H-bonds formed between the hydrogen atoms on the pyrimidine ligands and the oxygen atoms of the two POM anions. All other hydrogen atoms have been omitted for clarity.....	220
6.8	(left) The asymmetric unit of <b>29</b> with the cation shown as 50% thermal ellipsoids and all other atoms in stick representation. In this figure, Mo is light blue, C gray, H light gray, N blue, and O red. The three unique Cu(I) centers, each with different coordinated components is shown on the right. In this figure, all non-hydrogen atoms belonging to the asymmetric unit are labeled.....	224
6.9	A single chain (top) of linked Cu(I) coordinated triangles and a side view (bottom) with the POM anions in place as is found in <b>29</b> . Both are shown in 50% thermal ellipsoids. Hydrogen atoms and the included MeCN solvent have been omitted...	225

6.10	The 1-D chain from <b>30</b> shown (left) lengthwise and (right) as viewed from the end in 50% thermal ellipsoids (anion in stick representation). The unique Cu and the associated nitrogen atoms and anion in the asymmetric unit are labeled and carbons unlabeled in gray. Hydrogen atoms have been omitted for clarity.....	227
6.11	Two chains as they stack together in <b>30</b> shown in 50% thermal ellipsoids. The anions are shown in stick representation and the hydrogen atoms have been omitted for clarity.....	228
6.12	A stick representation of the chains in <b>30</b> as they take on the appearance of a layered solid.....	229
6.13	The unit cell of <b>31</b> with the atoms belonging to the asymmetric unit labeled. Two additional pyrimidine ligands are included to illustrate the trigonal coordination of Cu(2). All atoms are shown as 50% thermal ellipsoids with hydrogen atoms omitted for clarity.....	235
6.14	The two Cu(I) centers in <b>31</b> combine to form a square building block unit. Shown as 50% thermal ellipsoids with hydrogen atoms omitted for clarity.....	236
6.15	Stick representation of (top) a face view of a single layer in <b>31</b> showing only the anion inside the layer in the peanut shaped cavities.....	237
6.16	That same layer as shown in Figure 6.15 as seen from the side (bottom) showing the positioning of the outer anion. Anions are shown as spheres and the hydrogen atoms are omitted.....	238
6.17	Stick representation of two layers in <b>31</b> as they are stack together. The perchlorate anion is shown as spheres and the hydrogen atoms have been omitted for clarity..	239
6.18	A side-by-side comparison of (left) <b>34</b> and <b>35</b> . The unit cell is doubled for <b>34</b> so a view of the porous network can be seen and compare to the tightly woven network of <b>35</b> . The anions have been omitted in <b>35</b> while both structures hydrogen atoms are omitted for clarity.....	246
6.19	The anion cage found in <b>34</b> . Hydrogen atoms are omitted for clarity.....	248
6.20	The three copper units found in <b>36</b> shown as 50% thermal ellipsoids. Hydrogen atoms and anions have been omitted.....	251
6.21	Two views of the cages from both (top) <b>36</b> and (bottom) <b>33</b> . Hydrogen atoms have been omitted for clarity.....	252
7.1	The two unique copper coordination tetrahedra of <b>37</b> and <b>38</b> . Hydrogen atoms have been omitted and the non-hydrogen atoms are represented as 50% ellipsoids.....	264

7.2	Stick representation of the cationic framework comprising the unit cell of <b>37</b> and <b>38</b> . The triflate cations are shown as ball and stick figures while the hydrogen atoms have been omitted for clarity. (b) An expanded, four unit cell view of <b>37</b> and <b>38</b> . The Cu – Cu bonds replace the bridging pyrimidines revealing a zeolite analog formed from the cationic network.....	266
7.3	The Cu(I) coordinated cage with anion in place for (top) <b>37</b> and (bottom) <b>38</b> . The hydrogen atoms have been omitted.....	267
7.4	One of the triflate anions as it sets into a corner in the <i>supercage</i> found in <b>37</b> . The anion and the hydrogen atoms associated with the H-bonding are shown as spheres while the rest of the structure is in stick representation.....	268
7.5	One of the two PF <sub>6</sub> <sup>-</sup> anions that sit in the supercage in <b>38</b> shown as spheres along with their H-bonded hydrogen atoms. The rest of the structure is in stick representation.....	269
7.6	The third PF <sub>6</sub> <sup>-</sup> anion found in the supercage in <b>38</b> shown as spheres along with their H-bonded hydrogen atoms. The rest of the structure is in stick representation.....	270
7.7	The anion exchange of triflate with BF <sub>4</sub> <sup>-</sup> and PF <sub>6</sub> <sup>-</sup> .....	271
7.8	The removal of the <sup>99m</sup> TcO <sub>4</sub> <sup>-</sup> radioanion in competition with other oxoanions. Each anion exchange was labeled with 30 μCi of <sup>99m</sup> TcO <sub>4</sub> <sup>-</sup> and monitored over a 22 hour period. ReO <sub>4</sub> <sup>-</sup> used as a surrogate for the long half lived, ( <sup>99</sup> Tc) pertechnetate anion.....	273
7.9	The XRPD patterns for <b>37</b> , before and after selected anion exchanges.....	274

## Supramolecular Chemistry and Porous Functional Solids

### 1.1 Introduction

There has been a virtual explosion in the research and development of functional porous solids in the past several years. Crystal engineering of these varied types of inorganic, organic, and metal-organic materials represents a rapidly expanding field that offers a seemingly unlimited source for new types of materials. The growing popularity in this type of research is indeed brought on by the ever-increasing demand arising from industry, information technology, and growing environmental concerns. The design of these materials by way of metal-organic hybrid coordination solids are rapidly taking the lead as they offer routes to materials with potential applications such as catalysis,<sup>1</sup> non-linear optics,<sup>2</sup> solvent extraction,<sup>3</sup> gas absorption,<sup>4</sup> and ion exchange.<sup>5</sup>

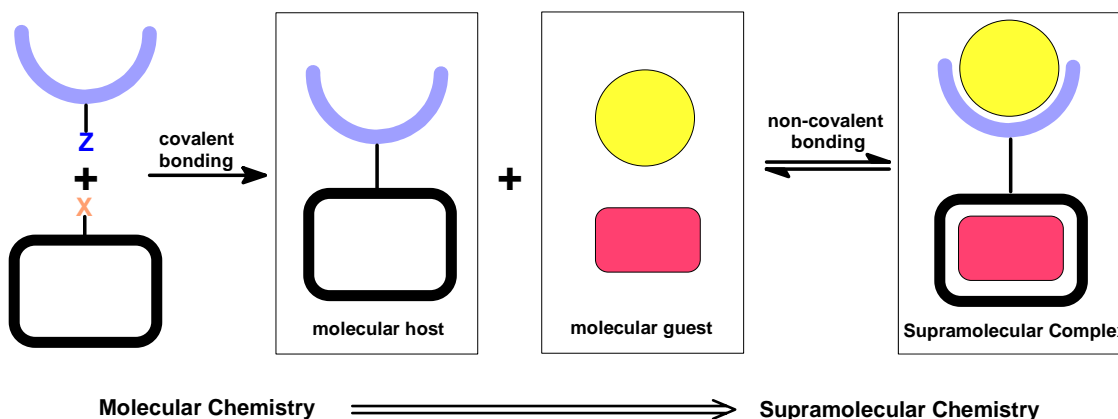
Adding to this need-based drive to produce new functional solids, the actual development of our current abilities and understanding also fuels this effort. In a sort of *quid pro quo* relationship, the same evolving technology creating the demand for these materials is also responsible for the improved methods used in today's research. For example, although X-ray crystallography has been around for several decades, in light of the recently developed high-speed personal computers, we can now get high quality results in a matter of hours that once took months to develop with much lower resolution and



accuracy.<sup>6</sup> Along with this increased ability to examine complex materials also comes our increased understanding of the intermolecular interactions in the study of *crystal engineering* as introduced by G. M. J. Schmidt in his study of organic solid-state chemistry.<sup>6,7</sup> Schmidt's ideas about self-assembly and molecular recognition soon spread to other areas of chemistry and helped evolve a multidisciplinary study that encompassed materials derived from both organic and inorganic components. Jean-Marie Lehn introduced this new and exciting field of study to the scientific community around 1969, won a Nobel prize in 1987 with related work in this area, and gave this study its name of which we have come to know today as *supramolecular chemistry*.<sup>8,9</sup>

## 1.2 Supramolecular Chemistry: Definitions and Design

*Supramolecular chemistry* is popularly defined simply as the “chemistry beyond the molecule.” Lehn describes supramolecular chemistry as “a highly interdisciplinary field of science covering the chemical, physical, and biological features of the chemical species of greater complexity than molecules themselves, that are held together and organized by intermolecular (non-covalent) binding interactions.”<sup>9</sup> While molecular chemistry deals with covalently bonded atoms forming molecules, supramolecular chemistry binds whole molecules via intermolecular forces and, thus, uses those molecules as building blocks in order to form new supramolecular *complexes*.<sup>9,10</sup> The illustration in Figure 1.1 shows the relationship between the molecular and supramolecular chemistry.<sup>10</sup>



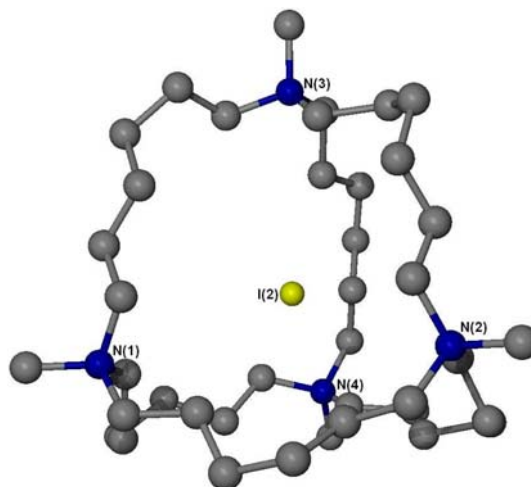
**Figure 1.1** Molecular chemistry is responsible for making the molecular building blocks that are brought together to form the supramolecular complex.

The intermolecular forces we speak of here are one of the key components in supramolecular chemistry. While these forces could be considered the “supramolecular glue” that binds the molecules together, they are also responsible for structural design as well as the unique properties these materials can exhibit. These intermolecular forces include (1) electrostatic attraction, (2) hydrogen bonding, (3) cation –  $\pi$  and  $\pi$  –  $\pi$  stacking interactions, and (4) van der Waals forces. The strength of these forces range from 350 kJ mol<sup>-1</sup> to 2 kJ mol<sup>-1</sup> and are considerably weaker than covalent bonds, which range from 350 kJ mol<sup>-1</sup> to 942 kJ mol<sup>-1</sup> (for a triple N<sub>2</sub> bond).<sup>11</sup> Details of these forces are as follows.

(1) *Electrostatic Attraction* consists of three subgroups.

- a. *Ion – Ion* interactions are the interactions between a cation and counter anion. These type of bonds are the strongest of the intermolecular forces with bond energies ranging 100 – 350 kJ mol<sup>-1</sup>.<sup>11</sup> Although not necessarily a supramolecular complex, the strong bond formed in solid NaCl is a good example of an ion – ion interaction. The macrotricyclic receptor, shown in Figure 1.2 represents a more supramolecular example of an ion-ion interaction with an iodide anion inclusion in a cationic host receptor.<sup>12</sup>

Prepared as a tetraiodide salt, one of the iodide ions was found bound in the center of the receptors cavity, equidistant from each of the four positively charged nitrogen atoms.<sup>10, 11, 12</sup>

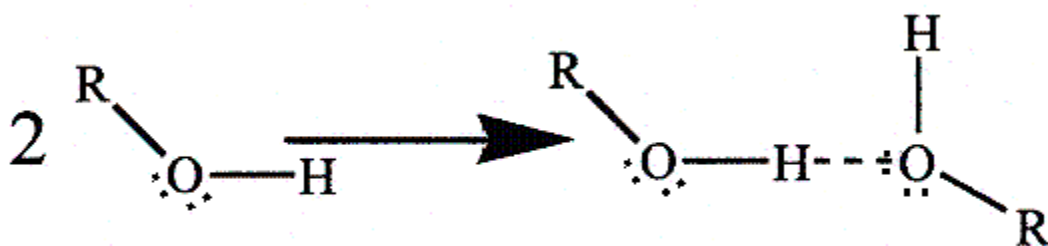


**Figure 1.2** Crystal structure of the macrotricyclic receptor with the guest iodide anion in the center. Carbon atoms are gray, nitrogen atoms blue and labeled, and the iodide atom is green and labeled.<sup>10, 12</sup>

- b. *Ion – Dipole* interactions with bond energies ranging  $50 - 200 \text{ kJ mol}^{-1}$  are described as the bonding between an ion and a polar molecule.<sup>11</sup> This can be seen in the bonding of water to sodium as NaCl disassociates in water forming the octahedral  $\text{Na}(\text{H}_2\text{O})_6^+$  complex. This also includes the *coordinative* (or dative) bonds between non-polarisable metal cations with hard base ligands. However, those coordination bonds involving transition metal cations to a Lewis base ligand (such as those found with the copper(I) coordination compounds) also exhibit a considerable amount of covalent interaction demonstrating a merging of the supramolecular and molecular definitions.
- c. *Dipole – Dipole* interactions are the last of these types of bonding forces

with bond energies ranging from 5 – 50 kJ mol<sup>-1</sup>.<sup>11</sup> Those most common are found in polar liquids, such as water, alcohols, and ketones and are more comparable to hydrogen bonding than the ionic variety.

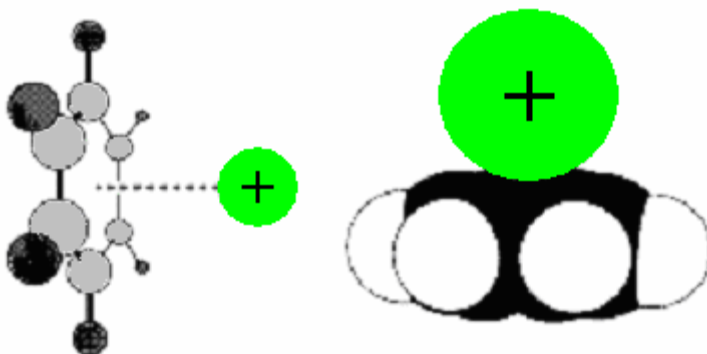
(2) *Hydrogen Bonding* is unique in its own right, being a dipole – dipole interaction between a hydrogen atom (attached to either an electronegative atom or electron withdrawing group) and an adjacent molecule's dipole. These types of bonds come in a wide range of energies from 4 – 120 kJ mol<sup>-1</sup> and constitute a major portion of bonding in supramolecular chemistry.<sup>11, 13</sup> They are described as the “masterkey interaction” because of their relative strength and highly directional nature.<sup>11</sup> Figure 1.3 shows how methanol H-bonds with itself. The hydrogen on one molecule is attracted to a lone pair on the oxygen, causing the directional characteristic of this important bonding interaction. The hydrogen bond's role in biological systems best illustrates its importance, as they are responsible for the shape and behavior of proteins and enzymes, including the well known double helix of DNA.<sup>11, 13</sup>



**Figure 1.3** Two methanol molecules showing directional H-bonding with each other.

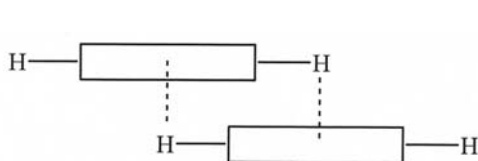
- (3) The two types of  $\pi$  interactions are
- cation –  $\pi$*  interactions, in which alkaline, alkaline earth metal cations, and

even molecular cations can interact with the  $\pi$  electrons on an aromatic hydrocarbon or C=C double bond.<sup>11, 14</sup> Figure 1.4 shows an example this as a potassium cation interacts with the aromatic benzene molecule.<sup>14</sup> These types of interactions have bond energies ranging 5 – 80 kJ mol<sup>-1</sup> and are also a very important component in biological systems.<sup>11, 14</sup>

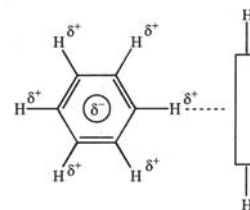


**Figure 1.4** A schematic of the K<sup>+</sup>-benzene cation –  $\pi$  interaction showing (left) the cation positioning over benzene along the 6-fold axis and (right) a space-fill model showing the K<sup>+</sup>-benzene complex at its optimized geometry.<sup>14</sup>

- b.  $\pi - \pi$  interactions, which are weak (0 – 50 kJ mol<sup>-1</sup>) electrostatic attractions between two aromatic rings.<sup>11</sup> These can either be face-to-face stacking, as seen in Figure 1.5a, or edge-to-face stacking as shown in Figure 1.5b.<sup>11</sup> Note that in the face-to-face stacking, the rings are offset from each other. Direct face – to – face stacking (in the case of two benzene molecules)



**Figure 1.5a** Face-to-face  $\pi$ -stacking showing the offset positioning of the rings.



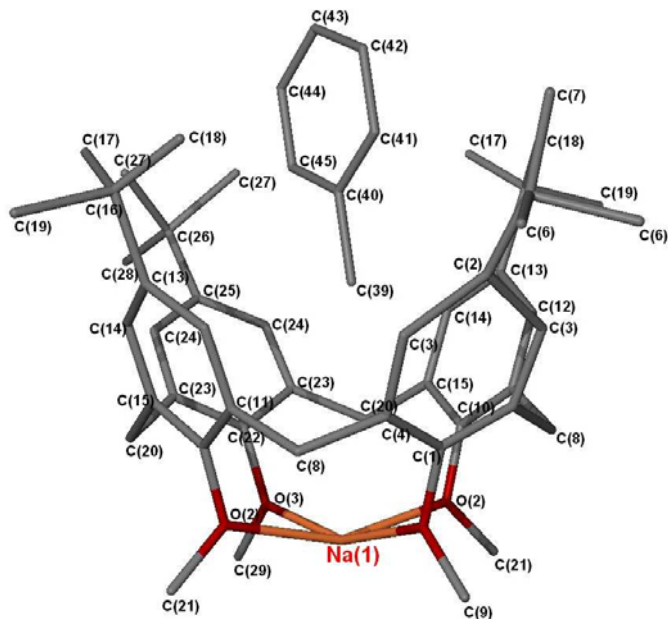
**Figure 1.5b** Edge-to-face  $\pi$ -stacking

would be repulsive. Substitutions on or about the aromatic rings involved,

however, lead to appropriate variations of the  $\pi - \pi$  stacking geometries.<sup>16</sup>

*Van der Waals forces* are the weakest of all the intermolecular forces with bond energies of  $< 5 \text{ kJ mol}^{-1}$ .<sup>11</sup> These forces are electrostatic forces between an electron cloud of one atom that is polarized by the nucleus of an adjacent atom.<sup>11</sup> These forces are non-directional and have limited use in supramolecular complex design. However, this type of bonding can be useful in the formation of *inclusion compounds*, which are crystalline lattices or molecular cavities that have molecules (such as organic solvents) loosely incorporated within their structure. Figure 1.6 shows the [*p-tert*-butylmethoxycalix[4]arene-sodium-toluene]<sup>+</sup> cation inclusion complex in which toluene is believed to be held in place by weak van der Waals interactions while the sodium cation is bound by much stronger ion-dipole forces.<sup>11, 18</sup>

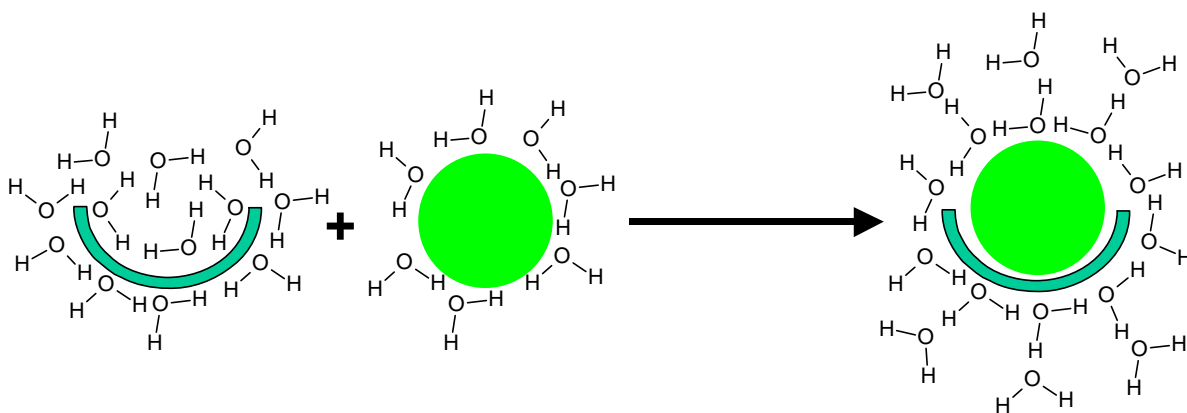
In addition to the aforementioned forces, there are two other driving forces that also dictate structure and properties in a supramolecular complex. *Close Packing* of solid-state structures, although not necessarily a force in itself, is very significant in structure determination nonetheless. In essence, it is the result of a molecular system seeking to maximize the packing forces as it arranges into a crystalline form.<sup>11, 19</sup> It has commonly been simplified in saying that “Nature abhors a vacuum” as these systems make the most use of empty space as possible.<sup>11</sup> A few materials, such as the zeolites shown in section 1.3, have structures composed of ridged frameworks that resist the close packing driving force and allow vast amounts of empty space to remain. We will show in later sections how the zeolites have inspired the supramolecular chemist in the design of synthetic porous solids.



**Figure 1.6** The X-ray crystal structure showing the  $[p\text{-tert-butylmethoxycalix[4]arene-sodium-toluene}]^+$  cation inclusion complex.<sup>11, 18</sup>

Finally, *hydrophobic effects* also play an important role in supramolecular chemistry.<sup>11</sup>

This is associated with those species that are excluded from a polar solvent such as water because they are insoluble or weakly soluble in that system. The result is the isolation of those insoluble species as the water (or other polar solvents) bond with one another, effectively squeezing out the insoluble species. These hydrophobic species agglomerate together, much like oil beads together when placed in water. This isolation effect is important for placing an insoluble guest into a hydrophobic host. As shown in Figure 1.7, when two hydrophobic species (as a host and a guest) are united in a polar solvent, the disruption to the solvent is decreased (since one hydrophobic species disrupts a system less than two), resulting in a favorable increase of entropy and the system's overall free energy reduction.<sup>10, 11</sup>



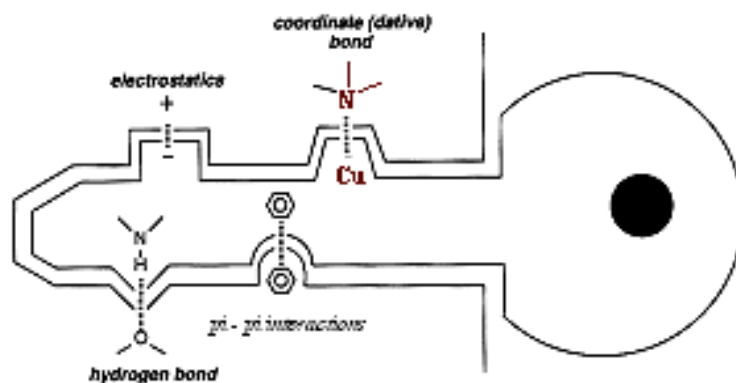
**Figure 1.7** The hydrophobic effect brings a guest and host together.

All of the intermolecular forces described above are put to use in the design of the supramolecular complex. In many cases, these complexes make use of all the forces listed. The novice might look at such an endeavor as haphazard, thinking that with so much going on, one could never predict what the final product might actually be. The supramolecular chemist, on the other hand, knows that the molecular building blocks often will follow a specific path as they *self-assemble* to form the supramolecular complex.

The term *self-assembly* (as used in supramolecular chemistry) refers to the spontaneous process by which molecular components come together to form the most thermodynamically favored complex under the given set of conditions.<sup>9, 11</sup> Supramolecules produced by this process are the result of a reversible, recognition-directed association of the molecular components (host and guest) being brought together by a multitude of intermolecular forces.<sup>9, 11</sup> The “haphazardness” of this process is avoided since each molecule in the final product has joined with only those molecules that possess *complimentary* forces or connection points. In a sort of *lock-and-key* arrangement, as first introduced by Emil Fisher in 1894 and illustrated in Figure 1.8, the receptor sites on the host are complimentary to those on the guest.<sup>10, 20</sup>



Although each component may interact with all others in a multitude of positions while going through the self-assembly process, these interactions are reversible and the self-assembly process continues until a stable structure of minimum energy is obtained. In many cases, this self-assembly is as simple as two components with complimentary sites coming together.<sup>9</sup> These “complimentary sites” are more aptly called *supramolecular synthons*, which are defined by Gautam Desiraju as being “structural units within

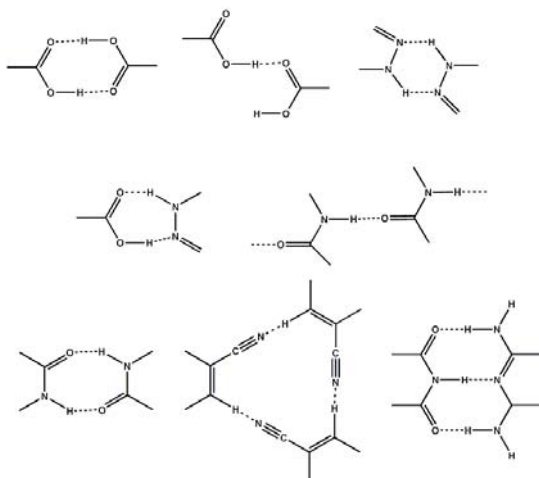


**Figure 1.8** The lock and key principle illustrating how the molecular forces of a host are complimentary to those of its guest in a supramolecular complex.<sup>10</sup>

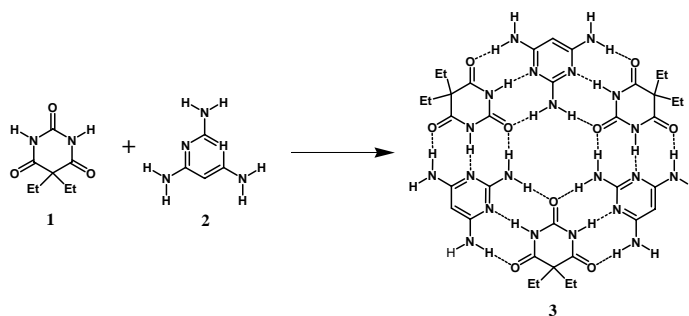
supermolecules which can be formed and/or assembled by known or conceivable synthetic operations involving intermolecular interactions.”<sup>21</sup> Figure 1.9a shows a few typical synthons and how can they join with each other, forming larger complexes. Examples of synthons at work can be seen in Figure 1.9b as it is shown how the self-assembly of barbituric acid with 2,4,6-triaminopyrimidine could lead to the formation of either a one-dimensional polymeric chain or a discrete macrocycle.<sup>9,22</sup>

Of course, this process is far from original as it is one of the major features in biological systems.<sup>10</sup> Enzymes owe their high specificity to catalyze a single reaction solely to the nature of the complimentary molecular systems.<sup>10,11</sup> The most important example of the lock and key principle, one responsible for the continuous replication of life

itself, is in the formation of the double helix of DNA as two antiparallel strands of genetic material are held together by complimentary hydrogen bonds between pairs of purine and pyrimidine bases positioned along each strand.<sup>10</sup>

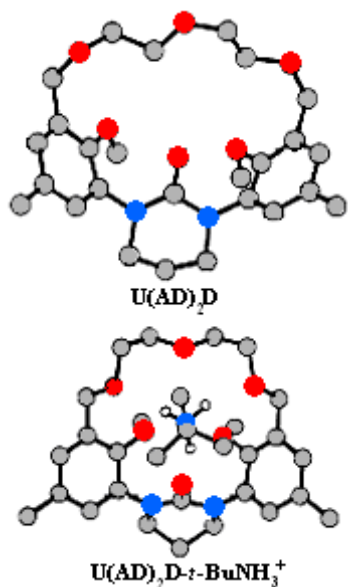


**Figure 1.9a**  
A few examples of synthons and how they fit together forming the supramolecular complexes.

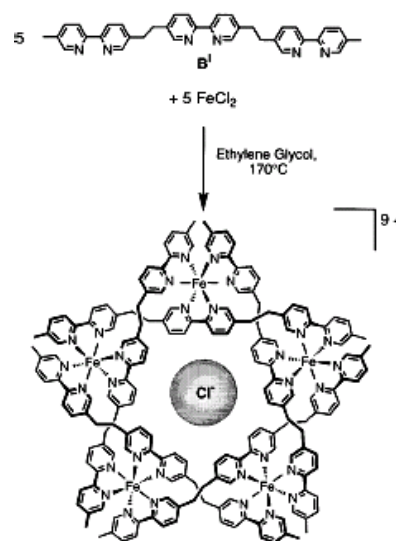


**Figure 1.9b**  
Synthons allow barbituric acid **1** and 2,4,6-triaminopyrimidine **2** to fit together forming a macrocycle **3**.<sup>22</sup>

In addition to the lock and key principle, self-assembly is also controlled by using other organizing techniques such as cation and anion *templation*. Not only can the ionic forces lock a cation or anion into a host complex, these forces can also be responsible for the overall structure of the complex. Figure 1.10a shows how the  $t\text{-BuNH}_3^+$  cation can organize the semi-rigid framework of an organic host.<sup>23</sup> As the cation is positioned into the host, the electronegative oxygen atoms are directed symmetrically towards the cation's positive charge.<sup>23</sup> Complexes can also be formed around a positive or negatively charged ion allowing the ion to act as a template in the self-assembly. In many cases both the cation and anion work together to form a complex in this way. In the case shown in Figure 1.10b, both the electrostatic attraction of the  $\text{Cl}^-$  anion with the cationic framework and the octahedral coordination bonds formed between the organic ligand and  $\text{Fe}^{2+}$  play a part in the formation of this five-sided pentanuclear circular helicate.<sup>24</sup>



**Figure 1.10a** The addition of the  $t\text{-BuNH}_3^+$  cation helps to organize a hemispherand complex.<sup>23</sup>



**Figure 1.10b** Both the  $\text{Fe}^{2+}$  cations and the  $\text{Cl}^-$  anion act as templates to form this pentanuclear circular helicate.<sup>24</sup>

Finally, since these reactions are usually carried out in a variety of solvents, each solvent can exhibit its own unique degree of influence on the self-assembly process. In addition to the hydrophobic effect mentioned earlier, there can also exist binding forces between the host and solvent, or guest and solvent that are essentially the same type as those between the host and guest.<sup>25</sup> During self-assembly, solvents are competing with all other species in the reaction for binding sites.<sup>25</sup> The extent of this competition should vary considerably as the type of solvent is varied, just as binding abilities vary with different hosts and guests. In later sections, we will show the profound influence the cation, anion and solvent actually have in the self-assembly of several metal-organic complexes.

### 1.3 Natural Porous Solids: Zeolites and Clays

As was pointed out earlier, many of the supramolecular designs and strategies were inspired by Nature's own design of biological systems. In the same light, we can also learn

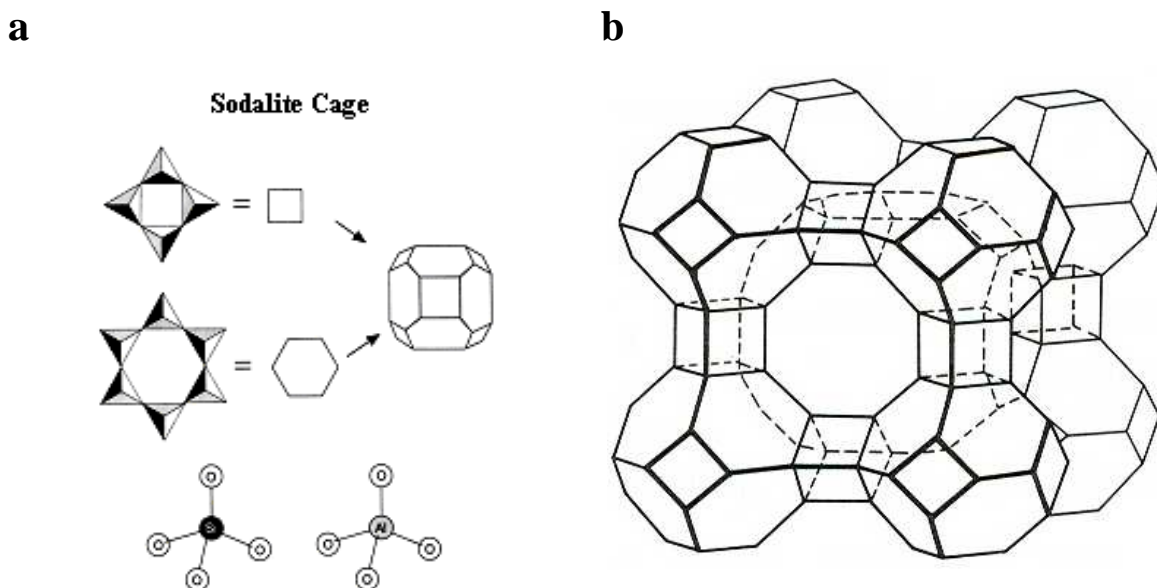
from the earlier creations (i.e., the silicate minerals that comprise the bulk of our planet's crust and have been present long before even the simplest of life had evolved). In keeping with the subject at hand, we will examine those silicate minerals that developed as zeolites and clays: Nature's own functional porous solids.

Zeolites are crystalline, hydrated aluminosilicate minerals having infinite, open, three-dimensional structures. These naturally porous solids are the result of the slow reaction of saline water with volcanic glass.<sup>27</sup> Its structure is generally composed of corner shared  $\text{SiO}_4$  and  $\text{AlO}_4$  tetrahedra resulting in the formation of a microporous network. These pores vary from 4 to 7 Å in diameter, channel directly through the solid, and are a natural haven for water molecules.<sup>27</sup> In fact, the name *zeolite*, given by Baron Axel Cronsted in the mid 18<sup>th</sup> century, derives from the Greek for "boiling stone" as Cronsted observed that this mineral bubbled and steamed upon heating.<sup>27</sup> The microporous networks also provide an extraordinarily high amount of exposed surface. Described as being virtually *all* surface area, one gram of a typical zeolite has the surface area equal to 900 square meters!<sup>27</sup>

The many variations in zeolites are seen by the variation in the  $\text{Al}^{3+}/\text{Si}^{4+}$  ratio as well as in the counter anion.<sup>30</sup> Since each of the tetrahedra in the zeolite network are corner shared, the  $\text{SiO}_4$  units are uncharged while the  $\text{AlO}_4$  units bear a negative charge. This results with the network exhibiting a negative charge, dependant on the amount of aluminum substituted into the formula. Counter anions are present within the porous network to balance the negative charge. The anions most commonly found are metals from Group 1 or 2 but these can also be molecular organic anions, as found in some synthetic zeolites.<sup>28, 30</sup>

Figure 1.11a shows how the zeolite network consists of cubic cages formed by a

smaller *secondary building unit* (SBU). These SBUs are linked by oxygen bridges between the adjacent faces.<sup>27, 28, 30</sup> One of the first synthetic zeolites, Zeolite A (Figure 1.11b) has the formula,  $\text{Na}_{12}(\text{AlO}_2)_{12}(\text{SiO}_2)_{12} \cdot x\text{H}_2\text{O}$ . Eight SBUs are linked into a cubic



**Figure 1.11** (a) The  $\text{SiO}_4$  and  $\text{AlO}_4^-$  tetrahedra as they form the *Secondary Building Unit* (SBN).<sup>27</sup> (b) The SBN are linked together via oxygen bonds to form the larger  $\alpha$ -cavity as in Zeolite A.<sup>29</sup>

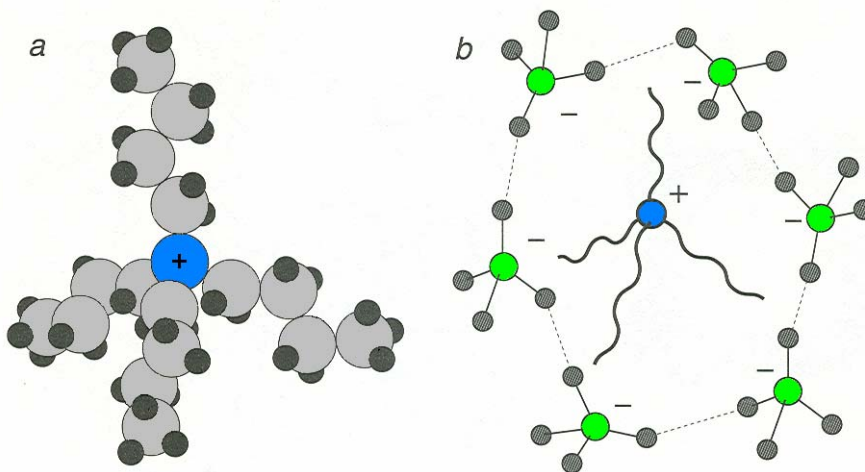
pattern forming a larger central cavity called the  $\alpha$  cage or the *supercage*.<sup>28, 29</sup> In this example, the  $\alpha$  cages share octagonal faces, with an open diameter of 4.20 Å.<sup>29</sup> This supercage is home for both the sodium anion and the water contained in the structure. Since these cages are channeled throughout the structure, the water can be reversibly removed and the anions can readily exchange with other anions.<sup>28</sup>

The unique properties of zeolites were first realized as far back as the mid 19<sup>th</sup> century when they were noted to undergo anion exchange and solvent absorption. By the 1950's, zeolites became well known for their use in catalysis and as molecular sieves.<sup>27, 28</sup> Earlier studies began to rely on synthetically developed zeolites because of the natural forms lack of availability. Although there has been dramatically increasing success in locating natural

zeolite resources as well as developing applications for their use,<sup>31</sup> synthetic varieties continued to emerge, providing an even greater selection of pore shapes and sizes.<sup>28, 30, 32</sup>

Metals such as gallium, boron, and beryllium have even been incorporated into the synthetic zeolite structure in an attempt to ‘fine tune’ the zeolite’s catalytic properties.<sup>27, 32</sup> Phosphorous, for example, can be used in place of silicon, which, in conjunction with aluminum, can form a variety of aluminophosphate, zeolite-like materials. In 1988, researchers at Virginia Polytechnic Institute synthesized an aluminophosphate zeolite that was found to have unusually large pores and demonstrated unique catalytic activity.<sup>27</sup>

Figure 1.12 illustrates what could be considered as an early form of inorganic supramolecular chemistry, employed in the early 1960’s. In this example, George Kerr’s team at Mobile Oil used an organic tetraalkylammonium anion as a *template* to control the size and shape of a synthetic zeolite’s pore network.<sup>28</sup> This technique eventually led to the discovery of one of the most important zeolitic catalyst called ZMS-5, which has the ability to catalytically convert methanol to gasoline.<sup>28, 33</sup>

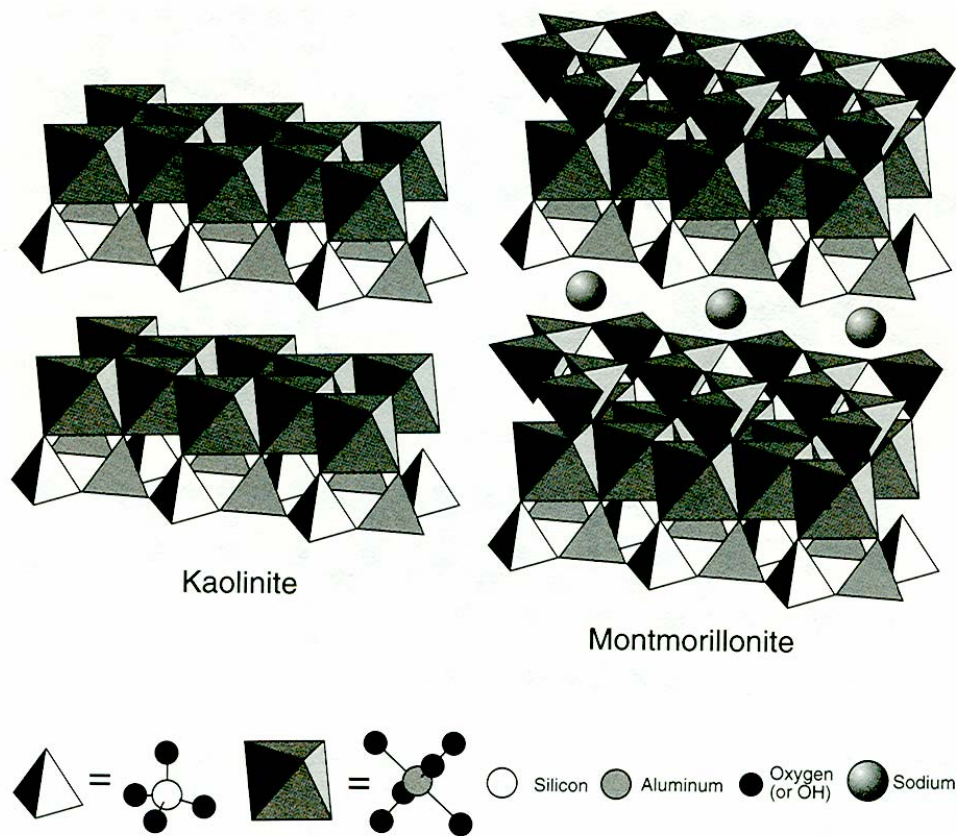


**Figure 1.12** The four appendages of the positively charged tetraalkylammonium anion can act as a template around which silicate and aluminate ions link together to form the walls of the zeolite’s cavity. The alkyl chain appendages were varied from 3 to 7 carbons long to produce different size pores.<sup>28</sup>

*Clays* are a member of a silicate class known as the *phyllosilicates*, derived from the Greek for ‘sheets’ in reference to how the silicates and aluminates in the clays link together to form two-dimensional sheets or stacked layers.<sup>34, 35</sup> This family of abundant and important minerals also includes talc and various micas, and are (more often than not) found containing other metals, such as lithium, magnesium and iron.<sup>28, 35</sup> Instead of channeling pores, clays have gaps between each layer that allow the reversible inclusion of solvents and gasses as well as an available route for ion exchange, catalysis, and a wide variety of other important chemical reactions.<sup>28, 35</sup> There are two basic types of clay structures: the 1:1 type, in which each layer is composed of a layer of linked silicate tetrahedra capped off by octahedrally coordinated sheets of either *gibbsite*  $[Al_2(OH)_6]$ , or *brucite*  $[Mg_2(OH)_6]$  units; and the 2:1 type, in which the octahedra layer is sandwiched in-between two layers of linked silica tetrahedra.<sup>28, 35</sup>

Kaolinite  $[Al_2Si_2O_5(OH)_4]$ , shown in Figure 1.13, is a typical example of the 1:1 type clay and is the main constituent of china clay<sup>28, 35, 36</sup> The layers of kaolinite are uncharged and, as they stack together (like pages in a book), there is no ionic bonding in-between them; each layer is bound to the other by weak hydrogen bonds.<sup>35, 37</sup> Disorders in the ‘ideal’ kaolinite formula do occur with a typical disorder seen as  $[Al_{1.8}Fe_{0.1}Mg_{0.1}]Si_2O_5(OH)_4$ , which results in an overall negative charge on the layers.<sup>36</sup> This charge is balanced by the inclusion of cations (such as  $Ca^{2+}$ ) between the layers, which accounts for reports of cation exchange abilities found with some types of kaolinite-like clays.<sup>36, 38</sup>

Montmorillonite  $[Na_{0.6}Al_{3.4}Mg_{0.6}Si_8O_{20}(OH)_4] \cdot H_2O$ , also shown in Figure 1.13, is an example of a 2:1 type clay and is also called a *smectic clay* because of its ability to swell

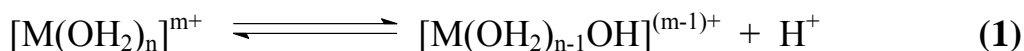


**Figure 1.13** *Kaolinite* is an example of the 1:1 type and *Montmorillonite* 2:1 type clay.<sup>28</sup>

and absorb large amounts of water.<sup>28, 35, 36</sup> The chemistry of the smectic clay is considerably diverse and includes cation exchange, as well as a wide variety of acid-catalyzed organic reactions.<sup>35</sup> The cation exchange and storage ability of this type of clay is very important in maintaining proper soil chemistry.<sup>35</sup> The isomorphous substitutions of  $\text{Al}^{3+}$  for  $\text{Si}^{4+}$  in the tetrahedral layers or  $\text{Mg}^{2+}$  for  $\text{Al}^{3+}$  in the octahedral layers cause the layers to develop a negative charge.<sup>35, 36</sup> This charge is balanced by the inclusion of hydrated metal cations such as  $\text{Na}(\text{H}_2\text{O})_n^+$ ,  $\text{Ca}(\text{H}_2\text{O})_n^{2+}$ , or  $\text{Mg}(\text{H}_2\text{O})_n^{2+}$  in-between the clays layers.<sup>35, 39</sup> These cations are weakly bound and can easily exchange with other cations from an aqueous solution.<sup>35, 40</sup>



There are also several clay-mediated organic reactions due to the clay's naturally high degree of Brønsted and Lewis acidity. The Brønsted acidity is due to the dissociation of the exchangeable cation's coordinated water molecules (Equation 1).<sup>35, 41</sup>



This type of acidity depends upon the water content and can be increased, to an extent, by dehydration of the clay material.<sup>35, 41a, 42</sup> This procedure tends to be problematic as too much dehydration can lead to reduced acidity as well as permanent collapse of the clay layers.

The Lewis acidity is due to exposed  $\text{Al}^{3+}$  and  $\text{Fe}^{3+}$  cations at breaks in the clays crystalline network.<sup>35, 43</sup> It is possible to increase this type of acidity by heating the clay at temperatures  $>300^\circ \text{C}$ .<sup>35</sup> At these temperatures, dehydration is again an issue and as before, leads to the collapse of the clay layers, ending the materials usefulness as a porous solid.

Clays can also serve as catalyst support material as a variety of metal cations such as the Pt tetraammine cation,  $\text{Pt}(\text{NH}_3)_4^{2+}$ , can replace the materials original  $\text{Na}^+$  or  $\text{K}^+$  ion (as it may be).<sup>32</sup> The deposition of metal chlorides (with Zn, Cu, Mg, Co, Ni, Cd, or Al) into montmorillonite via a methanolic solution is also a favorite.<sup>32</sup> This process requires additional activation by heating at  $50 - 300^\circ \text{C}$  so, as can be imagined; dehydration can again be a problem.<sup>35</sup> Even if the clay preparation is successful, usage of the material for catalysis also generates heat, resulting in eventual dehydration and destruction of your catalytic material.<sup>32</sup>

In order to avoid this collapse of layers, support is added to the clay layers by propping the layers open with large molecular inorganic cations.<sup>35, 44, 45</sup> This process is known as *pillaring* and can not only add structural integrity to the clay but also results in a

porous solid much like the zeolite.<sup>35, 45</sup> This is accomplished by immersing a clay in water that contains the pillaring cation such as  $[Al_{13}O_4(OH)_{24}(H_2O)_{12}]^{7+}$  or  $(Nb_6Cl_{12})^{2/3+}$ . The clay swells as it absorbs the water, allowing the large pillar cation to exchange with the  $Na^+$  cation.<sup>28, 45, 46</sup> After the exchange is complete, the water is removed and the pillars remain in place, resulting a secured, porous solid with improved diffusion, sorption, and catalytic properties.<sup>28, 45, 46</sup> These pillars can even be designed from materials that add to the catalytic activity, further enhancing the clays functionality.<sup>28, 45, 46</sup>

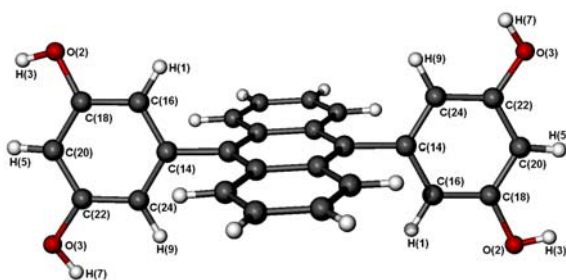
## 1.4 Supramolecular Zeolite and Clay Mimics

In the previous section we have shown how natural porous solids are versatile in both design and function. As we had just shown in the previous section, efforts to improve on Nature's own design of these materials have indeed been quite successful using such methods as elemental substitution in the basic formula, ion templation, and clay pillaring. As supramolecular chemist, we envision these porous materials constructed from molecular units joined by the traditional intermolecular forces. Not only do we look to mimic the zeolite's and clay's structure and behavior, but also to go beyond this and develop materials with novel design and functionality. There are several studies are underway in the development of supramolecular organic and metal-organic porous solids – far too great a number to mention all in this report. Therefore, we will attempt touch on a few key items and studies to present the general idea.

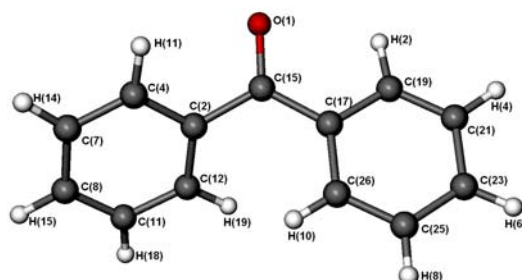
There is a distinct difference between the strong covalent/ionic bonding found in natural zeolites and clays, and the much weaker intermolecular forces as found in self-assembled, supramolecular materials. However, a true supramolecular zeolite or clay

mimic/analog should still meet the following criteria: the material should be capable of reversible guest-binding,<sup>47</sup> the guest molecules should be kept in internal cavities constructed by intermolecular forces,<sup>47, 48</sup> and these internal cavities should be maintained in the absence of the guest; or, at least be restored to original form when the guest is returned.<sup>47, 49</sup>

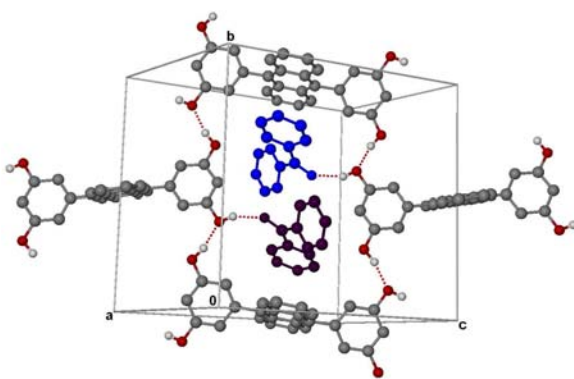
Keeping a purely organic porous solid together by only the weakest of the intermolecular forces has to be one of the greatest challenges for the supramolecular chemist. Figures 1.14a-d show the results of what is described as a successful synthesis of a zeolite analog.<sup>47</sup> The orthogonal anthrazene –bis(resorcinol) tetraol molecule shown in



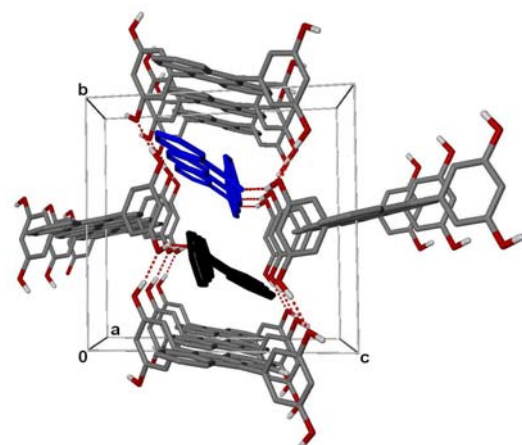
**Figure 1.14a** The anthrazene – bis(resorcinol) tetraol building block for the host network.<sup>47</sup>



**Figure 1.14b** Benzophenone – the guest molecule.<sup>47</sup>



**Figure 1.14c** A single enclosure formed by the hydrogen bonded bis(resorcinol) tetraol (black) with two guest benzophenones (blue and red). Hydrogen atoms have been omitted for clarity.<sup>47</sup>



**Figure 1.14d** Four overlapping host enclosures (black) with the benzophenone guests (blue and red). Hydrogen atoms have been omitted for clarity.<sup>47</sup>

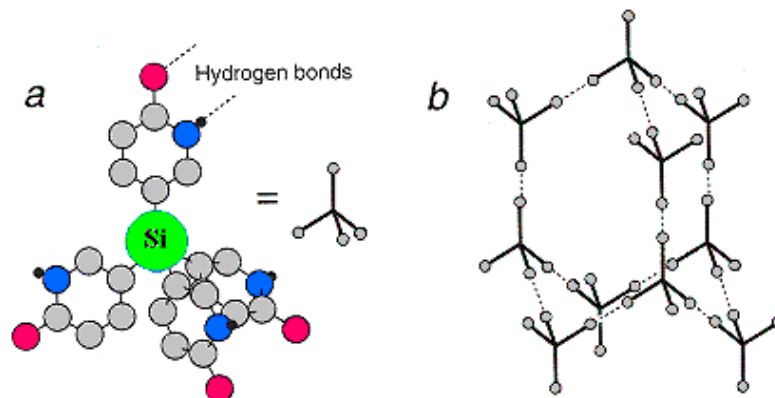
Figure 1.14a forms an extensive hydrogen-bonded host network of large supramolecular cavities.<sup>47</sup> Two benzophenone molecules, shown in Figure 1.14b, act as guests in each cavity. Figure 1.14c shows a single cavity host with benzophenone guests in place. Several overlapping layers are shown in Figure 1.14d, illustrating how the cavities line up and form channels through the solid.<sup>47</sup> Studies have shown that exchange of the benzophenone guest with a variety of other ketones was successful without destruction of the host network.<sup>47</sup>

This example brings us to another important concept used in supramolecular chemistry, *molecular tectonics*. The word *tectonic* is derived from the Greek referring to the design and construction of buildings or other structures.<sup>50</sup> Just as *plate tectonics* has been used by geophysicists to describe the structure of the earth's crust, crystal engineers have adopted the term *molecular tectonics* to describe the strategy for building predictable ordered molecular networks. In light of this, the anthrazene – bis(resorcinol) tetraol molecular building blocks from the previous example, are referred to as *tectons*, which are defined as “molecules whose interactions are dominated by attractive forces that induce the assembly of aggregates with controlled geometries.”<sup>51</sup>

While there are several other studies that make use of tectons similar to those used in the previous example,<sup>52</sup> others have adopted a more rudimentary approach by employing tectons with geometries similar to those tetrahedra found in zeolites and clays.<sup>53</sup> Figure 1.15a shows examples of this type of tecton as used by Jim Wuest at the University of Montreal.<sup>28, 53</sup> The silicon-centered tetrahedron pictured here exhibits dual hydrogen binding at each of the four vertices.<sup>28, 53a</sup>

As illustrated in Figure 1.15b, this tecton self-assembled into a 3-D diamondoid

structure<sup>28, 53a</sup> Crystal packing forces, however, strived to fill in the gaps, resulting in *interpenetration*, in which two independent tetrahedrally coordinated networks weaved in and out of each other.<sup>28, 53a</sup> Still, these structures continue to have considerable porosity and are able to include guest molecules such as propionic acid.<sup>53a</sup> Structures of this type were also found to be robust and exhibit zeolite-like characteristics, as the included acid



**Figure 1.15** (a) Tetrahedral tectons made by Jim Wuest and his colleagues that can form (b) diamonoid networks that tend to interpenetrate with each other.<sup>28</sup>


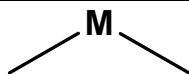

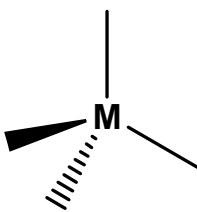
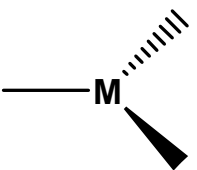
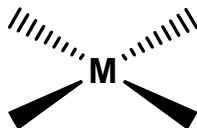
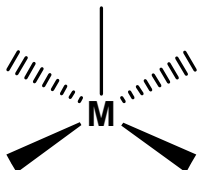
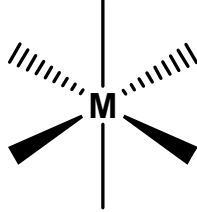
can be exchanged with similar acids while still maintaining the material's structural integrity.<sup>53a</sup>

The development of porous solids by way of transition metal coordination polymers results in the most silicate-like materials of all the supramolecular metal-organic methods mentioned so far. Not only does the tetrahedral and octahedral geometry of the metal ions coordination sphere match those building blocks found in the aluminosilicate minerals, but also the strong metal – to – Lewis base ligand coordination is much more like the covalent/ionic bond found in the aluminosilicate networks.<sup>11</sup> These coordination polymers can even offer a wider variety of structural possibilities as these porous solids can also utilize linear, bent, trigonal, T-shaped, square planar, and pyramidal coordination geometries about a variety of metal centers.<sup>54</sup> The various coordination geometries that

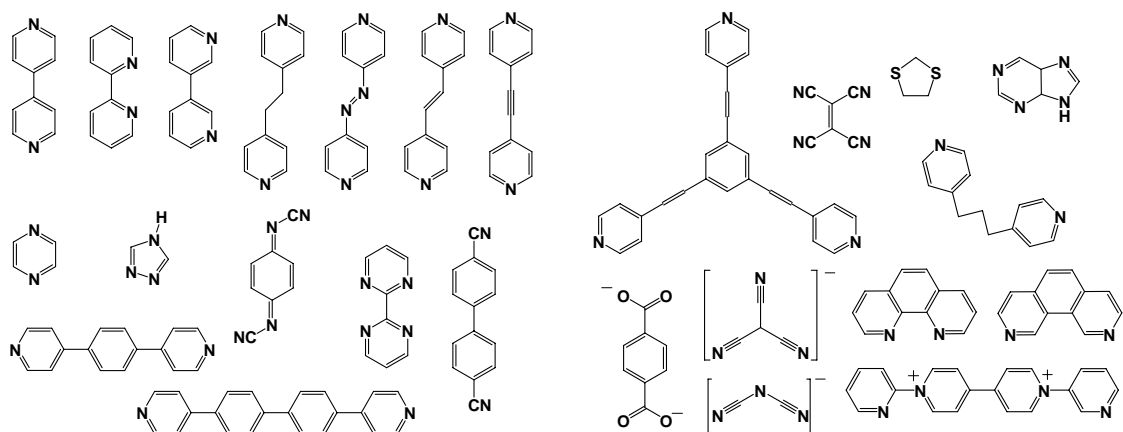
have been found are dependent on both the type of metal involved and on changes in the reaction conditions; such as the nature of the anion, ligand, or even the reaction solvent.<sup>55</sup>

Table 1.1 presents a few examples of those metal cations used along with the aforementioned coordination geometries. Included in the table are some examples of the

**Table 1.1** A few of the metal cations and the counter anions used by others along with the various metal coordination geometries available.

Metal Cations			Metal Coordination Geometries	
$\text{Cd}^{2+}$	$\text{Mn}^{2+}$	$\text{Ag}^+$		
$\text{Zn}^{2+}$	$\text{Cu}^{2+}$	$\text{Cu}^+$		
$\text{Pt}^{2+}$	$\text{Ni}^{2+}$	$\text{Fe}^{2+}$		
$\text{Co}^{2+}$	$\text{Co}^{3+}$	$\text{Fe}^{3+}$		
Anions				
$\text{Cl}^-$	$\text{NCS}^-$	$\text{BF}_4^-$		
$\text{PF}_6^-$	$\text{ClO}_4^-$	$\text{CF}_3\text{SO}_3^-$		
$\text{NO}_3^-$	$\text{HSO}_4^-$	$\text{SiF}_6^{2-}$		
$\text{N}_3^-$	$\text{CN}^-$	$\text{NO}_2^-$		

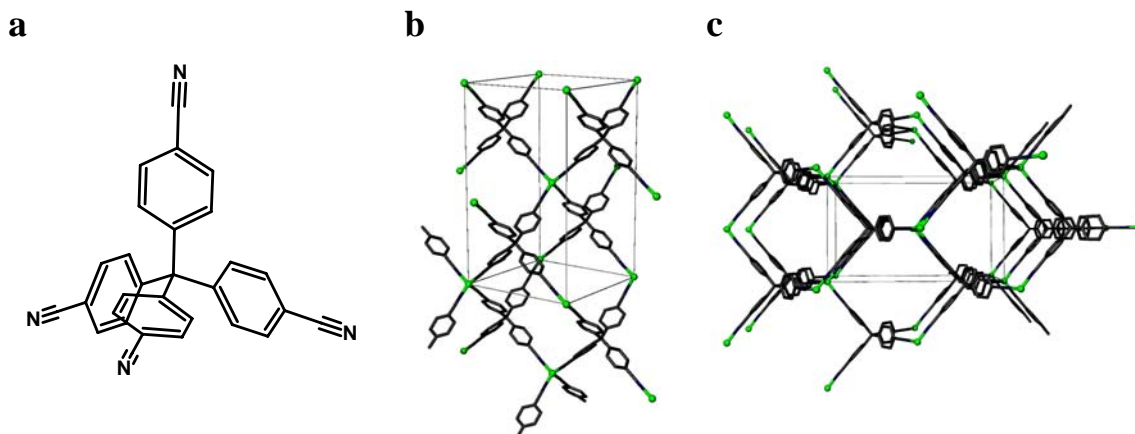
anions used, which are needed to balance the positive charge found on the coordination network. In some cases, the anions also can act as ligands, resulting in the formation of a neutral network. With the multitude of metal – anion combinations, along with the numerous varieties of bridging ligands available (just a few examples shown in Figure 1.16), there is tremendous potential to develop a virtually unlimited variety of porous coordination networks.<sup>54</sup>



**Figure 1.16** An assortment of organic bridging ligands; both neutral and charged.

The first porous coordination solid to exhibit anion exchange was reported by Richard Robson of the University of Melbourne in 1990. In his report, Robson had shown that the large cavity coordination solid,  $[\text{Cu}(4,4',4'',4'''\text{-tetracyanotetraphenylmethane})] \cdot \text{BF}_4 \cdot \text{C}_6\text{H}_5\text{NO}_2$  successfully undergoes anion exchange with  $\text{PF}_6^-$  anions while maintaining its structural integrity.<sup>54, 56b</sup> As shown in Figure 1.17, this diamond-like, non-interpenetrating network has large adamantane-like cavities with a volume (defined by the van der Waals surfaces surrounding ligand arms) of  $\sim 700 \text{ \AA}^3$ .<sup>56a</sup> This unusually large cavity is due to the use of the large, tetrahedral 4,4',4'',4'''-tetracyanotetraphenylmethane (tctpm) ligand, shown in Figure 1.17a. Each of the four “arms” on this tecton-like ligand extend to 8.856(2) Å as the nitrogen atoms on each end coordinate to a Cu center.<sup>56</sup> Figure 1.17b shows how the four Cu corners of the cavity’s center is bound by the parameters of the  $[13.620(2)]^2 ab$  face of the unit cell with the diagonal across this face being 19.26 Å and the diagonal along the c axis of the tetragonally distorted adamantane cavity at 22.64 Å.<sup>56</sup> The large cavity results in considerable disorder of both the nitrobenzene solvent and  $\text{BF}_4^-$  and is described as “essentially being ‘liquid’ nitrobenzene together with  $\text{BF}_4^-$  anions in the interstitial

space.”<sup>56a</sup>



**Figure 1.17** (a) The 4,4',4'',4'''-tetracyanotetraphenylmethane (tctpm) tecton and (b) as it coordinates to copper in the unit cell. The diamondoid extended network shown in (c) with its large, channeling cavities in view. Copper atoms are shown as green balls, while carbon and nitrogen atoms are gray and blue stick, respectively. Hydrogen atoms and both the anion and solvent were not included in the original crystal structure data because of unusually high crystallographic disorder.<sup>56</sup>

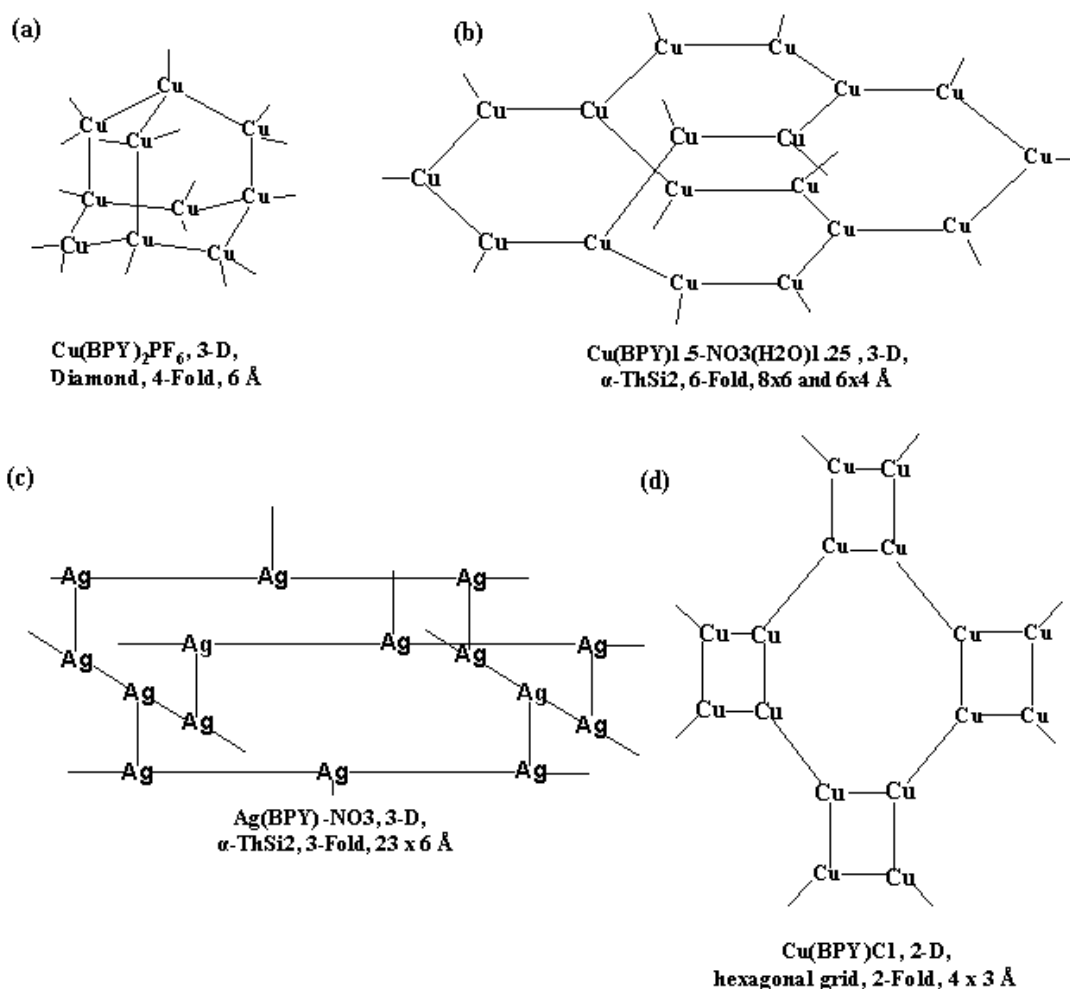
A few more examples of porous extended coordination networks are shown in Figure 1.18, including both cationic and neutral networks.<sup>57</sup> These structures demonstrate, in a small way, how a simple linear ligand, such as 4,4'-bipyridine (bpy), can act as rods linking metal centers to produce extended solids with diverse topologies and functionality. Each of these structures exhibit network interpenetration as packing forces attempt to fill the crystalline voids. Although network interpenetration could hamper the formation of porous solids, it also can provide important structural stability as intertwined networks act as reinforcement to the overall structure. The majority of these structures presented here have retained a variable degree of porosity, even with multiple interpenetrated networks.<sup>58</sup>

The host-guest ionic interactions were described as being too strong to permit successful anion exchange in the 4-fold interpenetrated diamond-like network shown in Figure 1.18a. Even with the presence of 6 Å pores, attempts to exchange the  $\text{PF}_6^-$  anion with  $\text{BF}_4^-$ ,  $\text{CN}^-$ , and  $\text{MoO}_4^{2-}$  resulted in an apparent breakdown of the network and formation of a condensed non-porous phase.<sup>57, 59a</sup> This is not the case, however, for those



structures shown in 1.18b and c; even with their own 6- and 3-fold interpenetration respectively.<sup>57, 59b, c</sup>

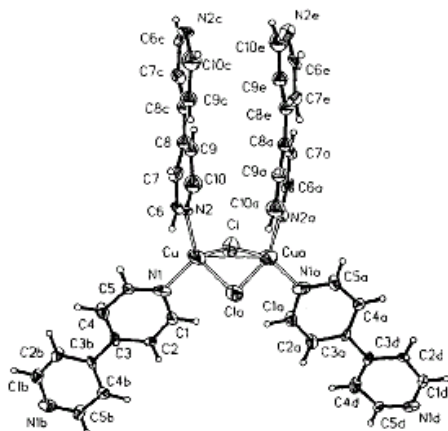
The structure of  $\text{Cu}(\text{bpy})_{1.5}\cdot\text{NO}_3\cdot\text{H}_2\text{O}$  (1.18b) facilitates anion exchange by using water-nitrate hydrogen bonded aggregates as guest.<sup>59b</sup> These aggregates are found within  $8 \times 6$  and  $6 \times 4 \text{ \AA}$  pores that are present in the six identical interpenetrated  $\text{Cu}(\text{bpy})_{1.5}^+$  networks. After thermally liberating the water guests, the nitrate anion can freely exchange with anions such as  $\text{BF}_4^-$  and  $\text{SO}_4^{2-}$ .<sup>57, 59b</sup>



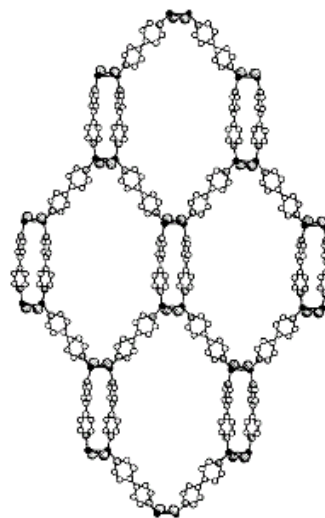
**Figure 1.18** Line representations of a few examples of metal – 4,4'-bipyridine (M – BPY) porous extended networks. The lines represent BPY, except for the vertical lines in (c) and the horizontal lines in (d), which, respectively, indicate Ag – Ag and Cu – Cu. The chemical formula, dimensionality of the M – BPY network, number of interpenetrating networks, and pore aperture size are listed, respectively, beneath each representation.<sup>57, 59</sup>

Large 23 x 6 Å rectangular channels in Ag(bpy)·NO<sub>3</sub> (1.18c) result from the Ag-bpy chains, which are then linked by Ag–Ag bonds of 2.977(1) Å to form a 3-D network.<sup>57, 59c</sup> Even with this structure's three interpenetrated networks, the nitrate guest appears to be weakly bound as it can readily exchange with PF<sub>6</sub><sup>-</sup>, BF<sub>4</sub><sup>-</sup>, SO<sub>4</sub><sup>2-</sup>, or MoO<sub>4</sub><sup>2-</sup> without any apparent degradation of the framework integrity.<sup>57, 59c</sup>

The extended structure of [Cu(bpy)Cl] is an example of a neutral porous structure because the chloride anions have coordinated to the metal center. This type of synthesis is described as utilizing a building-block approach as chloride bridged Cu(I) dimers are linked by bpy rods.<sup>59d</sup> The building-block, as shown in Figure 1.19, is composed of two Cu(I) centers bridged by chloro ligands, with two linked bpy ligands forming a slightly distorted tetrahedron about both metal centers.<sup>59d</sup> The bpy ligands bridge to other Cu(I) dimeric units,



**Figure 1.19** The  $\mu_2$ -chloro-bridged Cu(I) dinuclear building-block found in [Cu(bpy)Cl]. Non-hydrogen atoms are represented by 50% thermal ellipsoids.<sup>59d</sup>



**Figure 1.20** A portion of the infinite porous sheet formed by the organization of the building-block unit, [Cu(bpy)Cl]<sub>4</sub>. Hydrogens have been omitted for clarity. Dark spheres, Cu; Large grey spheres, Cl; small white spheres, C and N.<sup>59d</sup>

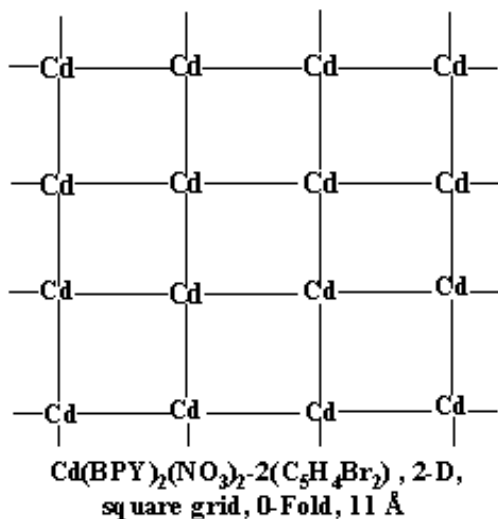
resulting in the formation of an infinite hexagonal sheet (Figure 1.20) with pores measuring  $16 \times 26 \text{ \AA}$ .<sup>59d</sup> However, the perpendicular interpenetration by other  $[\text{Cu}(\text{bpy})\text{Cl}]_n$  sheets fill most of the space in the pores, resulting in only  $4 \times 3 \text{ \AA}$  pores to remaining in the structure.<sup>57, 59d</sup> Even with this, the channeled pores still resemble those found in some zeolite molecular sieves and an investigation was reportedly ongoing to determine this materials potential use in water absorption or gas separations.<sup>59d</sup>

Another important property sought with porous coordination solids is their ability to act as host and take on guest molecules into their porous network. The first reported absorption of gases at ambient temperature using coordination solids came from the Susumu Kitagawa group of the Tokyo Metropolitan University in 1997.<sup>60</sup> The coordination of 4,4'-bipyridine resulted in the formation of an extended solid with  $3 \times 6$  and  $3 \times 3 \text{ \AA}$  channeling pores, which, upon removal of the water guest, this porous solid was found to readily and reversibly absorb  $\text{CH}_4$ ,  $\text{N}_2$ , and  $\text{O}_2$  gases without the decomposition of its porous network.<sup>60</sup> Several porous coordination solids with gas absorption abilities have been developed since this first discovery.<sup>61</sup>

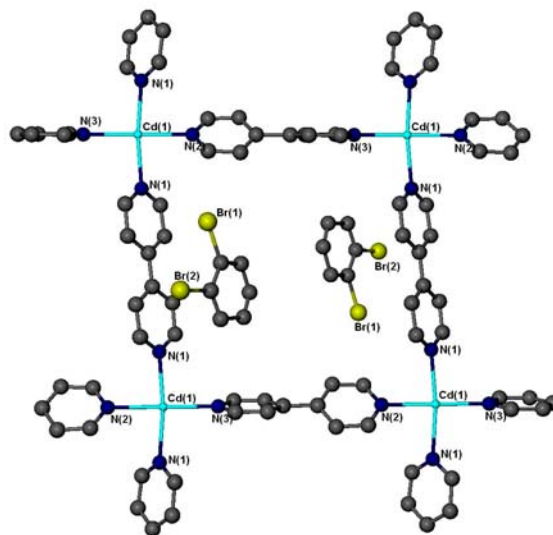
Aside from anion exchange and sorption qualities, coordination solids are beginning to be recognized for their value in catalysis as well.<sup>62</sup> The metal ions are widely used as soluble species to carry out catalytic organic transformations in a homogeneous solution. One advantage in using coordination polymers is that the metal ions can serve as heterogeneous catalyst sites, which is not actually part of the reaction solution and can be easily recovered after the catalysis operation is complete. As was mentioned earlier, this is one major use for the zeolites and clays, and it is slowly becoming an area of great interest for coordination polymers as well. Some of the catalytic reactions already performed by

coordination polymers are Ziegler-Natta polymerization,<sup>62g</sup> Diels-Alder reaction,<sup>62d, e</sup> transesterification,<sup>62b</sup> hydrogenation and isomerization,<sup>62i, j, k</sup> and cyanosilylation of aldehydes.<sup>62a</sup>

The 2-D coordination network of  $[\text{Cd}(\text{NO}_3)_2(\text{bpy})_2]_n$ , has the ability to catalyze the cyanosilylation of aldehydes in a shape selective manner.<sup>62a</sup> A line representation of the *o*-dibromobenzene clathrate version,  $[\text{Cd}(\text{NO}_3)_2(\text{bpy})_2] \cdot 2(\text{C}_6\text{H}_4\text{Br}_2)$ , is shown in Figure 1.21a and illustrates the square pores found in this 2-D, layered network. This network is both neutral and non-interpenetrating, and has a pore size of around 11 Å. Figure 1.21b shows the crystal structure of a single square with the clathrated *o*-dibromobenzene in place.<sup>62a</sup> This compound selectively form a clathrate with either *o*-dibromobenzene or *o*-dichlorobenzene



**Figure 1.21a** Line representation of the 2-D network of  $[\text{Cd}(\text{bpy})_2(\text{NO}_3)_2] \cdot 2(\text{C}_6\text{H}_4\text{Br}_2)$ . Each line represents a bpy connecting rod.<sup>59</sup>



**Figure 1.21b** A single square unit of the clathrate complex. Hydrogens and nitrate anions were omitted for clarity. Carbon atoms are gray while all other atoms shown are labeled.<sup>62a</sup>

while crystallized in the presence of their meta and para isomers.<sup>62a</sup> This selectivity is reflected in the  $[\text{Cd}(\text{NO}_3)_2(\text{bpy})_2]$  materials catalytic activity as 3-tolualdehyde was

cyanosilylated twice as efficiently (40%) as was 2-tolualdehyde (19%).<sup>62a</sup> This shape selectivity was attributed to the steric differences between each of the molecules as well as the cavity size of the material.<sup>62a</sup>

Our group chose to investigate the development of silicate-like porous materials made exclusively from the tetrahedral and trigonal coordination sphere found with the Cu(I) metal cation.<sup>63, 64</sup> To date, we have produced several novel one-, two-, and three-dimensional structures using a variety of bridging ligands such as pyrimidine,<sup>65</sup> 3,3'-bipyridine,<sup>66</sup> 4,7-phenanthroline,<sup>67</sup> bis(4-pyridyl)ethylene,<sup>68</sup> bis(4-pyridyl)ketone,<sup>69</sup> bis(4-pyridyl)oxime,<sup>69</sup> and 4,4'-bipyridine.<sup>70</sup>

One of our most promising efforts in development of a zeolite analog comes from the use tetrahedral building block produced by the self-assembly reaction of  $[\text{Cu}(\text{MeCN})_4]\text{X}$  ( $\text{X}$  = counter anion) with the bridging pyrimidine (pyrim) ligand as shown in Equation 2.

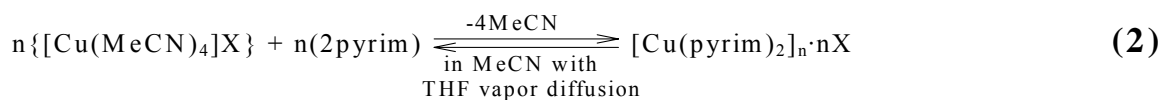
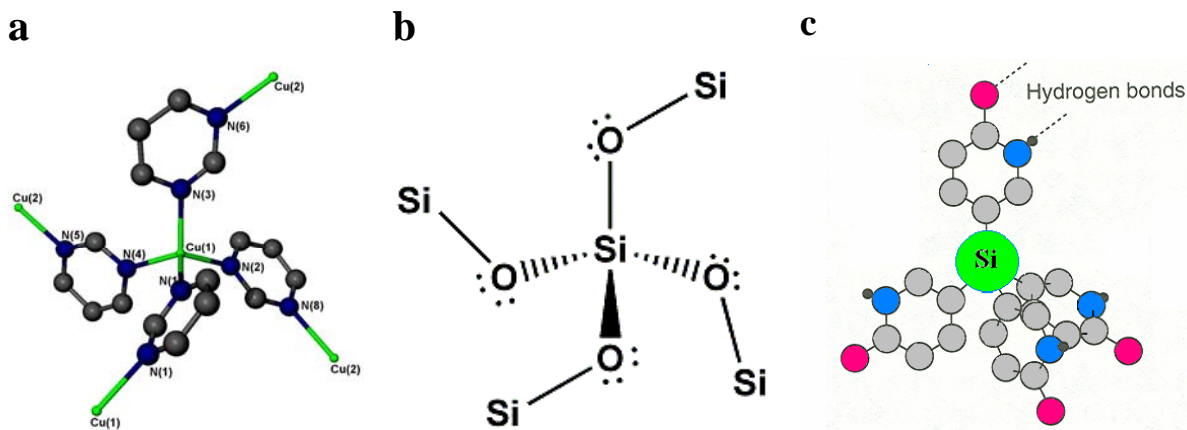
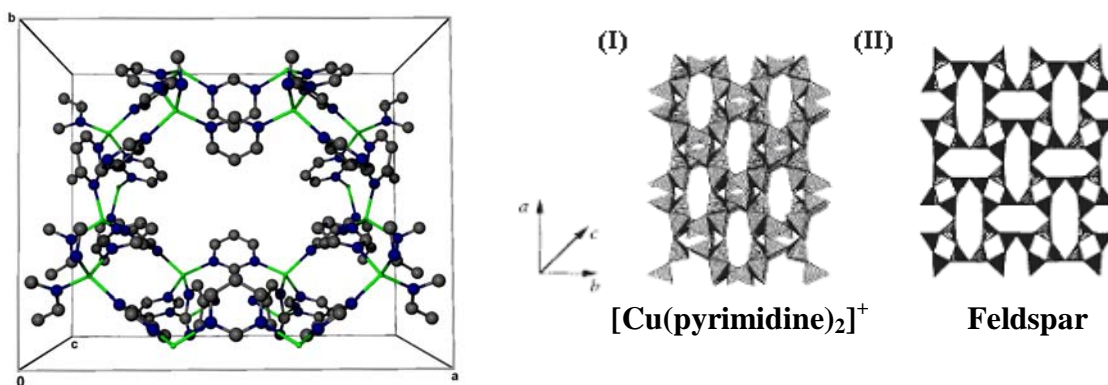


Figure 1.22 compares (a) the corner shared  $[\text{Cu}(\text{pyrimidine})_2]^+$  with the (b) silicate and (c) the tetrapyridylsilane tecton (Sec. 1.4) and shows how each of the three tetrahedral ligands have similar angles as they bridge from one tetrahedron to another. In all three cases, the ligands are free to rotate on the Cu – N, Si – O, and Si – C bond, respectively. This provides a considerable amount of variability in the bonding geometries, leading to a variety of different structures from the same building block. While we have already pointed out the variety exhibited by the numerous zeolite structures, we will demonstrate later on how the Cu(I)/pyrimidine coordinated tetrahedron is, more-or-less, the building block for a variety of Cu(I) coordination solids.



**Figure 1.22** (a)  $[\text{Cu}(\text{pyrimidine})_2]^+$ , (b) silicate, and (c) tetrapyrildsilane tecton showing the similar angled coordination, covalent, and hydrogen bonding, respectively.

Figure 1.23a shows the crystal structure of  $[\text{Cu}(\text{pyrimidine})_2]\text{BF}_4$ ; which was the first structure crystallized from the Cu(I) – pyrimidine system.<sup>65</sup> This result was of considerable interest since the structure bore a striking resemblance to that of the naturally occurring aluminosilicate, feldspar, as shown in figure 1.23b. Additionally, although the Cu(I)/pyrimidine network has considerable porosity with pores apertures of  $\sim 6 \times 6 \text{ \AA}$ , there was no network interpenetration. The  $\text{BF}_4^-$  anions and highly disordered tetrahydrofuran

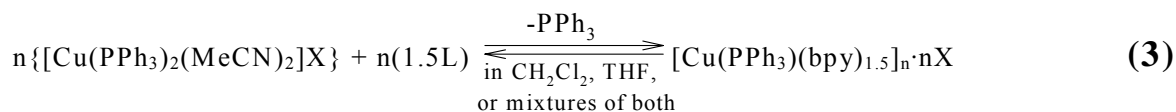


**Figure 1.23a** Crystal structure of the network unit cell of  $[\text{Cu}(\text{pyrimidine})_2]\text{BF}_4$  (view down the  $c$  axis). Cu atoms: green, N atoms: blue, C atoms: grey, hydrogen atoms and anion are omitted for clarity.<sup>65</sup>

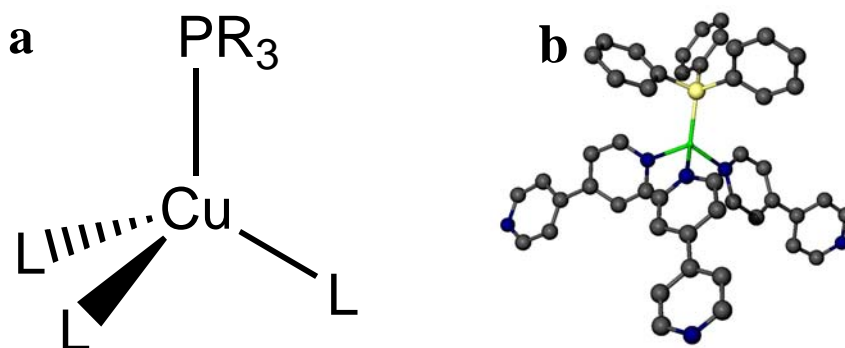
**Figure 1.23b** (I) The polyhedral packing diagram of  $[\text{Cu}(\text{pyrimidine})_2]\text{BF}_4$ . The centroids of the pyrimidine ligand are defined by the sides of the polyhedra. The Cu(I) cations (located at the center of the tetrahedra) are omitted, as are the anions, for clarity. (II) Schematic view of the feldspar structure viewed down the  $a$  axis.<sup>65</sup>

(THF), and nitrobenzene solvent are then found within the network cavities.

We needed to modify the Cu(I) tetrahedra slightly in order to make a two-dimensional layered coordination solid from a three-dimensional building block. Just as the natural clay's silica tetrahedra are capped off by octahedrally coordinated sheets of either *gibbsite* [Al<sub>2</sub>(OH)<sub>6</sub>], or *brucite* [Mg<sub>2</sub>(OH)<sub>6</sub>] units, we capped off the Cu(I) tetrahedra, in this case, with a terminal phosphine (PR<sub>3</sub> R = Ph or ) ligand. Equation 3 shows how the [Cu(PPh<sub>3</sub>)<sub>2</sub>(MeCN)<sub>2</sub>]X (X = counter anion) reacts with the bridging ligand (L) to form the modified Cu(I) tetrahedra.



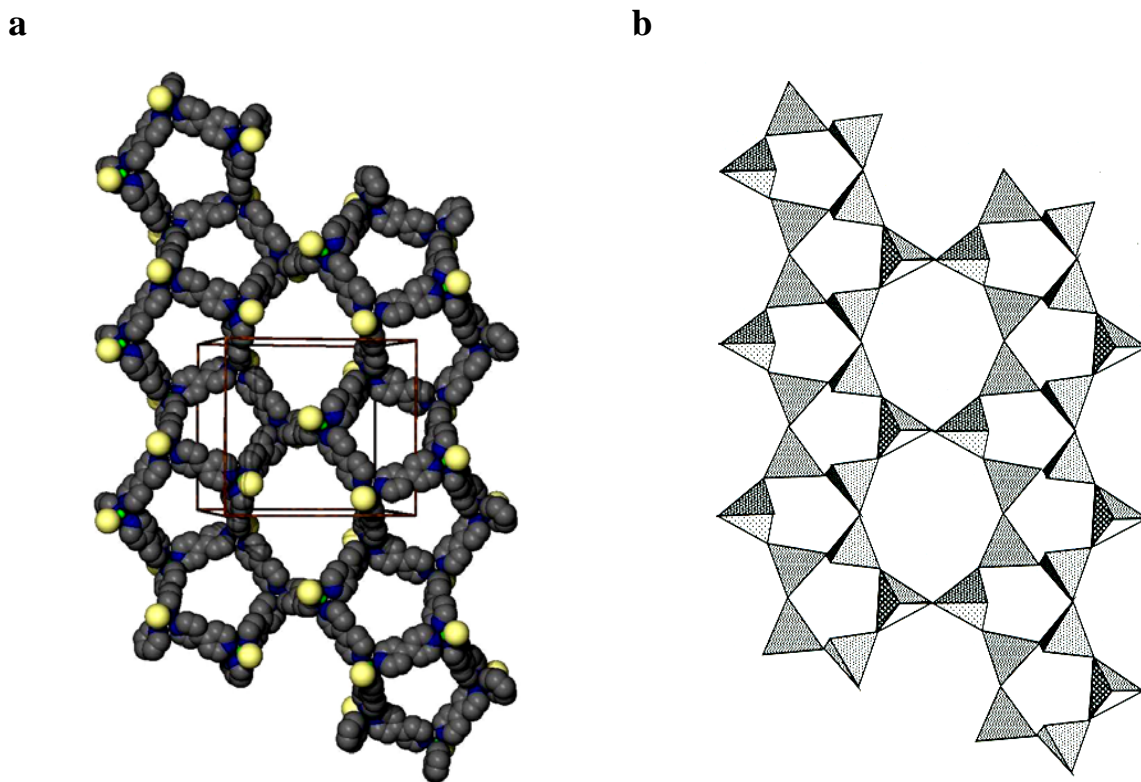
This modification results in the occupation of only three of the four coordination sites by bridging ligands, which should direct the structure into a two-dimensional, layered coordination solid. A structural diagram of the modified Cu(I) tetrahedron is shown in Figure 1.24a and a single tetrahedral building block of [Cu(PPh<sub>3</sub>)(bpy)<sub>1.5</sub>]<sup>+</sup> in Figure 1.24b as it appears in a layered Cu(I) coordination solid.



**Figure 1.24** (a) A general formula diagram of the modified Cu(I) tetrahedra and (b) a single tetrahedron capped by the terminal phosphine ligand from crystal data of a typical [Cu(bpy)<sub>1.5</sub>(PPh<sub>3</sub>)]<sup>+</sup> layered network.

Surprisingly, it was the linear bridging, 4,4'-bipyridine rod (instead of the angled pyrimidine) that produced the first clay-like, non-interpenetrated, layered structure. Figure 1.25 shows a single layer of the [Cu(bpy)<sub>1.5</sub>(PPh<sub>3</sub>)]BF<sub>4</sub>·(THF)<sub>1.33</sub>·(CHCl<sub>3</sub>)<sub>0.33</sub> network

along with the polyhedral packing illustration of the natural silicate, *nekoite*,  $\text{Ca}_3(\text{Si}_6\text{O}_{15}) \cdot 7\text{H}_2\text{O}$ , for comparison.<sup>34, 63, 70</sup> Although there is a close resemblance between these two structures, while the nekoite silicate has an anionic network with  $\text{Ca}^{2+}$  cations and water included within the cavities of the network, the Cu(I)/bpy coordination forms a cationic network with  $\text{BF}_4^-$  anions and solvent found within its cavities.



**Figure 1.25** (a) The single layer of the cationic network found with  $[\text{Cu}(\text{bpy})_{1.5}(\text{PPh}_3)]\text{BF}_4 \cdot (\text{THF})_{1.33} \cdot (\text{CHCl}_3)_{0.33}$ . The phosphines are yellow (with the phenyl rings removed for clarity), the nitrogen atoms blue, carbon atoms gray, and copper is green (but mostly obscured by the phosphine and carbon atoms). The hydrogen atoms have been omitted for clarity. (b) Also shown in comparison is the polyhedral packing of nekoite.<sup>63</sup>

Another striking difference is the size of the building blocks used for each network. The  $[\text{Cu}(\text{bpy})_{1.5}(\text{PPh}_3)]^+$  building block is much larger ( $\text{Cu} - \text{bpy}$  centroid = 5.6 Å) than that of the silicate's ( $\text{Si} - \text{O} = 1.62$  Å), offering the possibility of a much larger pore system.<sup>63</sup>

## 1.5 Supramolecular Isomerism in Porous Coordination



## Solids

With coordination solids, the overall architectures might be determined by the geometry and, flexibility or rigidity of the Lewis base linker, along with the stereochemical preference of the coordinated metal cation.<sup>71</sup> However, a large number of reactions lead to variable results as the network self-assembly seems to be influenced by the presence of different solvents,<sup>72</sup> anions,<sup>73</sup> or even a combined variation of the two.<sup>74</sup> In many cases, variations in networks are seen with essentially the same molecular formula or same molecular building blocks, which is thought of as a form of polymorphism and aptly dubbed as *supramolecular isomerism*.<sup>75</sup>

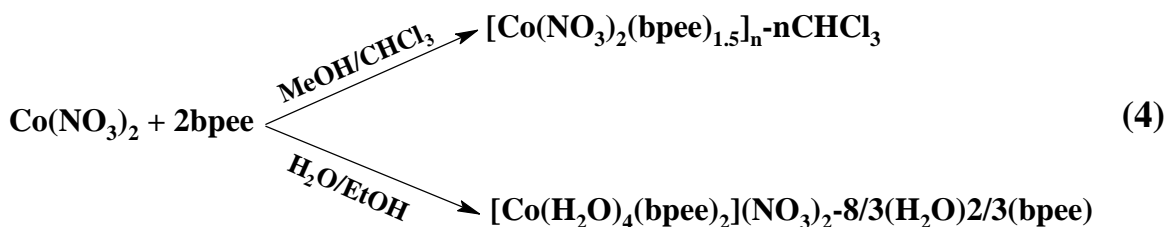
The term *polymorphism* in itself refers to the existence of two or more crystalline structures with the same molecular formula.<sup>76</sup> Since the majority of the coordination network isomers result from the inclusion of either a different anion or solvent, it would be somewhat inaccurate to describe them all as being structural polymorphs.<sup>75</sup>

A closely related term, *pseudopolymorph*, which is well known in the pharmaceutical literature, can also be known simply as a *solvate* and refers to an isomer that was made by the addition of solvent to the basic structure.<sup>76, 77</sup> We would describe a coordination polymer pseudopolymorph as those compounds that have different solvent molecules as a coordinated part of the network; *not* those compounds in which the different solvent is only an included guest molecule. The coordination compounds of  $[\text{Cu}(\text{dpdo})_6](\text{ClO}_4)_2$  and  $[\text{Cu}(\text{dpdo})(\text{H}_2\text{O})_4](\text{ClO}_4)_2 \cdot 2\text{dpdo}$  are typical examples of coordination polymer solvates.<sup>78</sup> Some have argued, however, that solvates such as these should be considered as entirely different compounds from the crystal engineering point of view.<sup>75</sup>

Although there appears to be a small amount of confusion over a precise definition of

the supramolecular isomers, the basic concept is generally understood. Each structural anomaly, be it polymorphic, pseudopolymorphic, or something in-between, is an assembly of the same type of building blocks that were brought together (via self-assembly) in a different way because of a change in one or more of the synthetic variables.

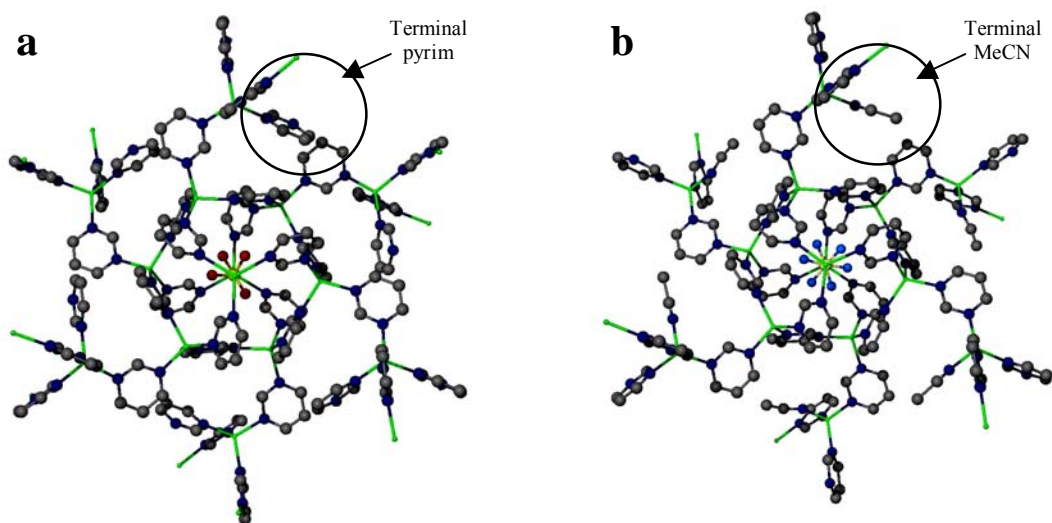
We have shown that supramolecular complexes are brought together by the interaction between host and guest molecule as they become bound by a variety of intermolecular forces. We have also shown that the same metal/ligand combination can lead to a variety of different network systems.<sup>57, 59a, b, d</sup> As was pointed out in Section 1.2, the binding forces between solvent and host, and solvent and guest are also just as real and significant; each offering their own degree of interaction as the self-assembly reaction progresses.<sup>24</sup> In some cases, the interaction is obvious as either the solvent or anion becoming involved in the resulting network. An example of this can be seen in equation 4 for the reaction of  $\text{Co}(\text{NO}_3)_2$  with 1,2-bis(4-pyridyl)ethylene (bpee).<sup>72a</sup>



The product can either form the anion coordinated neutral network when in a non-aqueous solvent system, or the water coordinated cationic complex when in an aqueous solvent system.<sup>72a</sup> These results are attributed to the formation of strong hydrogen bonds between water and the nitrate anion, and terminal coordinative bonds with the cobalt metal. This effectively disassociates the metal cation from the anion during self-assembly as well as blocking the formation of a polymeric network.<sup>78</sup>

In other cases, the cause is not so obvious and subtle changes in either the solvent or the anion used results in the formation of different networks composed of essentially the exact same building blocks. An excellent example of this, and directly related to this study are the supramolecular isomers found from those reactions to produce the Cu(I)/pyrimidine and the Cu(I)/4,4'-bipyridine coordination solids, as introduced in the last section.

The same Cu/pyrimidine tetrahedra that produced the feldspar-like structure was found to self-assemble into two entirely different structures by simply changing the counter anion.<sup>63</sup> Figure 1.26 shows those structures resulting from reactions containing the (a) perchlorate anion, forming  $[\text{Cu}(\text{pyrim})_{2.3}]\text{ClO}_4$ ; and the (b) hexafluorophosphate anion, forming  $[\text{Cu}(\text{pyrim})_{2.3}(\text{MeCN})_{0.33}]\text{PF}_6$ . Close examination of these two structures

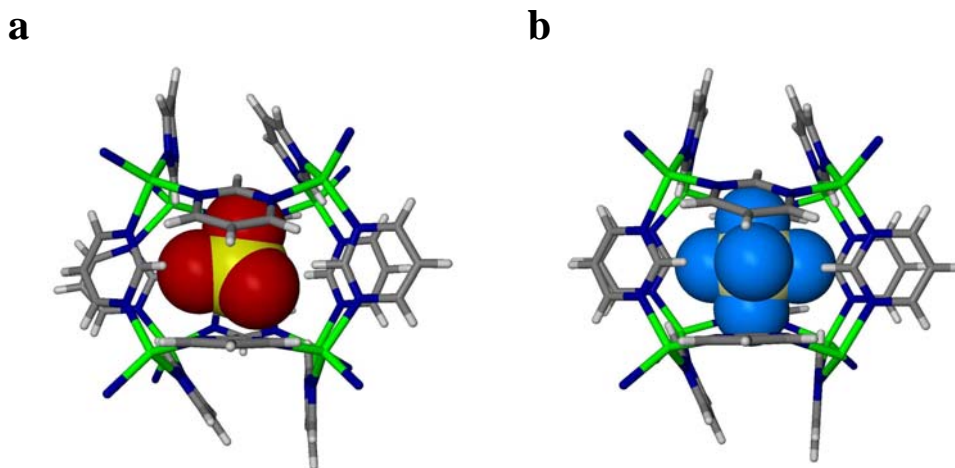


**Figure 1.26** A single hexagonal motif derived from the crystal structure of (a)  $[\text{Cu}(\text{pyrim})_{2.3}]\text{ClO}_4$  and of (b)  $[\text{Cu}(\text{pyrim})_{2.3}(\text{MeCN})_{0.33}]\text{PF}_6$ . One of the terminal pyrimidine and acetonitrile ligands on each, respectively, has been circled. Cu: green; N: blue; C: gray; O: red; F: blue; Cl and P: yellow. The hydrogen atoms and all but the centrally located anion in each structure have been omitted for clarity.

reveals how they are practically isostructural to each other. If it were not for the different anion found in each structure, these two structures might be considered as prime examples of pseudopolymorphism. In both cases, these are three-dimensional, non-interpenetrated cationic networks. Another striking feature is the structures complete lack of solvent; with

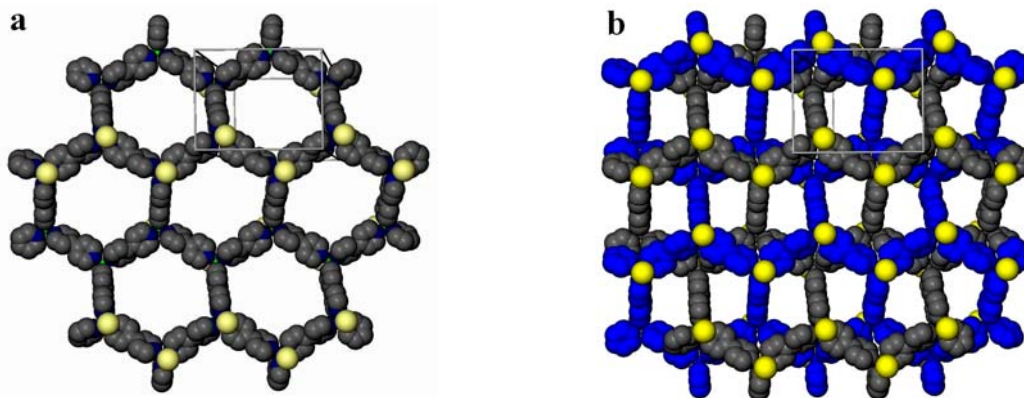
only the anions found within the small pores.

A much closer look at the anion positioning is shown in Figure 1.27a and b and reveals that each anion is enclosed in a box made up of eight Cu(I) tetrahedra. The presence of an anion entrapped inside a network cages such as these strongly suggest anion templation may be responsible for the structural isomerism. It is a pressing mystery, however, why the network holding the  $\text{ClO}_4^-$  anion is constructed exclusively by Cu – pyrimidine coordination, while the other network about the  $\text{PF}_6^-$  anion has included acetonitrile in its design. Even more of a mystery is why the quite similar  $\text{BF}_4^-$  anion did not also acts as a template to form such a network; instead of forming the feldspar analog.



**Figure 1.27** A close-up showing the (a)  $\text{ClO}_4^-$  and (b)  $\text{PF}_6^-$  anions trapped inside a cage made up of eight Cu(I) tetrahedra.

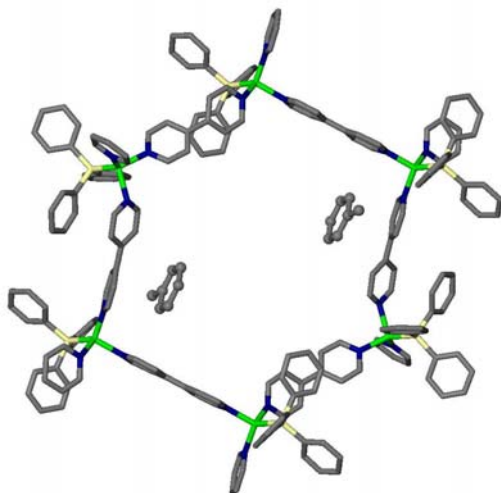
Variation in the coordination solid was also observed when we changed the solvent system from *THF* and  $\text{CHCl}_3$  (to produce original fused pentagonal layers) to using *toluene* and  $\text{CHCl}_3$ .<sup>63, 70</sup> This new solvent system produced two-fold interpenetrated layers of honeycomb-like hexagonal cells of  $[\text{Cu}(\text{bipy})_{1.5}(\text{PPh}_3)]\text{BF}_4 \cdot (\text{toluene}) \cdot (\text{CHCl}_3)_{1.5}$ . A single layer of the  $[\text{Cu}(\text{bpy})_{1.5}(\text{PPh}_3)]^+$  cationic layer is shown in Figure 1.28a while two



**Figure 1.28** (a) A space-fill representation of a single layer of  $[\text{Cu}(\text{bipy})_{1.5}(\text{PPh}_3)]\text{BF}_4 \cdot (\text{toluene}) \cdot (\text{CHCl}_3)_{1.5}$  structure's cationic network and (b) two layers as they interpenetrate each other. C: gray; P: yellow; N: blue; Cu: green. The second interpenetrated network in (b) is shown as all blue except for the phosphines. Phenyl rings from the phosphines and all hydrogen atoms have been omitted for clarity.

interpenetrating layers are shown in 1.28b. Although the pores of the honeycomb network are essentially bisected by the interpenetrated layer, there is still considerable void space between the layers of the structure, which is occupied by the anion and the solvate.

Although a direct relationship between the Cu(I) coordination network of fused pentagons and the THF solvent could not be established, there was evidence of considerable

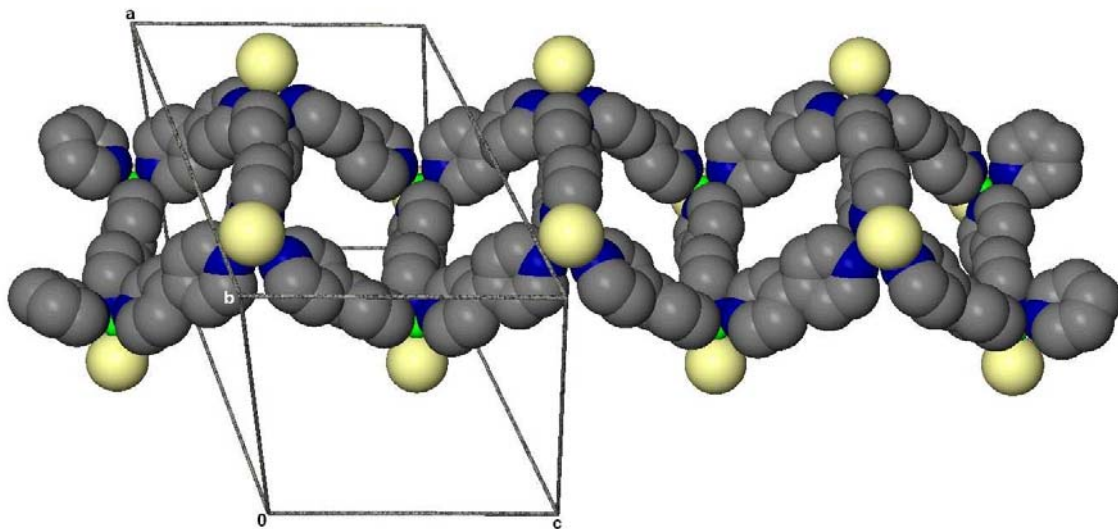


**Figure 1.29** A single hexagon showing the toluene  $\pi$ -stacking that occurs in  $[\text{Cu}(\text{bipy})_{1.5}(\text{PPh}_3)]\text{BF}_4 \cdot (\text{toluene}) \cdot (\text{CHCl}_3)_{1.5}$  between the toluene and the bpy ligands.

interaction between the toluene and the hexagonal network in the form of  $\pi$ -stacking. Shown in Figure 1.29, as the toluene interact with the bpy ligands, they are thought to be templating the self-assembly into the interpenetrated hexagon network that results.

An additional supramolecular isomer of the Cu/bpy coordination solid was uncovered;

this time when a different anion ( $\text{PF}_6^-$ ) was used while performing the reaction in the same THF/ $\text{CHCl}_3$  solvent system as was used with the pentagon layers.<sup>63</sup> Surprisingly, although the cationic network of this new structure has the same chemical formula as the other two coordination solids of  $[\text{Cu}(\text{bipy})_{1.5}(\text{PPh}_3)]^+$ , its structure (shown in Figure 1.30) is quite different as it forms, not layers, but one-dimensional, ladder-like chains of linked squares. As was with the other two structures, the anion and solvent reside within the pores formed by the coordination network. With all three of these coordination solids having the same cationic formula,  $[\text{Cu}(\text{bipy})_{1.5}(\text{PPh}_3)]^+$ , if the anion and solvent differences could be excused, these structures could be considered excellent examples of polymorphs, by the definition given.



**Figure 1.30** Space-fill representation of the ladder-like network found in the  $[\text{Cu}(\text{bpy})_{1.5}(\text{PPh}_3)]\text{PF}_6 \cdot (\text{CHCl}_3)_{1.5}$  structure. Cu: green; C: gray, N: blue, P: yellow. Phenyl rings on the phosphines and all hydrogens have been omitted for clarity.

At this point, we have shown how a circumstantial relationship between solvent and structure hinted of solvent templation, close examination of the material crystallized from the toluene solvent also has given us structural evidence that some sort of templation can and does occur in the self-assembly of these porous solids. Although the other structures

fail to show this same type of solid evidence, the results still hint of anion and solvent interactions based on the secondary evidence given. The occurrence of the ladder network with the  $\text{PF}_6^-$  anion only added to the mystery but was attributed to the faster rate of reaction found with those materials from the  $\text{PF}_6^-$  anion salt over that of the  $\text{BF}_4^-$  anion salt's reactions. This study's researcher, Susan Lopez admits, however, that this study had just begun and that much more conclusive data needed to be obtained.<sup>63</sup>

## 1.6 Dissertation Overview

The previous work done by our group in the development of both the zeolite and clay analogs had shown there was a close relationship with the anion and/or solvent and the development of supramolecular isomers in the Cu – pyrimidine and the Cu – bpy coordination networks. It was also evident that, even though results strongly indicated some sort of anion or solvent templation was involved, more examples, and more control over solution properties was needed. Therefore, this dissertation covers the continued investigation of these two systems in design and development. Specifically, we will present both the development of new supramolecular isomers in these systems and the study and discussion on the anion and solvent role in the self-assembly of these networks. As a finale, and in keeping with the ultimate goal of functional porous solid development, we will present one material's ability to perform selective anion exchange.

First, we will be examining the coordination solids produced from the Cu – bpy reactions as they vary with changes in both anion and solvent system (Chapter 3). We confined our study to those materials developed with the  $\text{BF}_4^-$ ,  $\text{PF}_6^-$ ,  $\text{ClO}_4^-$ ,  $\text{CF}_3\text{SO}_3^-$ , and  $\text{HSO}_4^-$  anions, and our selection of solvent systems using only  $\text{CHCl}_3$ , THF, toluene, and

varied ratios of CHCl<sub>3</sub>/THF and CHCl<sub>3</sub>/toluene mixtures.

Second, we present our examination of the anion and solvent interaction with the Cu(I) coordination leading to the self-assembly of the coordination solids (Chapter 4). The first part of this chapter pertains to the reaction of [Cu(MeCN)<sub>2</sub>(PPh<sub>3</sub>)<sub>2</sub>]X for X= BF<sub>4</sub><sup>-</sup>, PF<sub>6</sub><sup>-</sup>, ClO<sub>4</sub><sup>-</sup>, CF<sub>3</sub>SO<sub>3</sub><sup>-</sup>, and HSO<sub>4</sub><sup>-</sup> with the solvent alone, without any involvement of the bridging bpy ligand. Several structures involving anion and solvent coordination are shown with detailed discussion to follow.

Third, we will present an investigation/search for self-assembly structural *intermediates* (Chapter 5) as we show several structures developed from reactions with only 0.5 and 1.0 equivalents (eq.) of the bpy ligand (as opposed to 1.5 eq. needed for the layered coordination solids).

Fourth, our investigation focuses on those coordination solids produced by the Cu – pyrimidine reaction (Chapter 6). As with previous studies, we confined our investigation to those systems involving BF<sub>4</sub><sup>-</sup>, PF<sub>6</sub><sup>-</sup>, ClO<sub>4</sub><sup>-</sup>, CF<sub>3</sub>SO<sub>3</sub><sup>-</sup>, and PMo<sub>12</sub>O<sub>40</sub><sup>-</sup> anions. The solvent systems, while slightly different than with the clays, were also confined to only a few variations and included acetonitrile (MeCN), nitrobenzene (NO<sub>2</sub>Bz), nitromethane (NO<sub>2</sub>Me), dichloromethane, (CH<sub>2</sub>Cl<sub>2</sub>), benzene, and THF. In addition to the anion and solvent dependence, we will present how ligand stoichiometry also played an important role resulting in the formation of discrete, one-, two-, and three-dimensional Cu – pyrimidine coordination solids.

Lastly, Chapter 7 examines the large cavity [Cu<sub>3</sub>(pyrim)<sub>7.5</sub>(H<sub>2</sub>O)](CF<sub>3</sub>SO<sub>3</sub>)<sub>3</sub> · 3(THF) zeolite-analog and the quantitative competition exchange study between ReO<sub>4</sub><sup>-</sup> and the HSO<sub>4</sub><sup>-</sup>, H<sub>2</sub>PO<sub>4</sub><sup>-</sup>, ClO<sub>4</sub><sup>-</sup>, and NO<sub>3</sub><sup>-</sup> anions using a <sup>99m</sup>Tc radiotracer introduced as the TcO<sub>4</sub><sup>-</sup>



anion. This study has shown a successful exchange with both the  $\text{TcO}_4^-$  and  $\text{ReO}_4^-$  anions with only nominal hindrance of the exchange by other competing anions.

## References

1. (a) Fulita, M.; Kwon, Y. J.; Washizu, S.; *J. Am. Chem. Soc.* **1994**, *116*, 1151. (b) Sawaki, T.; Dewa, T.; Aoyama, Y.; *J. Am. Chem. Soc.* **1998**, *120*, 8640. (c) Seo, J. S.; Whang, D.; Lee, H.; Jun, S. I.; Oh, J.; Leon, Y. J.; Kim, K.; *Nature*, **2000**, *404*, 982.
2. (a) Evans, O. R.; Xiong, R. -G.; Wang, Z.; *J. Am. Chem. Soc.*, **1998**, *120*, 13272. (b) Lin, W.; Wang, Z.; Ma, L.; *J. Am. Chem. Soc.* **1999**, *121*, 11249. (c) Songping, D. H.; Xiong, R. -G.; *Polyhedron* **1997**, *16*, 3929. (d) Evans, O. R.; Xiong, R. -G.; Wang, Z.; Wong, G. K.; Lin, W.; *Angew. Chem. Int. Ed. Eng.* **1999**, *38*, 536
3. (a) Hoskins, B. F.; Robson, R.; *J. Am. Chem. Soc.*; **1990**, *112*, 1546 – 1554. (b) Gardner, G. B.; Kiang, Y. -H; Lee, S.; Asgaonkar, A.; Venkataraman, A.; *J. Am. Chem. Soc.* **1996**, *118*, 6946. (c) Yaghi, O. M. Li, G.; Li, H.; *Nature* **1995**, *378*, 703.
4. (a) Eddaoudi, M.; Li, H.; Yaghi, O. M.; *J. Am. Chem. Soc.* **2000**, *122*, 1391. (b) Li, H. Eddaoudo, M.; Groy, T. L.; Yaghi, O. M.; *J. Am. Chem. Soc.* **1998**, *121*, 8571. (c) Kondo, M.; Yoshitomi, T.; Seki, K.; Matsuzaka, H.; Kitagawa, S.; *Angew. Chem.* **1997**, *109*, 1844.
5. (a) Noro, S. -I.; Kituara, R.; Kondo, M.; Kitagawa, S.; Ishii, T.; Matsuzaka H.; Yamashita, M.; *J. Am. Chem. Soc.* **2002**, *124*, 2568. (b) Hoskins B. F.; Robson, R.; *J. Am. Chem. Soc.* **1990**, *112*, 1546. (c) Yaghi, O. M.; Li, H.; *J. Am. Chem. Soc.* **1996**, *118*, 295. (d) Min, K. S.; Suh, M. P.; *J. Am. Chem. Soc.* **2000**, *122*, 6834.
6. Moulton, B.; Zaworotko, M. J.; *Chem. Rev.* **2001**, *101*, 1629.
7. Schmidt, G. M. J.; *Pure Appl. Chem.* **1971**, *27*, 647.
8. Lehn, J. M.; *Pure Appl. Chem.* **1978**, *50*, 871.
9. Lehn, J. M.; *Supramolecular Chemistry: Concepts and Perspectives*, VCH: Weinheim, 1995.
10. Beer, P. D.; Gale, P. A.; Smith, D. K.; *Supramolecular Chemistry*, Oxford University Press, Oxford, NY; 1999.
11. Steed, J. W.; Atwood, J.; *Supramolecular Chemistry*, Wiley, West Sussex, England; 2000.

12. Schmidtchen, F. P.; Muller, G.; *J. Chem. Soc. Chem. Commun.* **1984**, 1115.
13. Jeffrey, G. A.; *An Introduction to Hydrogen Bonding*, Oxford University Press: Oxford, 1997.
14. Ma, J. C.; Dougherty, D.; *Chem. Rev.* **1997**, *97*, 1303.
15. Kumpf, R. A.; Dougherty, D.A.; *Science*, **1993**, *261*, 1708.
16. (a) Hunter, C. A.; Sanders, J. K. M.; *J. Am. Chem. Soc.* **1990**, *112*, 5525. (b) Hunter, C.; *Chem. Soc. Rev.* **1994**, 101.
17. Nishikiori, S. -H.; Yoshikawa, H.; Sano, Y.; Iwamoto, T.; *Acc. Chem. Res.* **2005**, *38*, 227.
18. Bott, S. G.; Coleman, A. W.; Atwood, J. L. *J. Am. Chem. Soc.* **1986**, *108*, 1709.
19. Kitaigorodski, A. I.; *Molecular Crystals and Molecules*, Academic Press: New York, 1973.
20. Fischer, E.; *Ber. Deutsch. Chem. Ges.* **1894**, *27*, 2985.
21. Desiraju, G. R.; *Angew. Chem. Int. Ed. Engl.* **1995**, *34*, 2311.
22. Lehn, J. -M; Mascal, M.; DeCain, A.; Fischer, J.; *J. Chem. Soc. Perkins Trans. 2*, **1992**, 461.
23. Cram, D. J.; Dicker, I. B.; Lein, G. M.; Knobler, C. B.; Trueblood; K. N.; *J. Am. Chem. Soc.* **1982**; *104*(24), 6827.
24. Hasenknopf, B.; Lehn, J.-M.; Boumediene, N.; Dupont-Gervais, A.; Van Dorsselaer, A.; Kneisel, B.; Fenske, D.; *J. Am. Chem. Soc.* **1997**; *119*(45), 10956.
25. Cram, D. J.; *Angew. Chem. Int. Eng. Ed.* **1986**, *25*, 1039.
26. Author not given, Zeolites, *Abbey Newsletter volume 20 #7Dec. 1996*, Abbey Publications Inc., 2004, Stanford University.
27. Ball, P; *Designing the Molecular World: Chemistry at the Frontier*, Princeton University Press, Princeton, 1994.
28. Ball, P. *Made to Measure: New Materials for the 21st Century*, Princeton University Press, Princeton, 1997.
29. Shriver, D. F.; Atkins, P.; Lngford, C. H.; *Inorganic Chemistry 2<sup>nd</sup> Ed.*; W. H. Freeman and Company, New York, 1994.

30. Baerlocher, Ch.; Meier, W. M.; Olson, D. H.; *Atlas of Zeolite Framework Types 2<sup>nd</sup> Ed.*, Elsevier Science B. V.; Amsterdam, 2001.
31. Mumpton, F. A.; *Proc. Natl. Acad. Sci. USA* **1999**, *96*, 3463.
32. Occelli, M. L.; Kessler, H.; *Synthesis of Porous Materials: Zeolites, Clays, and Nanostructures*, Marcel Dekker, Inc.; New York, 1997.
33. Dwyer, F. G.; Jenkins, E. E.; U. S. Patent 3941871, 1976.
34. Liebau, F. *Structural Chemistry of Silicates: Structure, Bonding, and Classification*; Springer-Verlag: New York, 1985.
35. Bruce, D. W.; O'Hare, D.; *Inorganic Materials*, John Wiley and Sons Ltd, West Sussex, 1992.
36. Worrall, W. D.; *Clays and Ceramic Raw Materials*, John Wiley and Sons, New York, 1975.
37. Quirk, J. P.; *Nature*, **1961**, *188*, 253.
38. (a) Foschamer, G.; *Ann. Roy. Agr. Coll. Sweden*, **1850**, *14*, 171. (b) Grimshaw, R. W.; *Chemistry and Physics of Clays*, Benn, London, 1971.
39. Bradley, W. F.; Grim, R. Re.; Clark, G. L.; *Zeit. Kryst.* **1937**, *97*, 216.
40. Fahn, R.; *Kolloid-Zeitschrift*, **1963**, *187*, 120.
41. (a) Mortland, M. M.; Raman, K. V.; *Clays and Clay Miner.* **1968**, *16*, 393. (b) Fripiat, J. J.; Cruz-Crumplido, M. I.; *Ann. Rev. Earth Planet Sci.* **1974**, *2*, 239. (c) Mortland, M. M.; *trans. 9<sup>th</sup> Int. Congr. Soil Sci.* **1968**, 691.
42. (a) Solomon, D. H.; Swift, J. D.; Murphy, A. J.; *J. Macromol. Sci. Chem.* **1971**, *A5*, 587. (b) Frenkel, M.; *Clays and Clay Miner.* **1974**, *22*, 435.
43. Theng, B. K. G.; *The Chemistry of Clay-organic Reactions*, Adam Hilger, London, 1974.
44. (a) Kikuchi, E.; Matsuda, T.; *Catal. Today* **1988**, *2*, 297. (b) Vaughan, D. E. W.; Lusier, R. J.; Magee, J. S.; *US Patent 4,176,090* **1979**. (c) Poncelet, G.; Schutz, A. in; *Chemical Reaction in Organic and Inorganic Constrained Systems*, Setton, R., Ed., Reidel, New York, 1986, pg 165.
45. Suib, S. L.; Tanguay, J. F.; Occelli, M. F.; *J. Am. Chem. Soc.* **1986**, *108*, 6972.

46. Diddams, P. A.; Thomas, J. M.; Jones, W.; Ballantine, J. A.; Purnell, J. H.; *J. Chem. Soc. Chem. Commun.* **1984**, 1340.
47. (a) Barton, T. J.; Bull, L. M.; Klemperer, W. G.; Loy, D. A.; McEnaney, B.; Misono, M.; Monson, P. A.; Pez, G.; Scherer, G. W.; Vartuli, J. C.; Yaghi, O. M.; *Chem. Mater.* **1999**, *11*, 2633. (b) Endo, K.; Sawaki, T.; Koyanagi, M.; Kobayashi, K.; Masuda, H.; Aoyama, Y.; *J. Am. Chem. Soc.* **1995**, *117*, 8341.
48. Lehn, J.-M.; *Angew. Chem. Int. Ed.* **1990**, 1304.
49. MacNicol, D. D.; McKendrick, J. J.; Wilson, D. R.; *Chem. Soc. Rev.* **1978**, *7*, 65.
50. Greenwood, N. N.; *Chem. Soc. Rev.* **1984**, *13(4)*, 353.
51. (a) Su, D.; Wang, X.; Simard, M.; Wuest, J. D.; *Supramolecular Chem.* **1995**, *6*, 171. (b) Wuest, J. D. in *Mesomolecules: From Molecules to Materials*, Mendenhall, G. D.; Greenberg, A.; Liebman, J. F.; Eds.; Chapman & Hall, New York, 1995; pg 107.
52. A few examples and references therein. (a) Bhogala, B. R.; Nangia, A.; *Cryst. Growth & Design*, **2003**, *3(4)*, 547. (b) Kumar, D. K.; Jose, D. A.; Dastidar, P.; Das, A.; *Chem. Mater.* **2004**, *16*, 2332. (c) Beatty, A. M.; Granger, K. E.; Simpson, A. E.; *Chem. Eur. J.* **2002**, *8(14)*, 3254. (d) Biradha, K.; Dennis, D.; MacKinnon, V. A.; Sharma, C. V. K.; Zaworotko, M. J.; *J. Am. Chem. Soc.* **1998**, *120*, 11894. (e) Sada, K.; Inoue, K.; Tanaka, T.; Tanaka, A.; Rpergyes, A.; Nagahama, S.; Matsumoto, A.; Miyata, M.; *J. Am. Chem. Soc.* **2004**, *126*, 1764. (f) Ruiz-Perez, C.; Lorenzo-Luis, P. A.; Hernandez-Molina, M.; Laz, M. M.; Gili, P.; Julve, M.; *Cryst. Growth & Design* **2004**, *4(1)*, 57. (g) Fowler, F. W.; Lauher, J. W.; *J. Phys. Org. Chem.* **2000**, *13*, 850.
53. (a) Wang, X.; Simard, M.; Wuest, J. D.; *J. Am. Chem. Soc.* **1994**, *116*, 12119. (b) Saied, O.; Maris, T.; Wang, X.; Simard, M.; Wuest, J. D.; *J. Am. Chem. Soc.* **2005**, *127*, 10008. (c) Brunet, P.; Simard, M.; Wuest, J. D.; *J. Am. Chem. Soc.* **1997**, *119*, 2737. (d) Simard, M.; Su, D.; Wuest, J. D.; *J. Am. Chem. Soc.* **1991**, *113*, 4496. (e) Laliberti, D.; Maris, T.; Wuest, J. D.; *J. Org. Chem.* **2003**, *69*, 1776. (f) Fournier, J.-H.; Maris, T.; Wuest, J. D.; Guo, W.; Galopinni, E.; *J. Am. Chem. Soc.* **2003**, *125*, 1002.
54. Kitagawa, S.; Kitaura, R.; Noro, S.-I.; *Angew. Chem. Int. Ed.* **2004**, 2334.
55. (a) Khlobystov, A. N.; Blake, A. J.; Champness, N. R.; Lemenovskii, D. A.; Majouga, A. G.; Zyk, N. V.; Schroder, M.; *Coord. Chem. Rev.* **2001**, *222*, 155. (b) Kitagawa, S.; Munakata, M.; *Trends Inorg. Chem.* **1993**, *3*, 437. (c) Munakata, M.; *Adv. Inorg. Chem.* **1998**, *46*, 173.
56. (a) Hoskins, B. F.; Robson, R.; *J. Am. Chem. Soc.*; **1989**, *111*, 5962, (b) Hoskins, B. F.; Robson, R.; *J. Am. Chem. Soc.*, **1990**, *112*, 1554.

57. Yaghi, O. M.; Li, H.; Davis, C.; Richardson, D.; Groy, T. L.; *Acc. Chem. Res.* **1998**, *31*, 474.
58. (a) Kondo, M.; Shimamura, M.; Noro, S.; Minakoshi, S.; Asami, A.; Seki, K.; Kitagawa, S.; *Chem. Mater.* **2000**, *12*, 1288. (b) Kituara, R.; Seki, K.; Akiyama, G.; Kitagawa, S.; *Angew. Chem.* **2003**, *115*, 444; *Angew. Chem. Int. Ed.* **2003**, *42*, 428. (c) Chen, B.; Eddaoudi, M.; Hyde, S. T.; O'Keeffe, M.; Yaghi, O. M.; *Science* **2001**, *291*, 1021. (d) Seki, K.; *Phys. Chem. Chem. Phys.* **2002**, *4*, 1968. (e) Biradha, K.; Fujita, M. *Angew. Chem.* **2002**, *114*, 3542; *Angew. Chem. Int. Ed.* **2002**, *41*, 3392. (f) Evans, O. R.; Lin, W.; *Chem. Mater.* **2001**, *13*, 2705.
59. (a) MacGillivray, L. R.; Subramanian, S.; Zaworotko, M. J.; *J. Chem. Soc., Chem. Commun.* **1994**, 1325. (b) Yaghi, O. M.; Li, H.; *J. Am. Chem. Soc.* **1995**, *117*, 10401. (c) Yaghi, O. M.; Li, H.; *J. Am. Chem. Soc.* **1996**, *118*, 295. (d) Yaghi, O. M.; Li, G.; *Angew. Chem. Int. Ed.* **1995**, *34*, 207.
60. Kondo, M.; Yoshitomi, T.; Seki, K. Matsuzaka, H.; Kitagawa, S.; *Angew. Chem. Int. Ed.* **1997**, *36*, 1725.
61. A few examples: (a) Noro, S.; Kitura, R.; Kondo, M.; Kitagawa, S.; Ishii, T.; Matsuzaka, H.; Yamashita, M.; *J. Am. Chem. Soc.* **2002**, *124*, 2583. (b) Noro, S.; Kitagawa, S.; Kondo, M.; Seki, K.; *Angew. Chem. Int. Ed.* **2000**, *39*, 2081. (c) Li, H.; Eddaoudi, M.; O'Keeffe, M.; Yaghi, O. M.; *Nature* **1999**, *402*, 276. (d) Seki, K.; Mori, W.; *J. Phys. Chem.* **2002**, 1380. (e) Seki, K.; *Chem. Commun.* **2001**, 1496. (f) Seki, K.; Takamizawa, S.; Mori, W.; *Chem. Lett.* **2001**, 332. (g) Eddaoudi, M.; Kim, J.; Rosi, N.; Vodac, D.; Wachter, J.; O'Keeffe, M.; Yaghi, O. M.; *Science* **2002**, *295*, 469. (h) Li, D.; Kaneko, K.; *J. Phys. Chem. B* **2000** *104*, 8940. (i) Chui, S. S. -Y.; Lo, S. M. -F.; Charmont, L. P. H.; Orpen, A. G.; Williams, I. D.; *Science*, **1999**, *283*, 1148.
62. (a) Fujita, M.; Kwon, Y. J.; Washizu, S.; Ogura, K.; *J. Am. Chem. Soc.* **1994**, *116*, 1151. (b) Seo, J. S.; Whang, D.; Lee, H.; Jun, S. I.; Oh, J.; Jeon, Y. J.; Kim, K.; *Nature* **2000**, *404*, 982. (c) Evans, O. R.; Ngo, H. L.; Lin, W.; *J. Am. Chem. Soc.* **2001**, *123*, 10395. (d) Sawaki, T.; Dewa, T.; Aoyama, Y.; *J. Am. Chem. Soc.* **1998**, *121*, 4793. (e) Pan, L.; Liu, H.; Huang, X.; Olson, D. H.; Turro, N. J.; Li, J.; *Angew. Chem. Int. Ed.* **2003**, *42*, 542. (f) Gomez-Lor, B.; Gutiérrez-Puebla, E.; Iglesias, M.; Monge, M. A.; Ruiz-Valero, C.; Snejko, N.; *Inorg. Chem.* **2002**, *41*, 2439. (g) Tanski, J. M.; Wolczanski, P. T.; *Inorg. Chem.* **2001**, *40*, 2026. (h) Tannenbaum, R.; *Chem. Mater.* **1994**, *6*, 550. (i) Tannenbaum, R. *J. Mol. Catal.* **1996**, *107*, 207. (j) Feinstein-Jaffe, I, Efraty, A.; *J. Mol. Catal.* **1987**, *40*, 1. (k) Naito, S.; Tanibe, T.; Saito, E.; Miyao, T.; Mori, W.; *Chem. Lett.* **2001**, 1178.
63. Lopez, S.; *PhD Thesis*, University of Missouri-Columbia, **2001**.
64. Knaust, J. M.; *PhD Thesis*, University of Missouri-Columbia, **2003**.

65. Keller, S. W.; *Angew. Chem. Int. Ed.* **1997**, *36*, 247.
66. Lopez, S.; Kahraman, M.; Harmata, M.; Keller, S. W.; *Inorg. Chem.* **1997**, *36*, 6138.
67. (a) Lopez, S.; Keller, S. W.; *Cryst. Eng.* **1999**, *2*, 101. (b) Lopez, S.; Keller, S. W.; *Inorg. Chem.*, **1999**, *38*, 1883.
68. Knaust, J. A.; Lopez, S.; Keller, S. W.; *Inorg. Chim. Acta* **2001**, *324*, 81.
69. Peng, Y.; *PhD Thesis*, University of Missouri-Columbia, **2000**.
70. Lopez, S.; Keller, S. W.; *J. Am. Chem. Soc.* **1999**, *121*, 6306.
71. (a) Hagrman, P. J.; Hgrman, D.; Zubieta, J.; *Angew. Chem. Int. Ed.* **1999**, *38*, 2638.
72. (a) Jung, O. -S.; Park, S.; Kim, K.; Jang, Ho; *Inorg. Chem.* **1998**, *37*, 5781. (b) Withersby, M. A.; Blake, A. J.; Champness, N. R.; Cooke, P. A.; Hubberstey, P.; Li, W. -S.; Schroder, M.; *Inorg. Chem.* **1999**, *38*, 2259. (c) Munakata, M.; Ning, G.; Kuroda-Sowa, T.; Maekawa, M.; Suenaga, Y.; Horino, T.; *Inorg. Chem.* **1998**, *37*, 5651. (d) Oh, M.; Carpenter, G. B.; Seigart, D. A.; *Organometallics*, **2003**, *22*, 2364. (e) Pedireddi, V. R.; Varughese, S.; *Inorg. Chem.* **2004**, *43*, 450. (f) Blake, A. J.; Champness, N. R.; Cooke, P. A.; Nicolson, J. E. B.; *Chem, Commun*, **2000**, 665. (g) Subramanian, S.; Zaworotko, M. J.; *Angew. Chem. Int. Ed.* **1995**, *34*, 2127.
73. (a) Hirsch, K. A.; Wilson, S. R.; Moore, J. S.; *Inorg. Chem* **1997**, *36*, 2960. (b) Yang, S, -P.; Chen, X. -M.; Ji, L. -N.; *J. Chem. Soc. Dalton Trans.* **2000**, 2337. (c) Lee, J. W.; Kim, E. A.; Kim, Y. J.; Lee, Y. -A.; Pak, Y.; Jung, O. -S.; *Inorg. Chem.* **2005**, *44*, 3151. (d) Jung, O. -S.; Kim, Y. J.; Lee, Y. -A.; Kim, K. -M.; Lee, S. S.; *Inorg. Chem.* **2003**, *42*, 844. (e) Withersby M. A.; Blake, A. J.; Champness, N. R.; Hubberstey, P.; Li, W. -S.; Schroder, M.; *Angew. Chem. Int. Ed.* **1997**, *36*, 2327. (f) Du, M.; Bu, X, -H.; Huang, Z.; Chen, S. -T.; Guo, Y. -M.; *Inorg. Chem.* **2003**, *42*, 552. (g) Schultheiss, N.; Powell, D. R.; Bosch, E.; *Inorg. Chem.* **2003**, *42*, 8886. Kim, H. -J.; Zin, W. -C.; Lee, M.; *J. Am. Chem. Soc.* **2004**, *126*, 7009. (h) Seward, C.; Chan, J.; Song, D.; Wang, S.; *Inorg. Chem.* **2003**, *42*, 1112.
74. (a) Lopez, S.; Keller, S. W.; *Inorg. Chem.* **1999**, *38*, 1883. (b) Lu, J.; Paliwala, T.; Lim, S. C.; Yu, C.; Niu, T.; Jacobsen, A. J.; *Inorg. Chem.* **1997**, *36*, 923. (c) Blake, A. J.; Champness, N. R.; Cooke, P. A.; Cicolson, J. E. B.; Wilson, C.; *J. Chem. Soc. Dalton Trans.* **2000**, 3811. (d) Ning, G. L.; Munakate, M.; Wu, L. P.; Maekawa, M.; Suenaga, Y.; Kuroda-Sowa, T.; Sugimoto, K.; *Inorg. Chem.* **1999**, *38*, 5668. (e) Roger, D. L.; Semeniuc, V. R.; Smith, M. D.; *Inorg. Chem.* **2004**, *43*, 537.
75. (a) Moulton, B.; Zaworotko, M. J.; *Chem. Rev.* **2001**, *101*, 1629. (b) Hennigar, T. L.; MacQuarrie, D. C.; Losier, P.; Rogers, R. D.; Zaworotko, M. J.; *Angew. Chem. Int. Ed.* **1997**, *36*, 972.

76. Threlfall, T. L.; *Analyst* **1995**, *120*, 2435.
77. (a) Jetti, R. K. R.; Boese, R.; Thallapally, P. K.; Desiraju, G. .; *Cryst. Growth Des.* **2003**, *3*, 1033. (b) Sarma J. A. R. P.; Desiraju, G. R.; *Polymorphism and Pseudopolymorphism in Organic Crystals: A Cambridge Structural Database Study*; In *Cryst. Eng.* **1999**, 325.
78. Parker, A. J.; *London Quart. Rev.* **1962**, *16*, 163.

# MATERIAL SYNTHESIS AND CHARACTERIZATION

## 2.1 Introduction

The following is a general description of the methods used to synthesize and characterize all of the copper(I) coordination solids we will present in this study. Included will be a listing of the general materials involved, the preparation of all of the starting materials, a detailed explanation of the various synthetic methods used to develop the final product, and a listing and description of the analytical techniques used in this study to characterize the materials. Single crystal and powder X-ray crystallography comprises the majority of the results, focus will be on these techniques.

## 2.2 General Experimental Section

### 2.2.1 *Materials*

*Caution! Perchlorate salts are explosive and should be handled in small quantities and with extreme care at all times.* Cu<sub>2</sub>O (Fisher), HPF<sub>6</sub>, HBF<sub>4</sub> (Aldrich); HClO<sub>4</sub>, H<sub>2</sub>SO<sub>4</sub> (Fisher); triflic acid (Acros); 4,4'-bipyridine, triphenylphosphine, pyrimidine (Aldrich); acetonitrile, benzonitrile, tetrahydrofuran, toluene, chloroform, dichloromethane,



benzene, nitrobenzene, nitromethane, and diethyl ether (Fisher); and, were used without further purification unless otherwise stated.

### 2.2.2 *Starting Material Synthesis*

All of the starting materials listed below were synthesized via modified literature methods.<sup>1, 2, 3</sup> Although each of the starting material products have a varying degree of air sensitivity, they were effectively stored for extended periods of time sealed in a glass vial and placed in a desiccator.

*Preparation of [Cu(MeCN)<sub>4</sub>]X, (X = BF<sub>4</sub><sup>-</sup> **SM1**, ClO<sub>4</sub><sup>-</sup> **SM2**, PF<sub>6</sub><sup>-</sup> **SM3**, SO<sub>3</sub>CF<sub>3</sub><sup>-</sup> **SM4**, HSO<sub>4</sub><sup>-</sup> **SM5**).*

In a 250 mL Erlenmeyer flask, Cu<sub>2</sub>O (0.30 g, 0.48 mmol) was suspended in 80 mL of MeCN. The acids of the appropriate anion (HBF<sub>4</sub>, HClO<sub>4</sub>, HPF<sub>6</sub>, HSO<sub>3</sub>CF<sub>3</sub>, or H<sub>2</sub>SO<sub>4</sub>) were added to the flask in 0.50 mL aliquots to 2.0 mL total volume of acid, with continuous stirring on a warm hotplate. The hotplate temperature was raised to bring the solution to a light boil, at which time most (if not all) of the Cu<sub>2</sub>O would be dissolved. The resulting clear, light blue solution was removed from the hotplate and allowed to cool to room temperature. Following this, the solution was poured directly into a flask containing 300 mL of diethyl ether (Et<sub>2</sub>O), at which time a white polycrystalline precipitate formed. The precipitate of **SM1-5** was collected by vacuum filtration, washed with three 2.0 mL aliquots of Et<sub>2</sub>O, and dried under a moderate vacuum.

The product was purified via recrystallization by, first dissolving the precipitate of **SM1-5** in a minimal amount of MeCN. The resulting solution was filtered by vacuum filtration and the filtrate was poured into 200 mL of diethyl ether. The resulting white

polycrystalline precipitate of **SM1-5** was vacuum filtered, washed with a small amount of Et<sub>2</sub>O, dried under vacuum, and stored in a desiccator.

*Preparation of [Cu(MeCN)<sub>2</sub>(PPh<sub>3</sub>)<sub>2</sub>]X (X = BF<sub>4</sub><sup>-</sup> **SM6**, ClO<sub>4</sub><sup>-</sup> **SM7**, PF<sub>6</sub><sup>-</sup> **SM8**, SO<sub>3</sub>CF<sub>3</sub><sup>-</sup> **SM9**, HSO<sub>4</sub><sup>-</sup> **SM10**).*

In a 50 mL Erlenmeyer flask, **SM1-5** (0.300 g, 0.95, 0.92, 0.82, 0.79, and 0.92 mmol, respectively) was dissolved in 10 mL of CH<sub>2</sub>Cl<sub>2</sub>, after which 2.0 mol equivalents of PPh<sub>3</sub> was added and also allowed to dissolve. The resulting pale yellow solution was poured into a flask containing 200 mL of Et<sub>2</sub>O. The resulting white polycrystalline precipitate of **SM6-10** was vacuum filtered, washed with a small amount of Et<sub>2</sub>O, and dried under a vacuum.

The product was purified via recrystallization by first dissolving the precipitate of **SM6-10** in a minimal amount of MeCN. The resulting solution was filtered by vacuum filtration and the filtrate was poured into 200 mL of diethyl ether. The resulting white polycrystalline precipitate of **SM6-10** was vacuum filtered, washed with a small amount of Et<sub>2</sub>O, dried under vacuum, and stored in a desiccator.

*Preparation of [Cu(PhCN)<sub>4</sub>]X, (X = BF<sub>4</sub><sup>-</sup> **SM11**, ClO<sub>4</sub><sup>-</sup> **SM12**, PF<sub>6</sub><sup>-</sup> **SM13**, SO<sub>3</sub>CF<sub>3</sub><sup>-</sup> **SM14**).*

In a 250 mL Erlenmeyer flask, Cu<sub>2</sub>O (0.300 g, 0.48 mmol) was suspended in 80 mL of PhCN. The acids of the appropriate anion (HBF<sub>4</sub>, HClO<sub>4</sub>, HPF<sub>6</sub>, or HSO<sub>3</sub>CF<sub>3</sub>) were added to the flask in 0.50 mL aliquots to 2.0 mL total volume of acid, while continuous stirring on a warm hotplate. The hotplate temperature was raised to bring the solution to a

light boil, at which time most (if not all) of the  $\text{Cu}_2\text{O}$  would be dissolved. The resulting clear, light yellow solution was removed from the hotplate and allowed to cool to room temperature. Following this, the solution was poured directly into a flask containing 300 mL of diethyl ether ( $\text{Et}_2\text{O}$ ), at which time a yellow polycrystalline precipitate formed for **SM11-13**. The crystalline precipitate of **SM11-13** is collected by vacuum filtration, washed with three 2.0 mL aliquots of  $\text{Et}_2\text{O}$ , and dried under vacuum. For **SM14** (the triflate material), a yellow oil settled on the bottom of the flask instead of a precipitate. This oil was extracted with a glass pipette and then placed under vacuum to draw off any residual  $\text{Et}_2\text{O}$ . Over time, this oil solidified into a sticky yellow solid and was used without further recrystallization.

The other three crystalline products (**SM11-13**) were purified via recrystallization by, first dissolving the crystalline precipitate of **SM11-13** in a minimal amount of PhCN. The resulting solutions were filtered by vacuum filtration and the filtrates were poured into 200 mL of diethyl ether. The resulting yellow polycrystalline precipitate of **SM6-8** was vacuum filtered, washed with a small amount of  $\text{Et}_2\text{O}$ , and dried under vacuum.

#### *Preparation of $[\text{Cu}(\text{MeCN})_4]_3\text{PMo}_{12}\text{O}_{40}$ **SM10***

To 250 mL Erlenmeyer flask containing a slurry of  $\text{Cu}_2\text{O}$  (2.2 mg, 15.4 mmol) in MeCN (100 mL),  $\text{H}_3\text{PMo}_{12}\text{O}_{40}$  (18.8 mg, 10.3 mmol) was slowly added while stirring and gently heating the flask on a hotplate. With continued stirring and heat, an additional 300 mL of MeCN was added, resulting in a clear, orange solution. This solution was filtered to remove any non-reacted  $\text{Cu}_2\text{O}$  and the filtrate was poured into a flask containing 300

mL of Et<sub>2</sub>O, resulting in the formation of an orange/brown polycrystalline precipitate of **SM10**. This precipitate was collected by vacuum filtration and dried under vacuum.

### 2.2.3 *Synthesis of the Cu(I) Coordination Clay and Zeolite*

#### *Analogs*

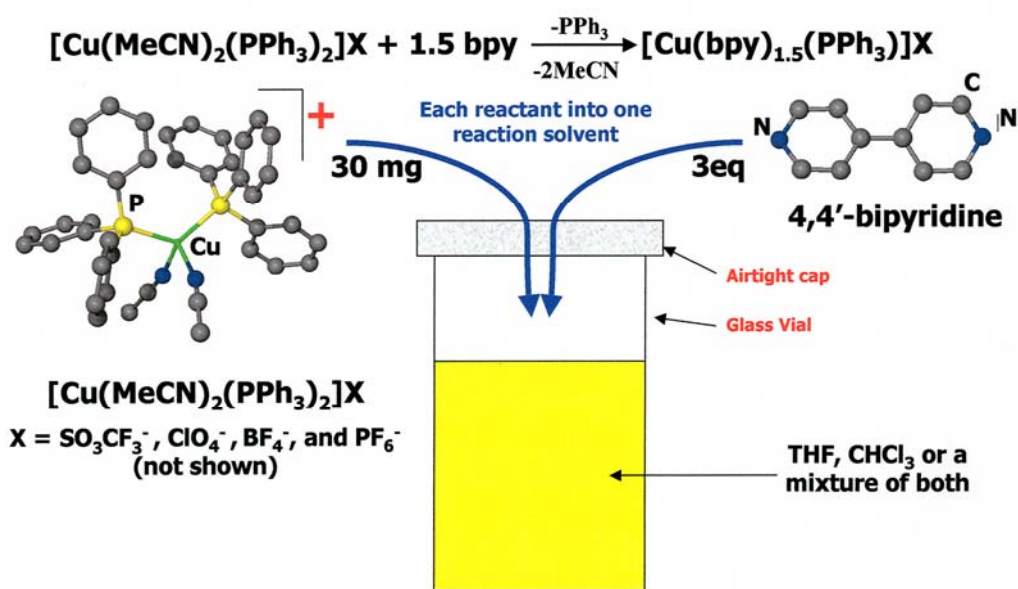
Probably one of the greatest advantages of working with Cu(I) coordination polymers is the relative ease of the synthesis involved to produce these functional porous solids. Essentially, the synthesis involves a solvent-born, self-assembly reaction between the Cu(I) starting material and the appropriate bridging ligand, usually carried out at room temperature. Crystal growth from solution can offer both added control in the crystallization process as well as provide routes not available thru more traditional high temperature syntheses.<sup>4</sup> This makes it possible to grow crystals that are relatively unstable at higher temperatures, or exist as several polymorphic forms at various temperatures and are difficult to obtain in pure form under standard high temperature conditions.<sup>5</sup>

In order for this crystallization to be effective in our case, the solvent must dissolve the reactants and allow the self-assembly reaction to progress until a crystalline, polymeric solid is obtained. In several reactions, the polymeric solid is only slightly soluble in the reaction solvent so crystallization appears spontaneously as the polymer takes form.<sup>5,6</sup>

Figure 2.1 shows a typical reaction set-up to used produce the Cu(I) layered coordination solids, which we will discuss in more detail in Chapter 3. The reaction is carried out in a variety of solvents, with the product generally forming within minutes to several hours after first initial mixing of the reactants. A 2-fold excess of the bridging bpy

ligand is used to facilitate a complete reaction leading to the successful formation of the extended solids.

The solubility of the starting material and product is of such a degree in these reactions (in a few select solvents as shown) that allows for the slow growth of single crystals. The previous work done by Susan Lopez relied on the layering of THF or toluene onto the CHCl<sub>3</sub> reaction solvent to produce her polymorphs.<sup>1,7</sup> We found, however, that simply making solvent mixtures with varying ratios of THF/CHCl<sub>3</sub> and toluene/CHCl<sub>3</sub> provided much more experimental control while still maintaining a suitable reaction solvent to produce the product in crystalline form.

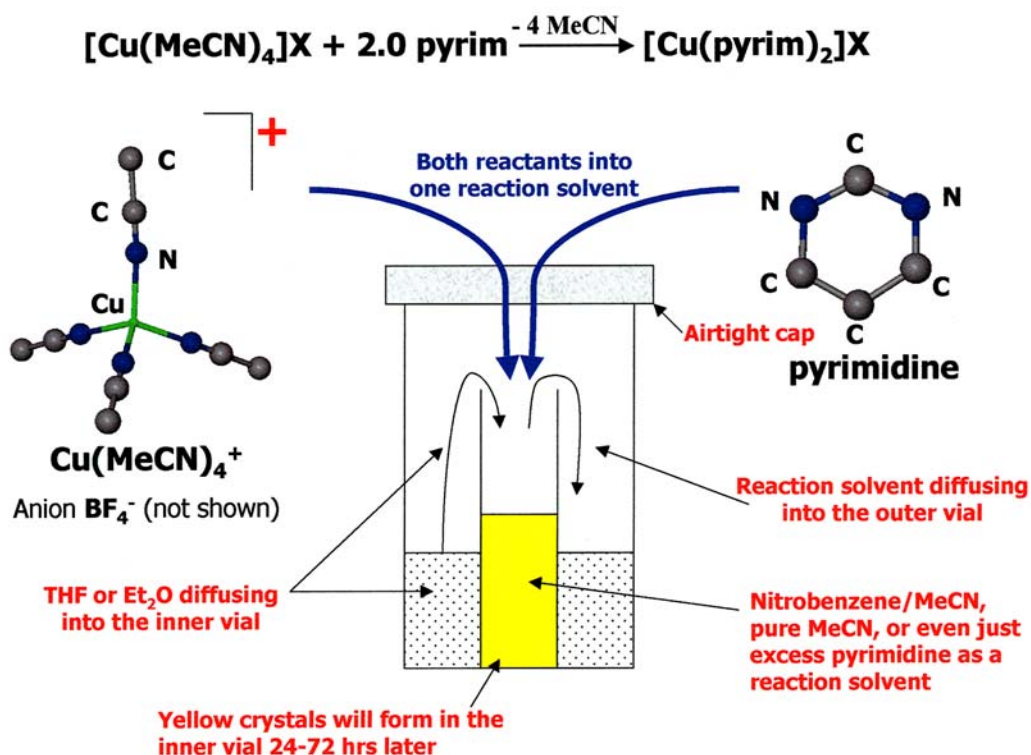


**Figure 2.1** A typical Cu(I)/bpy reaction which produce the layered coordination solid structures.

In many other reactions, such as those that produce the 3-D networks of the zeolite-analogs, the product is so insoluble that only a polycrystalline precipitate would form unless a strongly coordinating solvent is used to retain the reactants in solution. To promote single crystal formation, this reaction solvent requires a slow addition of a

*crystallizing* solvent (one in which the product is relatively insoluble) to the reaction solvent. This is accomplished thru use of a crystallization technique called *solvent vapor diffusion*.

The reactions involving the  $\text{Cu}(\text{MeCN})_4\text{X}$  or  $\text{Cu}(\text{PhCN})_4\text{X}$  starting materials with pyrimidine are usually carried out in MeCN or PhCN solvents, respectively. Since these solvents can also act as ligands and can effectively exchange with the other ligands (including the bridging pyrimidine ligand) on the Cu(I) center, the product tends to remain in solution until the crystallizing solvent is introduced. As shown in Figure 2.2, these reactions take place in the smaller, inner vial, while the crystallizing solvent ( $\text{Et}_2\text{O}$  or THF) found in the larger outer vial. As the reaction commences, each solvent (that of



**Figure 2.2** A typical vapor diffusion reaction used in the Cu(I)/pyrimidine reactions that produce the zeolite-analogs.

the reactant and of the crystallizer) slowly diffuses into each other, forming mixtures of the two solvents. As the crystallizing solvent concentration in the reaction mixture slowly increases, the crystalline Cu(I) coordination product begins to appear.

This vapor diffusion is a typical equilibrium process, with both the reaction solvent diffusing out of the small vial as the crystallization solvent diffuses in. Each solvent, however, diffuses at its own rate depending on solvent's particular enthalpy of vaporization ( $\Delta H_{\text{vap}}$ ). Those solvents with a lower  $\Delta H_{\text{vap}}$ , such as Et<sub>2</sub>O ( $\Delta H_{\text{vap}}(25^\circ\text{C}) = 27$  kJ/mol) will diffuse at a much faster rate than those with a higher value, such the MeCN ( $\Delta H_{\text{vap}}(25^\circ\text{C}) = 33$  kJ/mol) used in this example. The results are that the total volume of solvent in the reaction vial begins to increase as more Et<sub>2</sub>O diffuses into vial then MeCN diffuses out.

When THF ( $\Delta H_{\text{vap}}(25^\circ\text{C}) = 32$  kJ/mol) is used as the crystallizing solvent, the reaction solvent volume may slightly decrease over time. However, equilibrium rules still apply, as both the solvents in the reaction vial as well as the solvent in the outer vial are slowly becoming solvent mixtures of equal ratios. As this occurs, the crystallization of the polymeric porous solid is realized just as it has been with the more volatile Et<sub>2</sub>O as the crystallizing solvent. Surprisingly, as we will show in Chapter 5, there appears to be little difference between the use of either Et<sub>2</sub>O or THF as the crystallizing solvent in relation to the final Cu(I) polymeric product that is formed in these particular reactions.

## 2.3 Material Characterization and X-ray

### Crystallography

#### 2.3.1 General Methods

What we consider as the *general methods* of material characterization include those methods that only provide limited information; little, if any, that may be helpful in identifying what type of structure has been developed. Those general methods used in this study include nuclear magnetic resonance (NMR) and Fourier transform-infrared (FT-IR) spectroscopy, as well as thermogravimetric analysis (TGA).

Both the NMR and FT-IR spectroscopic methods are powerful tools for the identification of organic and organometallic compounds. However, they fall short of this ability in the examination of our Cu(I) polymers while in solution because of the rapid ligand exchange that these type of materials can exhibit while in solution. For the most part, these methods simply do not supply enough information to distinguish one coordination network from another. In any case, the data obtained from either of these two methods can be used to identify (and verify) the basic components present in the final structure.

Through the use of  $^1\text{H}$  NMR spectroscopy, for example, we can easily identify the organic ligands present in our sample as well as obtain a quantitative comparison of all the components by integration of the individual peaks found in the spectrum. This can be useful in preliminary examination of crystalline product prior to X-ray diffraction studies, as a back-up verification of single crystal X-ray diffraction structural data, or to determine the formula of any polycrystalline precipitates.



NMR spectroscopy can also be considerably valuable to identify solvated molecules that are so disordered throughout the structure that X-ray diffraction data fails to identify them completely. An example of this can be seen in the study done on the feldspar-analog in which an  $^1\text{H}$  NMR spectra of the crystalline product dissolved in  $[\text{d}_6]\text{DMSO}$  revealed the presence of both nitrobenzene and THF even though X-ray crystallographic methods failed to pinpoint these species in the structure.<sup>8</sup> Further examples of these types of analysis are presented throughout the entirety of this dissertation.

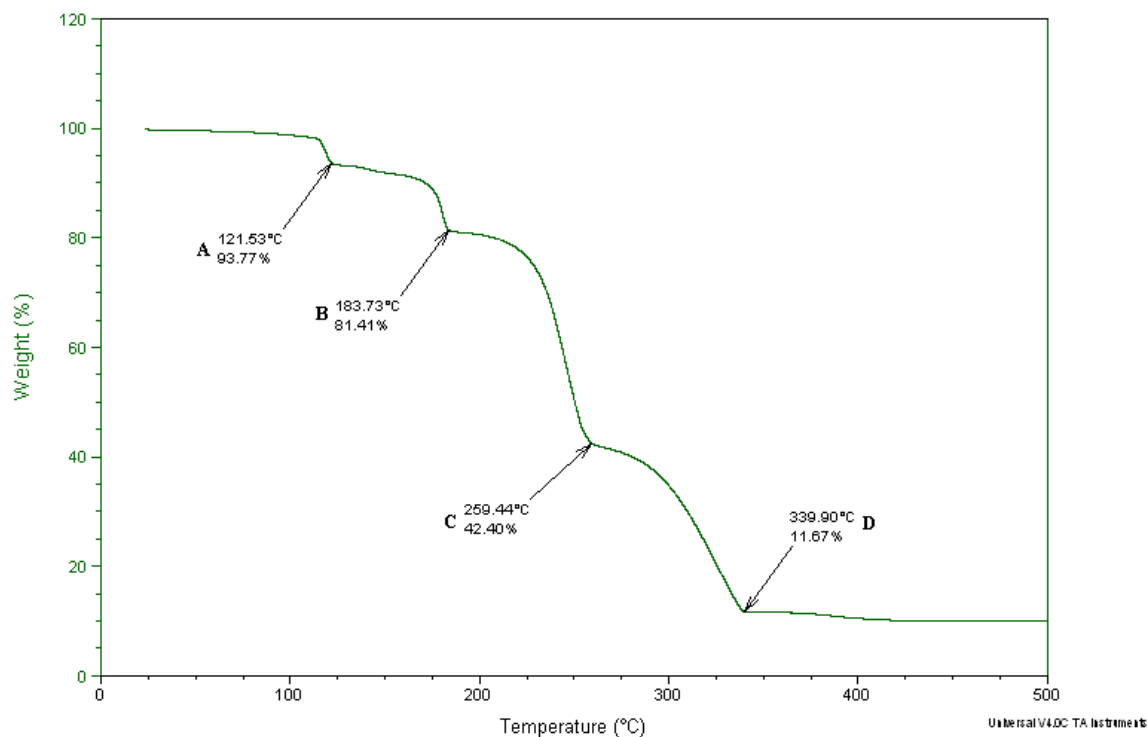
Although FT-IR spectroscopy has been the analysis of choice by others to observe the anion exchange abilities of these materials,<sup>9</sup> we found that the NMR can also be quite useful in this study as well. As we will show in Chapter 5, the  $\text{BF}_4^-$ ,  $\text{PF}_6^-$ , and  $\text{SO}_3\text{CF}_3^-$  anion exchange from solution to solid can be followed by using  $^{19}\text{F}$  NMR analysis. The greatest advantage of this type of analysis is that the exchange can be observed in situ, as consecutive scans of a solution can be performed while the exchange is in progress.

The TGA data is developed by graphically recording the weight loss of a material as it is subjected to a slowly rising temperature. Several studies have shown how the TGA data obtained from various coordination polymers provides information on the various ligand bond strength and solvent retention within the porous network.<sup>10</sup> An example of typical TGA data can be seen in Figure 2.3, as collected from the thermal decomposition of the layered coordination solid,  $[\text{Cu}(\text{bpy})_{1.5}(\text{PPh}_3)]\text{BF}_4 \cdot (\text{THF})_{1.33} \cdot (\text{CHCl}_3)_{0.33}$ , developed by Susan Lopez and presented in Section 1.5.<sup>1, 7</sup>

Sample: [Cu(bipy)1.5(PPh3)]BF4  
Size: 7.0950 mg  
Method: Ramp  
Comment: Cu and BF4 layered pentagons

TGA

File: D:\...Cu and BF4 layered pentagons.001  
Operator: Knight  
Run Date: 22-Jun-2004 11:18  
Instrument: TGA Q50 V4.7 Build 151



**Figure 2.3** The thermal decomposition of a layered coordination solid showing the systematic loss of the ligands.

The data indicates that the material remains stable up to a temperature of  $\sim 121^\circ\text{C}$ , at which point there is a small 6.33% weight loss, which could correspond to the loss of the  $\text{CHCl}_3$  solvent (theoretical 5.1%). The second 12.36% loss at  $\sim 184^\circ\text{C}$  is an even closer match to the solvated THF (theoretical 11.72%) also found within in the structures layered polymeric network. The last two weight losses of 39.01% at  $259^\circ\text{C}$  and 30.73% at  $340^\circ\text{C}$  correspond to the  $\text{PPh}_3$  (theoretical 33.99%) and the bridging bipy ligand (theoretical 30.36%), respectively.

Although results like this can give us insight on how the various components of the material are bonded in the coordination network, it gives us little (if any) information

regarding the network's actual structure. However, this method can take part in the comparison of the ligand bonding of similar (yet slightly different) compounds as will be shown later in Chapter 4. In advance studies of the porous solids, TGA should be useful for determining the inclusion of either a particular solvent or gas molecule as these materials' functionality is put to the test. In several cases the use of TGA was restricted since many of the products contained the perchlorate anion, which tends to make these materials potentially explosive. Initial TGA studies show that these types of materials appear to detonate when the instrument reaches temperatures of  $\sim 150^\circ\text{C}$ .

## 2.3.2 *Crystallography and X-ray Diffraction*

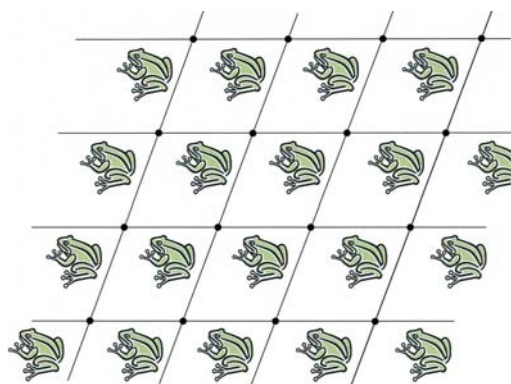
### 2.3.2.1 *Crystallography*

By far the most powerful tool at our disposal for the characterization of porous coordination solids is the single crystal X-ray crystallography. This technique provides us with an accurate account of the structure and properties of our materials crystalline state. Additional advanced analytical and graphical tools associated with this process allows for an in-depth study of the materials chemistry and provides us with the means to effectively communicate these results to others. In the following paragraphs, we will present a brief introduction to crystallography and X-ray diffraction as well as define some key concepts and terms that are used throughout this dissertation.

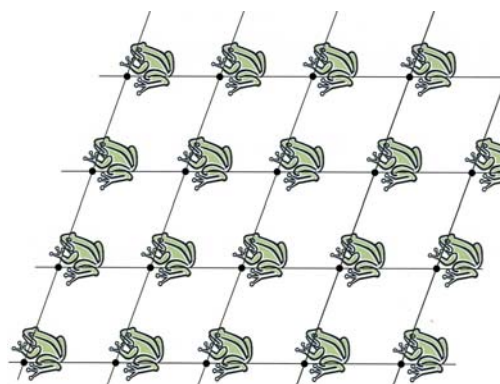
The term *crystallography*, itself, is the study of the structure and properties of the crystalline state. The notion of what a *crystal* really is might be based solely on visual observations, describing crystals as having flat surfaces with sharp edges such as seen with the precious gems or the all too common quartz crystals. This definition breaks down when we consider all the crystalline solids, including polycrystalline solids with crystals

so small that the material more resembles an amorphous powder, than that of a crystalline solid. A more precise definition is that *a crystal consists of atoms that are arranged in a three-dimensional periodically repeating pattern.*<sup>11</sup>

These patterns of atoms, as they combine to form molecules, which in turn form patterns of molecules, are defined by sectioning off the smallest unit of the solid that repeats over and over again in regular intervals. In the example shown in Figure 2.4a, a two-dimensional wallpaper pattern represents what these sections might look like for a



**Figure 2.4a** A pictorial representation of the lattice points in two-dimensional net.



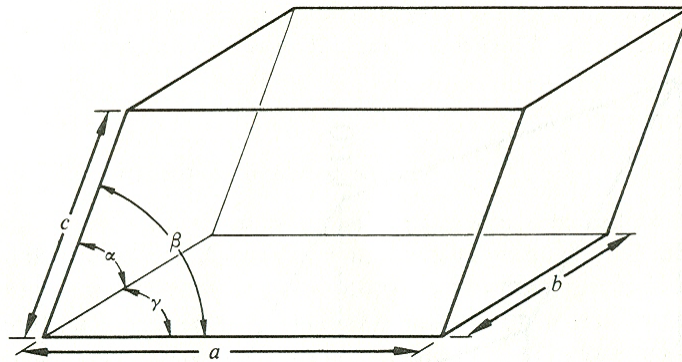
**Figure 2.4b** A different selection of lattice points simply shifts the positioning of the 2-D net.

periodically repeating structure. A random point can be selected in this pattern with its repeated location identified throughout the pictorial. As we connect these points, a series of parallelograms are formed with each cell defining the basic component of the wallpapers structure.

Each of these points, called the *lattice points*, have identical positions within the net with each point having exactly the same surroundings. Other lattice points in this design can easily be selected and would be just as valid of choice. For example, we could choose a point 2 cm left of each point and still claim each and every one of those new points as the lattice points. We can even choose a point off the established net; in the middle of each cell, for example. Even with this choice, a similar net can be drawn (Figure 2.4b) as

we connect each of the new lattice points together as before; resembling more like we simply shifted the net while holding the wallpaper stationary.

Of course, our crystalline solids reside in a three-dimensional net. We can adjust our design by simply adding depth to our net, which generates a series of identical parallelepipeds with definite  $a$ ,  $b$  and  $c$  sides and corresponding  $\alpha$ ,  $\beta$ , and  $\gamma$  angles. Each of these individual parallelepipeds, as shown in Figure 2.5, are the defining feature of our

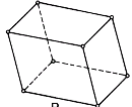
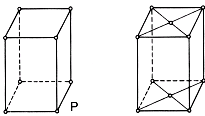
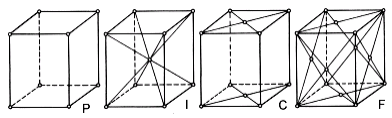
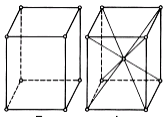
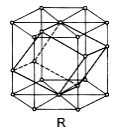
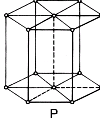
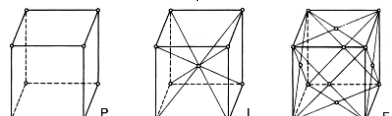


**Figure 2.5** The Unit Cell showing the  $a$ ,  $b$  and  $c$  sides as well as the corresponding  $\alpha$ ,  $\beta$ , and  $\gamma$  angles.

crystalline solid and are called the *unit cell* of the structure. The contents within a unit cell repeat over and over again and, if we know the atomic arrangement inside a unit cell, we then know the atomic arrangement of the entire crystalline solid. Smallest repeating collection of atoms unique for every structure is called the *asymmetric unit*. The asymmetric unit is the most basic form of the crystalline structure as each atom in this unit are related to all the other atoms in the crystal via a variety of symmetry elements of which we will explore in greater detail below.

Every unit cell is classified into one of seven crystal systems, each having symmetrical restrictions placed on the lattice vectors, providing each system with distinctive and unique geometric parameters. The triclinic system, for example has no

restrictions placed on the unit cell dimensions, while the monoclinic is similar with the exception that  $\alpha = \lambda = 90^\circ$ . As all possible centering occurrences are taken into account, these seven crystal systems develop into fourteen *Bravais lattices*. These types of centering include body centering (symbol I), C-centered (symbol C), and the centering of all four faces as face-centered (symbol F). A cell lacking any type of centering is designated as a primitive (symbol P) cell. The seven crystal systems and the restrictions placed on the axial systems along with the fourteen Bravais lattices can be seen in Table 2.1.

Crystal System	Restrictions on the axial system	Bravais Lattices
Triclinic	$a \neq b \neq c,$ $\alpha \neq \beta \neq \lambda$	
Monoclinic	$a \neq b \neq c,$ $\alpha = \lambda = 90^\circ, \beta > 90^\circ$	
Orthorhombic	$a \neq b \neq c,$ $\alpha = \beta = \lambda = 90^\circ$	
Tetragonal	$a = b \neq c,$ $\alpha = \beta = \lambda = 90^\circ$	
Trigonal	$a = b = c,$ $\alpha = \beta = \lambda \neq 90^\circ$ (rhombohedral axis) or $a = b,$ $\alpha = \beta = 90^\circ, \lambda = 120^\circ$ (hexagonal axis)	 (the rhombohedral cell is shown within the hexagonal cell)
Hexagonal	$a = b,$ $\alpha = \beta = 90^\circ, \lambda = 120^\circ$	
Cubic	$a = b = c,$ $\alpha = \beta = \lambda = 90^\circ$	

It should be noted that there is a similarity between the trigonal and hexagonal systems in which symmetry guarantees that cells with  $a = b$ ,  $\alpha = \beta = 90^\circ$ ,  $\lambda = 120^\circ$  can be chosen with both of these systems. In this case, the two systems are distinguished from each other by the trigonal system having a 3-fold axis of symmetry while the hexagonal systems has a 6-fold axis. A trigonal cell with these dimensional restrictions, however, may not turn out to be primitive; leading to the selection of a rhombohedral (symbol R) cell with  $a = b = c$ ,  $\alpha = \beta = \lambda \neq 90^\circ$  dimensions. This cell resembles that of a cubic cell, which has been elongated on one diagonal of the cube (with the trigonal threefold axis about that diagonal) and fits neatly within the original hexagonal cell.

These crystal systems are further categorized by the various symmetry elements that they are associated with. A listing of these symmetry elements, a brief description of the symmetry operation, and the symbol used can be seen in Table 2.2. Spectroscopists commonly use the Schoenflies symbols while crystallographers prefer the Hermann-Mauguin or international symbols.

**Table 2.2** Symmetry operations and symmetry elements

Symmetry Element	Symmetry operation	Schoenflies Symbol	Hermann-Mauguin Symbol
	Identity *	E or $C_1$	1
n-fold symmetry axis	Rotation by $360^\circ/n$	$C_n$	$n$
Mirror plane	Reflection	$\sigma$	$m$
Center of inversion	Inversion	i or $C_i$	-1
n-fold axis of improper rotation **	Rotation by $2\pi/n$ followed by reflection perpendicular to the rotation axis	$S_n$	N/A
		$C_{ni}$	-n

\*The symmetry element can be thought of as the molecule as a whole.

\*\*Note the equivalences  $S_1 = \sigma$  and  $S_2 = i$

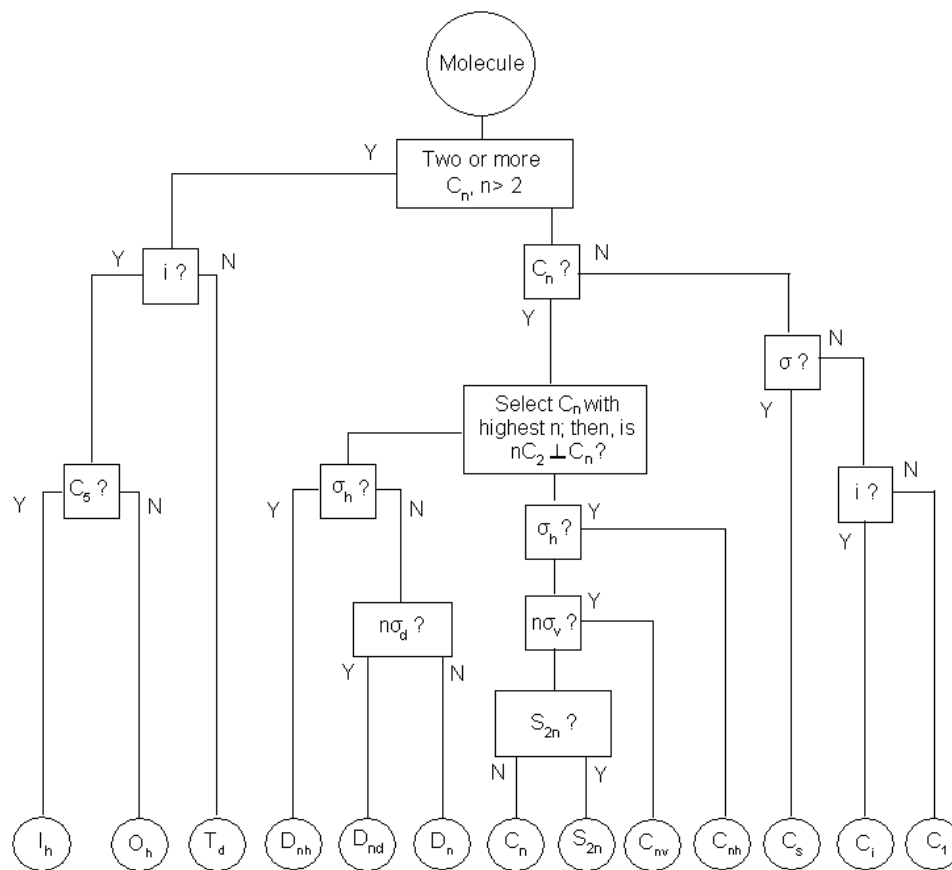
Although the symbols vary when defining either molecules or crystal systems, in most cases the same symmetry rules apply. Improper rotation is the exception to this, however, since the Schoenflies symbol  $S_n$  refers to a combination of a  $2\pi/n$  rotation followed by a mirror reflection while the Hermann-Mauguin symbol  $\bar{n}$  refers to a  $2\pi/n$  rotation followed by inversion through a point. This operation is more as  $C_{ni}$  in Schoenflies notation. As a result of this difference in symmetry operations, for those elements where  $n$  is odd,  $S_n = \bar{2n}$  and  $\bar{n} = S_{2n}$ . Thus  $S_1 = \bar{2} = m$ ,  $\bar{1} = S_2 = i$ ,  $S_3 = \bar{6}$ ,  $\bar{3} = S_6$ ,  $S_5 = \bar{10}$ , and  $S_{10} = \bar{5}$ . Only when  $n = 4$  as  $S_4$  and  $\bar{4}$  are these two operations equivalent.

Like the molecules, the asymmetric units in these crystal systems utilize several symmetry elements collectively in what are known as *point groups*. This group derives its name from the way molecules have one point that remains in a fixed position under all the symmetry operations. The flow chart shown in Figure 2.6 shows how all the point groups are derived from the various symmetry element conditions. Included in this chart are all the variations of the mirror plane element; as the vertical  $\sigma_v$ , horizontal  $\sigma_h$ , and diagonal  $\sigma_d$  mirror plane. The linear groups,  $D_{\infty h}$  and  $C_{\infty v}$ , are not included in this scheme since they are also not present in the crystal systems.

Each point group is assigned to the seven crystal systems depending upon the symmetry operations that are possible with that particular unit cell. It is, in fact more accurate to say that the unit cell is derived from the point groups rather than to say the opposite being true. A crystal is said to be monoclinic, for example, if symmetry elements are present that impose a restriction on that lattice vectors only requiring that  $\alpha = \lambda = 90^\circ$ .



**Figure 2.6** Determination of Point groups.<sup>12</sup>



Only the  $C_2$ ,  $C_5$ , and  $C_{2h}$  point groups impose these, and only these, restrictions on the lattice vectors, making them the monoclinic point groups. Likewise, the  $C_1$ , and  $C_i$  point groups impose no restrictions on the lattice vectors making them characterize the triclinic system. This continues to hold true for the rest of the crystal systems as each system point group members impose *only* those lattice vector restrictions inherent to that particular system. Table 2.3 list the seven crystal systems along with the appropriate thirty-two crystallographic point groups.

**Table 2.3**  
The 32 Crystallographic Point Groups

Crystal System	Schoenflies Symbol	Herman-Mauguin Symbol
Triclinic	$C_1$	1
	$C_i$	-1
Monoclinic	$C_2$	2
	$C_s$	$m$
	$C_{2h}$	$2/m$
Orthorhombic	$D_2$	222
	$C_{2v}$	$mm2$
	$D_{2h}$	$mmm$
Tetragonal	$C_4$	4
	$S_4$	-4
	$C_{4h}$	$4/m$
	$D_4$	422
	$C_{4v}$	$4mm$
	$D_{2h}$	$-42m$
	$D_{4h}$	$4/mmm$
Trigonal	$C_3$	3
	$C_{3i}$	-3
	$D_3$	32
	$C_{3v}$	$3m$
	$D_{3d}$	$-3m$
Hexagonal	$C_6$	6
	$C_{3h}$	-6
	$C_{6h}$	$6/m$
	$D_6$	622
	$C_{6v}$	$6mm$
	$D_{3h}$	$-6m2$
	$D_{6h}$	$6/mmm$
Cubic	$T$	23
	$T_h$	$m3$
	$O$	432
	$T_d$	$-43m$
	$O_h$	$m3m$

The Herman-Mauguin symbols used for the thirty-two crystallographic point groups have become more complex as they now refer to combinations of symmetry elements. Crystallographer prefers this type of notation because it is easily extended to include the translational symmetry elements we will introduce shortly and because directions of the

symmetry axis can be deduced from analysis of these types of symbols. The following summary should help with the understanding of these types of symbols:

1. Each of the symbols components refers to a different direction. Combination terms of  $2/m$ ,  $4/m$ , and  $6/m$  are single components, thus refer to only one direction. For example, in  $6/mmm$ , the  $6/m$  is a single component that reads as “six over m” and refers to a mirror plane that is perpendicular to a 6-fold rotational axis.
2. The location of  $m$  indications the direction that is normal to the mirror plane.
3. In an orthorhombic system with the axis labeled  $x$ ,  $y$ , and  $z$ ; the three directions are mutually perpendicular and the symbol  $mm2$  refers to mirror planes perpendicular to the  $x$  and  $y$ , and a 2-fold axis parallel to the  $z$  axis.
4. In the tetragonal system, there is always either 4 or  $\bar{4}$  in the first position and refers to the  $z$  direction. The mutually perpendicular  $x$  and  $y$  axes are handled by the second component, while the third component refers to the directions in the  $xy$  plane that bisect the angles formed by the  $x$  and  $y$  axes.
5. For the trigonal and hexagonal systems, the 3 and  $\bar{3}$  or 6 and  $\bar{6}$ , respectively refer to the  $z$  direction and symmetry in directions ( $120^\circ$  or  $60^\circ$  apart) normal to these rotational axes are referred to in the second component of the symbol.
6. The third symbol in the hexagonal system indicates the symmetry in the direction bisecting the angles between the directions of the second component.

7. In the cubic system, the 3 in the second position refers to the four body diagonals of the cube. The first component refers to the axis of the cube while the third component refers to the face diagonals.

In order to complete our categorization of crystalline solids, we need to add two more symmetry elements unique to these periodic, three-dimensional systems. In the description of point groups, it was indicated that one point of the molecule remains fixed during the each symmetry operation. While point group symmetry is complete for individual, finite molecules of crystals, we must also consider the symmetry from molecule to molecule that exist in an infinite state throughout the crystalline solid. To satisfy this criterion, we need to add *translational symmetry* to the list in the form of *screw axes* and *glide planes*.

The *screw axes* are denoted by the symbol  $n_p$ , which signifies a rotation of  $360^\circ/n$  radians followed by a  $p/n$  translation along the axis of rotation. For example, with a  $2_1$  component (read as “two-one”), there would be a  $180^\circ$  rotation followed by  $1/2$  of a unit cell translation parallel to the axis. In the same light, a  $4_1$  component would signify a  $90^\circ$  rotation followed by  $1/4$  of a unit cell translation. All the possible screw axes are  $2_1$ ,  $3_2$ ,  $4_1$ ,  $4_2$ ,  $4_3$ ,  $6_1$ ,  $6_2$ ,  $6_3$ ,  $6_4$ , and  $6_5$ .

The *glide plane* consists of a reflection on a plane followed by a translation in the direction of the indicated axis. *Axial glides* along  $a$ ,  $b$ , or  $c$ , are denoted by the symbol  $a$ ,  $b$ , or  $c$  and are indicative of a reflection on a plane followed by a translation of  $a/2$ ,  $b/2$ , or  $c/2$ , respectively. *Diagonal glides* are denoted by  $n$  and involve a translations parallel to the face diagonal as  $(a + b)/2$ ,  $(b + c)/2$ , or  $(c + a)/2$  translations. Finally, *diamond*

*glides*, denoted by  $d$ , are translation of  $(a \pm b)/4$ ,  $(b \pm c)/4$ , or  $(c \pm a)/4$ ; or  $(a \pm b \pm c)/4$  for tetragonal and cubic.

The addition of these translational symmetry elements to the symmetry model leads to the formation of 230 *space groups* as shown in entirety in Table 2.4. A detailed listing

**Table 2.4** The 230 Space Groups

TRICLINIC						
P 1	P-1					
MONOCLINIC						
P 2	P 2 <sub>1</sub>	C 2	P m	P c	C m	C c
P 2/m	P 2 <sub>1</sub> /m	C 2/m	P 2/c	P 2 <sub>1</sub> /c	C 2/c	
ORTHORHOMBIC						
P 2 2 2	P 2 2 2 <sub>1</sub>	P 2 <sub>1</sub> 2 <sub>1</sub> 2	P 2 <sub>1</sub> 2 <sub>1</sub> 2 <sub>1</sub>	C 2 2 2 <sub>1</sub>	C 2 2 2	F 2 2 2
I 2 2 2	I 2 <sub>1</sub> 2 <sub>1</sub> 2 <sub>1</sub>	P m m 2	P m c 2 <sub>1</sub>	P c c 2	P m a 2	P c a 2 <sub>1</sub>
P n c 2	P m n 2 <sub>1</sub>	P n a 2 <sub>1</sub>	P n n 2	C m m 2	C m c 2 <sub>1</sub>	C c c 2
A m m 2	A b m 2	A m a 2	A b a 2	F m m 2	F d d 2	I m m 2
I b a 2	P m m m	P n n n	P c c m	P b a n	P m m a	P n n a
P m n a	P c c a	P b a m	P c c n	P b c m	P n n m	P m m n
P b c n	P b c a	P n m a	C m c m	C m c a	C m m m	C c c m
C m m a	C c c a	F m m m	F d d d	I m m m	I b a m	I b c a
I m m a						
TETRAGONAL						
P 4	P 4 <sub>1</sub>	P 4 <sub>2</sub>	P 4 <sub>3</sub>	I 4	I 4 <sub>1</sub>	P -4
I -4	P 4/m	P 4 <sub>2</sub> /m	P 4/n	P 4 <sub>2</sub> /n	I 4/n	I 4 <sub>2</sub> /n
P 4 2 2	P 4 2 <sub>1</sub> 2	I 4 <sub>1</sub> 2 <sub>1</sub> 2	P 4 <sub>2</sub> 2 2	P 4 <sub>2</sub> 2 <sub>1</sub> 2	P 4 <sub>3</sub> 2 2	P 4 <sub>3</sub> 2 <sub>1</sub> 2
I 4 2 2	P 4 m m	P 4 b m	P 4 <sub>2</sub> c m	P 4 c c	P 4 n c	P 4 <sub>2</sub> m c
P 4 <sub>2</sub> b c	I 4 m m	I 4 c m	I 4 <sub>1</sub> m d	I 4 <sub>1</sub> c d	P -4 2 m	P -4 2 <sub>1</sub> m
P -4 2 <sub>1</sub> c	I -4 m 2	P -4 c 2	P -4 n 2	P -4 m 2	I -4 c 2	I -4 2 m
P -4 b 2	P -4 n 2	P -4 m 2	I -4 c 2	I -4 2 m	I -4 2 d	P 4/m m m
P 4/n m m	P 4/n b m	P 4/n n c	P 4/m b m	P 4/m n c	P 4/n m m	P 4/n c c
P 4 <sub>2</sub> /m m c	P 4 <sub>2</sub> /m c m	P 4 <sub>2</sub> /n b c	P 4 <sub>2</sub> /n n m	P 4 <sub>2</sub> /m b c	P 4 <sub>2</sub> /m n m	P 4 <sub>2</sub> /n m c
P 4 <sub>2</sub> /n c m	I 4/m m m	I 4/m c m	I 4 <sub>1</sub> /a m d	I 4 <sub>1</sub> /a c d		
TRIGONAL						
P 3	P 3 <sub>1</sub>	P 3 <sub>2</sub>	R 3	P -3	R -3	P 3 1 2
P 3 2 1	P 3 <sub>1</sub> 1 2	P 3 <sub>1</sub> 2 1	P 3 <sub>2</sub> 1 2	P 3 <sub>2</sub> 2 1	R 3 2	P 3 m 1
P 3 1 m	P 3 c 1	P 3 1 c	R 3 m	R 3 c	P -3 1 m	P -3 1 c
P -3 m 1	P -3 c 1	R -3 m	R -3 c			
HEXAGONAL						
P 6	P 6 <sub>1</sub>	P 6 <sub>5</sub>	P 6 <sub>2</sub>	P 6 <sub>4</sub>	P 6 <sub>3</sub>	P -6
P 6/m	P 6 <sub>3</sub> /m	P 6 2 2	P 6 <sub>1</sub> 2 2	P 6 <sub>5</sub> 2 2	P 6 <sub>2</sub> 2 2	P 6 <sub>4</sub> 2 2
P 6 <sub>3</sub> 2 2	P 6 m m	P 6 c c	P 6 <sub>3</sub> c m	P 6 <sub>3</sub> m c	P -6 m 2	P -6 c 2
P -6 2 m	P -6 2 c	P 6/m m m	P 6/m c c	P 6 <sub>3</sub> /m c m	P 6 <sub>3</sub> /m m c	
CUBIC (minus sign in front of triad optional)						
P 2 3	F 2 3	I 2 3	P 2 <sub>1</sub> 3	I 2 <sub>1</sub> 3	P m 3	P n 3
F m 3	F d 3	I m 3	P a 3	I a 3	P 4 3 2	P 4 <sub>2</sub> 3 2
F 4 3 2	F 4 <sub>1</sub> 3 2	I 4 3 2	P 4 <sub>3</sub> 3 2	P 4 <sub>1</sub> 3 2	I 4 <sub>1</sub> 3 2	P -4 3 m
F -4 3 m	I -4 3 m	P -4 3 n	F -4 3 c	I -4 3 d	P m 3 m	P n 3 n
P m 3 n	P n 3 m	F m 3 m	F m 3 c	F d 3 m	F d 3 c	I m 3 m
I a 3 d						

of these space groups can be found in the *International Tables for Crystallography*.<sup>13</sup> These tables contain detailed information regarding the various symmetry operations involved such as listings of the *equivalent positions* (those equivalent atomic positions that are generated by point group or translational symmetry) and *special positions* (those positions that place an atom directly on a point of symmetry).

One last definition relates to our understanding of the crystalline solid as well as how we will use X-ray diffraction as a tool to reveal the structure of these solids. As we had stated early on, each crystalline structure is composed of a series of repeating lattice points that relate to each other by a three-dimensional net that is unique for that particular crystalline solid. We can, in fact, identify an infinite series of parallel planes that hold sets of these lattice points in common and, as these planes repeat throughout a solid, we can identify a common distance,  $d$ , in-between each plane. We will show how it is the distances between the lattice planes the X-ray diffraction will detect and with that information, we can generate a series of coordinates of the various lattice planes present and use this information to deduce the solids crystalline structure. Those layer coordinates in question are called the *Miller indices* and are designated by the symbols  $h$ ,  $k$ , and  $l$ .

These *Miller indices* can be seen in data as  $(h\ k\ l)$  and are simply thought of as the  $(h, k, l)$  plane of the structure. These indices are derived from where the plane intersects on  $(a, b, c)$  coordinates of the unit cell and are, for convenience and simplicity, the reciprocals of the  $(a, b, c)$  values. For example, a plane intersecting at points  $(1/2, 2/3, 1)$  would have Miller indices of  $(2\ 3/2\ 1)$  or equivalently at  $(4\ 3\ 2)$ . Similarly, intercepts at  $(\infty, 1, 2/5)$  would have Miller indices of  $(0\ 1\ 5/2)$  or  $(0\ 2\ 5)$ .

These indices are mathematically related to the unit cell and distances in such a way that makes X-ray diffraction such a powerful tool that it is. For the orthorhombic, tetragonal, and cubic systems; the unit cells axes are mutually perpendicular resulting in,<sup>14</sup>

$$1/d = (h^2/a^2 + k^2/b^2 + l^2/c^2)^{1/2} \quad \mathbf{2.1}$$

In the other crystal systems, where the axes are not perpendicular, the following general formula can be used,<sup>14</sup>

$$d = V[h^2b^2c^2\sin^2\alpha + k^2a^2c^2\sin^2\beta + l^2a^2b^2\sin^2\gamma + 2hlab^2c(\cos\alpha\cos\gamma - \cos\beta) + 2hkabc^2(\cos\alpha\cos\beta - \cos\gamma) + 2kla^2bc(\cos\gamma\cos\beta - \cos\alpha)]^{-1/2}$$

## 2.2

where  $V$  is the unit cell volume given by,<sup>14</sup>

$$V = abc(1 - \cos^2\alpha - \cos^2\beta - \cos^2\gamma + 2\cos\alpha\cos\beta\cos\gamma)^{1/2}$$

## 2.3

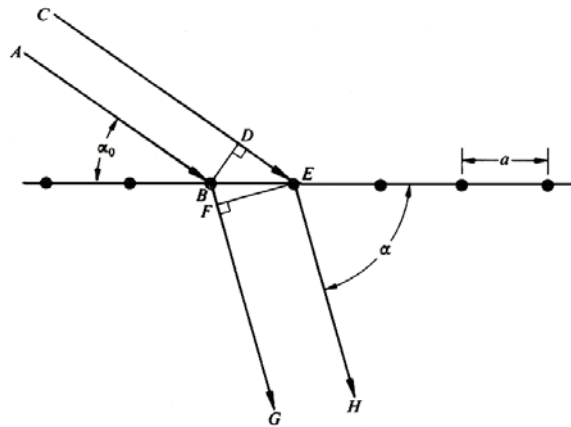
The significance of the distances between the crystalline planes will be made clear in the section to follow.

### 2.3.2.2 X-ray Diffraction

The idea of using X-ray diffraction to determine a crystalline structure originates from earlier diffraction studies done with visible light. The behavior of light was being observed as it diffracted thru a grating as early as 300 years ago. By 1820, the first diffraction grating patented by Joseph von Fraunhofer (1787-1826), a Munich optical worker.<sup>15</sup> From these collective studies, it was shown that light passing through glass having scratches at periodic intervals (gratings) would result in both destructive and constructive interference, depending upon the angle of the diffracted light ray. The

resulting pattern of light produced a series of lighted spots separated by dark voids radiating from the center of an observation screen. It was determined that there was a mathematical relationship between the wavelength of light used, the angle of diffraction, and the periodic distance between the grating slits.

The sample grating shown in Figure 2.7 shows how the derivation of the angles is based on where the position of the scattered intensity is maximum. At the point the incident beam arrives at the grating at the angle  $\alpha_0$ , incident ray  $CE$  must have traveled farther than  $AB$  and after the grating ray  $BG$  must travel farther than  $EH$ . The difference of path lengths of  $CDEH$  and  $ABFG$  is  $DE - BF$ , which must be equal to a whole number of the wavelength of the light,  $DE - BF = n\lambda$ , if constructive interference is to be observed at angle  $\alpha$ . Since  $DE = a\cos\alpha_0$  and  $BF = a\cos\alpha$ , then  $a(\cos\alpha_0 - \cos\alpha) = n\lambda$ , providing us with the means to find the repeating distance,  $a$ , of the diffraction grating.



**Figure 2.7** Light being diffracted by a grating with distance  $a$ .

X-rays are electromagnetic radiation with wavelengths of around 100 pm that are produced by bombarding a metal with high-energy electrons. Wilhelm Röntgen first discovered X-rays in 1895 and about seventeen years later, Max von Laue, suggested that X-rays might be diffracted when passing through a crystal lattice much like light is



diffracted as it passes through a grating. Laue had come to realize that the wavelengths of the X-rays were very much comparable to the distance between the crystal lattice planes.

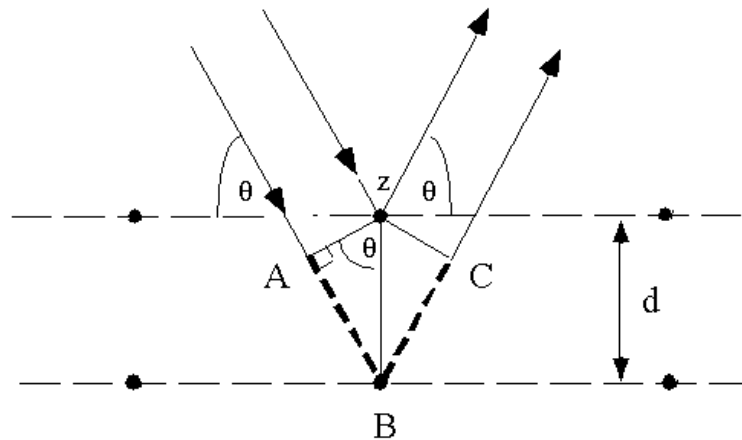
As the X-rays encounter the electron clouds surrounding the atoms of the crystal, they are reradiated or scattered by two modes of scattering; the *Compton* scatter and the *coherent* scatter. The Compton scatter is an inelastic scatter in which some of the X-rays photon energy is lost during the collision process. As the photon encounters an electron, it is absorbed and a new photon of lower energy is emitted. This photon not only has a longer wavelength and different phase (thus considered an *incoherent* photon), but it is also emitted in arbitrary directions and, for this reason, is of no use in diffraction studies. The coherent scatter is a perfectly elastic collision with the photon changing directions but losing no energy as it collides with the electrons.

W. H. Bragg imagined diffraction occurring as X-rays underwent coherent scattering in an encounter with a crystalline solid and likened this diffraction to that of reflection of light by a plane mirror. Since these mirror planes are actually the periodic lattice planes of a crystalline solid, like in the grating example, the pattern formed by the constructive interference can only occur at angles where the path length of the successive planes is equal to a whole number of wavelengths. An example of this is illustrated in Figure 2.8 showing how when X-rays of wavelength  $\lambda$  are incident at angle  $\theta$  with a set of planes with spacing  $d$ , the rays will be in phase and produce reflections only if  $AB + BC = n\lambda$ . Elementary trigonometry shows that  $AB = BC = d\sin\theta$ , resulting in the equation,

$$2d\sin\theta = n\lambda$$

#### 2.4

of which has come to be known as *Braggs Law*.

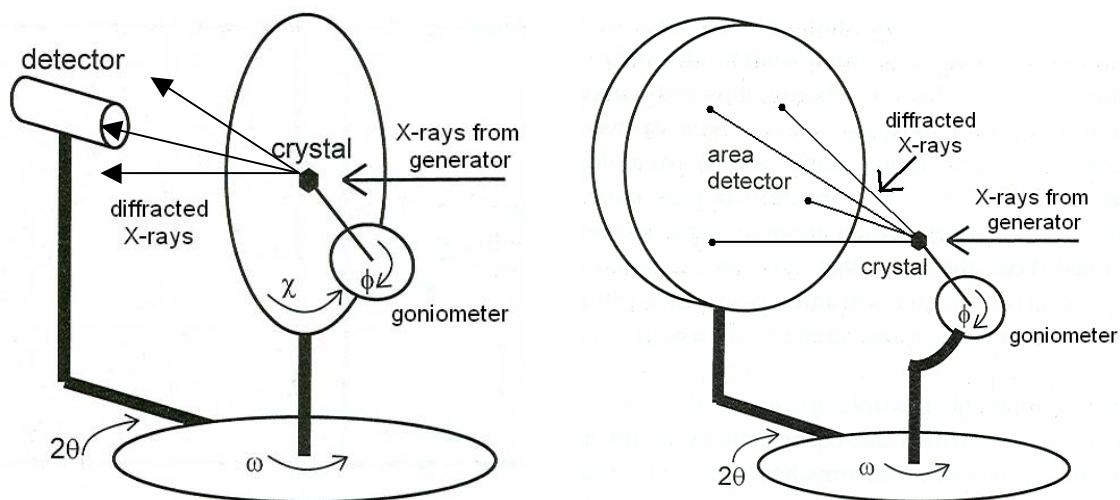


**Figure 2.8** As an X-ray beam reflects off a set of planes, Bragg's law states that constructive interference only occurs when  $n\lambda = 2d\sin\theta$ .

Although there are several methods available to record and analyze single crystal X-ray diffraction patterns, we will focus our discussion on the method used for all the structures presented in this study. Earlier X-ray diffraction studies relied on the use of photographic film to record the diffraction patterns, and long, laborious measurements and calculations just to determine a unit cell of a structure. Beyond the 1960's, computer-controlled X-ray *diffractometers* came into use, greatly reducing the time to collect meaningful data, while dramatically increasing the quality of the output. Today's semiconductor-based electronic detectors coupled with high-speed computers with state of the art software programming have reduced what were once months of tedious work, to only a few hours fairly simple program operation.

In Figure 2.9, we show drawings of two types of diffractometers. The model on the left is called a *four-circle diffractometer* and initially used either the gas filled Gieger-Muller or proportional detectors, which were superseded by scintillation detectors as the technology evolved. This type of diffractometer was far superior to the earlier

photographic given its computer-controlled automation (with full crystal rotation abilities) and precision in both the peak intensities and angles of the X-ray reflections. The disadvantage to this type of diffractometer is that it is limited to detecting only one reflection at a time. A full data set of reflections can take several days collection time and is largely dependant on the unit cell size. Doubling a cell size translates into double the amount of individual reflections the system must search for.

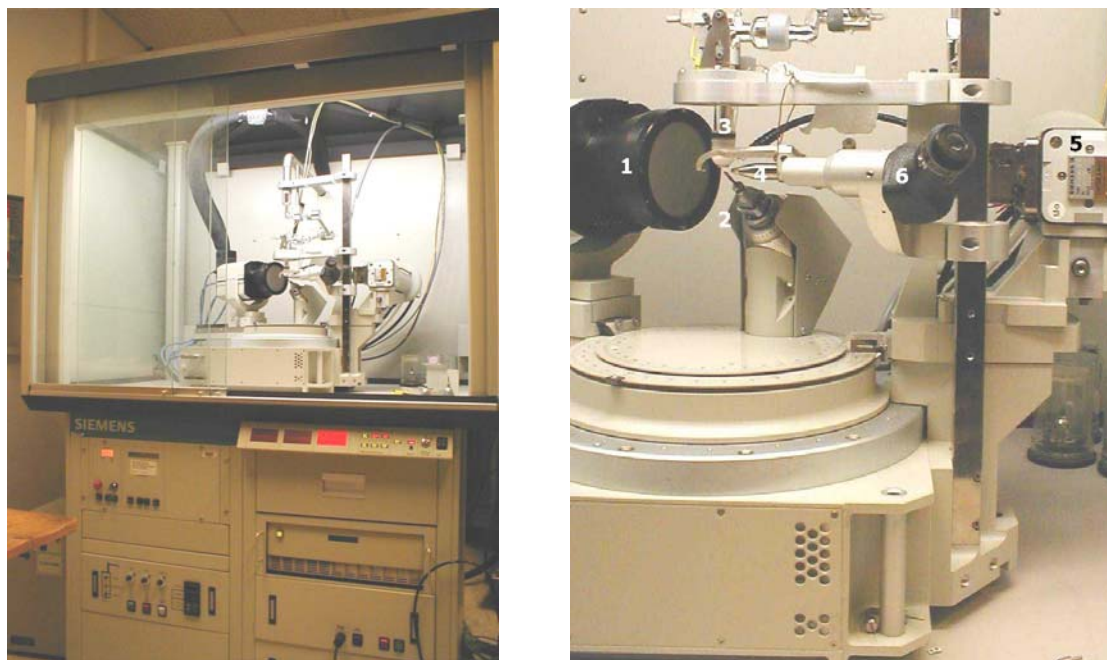


**Figure 2.9** Drawings of two types of diffractometers with the (left) earlier *four-circle* design and (right) the more modern *area detector* design.

The more recent model, shown on the right, is aptly called an *area detector diffractometer*. While the four-circle model was limited by only seeing reflections in a horizontal plane, the area detector can detect numerous reflections simultaneously in two-dimensions. This eliminates the need for the  $\chi$  crystal rotation; greatly reducing the amount of crystal rotations to collect a full data set. The area detectors run time is relatively independent of cell size since a larger unit cell only means that there are more reflections per crystal position. In most instances, data collection only runs from 5 to 12 hrs time, depending upon the intensity of the reflections. Those crystals exhibiting strong

reflections may require 5 – 10 second X-ray exposure per frame, while the weaker reflections may call for 20 – 30 second exposures.

There are a wide variety of area detectors, each based on slightly different technologies with varying degrees of size, spatial resolution, speed of data collection, and cost and each with continued developments as the technology advances. A favorite style of many researchers as well as the chief instrument used in this particular study is the Siemens SMART X-ray diffractometer system equipped with a CCD (charge-coupled device) detector. Figure 2.10 shows a full view of this instrument on the left with a close-up of the crystal mounting and CCD detector shown on the right.

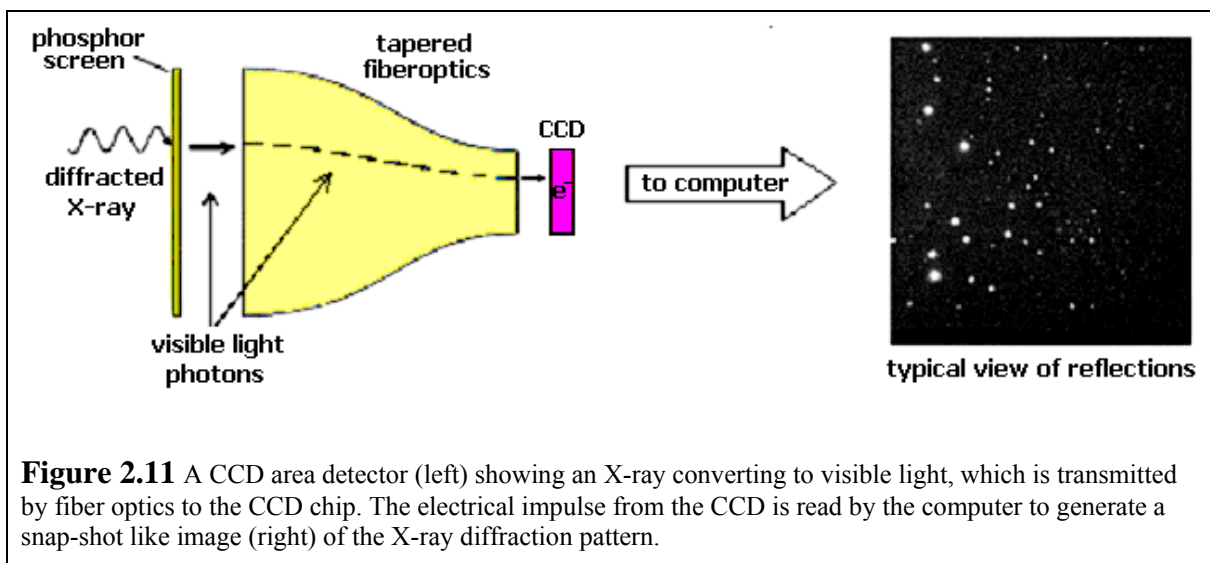


**Figure 2.10** Photos of the Siemen SMART single crystal X-ray diffractometer shown (left) in its operation cabinet and (right) a close-up showing the basic components. Shown are 1. CCD detector, 2. goniometer and crystal mounting, 3. nitrogen cryogenic port, 4 X-ray gun, 5. X-ray generator, 6. centering microscope.

One of the most advantageous features of this device is its compact size. The only other components (not shown) are a small cooling system for the CCD, a liquid nitrogen storage tank and transfer reservoir for the crystal cryogenic system, and a standard PC for

data collection and analysis. The basic components are numbered in the close-up on the right showing the: (1) CCD detector, (2) crystal mount with the goniometer (for crystal centering), (3) liquid nitrogen cryogenic delivery port to cool the crystal to  $-100^{\circ}\text{C}$ , (4) port for the initial monochromatic X-ray beam, (5) Mo based X-ray generator [ $\text{Mo}(\text{K}_{\alpha}) = 0.71070\text{ \AA}$ ], and (6) optical microscope to visually center the crystal.

The CCD area detector used with the SMART system represent a major advance in detector technology. For a typical CCD detector, as shown in Figure 2.11, as diffracted X-ray photons impinge on a phosphor screen (of gadolinium oxysulfide, for example) producing a visible light photon. This photon is conducted to a CCD chip by way of a tapering fiber optic system, at which eight electrons are produced per one initiating X-ray photon. The reflection pattern captured by the CCD (shown on the right of Figure 2.11) is clear and precise and is, in fact, much like an electronic version of photographic film.



In a typical run, some 1300 – 1800 individual frames of X-ray reflections such as the one shown above are collected. This results in thousands to tens of thousands of reflections needing to be processed before a structure can be realized. Such a task is next

to impossible without the automation available in the modern diffractometer as well as the related computer software available to carry out this process in an efficient manner. The user is usually confronted only a few choices to make at various stages of the data collection and processing, including the final structure solution and refinement. Although major portions of the procedures are math intensive and considered as computer *black box* methods, we will present a brief outline of the steps as they lead up to the final structure solution.

The first step in single crystal X-ray diffraction is the identification of a single crystal. For transparent crystals, such as in this study, the single crystal determination method of choice is called *polarized optical microscopy*. With this method, a crystal is placed under a microscope equipped with polarized light. As the crystal is rotated while under the scope, the polarized light is blocked out with one crystal orientation while fully transmitted as the crystal is rotated further. The complete extinction of polarized light as a crystal is rotated into one position is a strong indication that the crystal is single and suitable for X-ray diffraction analysis. The initial data collection to determine the unit cell will also indicate whether or not the crystal is single, as we will explain in greater detail below.

The next step is to mount the crystal on the goniometer. This is usually accomplished by adhering the crystal on the end of a glass fiber that has initially been cemented into a brass fitting (which, in turn, fits into the head of the goniometer). Coating the crystal with some light silicon oil provides enough adhesion for this task, as well as protects the crystal from continuous exposure to air. As the goniometer is placed into position on the diffractometer, the crystal is further protected from decomposition as

it is cooled to nearly  $-100^{\circ}\text{C}$  by a steady stream of  $\text{N}_2$ /liquid  $\text{N}_2$  mixture delivered by the built-in cryogenic system. The crystal is then centered in the crosshairs of the diffractometer's optical scope by variations of the three positioning adjustments found on the goniometer.

With the crystal now mounted and centered, we can now begin to collect the initial 60 – 90 reflection frames (called the *matrix*), which are comprised of three small sets of frames (20 – 30 frames each) taken at different locations about a hemisphere of the crystal. This reflection *sampling* is used to verify the quality of the crystal as well as present a first glimpse of the structure's unit cell dimensions. Aside from the routine set-up procedures inherent to the particular instrument being used, the process is essentially automatic. The entire data collection time spans some 20 – 60 minutes, depending on only the amount of frames to collect and the length of X-ray exposure set per frame. At the end of the run, the SMART system automatically scans each frame, generating a list of unique reflections with relevant information such as intensity and incident angle. Following this, the system proceeds with the process of indexing the cell and determination of the Bravais lattice.

Further refinement of the unit cell can be performed by the user but is not generally necessary at this point. If the resulting data with the associated *standard uncertainties* (s.u.),  $\sigma(I)$ , as calculated from the known statistical properties of the X-ray generation and diffraction process, are within acceptable standards, (as recognized by the experienced user) then the process can continue to the collection of a full data set. If this is not the case, then another crystal must be chosen until data with acceptable standards is obtained.

As we stated earlier, the process of indexing the unit cell is essentially a computer black box method in which the crystal orientation, unit cell dimensions, and reflection indices have to be determined simultaneously. This is not a simple process and involves a series of complex calculations. However, these calculations are all based essentially on the Bragg equation and symmetry related observations. Initially, a reduced primitive cell is chosen in which, after examination of symmetry related intensities, the cell is refined to include any centering, and a final selection of the Bravais lattice and the crystallographic point group. The SMART system installation software includes all the black box operations needed to accomplish the afore mentioned tasks.<sup>16</sup>

After it is determined that a quality single crystal has been chosen, the full data set can then be collected. This process consists of the collection of three large sets of reflection frames (maximum 605 frames each) to cover the entire hemisphere of the crystal. A final set of 50 frames is collected that are identical to the first 50 and are used to check for crystal decomposition or moving during the collection process. The unit cell is determined as it was in the initial matrix collection; this time, only small representative samples taken through the entire data set are scanned for unique reflections, which are indexed as before. This time the user will perform a refinement on the unit cell to minimize the solution's uncertainty.

The next step involves the conversion of the intensities,  $I$  to *observed structure amplitudes*,  $|F_o|$  or  $F_o^2$  along with the conversion of  $\sigma(I)$  to  $\sigma(F_o)$  in a process known as *data reduction*. This process involves several operations such as *Lorenz-polarization* factors to correct for the partially polarization of radiation as it is reflected, correction for changes in the X-ray beam intensity or in the scattering power of the crystal during the



experiment, and absorption corrections to compensate for the different absorption effects in different crystal orientations. The reduction process also involves the merging and averaging of repeated and symmetry equivalent reflections, producing a unique and scaled set of data. At the conclusion of this process, a statistical analysis of the complete, unique data set is performed to identify the presence or absence of various symmetry elements to make a final determination the structure's space group.

All these processes are carried out in only a matter of 30 minutes or so, depending on the speed of your processor and the size of the data. As was before, the data reduction is performed via a software program (SAINT) provided by the SMART systems manufacturer equipped to handle the entire complex process with minimal user input.<sup>16</sup>

Following the data reduction, we are now ready to solve the structure. This is accomplished by generating an electron density distribution map of the unit cell from the data obtained from the X-ray reflections. The actual electron density of the unit cell is related to the intensity of the reflection pattern by Fourier transformation. The diffraction pattern is, in fact, the Fourier transformation of the electron density. Fourier transformation could be likened to a chord played on a piano that is transformed into the individual musical notes. In order to obtain the diffuse pattern of the unit cell's electron density, we need to mathematically recombine the individual reflections via a reverse Fourier transform indicated by the equation:<sup>17</sup>

$$\rho(xyz) = \frac{1}{V} \sum_{h,k,l} |F(hkl)| \cdot \exp[i\phi(hkl)] \cdot \exp[-2\pi i(hx + ky + lz)] \quad 2.5$$

Unfortunately, the phase of the reflections,  $\phi$  is not known, so these calculations cannot be performed directly. This results in what is called the *phase problem* and the two most

common methods used to get around this problem are called the *Patterson synthesis* and the *Direct methods* approach.

The Patterson synthesis involves a Fourier transformation of the squared amplitude,  $F_0^2$  with all the phases set to zero by the equation:<sup>17</sup>

$$P(xyz) = 1/V \sum_{h,k,l} |F(hkl)|^2 \cdot \exp[-2\pi i(hx + ky + lz)] \quad 2.6$$

Although the Patterson map generated by this operation looks like an electron density map, it represents vector between atoms instead of actual atoms within the unit cell.

While the peaks in the electron density map are proportional to the atomic numbers of the elements present, the Patterson peaks are proportional to the product of the atomic numbers of two atoms. With these results, heavier atoms are more easily identified and, after this is accomplished, further Fourier synthesis can be performed (as will be explained shortly) which will create an electron density distribution, which the user can then assign to atoms.

The direct method seeks an approximation of the phases from the measured intensities. This process involves the selection of some of the most important reflections and computing probable relationships among their phases. The most favorable choices found are then subjected to Fourier transformation and the resulting electron density map is examined for recognizable molecular features. With the direct method most if not all of the non-hydrogen atoms can be identified in the initial structure solution.

In many cases, mostly true for the Patterson synthesis, only a partial solution will be found at first. An additional Fourier synthesis will be necessary to reveal the remaining non-hydrogen atoms of the structure. Hydrogen atoms, with their minimal electron density will be handled in a different manner later on. For the rest of the atoms, we will

simply apply a Fourier transformation to the model to generate a new set of data,  $F_c$  along with its phase,  $\phi_c$ . Although performing a reverse Fourier transform on both the calculated values of  $F_c$  and  $\phi_c$  would only regenerate the original model, we can combine the experimental  $F_0$  with the calculated phase,  $\phi_c$ . This would result in a new model that is better than the original, revealing more features of the structure.

One other application of these calculated values are to verify the quality of the structure as the calculated value is compared to the experimental value giving what is called the residual factor or R-factor, defined as:<sup>17</sup>

$$R = \frac{\sum |F_0| - |F_c|}{\sum |F_0|} \quad 2.7$$

With a structure that was produced from fairly reliable data,  $R$  typically runs about 0.02 – 0.07 with the value being somewhat higher until the structure is completely refined. Variations of the residual factor include using  $F^2$  instead of  $|F|$  and squaring the differences to produce an even more statistically meaningful value as seen in:<sup>17</sup>

$$wR2 = \sqrt{\frac{\sum w(F_0^2 - F_c^2)^2}{\sum w(F_0^2)^2}} \quad 2.8$$

Residual values based on  $F^2$  are generally higher than the  $R$  values depending on the factoring components.

After all the non-hydrogen atoms have been found, the structure is then *refined* as all the atoms positions are mathematically adjusted to produce the best agreement between the observed and calculated diffraction pattern. This process is well known as the *least squares* analysis and is handled by either of the following equations:<sup>17</sup>

$$\sum w(|F_0| - |F_c|)^2 \text{ or } \sum w(F_0^2 - F_c^2)^2 \quad 2.9$$

Although the first based on  $F$  is most commonly used, the second equation based on  $F^2$  is gaining popularity.

The least squares analysis is related to the best-fit method used to install a common straight line through a set of data points on a graph. There are many more variables, however, involved with least squares. Important numerical parameters to refine on describe the positions and vibrations of the atoms in the Fourier transform equation. As each atom sits on  $x$ ,  $y$ , and  $z$  coordinates, they have a displacement parameter,  $U$  in which all three can be equal, having an *isotropic mean-square amplitude of vibration* or they can have varied vibrational modes in six different directions about the atoms origin as *anisotropic vibration*. The later of these two provides the more realistic and best fit. All the parameters being refined by each least squares performed may produce a closer fit than the previous one but still is not exact. Additional least squares operations must be performed until the variability in the parameters is negligible and essentially insignificant.

The least squares analysis will also provide a standard uncertainty. These s.u. values depend greatly upon the original s.u.'s obtained from the data collection and are related to the *goodness of fit*,  $G.O.F.$  value included with the structures results, which is another indicator of the structures reliability. Typical  $G.O.F.$  values are around 1.0 and only vary  $\pm 0.3$  for a good structure. Since these values depend upon those values found in the original data, it can truly be said that only good data will produce a good structure.

Following the refinement of the anisotropic displacement parameters, the hydrogen atoms can be put in place to complete the structure. In some cases of fairly strong data, electron density peaks representing the hydrogen atoms will appear. Generally, however,

the hydrogen electron density is too weak to assign a hydrogen atom to these peaks and especially so to obtain anisotropic refinement for the hydrogen atoms in place. Therefore, it is common practice to model the hydrogen atoms into the correct position using *constraints* in which the bond lengths are fixed and the atom left as isotropic with the refinement based more on the  $U$  values associated with the atom attached to the hydrogen.

At this stage, the structure is essentially complete. One final step is required to assure that all the variables are brought to the bare minimum value. This simply involves a long repetition of refinement cycles (15-20 cycles should do) and observing the structural shift parameters to confirm their eventual approach to a value at or close to zero. During this final refinement, the *Crystallographic Information File* (CIF), is created which contains important structural information such as atomic positions, bond lengths, and all the bond angles found in the asymmetric unit of the structure; and is an important file for the electronic publication of the structure and storage into huge structural databases such as the *Cambridge Structural Database* (CSD), developed by the Cambridge Crystallographic Data Centre, UK.<sup>18</sup>

The processes described up to this point may seem elementary with such a simple explanation as was given here, but, as we have stated, these processes involve complex calculations performed on thousands of data reflections. Many of these processes would be an incredibly labor-intensive task for the user to if it were not for the “black box” programs that are designed to perform these countless calculations in a matter of minutes or even seconds. While the both the data collection and its reduction is fairly easily handled by Brukers SMART and SAINT programs,<sup>16</sup> the calculations needed solve and

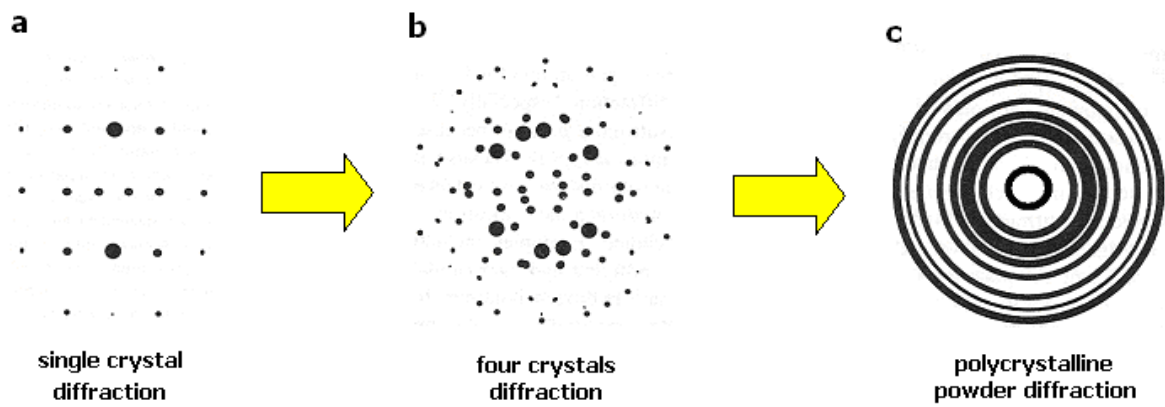
refine the structure are performed by way of the SHELX programs which can transform reduced data into a finished structure in a matter of minutes with good data and an experienced user.<sup>19</sup>

An additional program called XSEED acts as a base program which interfaces with the SHELX programs in order to provide a more PC windows friendly environment to perform the several steps of the structural refinement.<sup>20</sup> This program also allows for the ease of atom selection and parameter adjustments; considerably simplifying the entire process. In addition to refinement, the XSEED program acts as an analysis tool, allowing the user to examine angles and bond lengths with great ease as well as the ability to assemble asymmetric units or *grow* the structure in order to view the larger crystalline version. A final program that also interfaces with XSEED is a free-ware program called POV-Ray (*persistence of vision raytracer*), and is the graphics program, which is responsible for all the structural figures presented in this dissertation.<sup>21</sup>

In the single crystal X-ray diffraction just described, the reflections shown diffraction pattern produced each have a definite direction and angle dependant strictly upon the orientation of the crystal. In order to acquire a complete data set, the single crystal had to be rotated into several positions during the procedure.

If we had failed to isolate a single crystal and had performed the same procedure on a crystal comprised of two or more single crystals fused together, each crystal would produce a diffraction pattern simultaneously, forming a group of superimposed patterns. As we expand this thought, to include an infinite number of crystals found in our polycrystalline precipitate (as was produced in the syntheses shown in Sec. 2.2), this superimposed image would transform into a collection of circular patterns expanding out

from the origin with a  $2\theta$  radius. In the example shown in Figure 2.12 we show (a) a diffract of a single crystal, (b) how the same pattern looks with four crystal patterns superimposed on each other, and (c) how a polycrystalline sample of the same crystalline structure would look like. The latter of these examples illustrates the basis for *powder X-ray diffraction* and the data obtained from such an example would be called a *powder pattern* of that particular sample.



**Figure 2.12** Diffraction patterns of (a) a single crystal, (b) the four crystals, and (c) a polycrystalline sample.

Although we clearly lose a lot of valuable information when going from single crystal to powder samples, powder X-ray diffraction still is a powerful analytical tool and plays an important part in materials characterization. Just a few examples of what can be accomplished with this method are described below:

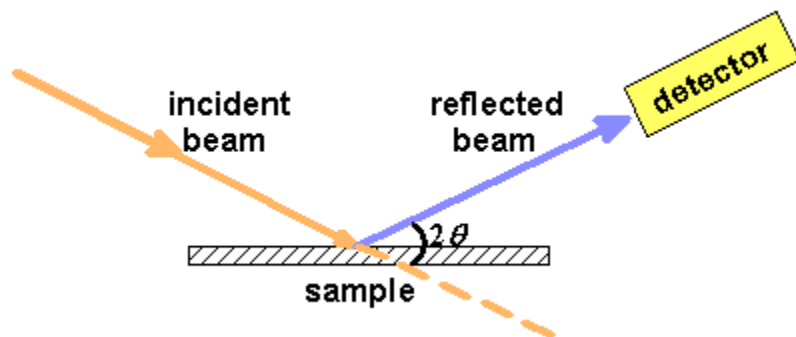
1. Quickly identify samples by comparing the powder pattern with known samples from a database or calculated patterns from single crystal data.
2. Quantitatively identify components of a mixture of phases or compounds when one or more of those phases are known structures.

3. Identify subtle structural changes such as observing a slight change in unit cell volume when one element is substituted for another in a known compound. In some cases, even the new atomic positions can be determined.
4. Observe phase transitions and solid-state reactions as they progress in real time as the diffraction experiment is performed over a period of time, or as temperature or pressure is varied.
5. Even determine the crystal structure of some simpler unknown compounds. This may be possible if the data is of very high resolution and the user is prepared to spend a great deal of time and effort in obtaining a solution.

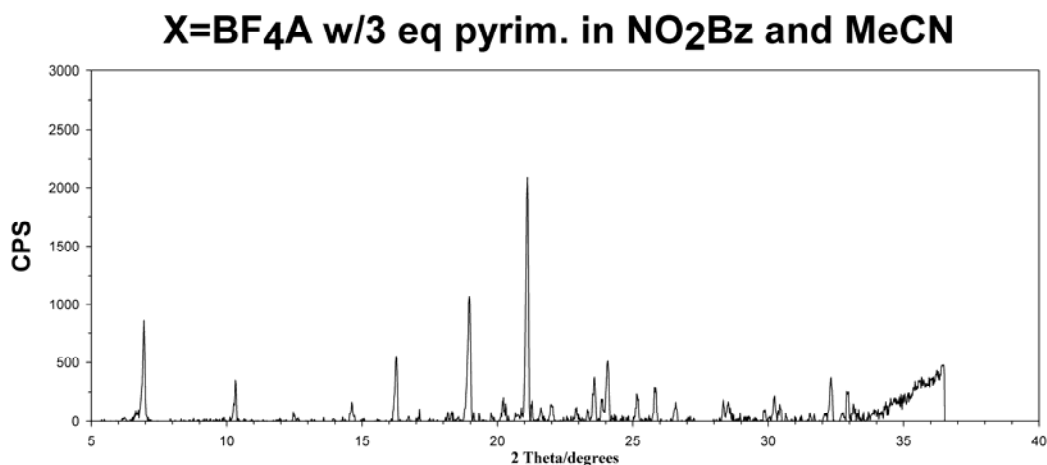
There is a wide variety of powder X-ray diffractometers available. Several older types utilize photographic film, as was the case in single crystal diffraction.<sup>22</sup> An X-ray imaging plate is the modern version of the photographic film, which presents an electronic readout of the powder pattern and was developed for medical radiography.<sup>23</sup> Probably the most common electronic detector relies on the X-ray incident beam to be reflected off a surface hold the powder sample while a detector is in position to record the reflected beam at various Bragg angles of  $2\theta$ . Although there are several variations of this design, the idea is relatively the same as shown in the drawing in Figure 2.13a. As this experiment progresses, the angle of both the incident beam and the detector (usually a scintillation or semiconductor



**a**



**b**



**Figure 2.13** (a) A drawing of a typical electronic powder X-ray diffractometer design and (b) a real-life example of powder X-ray diffraction data as collected from 5 to  $\sim 35$   $2\theta$ .

detector) are changed in order to collect a continuous sampling of reflection intensities from  $0 > 2\theta > 90$  of Bragg angles. Figure 2.13b shows a sample of actual data collected from one of our very own samples (the results of which will be explained in Chapter 5). These peaks may or may not match to other samples or theoretical powder patterns generated from single crystal data of a solved structure.

The example shown above shows how we use powder X-ray diffraction in our own studies to match and compare samples with existing powder data or simulated patterns. These simulated patterns may be developed from a variety of programs including one that

is also interfaced with the XSEED program. It is possible, though maybe with some difficulty, to develop a simple structure from a powder pattern. The difficulty increases with the increase of the structure's complexity resulting in several peaks, many of which overlap making separate direct measurements impossible.

Predicting a pattern from a known structure is a trivial matter for the trained user using modern computational methods, while doing the reverse is a difficult, time-consuming endeavor. Still, there are a variety of programs available to tackle this problem such as some popular auto-indexing programs like *TREVOR*, *ITO*, and *DICVOL*.<sup>22, 24</sup> Other programs such as the *EXPO* package that includes the *EXTRA* program to extract and integrate the Bragg peaks along with the *SIRPOW.92*, which searches for candidate atom positions.<sup>25</sup> The final refinement of the data is then handled by programs such as *GSAS* and *FULLPROF*.<sup>26</sup>

## References

1. Lopez, S.; *PhD Thesis*, University of Missouri-Columbia, **2001**.
2. Knaust, J. M.; *PhD Thesis*, University of Missouri-Columbia, **2003**.
3. Kubas, G.; *Inorg. Synth.*, **1979**, *19*, 90.
4. Tannenbaum, M. *Methods of Exeperimental Physics*, Vol. 6, Academic Press, New York, 1961.
5. Gilman, J. J.; *The Art and Science of Growing Crystals*, John Wiley & Sons Inc., New York, 1963.
6. Holden, S, Singer, P, *Crystals and Crystal Growing*, Anchor Books Doubleday & Company, Garden City, NY; 1960.
7. Lopez, S; *J. Am. Chem. Soc.*, **1999**, *121*, 6306.
8. Keller, S. W.; *Angew. Chem. Int. Ed.* **1997**, *36*, 247.
9. (a) Hoskins, B. F.; Robson, R.; *J. Am. Chem. Soc.* **1989**, *111*, 5962. (b) Hoskins, B. F.; Robson, R.; *J. Am. Chem. Soc.* **1990**, *112*, 1546. (c) Yaghi, O. M.; Li, H.; Groy, T. L.; *Inorg. Chem.* **1997**, *36*, 4292. (d) Yaghi, O. M.; Li, H.; *J. Am. Chem. Soc.* **1996**, *118*, 295. (e) Min, K. S.; Suh, M. P.; *J. Am. Chem. Soc.* **2000**, *122*, 6834. (f) Choi, H. J.; Suh, M. P.; *Inorg. Chem.* **2003**, *42*, 1151. (g) Hamilton, B. H.; Kelley, K. A.; Wagler, T. A.; Espe, M. P.; Ziegler, C. J.; *Inorg. Chem.* **2004**, *43*, 50.
10. A few examples: (a) Yan, Y.; Wu, C. -D.; He, X.; Sun, Y. -Q.; Lu, C. -Z.; *Cryst. Growth Design* **2005**, *5*, 821. (b) Murugavel, R.; Krishnamurthy, D.; Sathiyendiran, M.; *J. Chem. Soc., Dalton Trans.* **2002**, 34. (c) Hamilton, B. H.; Kelley, K. A.; Wagler, T. A.; Espe, M. P.; Ziegler, C. J.; *Inorg. Chem.* **2004**, *43*, 50. (d) Beauvais, L. G.; Shores, M. P.; Long, J. R.; *J. Am. Chem. Soc.* **2000**, *122*, 2763. (e) Gong, Y. -Q.; Wang, R. -H.; Zhou, Y. -F.; Lin, Z. -Z.; Hong, M. -C.; *J. Molec. Struc.* **2005**, *751*, 121.
11. Barrett, C. S.; *Structure of Metals*, 2<sup>nd</sup> ed.; McGraw-Hill, New York, 1952.
12. Adapted from, Shriver, D. F.; Atkins, P.; Langford, C. H.; *Inorganic Chemistry 2<sup>nd</sup> Ed.*, W. H. Freeman and Company, New York, 1994.
13. Hahn, T.; *International Tables for Crystallography*, D. Reidel Publishing Co., Boston, 1983.
14. Sands, D. E.; *Introduction to Crystallography*, Dover Publications, Inc.; New York, 1975.

15. (a) Bell, L.; *Phil. Mag.* **1888**, 25, 245. (b) Greenslade, T. B.; *Am. J. Phys.* **1973**, 41, 730.
16. Bruker (1998). *SMART* and *SAINTE*. Bruker AXS Inc.. Madison, Wisconsin, USA.
17. Clegg, W.; *Crystal Structure Determination*, Oxford University Press, Oxford, 1998.
18. Cambridge Crystallographic Data Centre (CCDC), 12 Union Road, Cambridge CB21EZ, UK; fax +44(0)1223-336033 or e-mail: [deposit@ccdc.cam.ac.uk](mailto:deposit@ccdc.cam.ac.uk).
19. (a) G. M. Sheldrick, *SHELXS-90, program for Structure Solution*; University of Gottingen: Germany, 1991. (a) G. M. Sheldrick, *SHELXL-90, program for Structure Refinement*; University of Gottingen: Germany, 1991.
20. L. Barbour, X-SEED, *Graphical Interface for SHEL-X*; University of Columbia, MO, 2000.
21. Cason, C.; Persistence of Vision Raytracer Pty. Ltd., (1996-2003), Victoria, Australia.
22. Klug, H. P.; Alexander, L. E.; *X-ray Diffraction Procedures for Polycrystalline and Amorphous Materials*, John Wiley and Sons, New York, 1974.
23. (a) Ito, M. Amemiya, Y.; *Nucl. Instrum. Methods Phys. Res.* **1991**, 369. (b) Miyahara, J.; Takahashi, K.; Amemiya, Y.; Kamiya, N.; Satow, Y.; *Nucl. Instrum. Methods Phys. Res.* **1986**, 572.
24. (a) Bish, D. L.; Post, J. E. (eds.); *Modern Powder Diffraction*, Mineralogical society of America, Washington, D. C.; 1989. (b) (TREOR) Werner, P. -E, Eriksson, L.; Westdahl, M.; *J. Appl. Cryst.* **1985**, 18, 367. (c) (ITO) Visser, J. W.; *J. Appl. Cryst.* **1969**, 2, 89. (d) (DICVOL) Boulton, A.; Louër, D.; *J. Appl. Cryst.* **1991**, 24, 987.
25. (a) (EXTRA) Altomare, A.; Burla, M. C.; Cascarano, G.; Giacovazzo, C.; Guagliardi, A.; Polidori, G.; Camalli, M.; *J. Appl. Cryst.* **1995**, 28, 842. (b) (SIRPOW.92) Altomare, A.; Burla, M. C.; Cascarano, G.; Giacovazzo, C.; Guagliardi, A.; Moliterni, A. G. G.; Polidori, G.; *J. Appl. Cryst.* **1994**, 27, 435.
26. (a) (GSAS) Larson, A. C.; Von Dreele, R. B.; *Los Alamos, Nat. Lab. Publication LAUR 86*, **1994**, 748. (b) (FULLPROF)Rodrigues-Carvajal, R.; *Abstracts of the Satellite Meeting on Powder Diffraction of the XV Congress of the IUCr.* **1990**, 127.

# **ANION AND SOLVENT DEPENDANCE OF THE COPPER(I)/4,4'-BIPYRIDINE COORDINATION SOLIDS**

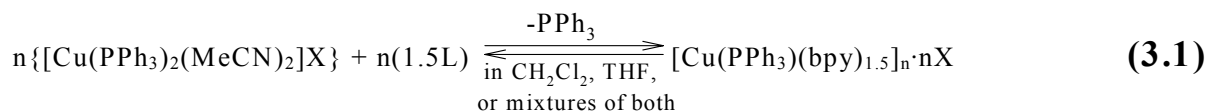
## **3.1 Introduction**

As was pointed out in Chapter 1, because natural clays are essentially composed of charged layers of coordinated silicates, they are ideal materials for both ion exchange and solvent extraction as well as a multitude of various catalytic applications.<sup>1</sup> Therefore, the strategy was to design materials that closely resemble the structure of natural clay minerals and in doing so, we would hopefully mimic the various properties clays exhibit.

We had previously shown in Section 1.5 that one way to achieve this goal is through the Cu – Cu bridging coordination of 4,4'-bipyridine (bipy) to three positions on a Cu(I) tetrahedral coordination sphere. The fourth position on the tetrahedra would be occupied by a terminal triphenylphosphine (PPh<sub>3</sub>) ligand, resulting in a layered coordination compound with the general formula of [Cu(bipy)<sub>1.5</sub>(PPh<sub>3</sub>)<sub>n</sub> X (X being a variety of monovalent anions).

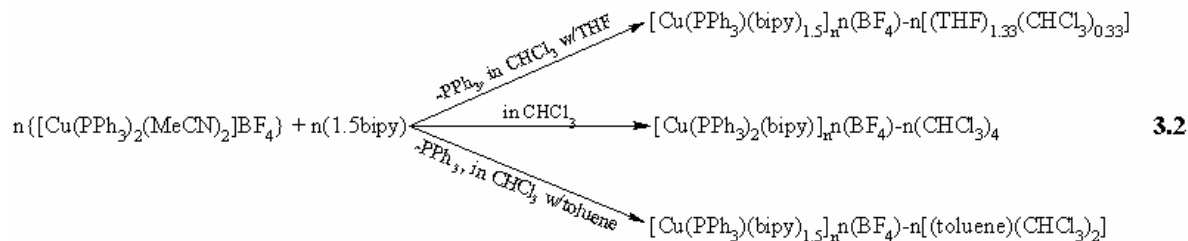
In our first attempt at synthesizing a layered porous solid, we found that by using only chloroform as the reaction solvent, only the one-dimensional chain of [Cu(C<sub>10</sub>H<sub>8</sub>N<sub>2</sub>)(PPh<sub>3</sub>)<sub>2</sub>]BF<sub>4</sub>•(CHCl<sub>3</sub>)<sub>4</sub> **1** was formed, as both PPh<sub>3</sub> ligands remained on the copper center.<sup>2</sup> Although it would seem most logical to simply use a mono-phosphine

material from the start, the use of the bis-triphenylphosphine starting material was deemed necessary because its increased solubility over the mono-PPh<sub>3</sub> material made it more compatible with the solvents we planned to use. In addition to this, the synthesis of the *bis*-PPh<sub>3</sub> material was already proven to provide a reliable source of starting material produced with minimum effort.<sup>3-6</sup> Given this, one of the most crucial components in the Cu-bpy reaction that forms the layered porous solid had to be the loss of a PPh<sub>3</sub> ligand as in:



We had finally achieved a successful reaction (as in Eq. 3.1) by carefully placing a small layer of THF on top the CHCl<sub>3</sub> reaction solvent and allowing the THF to slowly diffuse into the chloroform as the reaction progressed. This *solvent layering* technique resulted in the necessary removal of one PPh<sub>3</sub> ligand and the formation of the layered porous solid [Cu(C<sub>10</sub>H<sub>8</sub>N<sub>2</sub>)<sub>1.5</sub>(PPh<sub>3</sub>)]BF<sub>4</sub><sup>+</sup>(THF)<sub>1.33</sub>(CHCl<sub>3</sub>)<sub>0.33</sub> **2**, as reported by Lopez and published in 1999.<sup>2,7</sup> Substituting toluene for THF in this layered solvent technique led to the formation of [Cu(C<sub>10</sub>H<sub>8</sub>N<sub>2</sub>)<sub>1.5</sub>(PPh<sub>3</sub>)]BF<sub>4</sub><sup>+</sup>(toluene)(CHCl<sub>3</sub>)<sub>2</sub> **4**.<sup>2</sup>

Although both of these networks had relatively the same formula (both shown in Section 1.4 and 1.5), **2** has a coordination network composed of layers of fused pentagons while the network of **4** is an interpenetrated honeycomb-like layers of hexagonal cells.<sup>2</sup> Considering the reaction involving the materials with the BF<sub>4</sub><sup>-</sup> anion alone, we would need to modify the scheme to accommodate the reactions in the different solvent systems as shown:



Equation 3.2 shows how a single reaction can lead to three different products by making only subtle changes in the reaction conditions. The formation of the ladder type one-dimensional chain,  $[\text{Cu}(\text{C}_{10}\text{H}_8\text{N}_2)_{1.5}(\text{PPh}_3)]\text{PF}_6 \cdot (\text{CHCl}_3)_{1.5}$ , **5** (also presented in section 1.6) when the  $\text{PF}_6^-$  anion is used in place of  $\text{BF}_4^-$ , further complicates the cause and effect issue leading to the formation of the isomers formed with these types of reactions.

While it is obvious why the choice of metal coordination geometry or ligand used can profoundly affect the type of coordination network synthesized, it is less than obvious what affects the choice of counter anion or even the reaction solvent have on the self-assembly of the cationic network, especially in cases when neither of these species are found actually coordinated in the resulting cationic network. To date, there are several examples of structural alterations by way of variation of the anion or solvent alone.<sup>8</sup> Because of these studies, it is becoming increasingly clear that subtle changes in the type of anion or solvent used has a dramatic affect on the self-assembly process and the resulting geometry of the coordination network.<sup>9</sup>

During the course of our study we also came across the development of precipitates of which some would remain as such while others would transform into larger single crystals over time. In the field of crystal growth, this precipitate transformation is not an uncommon occurrence and could be attributed to a variety of known aging processes.

One such aging process is called *Ostwald ripening* (named by Liesegang after Wilhelm Ostwald who first introduced this anomaly in 1896), which is the process of how, in a single reaction, smaller crystals will dissolve in favor of the continued growth of larger crystals found in the same solution.<sup>10, 11</sup> This process is based on the Gibbs-Thompson relationship in which a crystalline solid adjusts to achieve minimum total surface free energy.<sup>11</sup> The larger crystals have reduced surface tension, which relates to having lower surface free-energy. This process could apply to our precipitate transformation but that implies that both the precipitate and the final single crystals are the same structure.

In some cases the precipitate and the single crystals are two different structures, or phases as they may be. During an aging process, these phases undergo a transformation to another phase, again one of lower free energy. This type of aging is also fairly common and follows *Ostwald's rule of staging*, which states that an unstable systems may go through a series of stages before reaching the most stable state.<sup>10b, 12</sup> Reactions such as ours, that are carried out in a reaction solvent system could be more specifically described as a *solvent-mediated reconstructive transformation*, since the metastable phase appears to dissolve while the stable phase nucleates and grows from solution.<sup>13</sup>

While the kinetic product may form as the first stage of our products development, the final product may be dictated solely upon which of the two phases are more soluble in the given solvent system. For the phase transition involving polymorph I converting to polymorph II, if polymorph II is the most stable, it would have a lower chemical potential than that of polymorph I as in,<sup>11</sup>

$$\mu_{solid}(\text{II}) < \mu_{solid}(\text{I}) \quad (3.3)$$



Given this and assuming ideal solution conditions exist (i.e., no solvent interaction), then at equilibrium we have:<sup>13</sup>

$$\mu_{solid}(\text{II}) = \mu_{eq}(\text{II}) = \mu_0 + RT \ln x_{eq}(\text{II}) \text{ and } \mu_{solid}(\text{I}) = \mu_{eq}(\text{I}) = \mu_0 + RT \ln x_{eq}(\text{I})$$

Resulting in: 
$$\mu_0 + RT \ln x_{eq}(\text{II}) < \mu_0 + RT \ln x_{eq}(\text{I}) \quad (3.4)$$

Where  $\mu_0$  is the standard chemical potential and  $x_{eq}$  is the solubility of the phase.

Therefore, 
$$x_{eq}(\text{II}) < x_{eq}(\text{I}) \quad (3.5)$$

This allows us to state that, at a given temperature, the most stable phase will have the lowest solubility *in any given solvent* under ideal solution conditions.

Of course, our products are not synthesized in *ideal* solutions. As was pointed out in Chapter 1, there are numerous solvent – solute interactions that the materials encounter as they go through the self-assembly process.

The synthesis of magnesium hydroxide is a good example of this type of aging process, as upon mixing of aqueous solutions of  $\text{MgCl}_2$  and  $\text{NaOH}$ , a precipitate of  $\text{MgOH}\cdot\text{OCl}\cdot 2\text{H}_2\text{O}$  first forms, which dehydrates and decomposes over time into  $\text{Mg}(\text{OH})_2$ .<sup>14</sup> There are several other studies involving metastable phase transformation, many of which seek out ways to control and exploit this transformation to develop new synthesis methods for important pharmacological compounds.<sup>15</sup> Similar to the Ostwald ripening, the phase transitioning system adjusts to achieve the minimum of total free energy with the more stable polymorph (being **3** in our case) having the lower free energy at a given temperature. In some cases this phase transformation is rapid while other cases show the metastable phase can remain in place for extended periods of time.

This portion of our study is a continuation of the study started by Susan Lopez as we will present those structures produced by the self-assembly reaction of

[Cu(bipy)<sub>1.5</sub>(PPh<sub>3</sub>)<sub>n</sub>X with 4,4'-bipyridine in a variety of solvent systems. Along with the previously mentioned reactions involving materials with the BF<sub>4</sub><sup>-</sup> and PF<sub>6</sub><sup>-</sup> anions, this investigation also includes materials containing ClO<sub>4</sub><sup>-</sup>, CF<sub>3</sub>SO<sub>4</sub><sup>-</sup>, and HSO<sub>4</sub><sup>-</sup> anions as well. The layered solvent technique was replaced with the use of carefully measured solvent mixtures of either the CHCl<sub>3</sub>:THF or CHCl<sub>3</sub>:toluene with the resulting structures reported as the THF or toluene concentrations were varied.

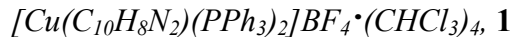
## 3.2 Experimental Section

### 3.2.1 General Methods

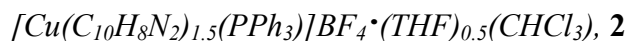
*Caution! Perchlorate salts are explosive and should be handled in small quantities and with extreme care at all times.* Cu<sub>2</sub>O, HPF<sub>6</sub>, HBF<sub>4</sub>, HClO<sub>4</sub>, H<sub>2</sub>SO<sub>4</sub> and 4,4'-bipyridine, (ACROS); acetonitrile, tetrahydrofuran, toluene, chloroform, dichloromethane, and diethyl ether (Fisher); triflic acid and triphenylphosphine (Aldrich), were used without further purification. All the [Cu(MeCN)<sub>2</sub>(PPh<sub>3</sub>)<sub>2</sub>]X salts for X = BF<sub>4</sub><sup>-</sup>, PF<sub>6</sub><sup>-</sup>, ClO<sub>4</sub><sup>-</sup>, CF<sub>3</sub>SO<sub>3</sub><sup>-</sup>, HSO<sub>4</sub><sup>-</sup>, were prepared as described in Chapter 2.

### 3.2.2 Synthesis

A few select structures previously synthesized and reported by Lopez have been included in the synthesis since they are also key components of this study. The syntheses noted are those developed for this particular study with the connection to the previous synthesis methods explained in Chapter 2. In each relevant case, the ownership has been duly noted and reference sited. For syntheses in which multiple solvent systems can be used, all known conditions are included in the descriptions below.



Previously reported by Lopez.<sup>2</sup> In a 20 mL vial were combined  $[\text{Cu}(\text{PPh}_3)_2(\text{MeCN})_2]\text{BF}_4$  (0.030 g, 0.040 mmol) in 4 mL of  $\text{CHCl}_3$  and 4,4'-bipyridine (0.016 g, 0.100 mmol) in 4 mL of  $\text{CHCl}_3$ . The vial was sealed and left at room temperature. Light yellow columnar crystals of **1** were harvested after 12 hours. Crystals of **1** were also produced in solvent mixtures of 9.5:0.5, 9.0:1.0, 8.5:1.5, 8.0:2.0, 7.5:2.5, and 7.0:3.0  $\text{CHCl}_3$ :THF ratios as well as 9.0:1.0, and at each 1.0 increments up to 6.0:4.0  $\text{CHCl}_3$ :toluene ratios.



In a 20 mL vial were combined  $[\text{Cu}(\text{PPh}_3)_2(\text{MeCN})_2]\text{BF}_4$  (0.030 g, 0.040 mmol) in 4 mL of a 7.0:3.0  $\text{CHCl}_3$ :THF solvent mixture and 4,4'-bipyridine (0.016 g, 0.100 mmol) in 4 mL of the same  $\text{CHCl}_3$ :THF mixture. The vial was sealed and left at room temperature. Yellow rhomboid crystals of **2** were harvested after 12 - 24 hours. Crystals of **2** were also produced in solvent mixtures of 8.0:2.0 and at each 0.5 increments up to 3.5:6.5  $\text{CHCl}_3$ :THF ratio.

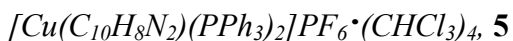


Previously reported by Lopez.<sup>2,7</sup> In a 20 mL vial were combined  $[\text{Cu}(\text{PPh}_3)_2(\text{MeCN})_2]\text{BF}_4$  (0.030 g, 0.040 mmol) in 4 mL of THF and 4,4'-bipyridine (0.016 g, 0.100 mmol) in 4 mL of THF. The vial was sealed and left at room temperature. Yellow prismatic crystals of **3** were harvested after 72 hours. Crystals of **3** were also

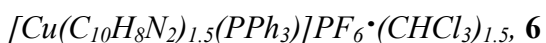
produced in CHCl<sub>3</sub>:THF solvent mixtures at ratios of 3.0:7.0 and continuing at 0.5 increments on up to the pure THF reaction solvent.



Previously reported by Lopez.<sup>2</sup> In a 20 mL vial were combined [Cu(PPh<sub>3</sub>)<sub>2</sub>(MeCN)<sub>2</sub>]BF<sub>4</sub> (0.030 g, 0.040 mmol) in 4 mL of a 6.0:4.0 CHCl<sub>3</sub>:toluene solvent mixture and 4,4'-bipyridine (0.016 g, 0.100 mmol) in 4 mL of the same CHCl<sub>3</sub>:toluene mixture. The vial was sealed and left at room temperature. Yellow rhomboid crystals of **4** were harvested after several days.

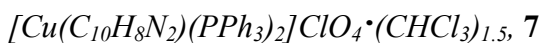


In a 20 mL vial were combined [Cu(PPh<sub>3</sub>)<sub>2</sub>(MeCN)<sub>2</sub>]PF<sub>6</sub> (0.030 g, 0.037 mmol) in 4 mL of CHCl<sub>3</sub> and 4,4'-bipyridine (0.016 g, 0.100 mmol) in 4 mL of CHCl<sub>3</sub>. The vial was sealed and left at room temperature. Light yellow prismatic crystals of **5** were harvested after 12 hours. Crystals of **5** were also produced in solvent mixtures of 9.5:0.5, 9.0:1.0, 8.5:1.5, 8.0:2.0, 7.5:2.5, and 7.0:3.0 CHCl<sub>3</sub>:THF ratios as well as 9.5:0.5, and 9.0:1.0 CHCl<sub>3</sub>:toluene ratios.

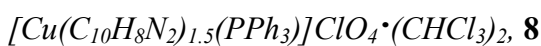


Previously reported by Lopez.<sup>2</sup> In a 20 mL vial were combined [Cu(PPh<sub>3</sub>)<sub>2</sub>(MeCN)<sub>2</sub>]PF<sub>6</sub> (0.030 g, 0.037 mmol) in 4 mL of a 8.0:2.0 CHCl<sub>3</sub>:THF solvent mixture and 4,4'-bipyridine (0.014 g, 0.092 mmol) in 4 mL of the same CHCl<sub>3</sub>:THF mixture. The vial was sealed and left at room temperature. Yellow rhomboid crystals of **6**

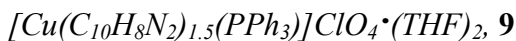
were harvested after 24 hours. Crystals of **6** were also produced in solvent mixtures of 7.5:2.5, 7.0:3.0, 6.5:3.5, 6.0:4.0, 5.5:4.5, and 5.0:5.0 CHCl<sub>3</sub>:THF ratios.



In a 20 mL vial were combined [Cu(PPh<sub>3</sub>)<sub>2</sub>(MeCN)<sub>2</sub>]ClO<sub>4</sub> (0.030 g, 0.039 mmol) in 4 mL CHCl<sub>3</sub> and 4,4'-bipyridine (0.016 g, 0.100 mmol) in 4 mL of CHCl<sub>3</sub>. The vial was sealed and left at room temperature. Light yellow columnar crystals of **7** were harvested after 12 hours. Crystals of **7** were also produced in solvent mixtures of 9.5:0.5, 9.0:1.0, and 8.5:1.5 CHCl<sub>3</sub>:THF ratios as well as 9.0:1.0, 8.0:2.0, 7.0:3.0, 6.0:4.0, and 1.0:1.0 CHCl<sub>3</sub>:toluene ratios.

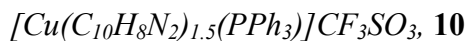


In a 20 mL vial were combined [Cu(PPh<sub>3</sub>)<sub>2</sub>(MeCN)<sub>2</sub>]ClO<sub>4</sub> (0.030 g, 0.039 mmol) in 4 mL of a 7.0:3.0 CHCl<sub>3</sub>:THF solvent mixture and 4,4'-bipyridine (0.016 g, 0.100 mmol) in 4 mL of the same CHCl<sub>3</sub>:THF mixture. The vial was sealed and left at room temperature. Yellow prismatic crystals of **8** were harvested after 12 hours. Crystals of **8** were also produced in solvent mixtures of 9.0:1.0 8.5:1.5, 8.0:2.0, and 7.5:2.5, CHCl<sub>3</sub>:THF ratios as well as 8.0:2.0, 7.0:3.0, and 6.0:4.0, CHCl<sub>3</sub>:toluene ratios.

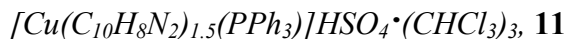


In a 20 mL vial were combined [Cu(PPh<sub>3</sub>)<sub>2</sub>(MeCN)<sub>2</sub>]ClO<sub>4</sub> (0.030 g, 0.039 mmol) in 4 mL of a THF and 4,4'-bipyridine (0.016 g, 0.100 mmol) in 4 mL THF. The vial was sealed and left at room temperature. Yellow prismatic crystals of **9** were harvested after

72 hours. Crystals of **9** were also produced in CHCl<sub>3</sub>:THF solvent mixtures at ratios of 6.5:3.5 and continuing at 0.5 increments on up to the pure THF reaction solvent.



In a 20 mL vial were combined [Cu(PPh<sub>3</sub>)<sub>2</sub>(MeCN)<sub>2</sub>]CF<sub>3</sub>SO<sub>3</sub> (0.030 g, 0.037 mmol) in 4 mL of CHCl<sub>3</sub> and 4,4'-bipyridine (0.016 g, 0.100 mmol) in 4 mL of CHCl<sub>3</sub>. The vial was sealed and left at room temperature. Yellow prismatic crystals of **10** were harvested after 12 hours. Crystals of **10** were also produced in all CHCl<sub>3</sub>:THF solvent mixtures, pure THF, as well as 9.5:0.5, and at each 0.5 increments up to 5.0:5.0 CHCl<sub>3</sub>:toluene ratios.



In a 20 mL vial were combined [Cu(PPh<sub>3</sub>)<sub>2</sub>(MeCN)<sub>2</sub>]HSO<sub>4</sub> (0.030 g, 0.039 mmol) in 4 mL of CHCl<sub>3</sub> and 4,4'-bipyridine (0.016 g, 0.100 mmol) in 4 mL of CHCl<sub>3</sub>. The vial was sealed and left at room temperature. Yellow prismatic crystals of **11** were harvested after 48 hours.

### 3.2.3 Single Crystal X-Ray Diffraction

Crystallographic data was collected using a Siemens SMART system with a CCD area detector (Mo K<sub>α</sub> = 0.71070 Å). In all cases, a single crystal of high quality (by uniform extinction of polarized light) was coated with light oil and then mounted on a tip of a glass fiber using small amount of silicon grease for adhesion. During data collection, the crystal was cooled to 173 K. The initial space group was determined by indexing

several dozen strong reflections and the structures were solved using Direct Methods.<sup>16</sup> The structure models were further refined using least-squares techniques.<sup>17</sup>

For each structure, the majority of the heavier atoms were located with the initial solution. Any remaining non-hydrogen atoms were usually located after the first or second refinements. Anisotropic thermal parameters were refined for all non-hydrogen atoms. The hydrogen atoms were included in calculated positions and refined as riding models with fixed  $U_{\text{iso}} = 1.2U_{\text{iso}}$  of the carbon atom to which they are bonded. All other structure-specific crystallographic details will be described below and listed in Table 3.1, 3.2 and 3.3.

#### *3.2.4 Powder X-Ray Diffraction and NMR Instrument Details*

Powder diffraction measurements were performed using a *Sintag X<sub>2</sub>* diffractometer at 40 kV and 20 mA for Cu K $_{\alpha}$  ( $\lambda = 1.54050 \text{ \AA}$ ). All samples were dried under vacuum for approximately 15-30 minutes. All  $^1\text{H}$  NMR measurements were made using a Bruker DRX 250 MHz NMR spectrometer. Samples for NMR analysis were vacuum filtered until dry and dissolved in deuterated DMSO for analysis.

<b>Table 3.1 Crystallographic Details for 1 – 4</b>				
	<b>1</b>	<b>2</b>	<b>3</b>	<b>4</b>
Empirical formula	CuC <sub>50</sub> H <sub>42</sub> Cl <sub>12</sub> N <sub>2</sub> F <sub>4</sub> P <sub>2</sub> B	CuC <sub>36.5</sub> H <sub>32.5</sub> N O <sub>0.5</sub> BF <sub>4</sub> P	CuC <sub>41</sub> H <sub>38</sub> N <sub>3</sub> ClO <sub>4</sub> BF <sub>4</sub> P	CuC <sub>37.7</sub> H <sub>28.5</sub> N <sub>3</sub> BF <sub>4</sub> P
Formula weight (g·mol <sup>-1</sup> )	1308.55	862.00	771.77	835.43
Temperature, K	173(2)	173(2)	173(2)	173(2)
Crystal System, Space group	Triclinic, P-1	Orthorhombic, P2(1)2(1)2	Monoclinic, P2 <sub>1</sub> /c	Monoclinic, C2/c
Unit cell dimensions				
<i>a</i> (Å)	12.866(2)	18.209(1)	26.201(1)	31.559(2)
<i>b</i> (Å)	15.843(3)	43.133(3)	23.579(1)	14.5795(8)
<i>c</i> (Å)	16.833(3)	9.9295(8)	19.075(1)	18.654(1)
$\alpha$ , deg	66.934(3)	90	90	90
$\beta$ , deg	89.585(3)	90	95.479(1)	101.974(1)
$\gamma$ , deg	72.825(3)	90	90	90
Z	2	8	12	8
Volume, Å <sup>3</sup>	2992.9(8)	7799(1)	11748(1)	8392.2(8)
$\rho_{\text{calc}}$ , g·cm <sup>-3</sup>	1.452	1.468	1.283	1.322
Absorption coefficient, mm <sup>-1</sup>	1.002	0.961	0.716	0.839
F(000)	1320	3504	4620	3391
Crystal size, mm	0.3 x 0.2 x 0.1	0.3 x 0.2 x 0.1	0.4 x 0.2 x 0.1	0.5 x 0.4 x 0.3
$\theta$ Range for data collection	1.47 to 23.00	1.32 to 22.50	1.16 to 23.00	1.32 to 22.50
Index ranges	-16 ≤ <i>h</i> ≤ 15 -20 ≤ <i>k</i> ≤ 16 -21 ≤ <i>l</i> ≤ 21	-16 ≤ <i>h</i> ≤ 20 -14 ≤ <i>k</i> ≤ 14 -22 ≤ <i>l</i> ≤ 22	28 ≤ <i>h</i> ≤ 28 -19 ≤ <i>k</i> ≤ 25 -20 ≤ <i>l</i> ≤ 20	-33 ≤ <i>h</i> ≤ 30 -12 ≤ <i>k</i> ≤ 15 -20 ≤ <i>l</i> ≤ 20
Reflections collected	19019	26978	48507	16203
Unique reflections	12942 R <sub>int</sub> = 0.0272	7208 [R <sub>int</sub> = 0.0424]	16213. [R <sub>int</sub> = 0.0675]	5453 [R <sub>int</sub> = 0.0539]
Completeness to $\theta$	27.14 (97.7 %)	23.24 (99.7 %)	23.00 (99.3)	22.50 (99.3 %)
Max/min transmissions	1.00000/ 0.810867	1.00000/ 0.689831	1.00000/ 0.862347	1.00000/ 0.768924
Data/restraints/ parameters	12942/0/696	11130/0/893	16213/15/1303	5453/0/451
Goodness of fit F <sup>2</sup>	1.015	1.149	1.045	1.087
Final R indices [ <i>I</i> > 2 $\sigma$ ( <i>I</i> )] <sup>a,b</sup>	R <sub>1</sub> = 0.0696 wR <sub>2</sub> = 0.1724	R <sub>1</sub> = 0.1002 <sup>†</sup> wR <sub>2</sub> = 0.2726	R <sub>1</sub> = 0.0898 <sup>†</sup> wR <sub>2</sub> = 0.2552	R <sub>1</sub> = 0.1012 <sup>†</sup> wR <sub>2</sub> = 0.2896
R indices (all data)	R <sub>1</sub> = 0.1000 wR <sub>2</sub> = 0.1917	R <sub>1</sub> = 0.1171 <sup>†</sup> wR <sub>2</sub> = 0.2953	R <sub>1</sub> = 0.1346 <sup>†</sup> wR <sub>2</sub> = 0.2848	R <sub>1</sub> = 0.1298 <sup>†</sup> wR <sub>2</sub> = 0.3124
Largest difference peak & hole (e·Å <sup>-3</sup> )	0.819/-0.772	2.067/-0.816 <sup>†</sup>	2.570/-0.977 <sup>†</sup>	2.357/-1.11 <sup>†</sup>
Structures were refined on F <sup>2</sup> for all data. <sup>a</sup> $R(F_o) = \sum   F_o  -  F_c   / \sum  F_o $ . <sup>b</sup> $R_w(F_o) = (\sum w   F_o  -  F_c  ^2 / \sum  F_o ^2)^{1/2}$ , $w = [ \sigma^2(F_o) + (0.002F_o)^2 ]^{-1}$ .				
<sup>†</sup> High indices and remaining Fourier peaks are the result of disordered solvent commonly found with porous solids.				



	<b>5</b>	<b>6</b>	<b>7</b>	<b>8</b>
Empirical formula	CuC <sub>50</sub> H <sub>42</sub> Cl <sub>12</sub> N <sub>2</sub> F <sub>6</sub> P <sub>3</sub>	Cu <sub>2</sub> C <sub>69</sub> H <sub>57</sub> N <sub>6</sub> Cl <sub>9</sub> F <sub>12</sub> P <sub>4</sub>	CuC <sub>50</sub> H <sub>42</sub> N <sub>2</sub> Cl <sub>13</sub> O <sub>4</sub> P <sub>2</sub>	CuC <sub>35</sub> H <sub>29</sub> N <sub>3</sub> Cl <sub>7</sub> O <sub>4</sub> P
Formula weight (g·mol <sup>-1</sup> )	682.85	1768.22	1321.19	898.27
Temperature, K	173(2)	173(2)	173(2)	173(2)
Crystal System, Space group	Triclinic P-1	Monoclinic, P2 <sub>1</sub> /c	Triclinic, P-1	Monoclinic, P2 <sub>1</sub> /c
Unit cell dimensions				
<i>a</i> (Å)	12.9210(9)	22.915(1)	12.887(3)	25.033(2)
<i>b</i> (Å)	15.668(1)	20.093(1)	15.721(3)	17.721(1)
<i>c</i> (Å)	16.548(1)	17.326(1)	16.889(4)	26.877(2)
$\alpha$ , deg	63.598(1)	90	66.435(3)	90
$\beta$ , deg	79.496(1)	111.052(1)	88.944(4)	93.218(1)
$\gamma$ , deg	80.277(1)	90	73.307(3)	90
Z	4	4	2	12
Volume, Å <sup>3</sup>	2935.8(4)	3710.0(4)	2986(1)	11903.72(2)
$\rho_{\text{calc}}$ , g·cm <sup>-3</sup>	1.545	1.578	1.470	1.504
Absorption coefficient, mm <sup>-1</sup>	1.056	1.057	1.044	1.103
F(000)	1374	3568	1336	5460
Crystal size, mm	0.4 x 0.3 x 0.25	0.3 x 0.2 x 0.1	0.3 x 0.2 x 0.1	0.4 x 0.3 x 0.1
$\theta$ Range for data collection	1.38 to 27.21	1.39 to 23.00	1.32 to 23.35	1.38 to 17.22
Index ranges	-16 ≤ <i>h</i> ≤ 16 -18 ≤ <i>k</i> ≤ 20 -21 ≤ <i>l</i> ≤ 21	-24 ≤ <i>h</i> ≤ 25 -22 ≤ <i>k</i> ≤ 14 -19 ≤ <i>l</i> ≤ 18	-14 ≤ <i>h</i> ≤ 14 -17 ≤ <i>k</i> ≤ 17 -18 ≤ <i>l</i> ≤ 18	-16 ≤ <i>h</i> ≤ 20 -14 ≤ <i>k</i> ≤ 14 -22 ≤ <i>l</i> ≤ 22
Reflections collected	20753	32650	15206	26978
Unique reflections	12596 [R(int) = 0.0184]	10350 [R <sub>int</sub> = 0.0351]	8187 [R <sub>int</sub> = 0.0571]	7208 [R <sub>int</sub> = 0.0424]
Completeness to $\theta$	27.21 (96.1 %)	23.00 (100.0 %)	23.25 (95.3 %)	27.40 (95.5 %)
Max/min transmissions	1.00000/0.788969	1.00000/ 0.785441	1.00000/ 0.755246	1.00000/ 0.716612
Data/restraints/ parameters	12596/0/667	10350/0/921	8187/0/696	7208/0/1378
Goodness of fit F <sup>2</sup>	1.027	1.392	1.091	1.005
Final R indices [ <i>I</i> > 2 $\sigma$ ( <i>I</i> )] <sup>a,b</sup>	R <sub>1</sub> = 0.0653, wR <sub>2</sub> = 0.1788	R <sub>1</sub> = 0.0653 wR <sub>2</sub> = 0.2030	R <sub>1</sub> = 0.1045 <sup>†</sup> wR <sub>2</sub> = 0.2606	R <sub>1</sub> = 0.0716 wR <sub>2</sub> = 0.1799
R indices (all data)	R <sub>1</sub> = 0.0838, wR <sub>2</sub> = 0.1957	R <sub>1</sub> = 0.1023 wR <sub>2</sub> = 0.2179	R <sub>1</sub> = 0.1791 <sup>†</sup> wR <sub>2</sub> = 0.3376	R <sub>1</sub> = 0.2018 <sup>†</sup> wR <sub>2</sub> = 0.2479
Largest difference peak & hole (e·Å <sup>-3</sup> )	1.799/-1.212 <sup>†</sup>	1.897/-1.364 <sup>†</sup>	1.332/-0.916 <sup>†</sup>	1.405/-1.344 <sup>†</sup>
Structures were refined on F <sup>2</sup> for all data. <sup>a</sup> $R(F_o) = \frac{\sum   F_o  -  F_c  }{\sum  F_o }$ . <sup>b</sup> $R_w(F_o) = \frac{(\sum w  F_o  -  F_c  ^2 / \sum  F_o ^2)^{1/2}}{w}$ , $w = [\sigma^2(F_o) + (0.002F_o)^2]^{-1}$ .				
<sup>†</sup> High indices and remaining Fourier peaks are the result of disordered solvent commonly found with porous solids.				

**Table 3.3 Crystallographic Details for 9 – 11**

	<b>9</b>	<b>10</b>	<b>11</b>
Empirical formula	CuC <sub>38.33</sub> H <sub>37.67</sub> N <sub>3</sub> O <sub>5.17</sub> CIP	CuC <sub>36</sub> H <sub>28</sub> N <sub>3</sub> O <sub>3</sub> Cl <sub>6</sub> F <sub>3</sub> PS	CuC <sub>36</sub> H <sub>31</sub> N <sub>3</sub> O <sub>4</sub> PS
Formula weight (g·mol <sup>-1</sup> )	753.01	947.94	1015.26
Temperature, K	173(2)	173(2)	173(2)
Crystal System, Space group	Monoclinic, P2 <sub>1</sub> /c	Hexagonal, R3	Triclinic, P1
Unit cell dimensions			
<i>a</i> (Å)	26.117(2)	16.926(2)	17.267(1)
<i>b</i> (Å)	23.779(2)	16.926(2)	17.397(2)
<i>c</i> (Å)	19.112(2)	25.344(4)	19.478(2)
$\alpha$ , deg	90	90	114.718(2)
$\beta$ , deg	94.530(2)	90	91.725(2)
$\gamma$ , deg	90	120	119.408(1)
Z	12	6	4
Volume, Å <sup>3</sup>	11832(2)	6288.2(1)	4399.6(8)
$\rho_{\text{calc}}$ , g·cm <sup>-3</sup>	1.268	1.5017	1.533
Absorption coefficient, mm <sup>-1</sup>	0.706	0.912	1.168
F(000)	4692	2202	2052
Crystal size, mm	0.4 x 0.2 x 0.2	0.3 x 0.2 x 0.2	0.4 x 0.3 x 0.2
$\theta$ Range for data collection	1.57 to 27.13	1.60 to 27.12	1.21 to 22.26
Index ranges	-13 ≤ <i>h</i> ≤ 13 -41 ≤ <i>k</i> ≤ 25 -16 ≤ <i>l</i> ≤ 18	-21 ≤ <i>h</i> ≤ 19 -21 ≤ <i>k</i> ≤ 21 -31 ≤ <i>l</i> ≤ 32	-22 ≤ <i>h</i> ≤ 22 -22 ≤ <i>k</i> ≤ 22 -24 ≤ <i>l</i> ≤ 24
Reflections collected	30272	13079	38804
Unique reflections	10779 [R <sub>int</sub> = 0.0911]	6002 [R <sub>int</sub> = 0.0671]	33906 [R <sub>int</sub> = 0.0319]
Completeness to $\theta$	27.20 (99.2 %)	27.12 (100.0)	27.16 (98.0 %)
Max/min transmissions	1.00000/ 0.836319	1.00000/ 0.680473	0.698260/ 0.718772
Data/restraints/parameters	26174/0/1287	6002/1/127	33906/3/1985
Goodness of fit F <sup>2</sup>	1.036	2.517 <sup>†</sup>	0.785
Final R indices [ <i>I</i> > 2 $\sigma$ ( <i>I</i> )] <sup>a,b</sup>	R <sub>1</sub> = 0.0834 wR <sub>2</sub> = 0.2422	R <sub>1</sub> = 0.2930 <sup>†</sup> wR <sub>2</sub> = 0.6147 <sup>†</sup>	R <sub>1</sub> = 0.0527 wR <sub>2</sub> = 0.1216
R indices (all data)	R <sub>1</sub> = 0.1650 wR <sub>2</sub> = 0.3051	R <sub>1</sub> = 0.3992 <sup>†</sup> wR <sub>2</sub> = 0.6674 <sup>†</sup>	R <sub>1</sub> = 0.1064 wR <sub>2</sub> = 0.1426
Largest difference peak & hole (e·Å <sup>-3</sup> )	2.569/-0.786	6.822/6.058 <sup>†</sup>	1.403/-0.747
Structures were refined on F <sup>2</sup> for all data. <sup>a</sup> $R(F_o) = \sum   F_o  -  F_c   / \sum  F_o $ . <sup>b</sup> $R_w(F_o) = (\sum w  F_o  -  F_c  ^2 / \sum  F_o ^2)^{1/2}$ , $w = [ \sigma^2(F_o) + (0.002F_o)^2 ]^{-1}$ .			
<sup>†</sup> Unusually large values are given because a final solution was not obtained for this structure as is explained in detail in Section 3.3.4.			

## 3.3 Results and Discussion

### 3.3.1 Reactions With the $\text{BF}_4^-$ Anion

With the reactions containing the  $\text{BF}_4^-$  anion, we first see the appearance of the one-dimensional chain of **1** at the very start with the solvent system consisting of pure  $\text{CHCl}_3$  as was expected.<sup>2</sup> As shown in Table 3.4, when the THF was first used in low concentration in the solvent system, **1** continues to be the only crystalline product.

When the THF concentration reaches 20% by volume in  $\text{CHCl}_3$ , another

**Table 3.4 Reactions with  $\text{BF}_4^-$**

CHCl <sub>3</sub> :THF Mixture		STRUCTURE		
% THF		1	2	3
0				
10				
20				
30				
40				
50				
60				
70				
80				
90				
100				

product begins to co-crystallize along with **1**.

Surprisingly, this new product is the structure of

$[\text{Cu}(\text{C}_{10}\text{H}_8\text{N}_2)_{1.5}(\text{PPh}_3)]\text{BF}_4 \cdot (\text{THF})_{0.5}(\text{CHCl}_3)$ , **2**,

which has a striking resemblance to ladder chains of

$[\text{Cu}(\text{C}_{10}\text{H}_8\text{N}_2)_{1.5}(\text{PPh}_3)]\text{PF}_6 \cdot (\text{CHCl}_3)_{1.5}$ , **6**, previously

reported by Lopez and mentioned in Section 1.6.<sup>2</sup> At

THF concentrations between 30 and 70 %, **2**

becomes the only crystalline product of this reaction.

With THF concentrations >70 % a

polycrystalline precipitate quickly develops, which

then is replaced by large prismatic crystals over the course of 3 or 4 days. Single crystal

X-ray analysis identified the structure of these new crystals to be the layered fused

pentagon structure of  $[\text{Cu}(\text{C}_{10}\text{H}_8\text{N}_2)_{1.5}(\text{PPh}_3)]\text{BF}_4 \cdot (\text{THF})_{1.33}(\text{CHCl}_3)_{0.33}$ , **3**.<sup>2, 7</sup> Since this

structure was the first structure synthesized by layering THF onto the  $\text{CHCl}_3$  reaction

solvent, this demonstrates how well the mixed solvent method compares to the layered

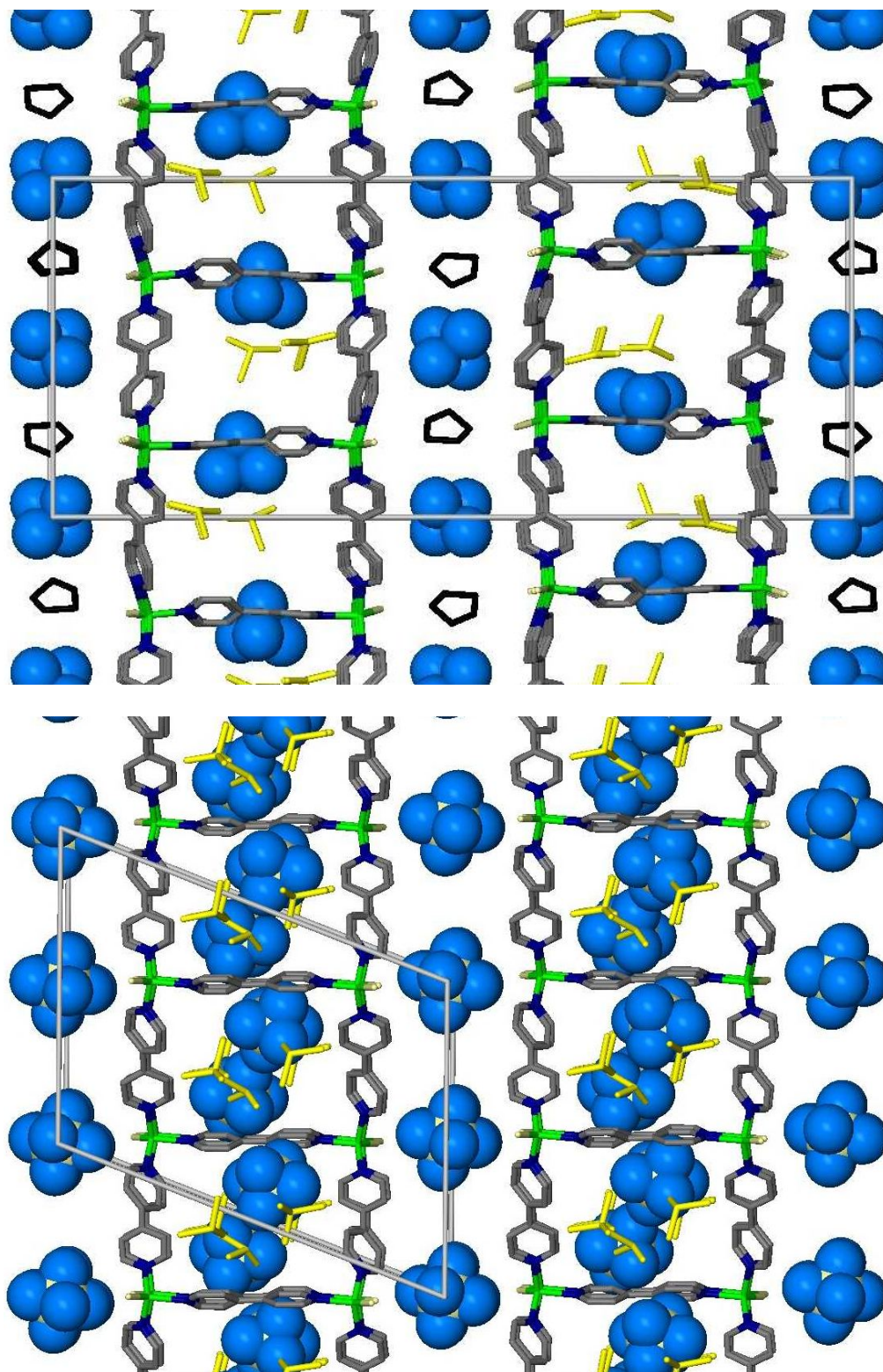
solvent technique. This also shows how we may have been mistaken to attribute the

formation of the ladder structure with the change from the  $\text{BF}_4^-$  to the  $\text{PF}_6^-$  anion. Most probably, the layered technique produced a situation of high THF concentration at the solvent interface, resulting in the bypass of products formed at lower THF concentrations such as the ladder structure with the  $\text{BF}_4^-$  anion.

In the comparison of the two ladder structures, we see that the structure with the  $\text{BF}_4^-$  anion, **2** is found in the orthorhombic  $\text{P2}_1\text{2}_1\text{2}$  space group while the structure with the  $\text{PF}_6^-$  anion, **6** is found in the monoclinic  $\text{P2}_1/\text{c}$  space group. Even still, both structures are very close to being isostructural.

The asymmetric unit of both **2** and **6** is composed of two unique copper atoms, each having three bpy ligands and one  $\text{PPh}_3$  ligand coordinated in a distorted tetrahedral geometry. The distances and angles of these two tetrahedra will be listed along with the rest of the structures in a comparison analysis to be shown in Section 3.3.4, Table 3.8. Also included in the asymmetric unit of **2** are two  $\text{CHCl}_3$  and one THF solvent molecules, one complete anion and two anions one half occupied as the boron atom sits on a two fold screw axis. There are also five large Fourier peaks remaining that most probably correspond to some highly disordered THF solvate of which refinement attempts have failed to produce a stable structure. The asymmetric unit of **6** has two fully occupied  $\text{PF}_6^-$  anions and three  $\text{CHCl}_3$  molecules. The only major difference between the two being the positioning of the anions and the inclusion of THF in-between the stacks of ladder chains; the crystal packing is essentially the same for both structures.

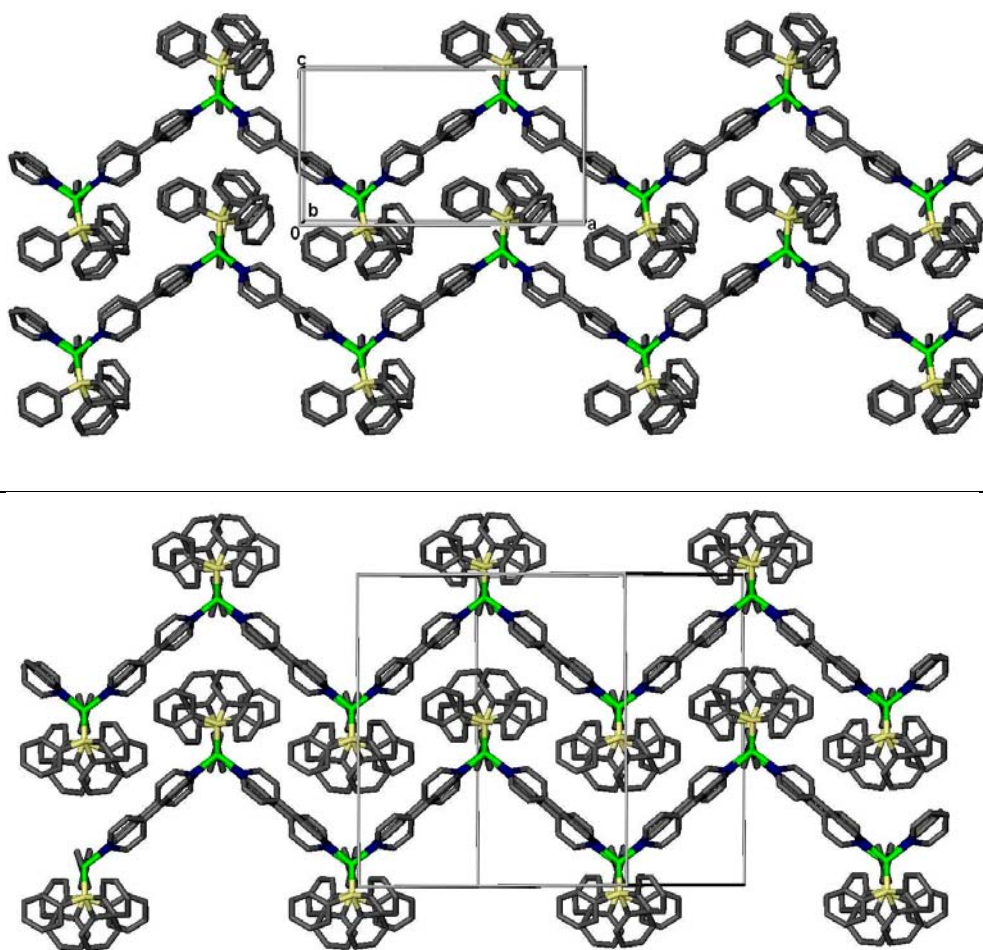
As shown in Figure 3.1, the  $\text{BF}_4^-$  anion in **2** sits predominately in the center of the bpy ligand while the  $\text{PF}_6^-$  anion in **6** is more associated with the Cu center. The solvated



**Figure 3.1** The ladder chain structures of (top) **2** looking down the *c*-axis and (bottom) **6** looking down the *b*-axis. In each structure, the anions are shown in space fill while the rest of the structure is shown in stick representation. The solvated THF in **2** is shown in black and the solvated  $\text{CHCl}_3$  in both is shown in yellow. The phenyl rings on the phosphine groups and the hydrogen atoms have been omitted for clarity.

THF in **2** seems to occupy the former position of the  $\text{PF}_6^-$  anion. We can only speculate that the inclusion of the THF solvent is the result of the additional space made available by the presence of the smaller  $\text{BF}_4^-$  anion. As we will indicate in the discussion of the reactions containing the  $\text{PF}_6^-$  anion, we have not encountered any structures of **6** with solvated THF included.

Figure 3.2 shows two chains stacked together as we look down the b-axis in **2** and

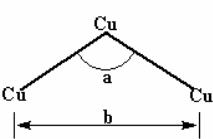
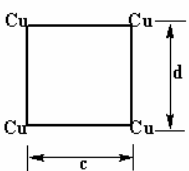


**Figure 3.2** A view of the stacked chains in (top) **2** as seen down the b-axis and also in (bottom) **5** viewing along a diagonal. Carbons are grey, nitrogen blue, copper green and phosphorous yellow. The anions, solvent molecules, and hydrogen atoms have been omitted for clarity.

diagonally in the unit cell of **6**. In both **2** and **6**, the ladder chains progress in a zigzag fashion and stack neatly on top of each other. Although the ladder chain stacking of the two structures is practically identical, there are some very subtle differences in the arrangement of the PPh<sub>3</sub> ligands.

From what we know about intermolecular forces, we can say that the change of anion as well as the inclusion of the THF solvent should alter the crystal packing forces to some extent. Further examination of these two structures does reveal some other subtle differences, which could relate back to the before mentioned changes. If you look closely at the two structures in Figure 3.1, you can see a slight elongation of the ladder chains in **2**, than that seen in the chains of **6**. A more accurate way to examine this is to compare the measurements of the Cu – Cu distances and Cu – Cu – Cu angles in each structures chain. Table 3.5 shows the angle formed along the chain and various distances as indicated. The wider angle (a) formed in **2** increases the non-linked Cu distance (b) in the chain 0.9 Å longer than that of **6**. There is no significant difference in the sides forming the square cavities and even with the other small differences; the two structures are relatively isomorphous to each other.

**Table 3.5** Angles and Distances of the Ladder Chain for Structures **2** and **6**.

	Position	<b>2</b>	<b>6</b>
	a	108.5°	100.8°
	b	18.2Å	17.3Å
	c	11.24Å	11.25Å
	d	11.24Å	11.18Å
		11.38Å	11.34Å

As was mentioned previously, there is a slightly different event that unfolds as the THF concentration surpasses 70% and continuing on up to 100% THF as **3** becomes the sole product in the reactions involving the BF<sub>4</sub><sup>-</sup> anion. Perhaps the reason for the total

absence of any other co-crystallization as **3** forms is that this structure's crystal formation is preceded by the reaction "crashing out" and forming a yellow, polycrystalline precipitate. As this reaction sits further, large, single crystals of **3** replace this precipitate over a period of 2 – 4 days. Although the eventual synthesis of **3** at some point in these THF:CHCl<sub>3</sub> reaction solvent mixtures was quite expected, development of these crystals from a polycrystalline precipitate was totally unforeseen.

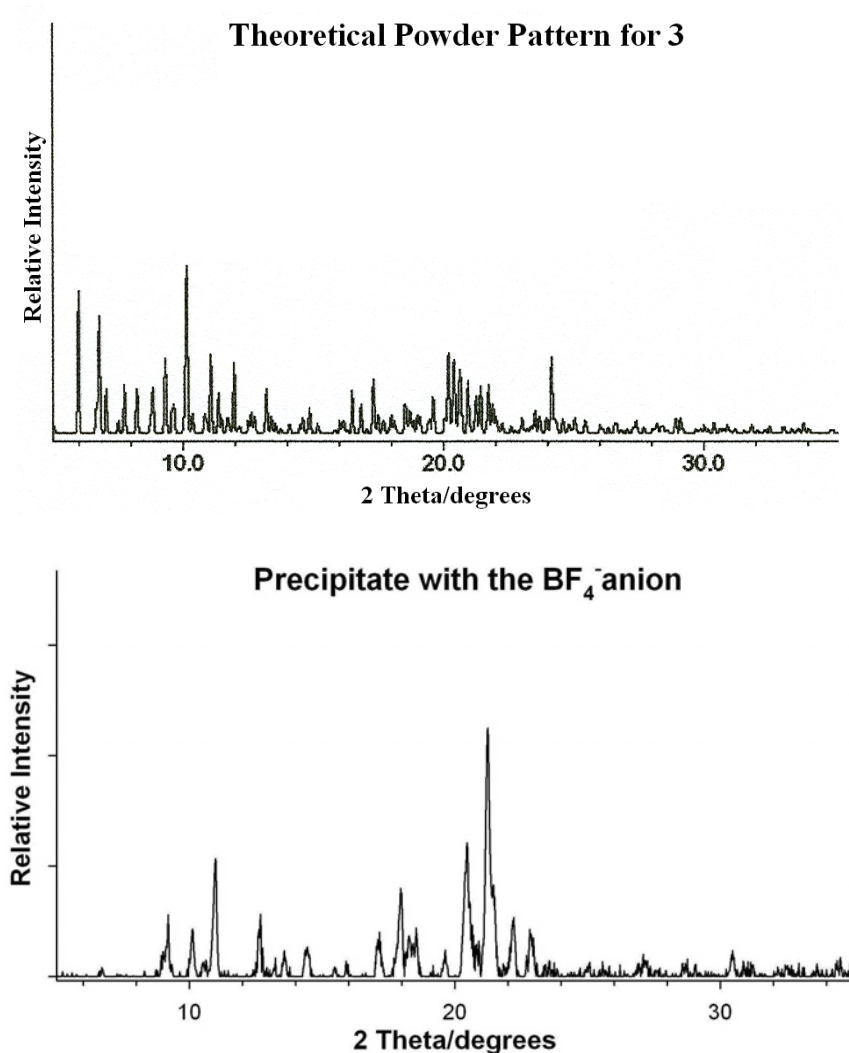
Considerable effort was employed to find ways to prevent this precipitation. Concentration adjustments, cooling or heating the reaction, or just careful mixing to avoid premature nucleation were all tried without success as the precipitate continued to form. It was only through subsequent observations and experimentation that led us to the conclusion that this precipitation was actually an inevitable yet necessary step in the synthesis of **3**. We found that, particular to these reactions involving the BF<sub>4</sub><sup>-</sup> anion, in no instance would there be the formation of **3** without first producing this precipitate and, in turn, in no instance has the precipitate failed to transform into single crystals of **3**.

Examination of the precipitate via <sup>1</sup>H NMR analysis indicates that the precipitate does, in fact, have the general formula similar to **3** as containing the correct bpy:PPh<sub>3</sub> ratio of 1.5:1. However, powder X-ray diffraction (XRPD) seems to indicate that there is a different crystalline phase present in the precipitate. Figure 3.3 compares the powder pattern generated from the precipitate with the theoretical pattern produced from the single crystal data of **3**. Clearly there is little, if any, structural similarity between the two crystalline compounds.

Although we might consider this as an example of Ostwald ripening, a more plausible explanation is that the reaction proceeds from precipitate to the single crystals



of **3** via a phase transformation process or, more precise, solvent-mediated reconstructive transformation as was describe at the beginning of this chapter. In this case, the precipitate that forms would be considered the kinetic product of a metastable phase (or polymorph) while the final single crystals of **3** represents the thermodynamically favored polymorph.<sup>11</sup> The phase transformation leading to **3** usually occurs over 24 – 72 hrs resulting in a complete transformation from precipitate to single crystals.



**Figure 3.3** A comparison of (left) the theoretical powder pattern for **3** with (right) an actual XRPD data of the precipitate that forms from the reaction if the BF<sub>4</sub><sup>-</sup> starting material with bpy in THF.

Interestingly, even samples of dried precipitate placed in a vial of fresh THF proceed to undergo phase transformation as the original product had, even with no other reactants in the solution! Those same samples placed in either  $\text{CHCl}_3$  or toluene remain as precipitate indefinitely. This is a strong indication that there is, in fact, a dependence or link between the type of solvent used and the phase transformation leading to the formation of the fused pentagon layered coordination solid.

The final item in this section concerns those reactions performed in the  $\text{CHCl}_3$ :toluene solvent systems. In the reactions performed in solvent ratios of 9.0:1.0 to 1.0:1.0  $\text{CHCl}_3$ :toluene, we saw the immediate formation of a light yellow precipitate which slowly transformed into light yellow, column-like crystals of **1**. In only two occasions (both at 6.0:4.0  $\text{CHCl}_3$ :toluene) did we discover the formation of the hexagonal layered structure of **4**, which was first reported by Lopez to be synthesized in toluene layered solvent reactions.<sup>2,7</sup>

$^1\text{H}$  NMR analysis revealed that the precipitate composition had a ligand ratio 1.0:2.0 bpy: $\text{PPh}_3$ . This makes sense since, in those reactions with lower toluene concentrations mentioned above, the next phase the precipitate transforms into is **1**, which has the same 1.0:2.0 bpy: $\text{PPh}_3$  ligand ratio. The XRPD analysis only shows that the precipitate was not quite crystalline with no useful peaks available for analysis. Even still, the precipitate appears to go through an ageing process as it slowly dissolves and is replaced by the single crystals of **1** over a period of 4 to 5 days. Those reactions in solvent systems with >50% toluene would form a persisting precipitate with no crystal growth even after several months.

### 3.3.2 Reactions With the $PF_6^-$ Anion

The reactions containing the  $PF_6^-$  anion resemble those reactions with the  $BF_4^-$  anion [in pure  $CHCl_3$  or the initial mixtures containing either THF or toluene]. However, in

**Table 3.6 Reactions with  $PF_6^-$**

CHCl <sub>3</sub> :THF Mixture % THF	STRUCTURE			
	5	6	UNK	Precip.
0				
10				
20				
30				
40				
50				
60				
70				
80				
90				
100				

reaction solvents with high THF or toluene concentrations, either a polycrystalline precipitate or crystalline clusters forms. Shown in Table 3.6, the one-dimensional chain of  $[Cu(C_{10}H_8N_2)(PPh_3)_2]PF_6 \cdot (CHCl_3)_4$ , **5** forms in pure  $CHCl_3$  as well as up to 30 % THF in the  $CHCl_3$ :THF mixtures. The ladder chains of  $[Cu(C_{10}H_8N_2)_{1.5}(PPh_3)]PF_6 \cdot (CHCl_3)_{1.5}$ , **6**

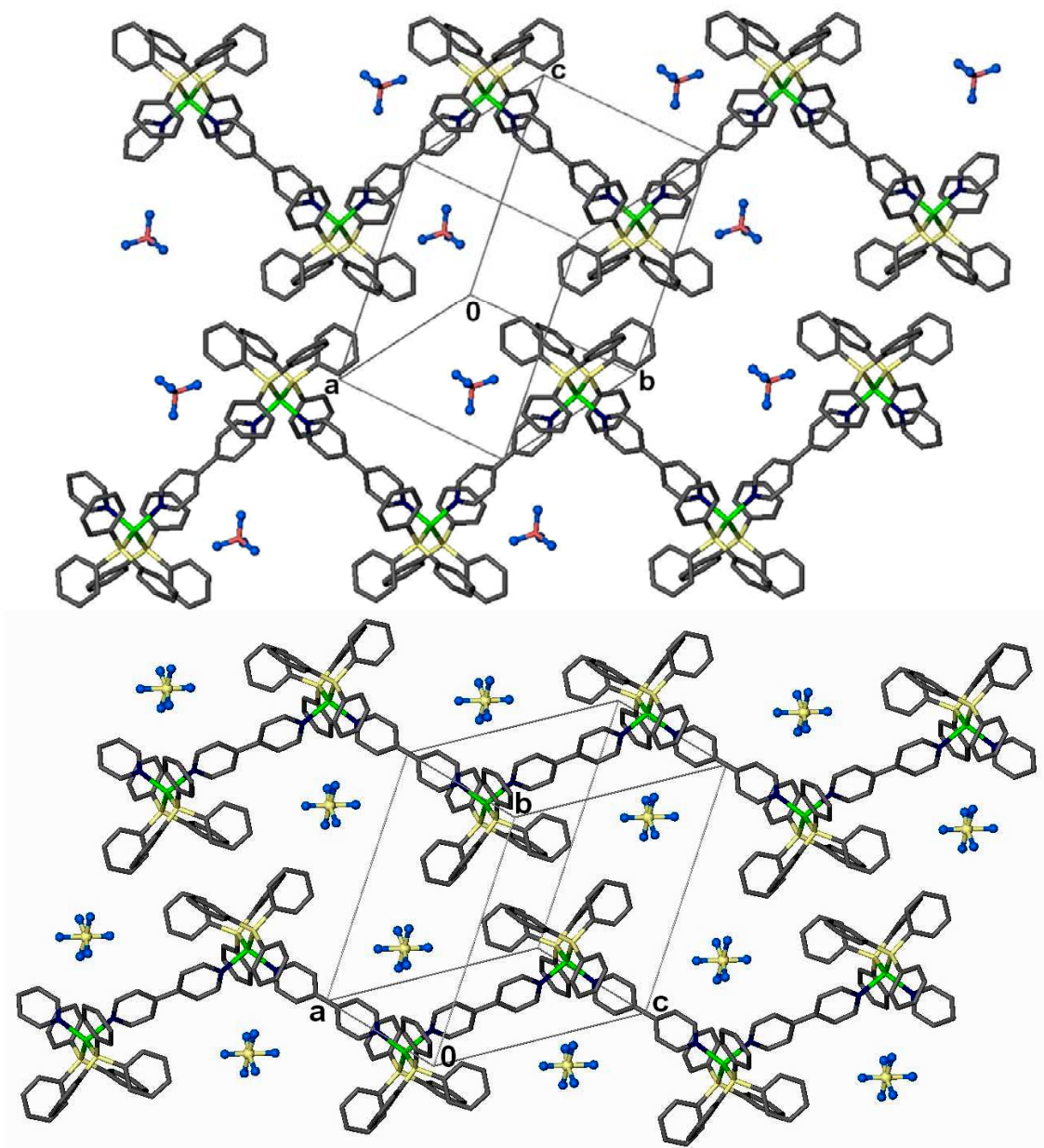
begins to co-crystallize with **5** in 20 – 30 % THF concentrations. At THF concentrations of >30 % by volume, small polycrystalline clusters with a structure yet unknown (UNK) begin to appear along with a polycrystalline precipitate. Both of these products co-crystallizing with **6** until, at THF concentrations >50 % on up to pure THF, only the precipitate remains.

**Table 3.7 Unit Cells for 1 & 5**

unit cell	1	5
dimensions		
<i>a</i> (Å)	12.866(2)	12.9210(9)
<i>b</i> (Å)	15.843(3)	15.668(1)
<i>c</i> (Å)	16.833(3)	16.548(1)
$\alpha$ , deg	66.934(3)	63.598(1)
$\beta$ , deg	89.585(3)	79.496(1)
$\gamma$ , deg	72.825(3)	80.277(1)

Table 3.7 shows how the two unit cells of **1** and **5** compare to each other. both structures crystallize in triclinic, P-1 cells, having very similar *a*, *b*, and *c* parameters. However, further examination shows that there is considerable

difference between the  $\alpha$ ,  $\beta$ , and  $\gamma$  angles of the two structures. As shown in Figure 3.4, the 1-D chains produced with the  $\text{BF}_4^-$  and  $\text{PF}__6^-$  anions (**1** and **5**) have very similar packing arrangements yet subtle differences between each structure; much like the differences that existed between the ladder structures of **2** and **6**.

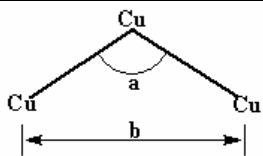


**Figure 3.4** The 1-D chains found in structures (top) **1** and (bottom) **5** shown in stick representation. The hydrogen atoms and  $\text{CHCl}_3$  molecules have been omitted for clarity. The chains in **1** progress along the  $ab$  diagonal while the chains in **5** progress along the  $ac$  diagonal.

The distances between each  $[\text{Cu}(\text{bpy})(\text{PPh}_3)_2]_n$  chains of both (top) **1** and (bottom) **5** relatively the same for both structures. This may explain why  $a$ ,  $b$ , and  $c$  of the two unit cells are so similar. However, a closer look at the chains reveals a difference between the

**Table 3.8** Angles and Distances of the 1-D Chain for Structures **1** and **5**.

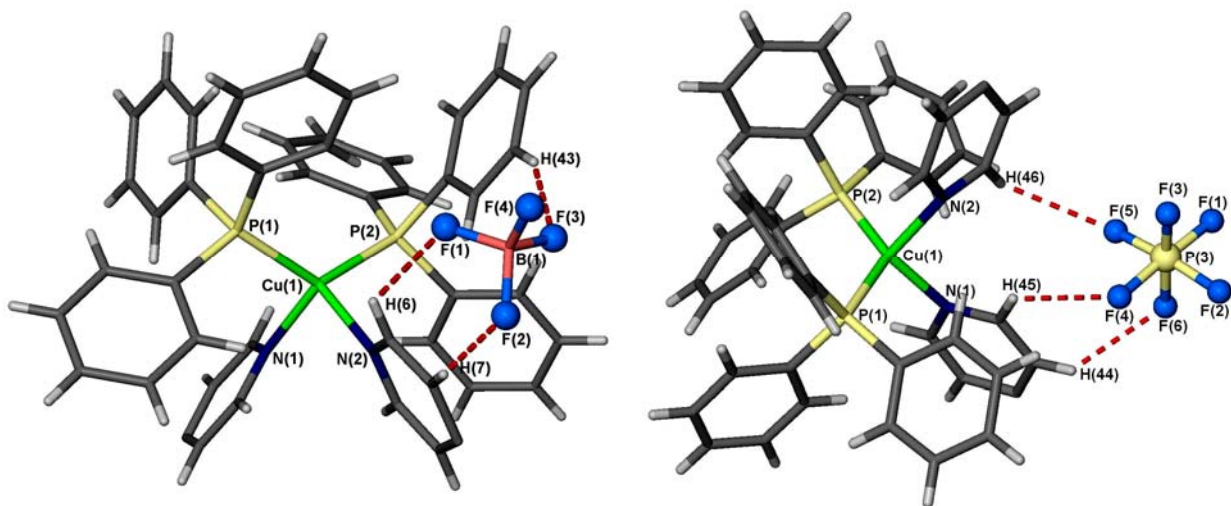
Position	<b>1</b>	<b>5</b>
a	99.35°	117.08°
b	17.21Å	19.05Å



two structures much like we found in the ladder structures as the chains in **5** are elongated with much wider angles than is found in **1**.

Table 3.8 list the angles formed by the  $\text{bpy} - \text{Cu} - \text{bpy}$  coordination, as well as the distance between the two non-coordinated coppers in the chain for both **1** and **5**. In this case, the 1-D chain with the  $\text{PF}_6^-$  anion is the structure with the wider angle, resulting in an elongated chain.

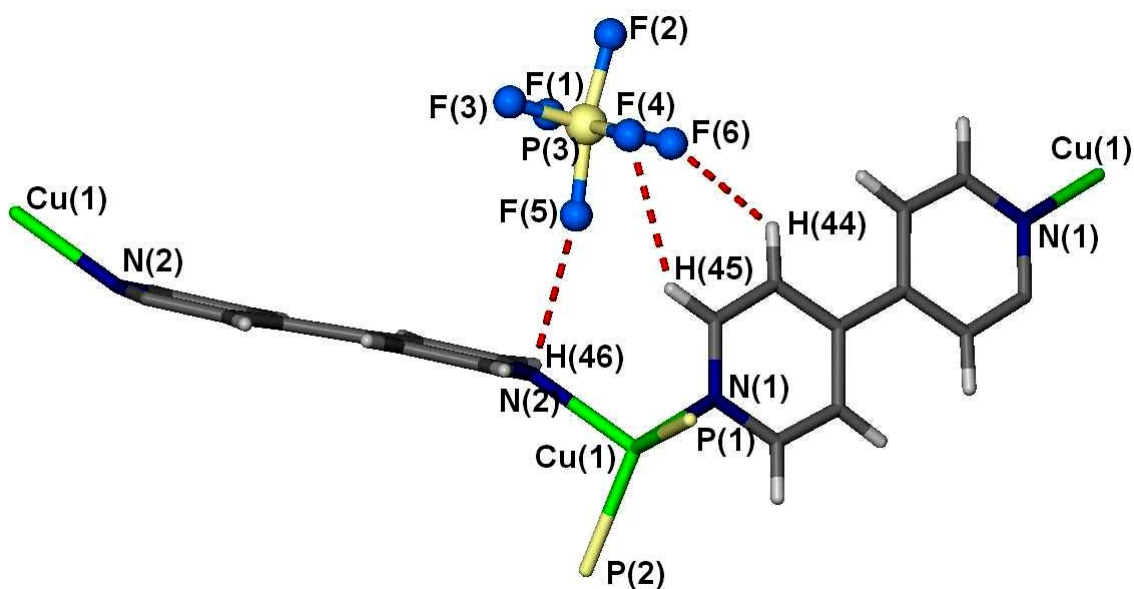
As was seen in the ladder structures, the positioning of the anion is also considerably different in each structure. Figure 3.5 shows how both  $\text{PF}_6^-$  and  $\text{BF}_4^-$  anions are rather distantly associated with the Cu center (5.235 Å and 5.617 Å, respectively). However, the  $\text{PF}_6^-$  anion (right) is located in the center of the  $\text{bpy} - \text{Cu} - \text{bpy}$  angle of the chain with three weak, H – F hydrogen bonds of  $\sim 2.6 - 2.9$  Å between the anion and the two bpy



**Figure 3.5** The two copper centers of (left) **1** and (right) **5** showing the anion positioning and close H – F interactions in each.

ligands. The  $\text{BF}_4^-$  anion is located in the cleft formed between the  $\text{PPh}_3$  and bpy ligands and appears to have three H – F hydrogen bonds with distances of  $\sim 2.4 - 2.9 \text{ \AA}$ ; this time between the  $\text{PPh}_3$  and bpy ligands.

Even with this weak hydrogen bonding in **5**, it is most likely that the positioning of the  $\text{PF}_6^-$  anion is causing steric interference that produces the wider angle in the chain. Closer inspection of **5** reveals an unusual bend in the Cu – N bond of the bpy ligands in **5**, much like what Lopez had noticed with the bpy ligands in the pentagonal layered structure of **3**.<sup>2</sup> Figure 3.6 shows two tetrahedra as they are bridged by a bpy ligand. The bend in the ligand, measured as  $\text{Cu}(1) - \text{N}(2) - \text{N}(2)$ , is  $156^\circ$ , while on the adjacent and more planar bpy ligand the  $\text{Cu}(1) - \text{N}(1) - \text{N}(1)$  angle is  $175^\circ$ . Those same angles for **1** both measure around  $175^\circ$ .



**Figure 3.6** A stick representation of two bpy bridged Cu tetrahedra of **5** showing the bending of the ligand at the Cu – N bond. The anion shown in isotropic spheres is shown in position with the three, weak H-bonds in place. Phenyl rings on the phosphines and  $\text{CHCl}_3$  molecules have been omitted.

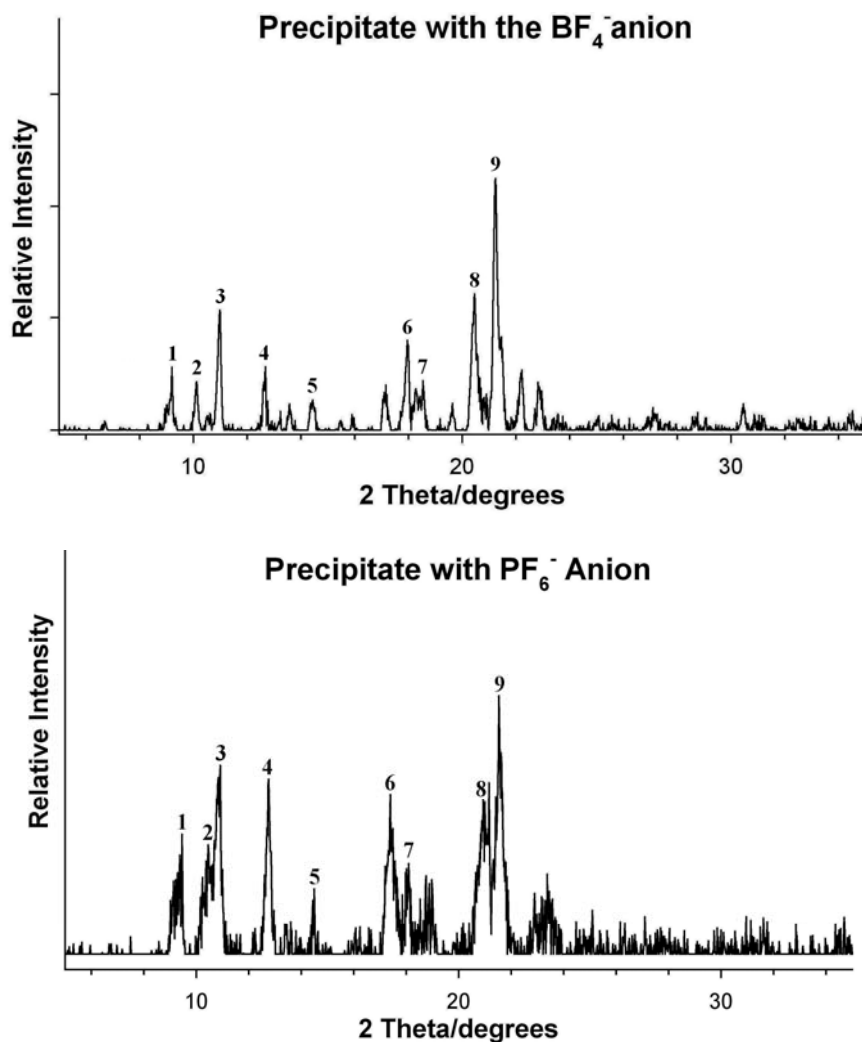
The bowed ligand in **3** (that Lopez had mentioned in her report) measures as  $153^\circ$  for  $\text{Cu}(1) - \text{N}(1) - \text{N}(2)$ . For the ladder structures, **2** and **6**, most the ligand bowing is at a

minimum with angles ranging from 172 - 174°. Only one ligand in **2** has a somewhat higher degree of bowing with the Cu(1) – N(3) – N(4) angle at 163°.

In the reaction solvent mixtures with THF concentrations at 50 – 60 %, small crystal clusters would co-crystallize along with a considerable amount of precipitate. These crystal clusters *did not* appear to come about because of a precipitate phase transformation (as was observed with the BF<sub>4</sub><sup>-</sup> material), nor did the precipitate ever seem to transform into any other product; even after several months left in contact with the solution. Both the crystal clusters and the precipitate proved to each have a 1.5:1bpy:PPh<sub>3</sub> ligand ratio (by <sup>1</sup>H NMR analysis) indicative to either **6** or of the layered coordination solids. We were unable to do much else with the crystal clusters as they were small, few in numbers, and not suitable for single crystal X-ray diffraction.

At THF concentrations >60 %, the precipitate would form as the sole product and remain as such for several months until the samples were sent for recycle. Not one sample of precipitate in these reactions exhibited the phase transformation as was observed in the BF<sub>4</sub><sup>-</sup> system; even attempts to promote this transformation by heating the precipitate/solvent mixture slightly (to ~50 – 90° C) failed to produce crystals suitable for diffraction. Even with this, both the <sup>1</sup>H NMR analysis (showing the 1.5:1.0 ligand ratio) and XRPD results indicate that the precipitates in both the BF<sub>4</sub><sup>-</sup> and PF<sub>6</sub><sup>-</sup> system are isostructural.

The powder patterns of both of these precipitates are shown in comparison in Figure 3.7. Upon comparing these two powder patterns, we can match several strong reflections. With a total of nine reflection matches, we can say with a relatively high degree of confidence that they are isostructural polycrystalline precipitates.



**Figure 3.7** Two spectra of XRPD data for precipitates generated from the reaction of bpy with the starting materials with (top) the  $\text{BF}_4^-$  and (bottom) the  $\text{PF}_6^-$  anions. The matching peaks of the two spectra are numbered.

At this point, we can only speculate why the precipitate with the  $\text{BF}_4^-$  anion transforms while that with the  $\text{PF}_6^-$  anion does not. As was pointed out earlier, the polymorph's solubility is a key component in its ability to undergo phase transformation. The slightly larger molecular weight of the precipitate containing the  $\text{PF}_6^-$  anion could change the solubility just enough to prevent the dissolution of this metastable compound and the resulting phase transformation. On the other hand, as the 1-D chain and ladder



structures with  $\text{PF}_6^-$  (**5** & **6**) had subtle differences from those with the  $\text{BF}_4^-$  anion (**1** & **2**), perhaps the same can be said for the precipitate as well. This structural difference may be responsible for the stabilization of this particular phase just enough to resist the phase transformation process. This precipitate proves to be stable even after several months, as verified by comparing two powder patterns of the same sample taken 4 months apart which proved to be identical.


For those reactions performed in the  $\text{CHCl}_3$ :toluene solvent systems, from solvent ratios of 9.5:0.5 and 9.0:1.0  $\text{CHCl}_3$ :toluene, we obtained similar results to those found with the  $\text{BF}_4^-$  anion. In both instances, there was an immediate formation of a light yellow precipitate, which transformed over the next few days into the prismatic crystals of **5**. Those reactions in solvent with  $\geq 10\%$  toluene would form a persisting precipitate with no crystal growth even after several months. Analysis of the precipitate by  $^1\text{H}$  NMR also indicated the 1.0:2.0 bpy: $\text{PPh}_3$  ligand ratio and, as in the  $\text{BF}_4^-$ , there were no reflections present in the XRPD pattern indicating the precipitate may be non-crystalline. Most likely the product being formed in both of these reactions is so insoluble in the  $\text{CHCl}_3$ :toluene solvent that the precipitate forms faster than the self-assembly can form any ordered compound.

### *3.3.3 Reactions With the $\text{ClO}_4^-$ Anion*

Those reactions between the starting material with the  $\text{ClO}_4^-$  anion and bpy in  $\text{CHCl}_3$ , the  $\text{CHCl}_3$ :THF solvent mixtures, and pure THF follow a similar, yet slightly different path as was seen in the similar reactions involving  $\text{BF}_4^-$  anion. As can be seen in Table 3.9, the first structure to appear is the one-dimensional chain of **7**, which is

isostructural to **1** and comparable to **5** (as was **1** comparable to **5**). The appearance of **7** continues as THF is first used in the solvent system and on up to about 20 – 25 % by

**Table 3.9 Reactions with  $\text{ClO}_4^-$**  volume THF.

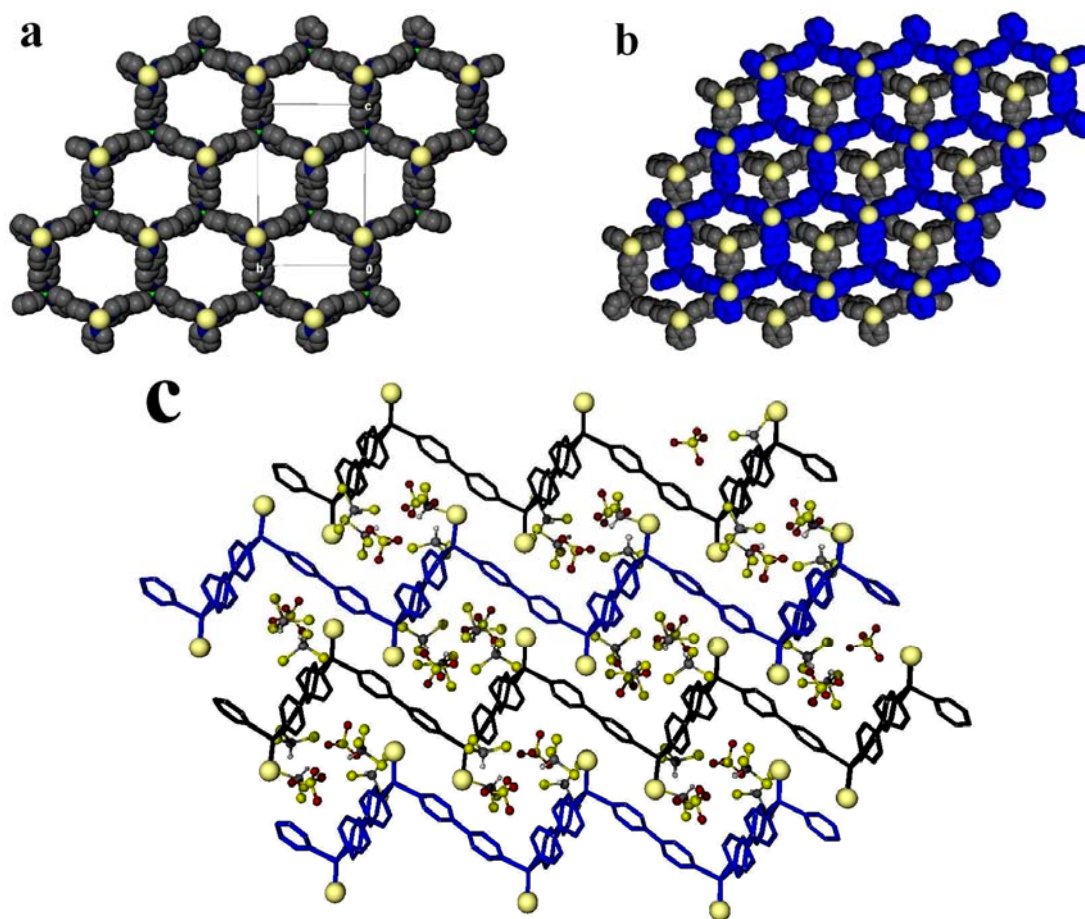
CHCl <sub>3</sub> :THF Mixture		STRUCTURE		
	% THF	7	8	9
INCREASING THF CONCENTRATION 	0			
	10			
	20			
	30			
	40			
	50			
	60			
	70			
	80			
	90			
	100			

Another compound co-crystallizes with **7**, which have the appearance of tiny, flat hexagons that are free-floating in the CHCl<sub>3</sub> reaction solvent. As THF is included in the reactions, large prismatic crystals appear of which X-ray analysis had determined to be the layered [Cu(C<sub>10</sub>H<sub>8</sub>N<sub>2</sub>)<sub>1.5</sub>(PPh<sub>3</sub>)]ClO<sub>4</sub>·(CHCl<sub>3</sub>)<sub>2</sub>, **8**. It was believed that the tiny flat hexagons might be the same material as **8** since <sup>1</sup>H NMR analysis indicated

this unknown to have the 1.5:1.0 bpy:PPh<sub>3</sub> ligand ratio. However, further analysis by X-ray diffraction was not possible because of the crystal size and also since only a small amount of this unknown was available at any given time.

Although <sup>1</sup>H NMR analysis indicated that **8** had the same ligand ratio found in either the ladder chains, or the layered pentagons, X-ray diffraction studies revealed a structure quite unlike either of them. As shown in Figure 3.8, the structure of **8** is comprised of layers of hexagons giving honeycomb-like appearance, similar to what is seen in the BF<sub>4</sub><sup>-</sup> anion's **4**. However, quite unlike **4**, the structure in **8** is *not* interpenetrated, and is seen as discrete, close fitting layers with the ClO<sub>4</sub><sup>-</sup> anion and solvated chloroform found occupying the space in-between the layers. In the top right and bottom representations in

Figure 3.8, it can be seen how the PPh<sub>3</sub> ligands are positioned almost directly in the middle of each of the layer's hexagon cavities.



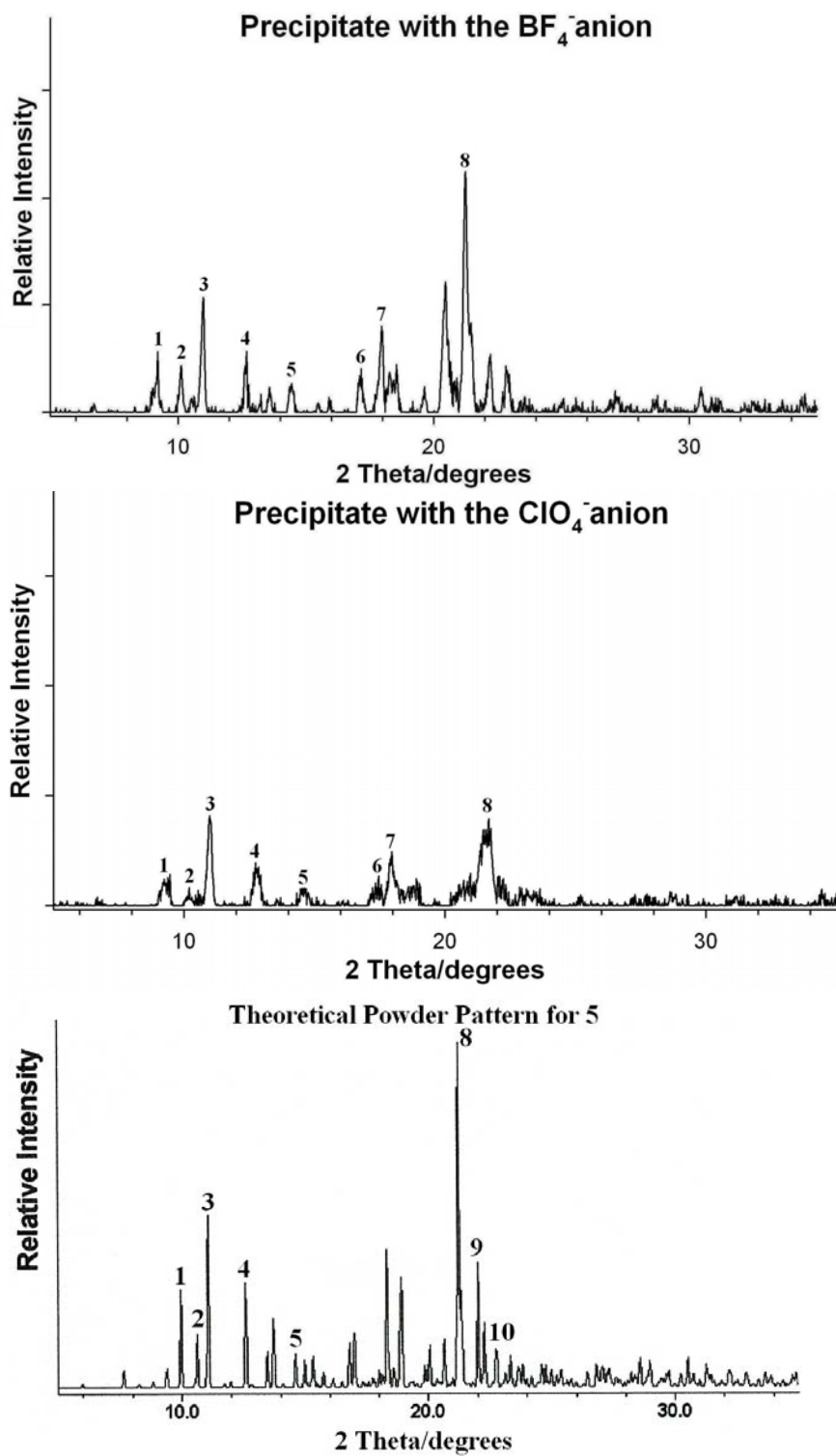
**Figure 3.8** The layered, honeycomb structure of  $[\text{Cu}(\text{C}_{10}\text{H}_8\text{N}_2)_{1.5}(\text{PPh}_3)]\text{ClO}_4 \cdot (\text{CHCl}_3)_2$  **8** showing a space fill representation of (a) a single layer and (b) two overlapping layers. (c) A side view of the layers in stick representation (phosphines shown as space fill) shows they stack together and the positioning of the anion and included solvent (both as ball and stick). Phenyl rings on the phosphines and hydrogens are omitted for clarity.

As the THF concentration is increased in the reaction solvent, **8** continues to be formed while the amount of **7** dwindles as more and more THF is included in the solvent mixture until, at 7.0:3.0  $\text{CHCl}_3$ :THF, **8** becomes the sole product of the reaction. It should be noted that in none of the reactions involving the  $\text{ClO}_4^-$  anion is the ladder type structure (as in **2** and **6**) ever formed.

Finally, at THF concentrations >30% by volume, a precipitate forms as the sole product; similar to what was seen in the  $\text{BF}_4^-$  reactions. This precipitate appears to follow the same solvent-mediated reconstructive transformation path as observed with that of  $\text{BF}_4^-$  as the precipitate slowly dissipates while large prismatic crystals form over a period of a few days. Also as with  $\text{BF}_4^-$ , dried precipitate with the  $\text{ClO}_4^-$  anions transforms just as completely when placed in fresh THF but not at all when placed in other solvents.

Analysis by  $^1\text{H}$  NMR of the precipitate confirms the 1.5:2.0 bpy: $\text{PPh}_3^-$  ligand ratio and the XRPD presents us with the expected powder pattern, quite comparable to that of the  $\text{BF}_4^-$  precipitate. As seen in Figure 3.9, both powder patterns match up as expected, although the reflections collected from the  $\text{ClO}_4^-$  material are somewhat weaker than that of the  $\text{BF}_4^-$  anion. This is a result of technique rather than product condition and is probably related to the quantity of precipitate used in each sample. In any case, the patterns match up enough to verify with high certainty that both of these precipitates have quite similar structures.

It is interesting to see that there appears to be several matching of peaks found in the theoretical powder pattern for structure **5** as well (Figure 3.9 bottom). There is some shifting in the peaks but this could be from the differences in the anion as well as the absence of  $\text{CHCl}_3$  solvate in either of the precipitates. This could be evidence showing a relationship between the perchlorates honeycomb layers and the fused pentagon layers of both the  $\text{BF}_4^-$  and  $\text{ClO}_4^-$  anions. If this relationship does indeed exist, we might consider the honeycomb layered as the kinetic product, which under the right conditions will undergo the solvent-mediated reconstructive transformation process forming the pentagonal cavity layers.



**Figure 3.9** Two spectra of XRPD data for precipitates generated from the reaction of bpy with the starting materials with (top) the BF<sub>4</sub><sup>-</sup>, (center) the ClO<sub>4</sub><sup>-</sup> anions, and the theoretical pattern found for **5**. The matching peaks of the two spectra are numbered.

The structural solution obtained from single crystal X-ray diffraction data confirms that the resulting prismatic crystals are that of  $[\text{Cu}(\text{C}_{10}\text{H}_8\text{N}_2)_{1.5}(\text{PPh}_3)]\text{ClO}_4 \cdot (\text{THF})_2$  **9**, which is completely isostructural (with the exception of having different anions) to the fused-pentagon layered structure of **3**. Although we present the formula with only the solvated THF included in the structure, this formula was acquired from a structure obtained from X-ray diffraction data of a crystal that was synthesized in pure THF. As either **3** or **9** is synthesized in the  $\text{CHCl}_3$ :THF solvent mixtures, both the  $\text{CHCl}_3$  and THF solvents are included in the structure. In turn, either of these same structures synthesized in only the THF will only have THF included in the structure. It is interesting to see how the  $\text{CHCl}_3$  is included in this structure type, even though the structures synthesis is not dependant upon the chloroforms presence. Such a solvent inclusion of *spectator* solvent implies that this material may possess useful solvent exchange abilities.

Those reactions with the  $\text{ClO}_4^-$  anion in the  $\text{CHCl}_3$ :toluene mixtures were slightly different than the other two anion's results. Although, only the 1-D chain of **7** appeared at low toluene concentrations, as the toluene concentration in the mixture was >10 %, the hexagonal layered network of **8** was formed once again. As was with the  $\text{CHCl}_3$ :THF reactions, only chloroform was found as the included solvent.

As the toluene concentration was >40%, a yellow precipitate formed as the only product. The results of  $^1\text{H}$  NMR and XRPD analysis by were similar to those found with the precipitates of the  $\text{BF}_4^-$  and  $\text{PF}_6^-$  anions; a 1.0:2.0 bpy: $\text{PPh}_3$  ligand ratio of what appears to be a non-crystalline precipitate. As did with the others, the precipitate remained as such, without any sign of phase transformation.

### 3.3.4 Reactions With the $CF_3SO_3^-$ Anion

Those reactions involving the  $CF_3SO_3^-$  (triflate) anion are probably the most surprising of all the reactions shown so far. There is no need to present a colorful chart or table for these reactions since the same structure is produced in all reaction solvents. With the exception of two cases involving the formation of a precipitate (see below), all the reaction solvent mixtures, including pure  $CHCl_3$  produce well formed, prismatic crystals of  $[Cu(C_{10}H_8N_2)_{1.5}(PPh_3)]CF_3SO_3$ , **10**.

It is unfortunate, however, that although we clearly obtain the exact same hexagonal R-1 unit cell for each crystal data collected, a complete structure solution has not been realized to this date. This difficulty is possibly attributed to a twinned crystal; however, the exact cause is unknown at this time. Several data sets have been collected with the same results and difficulty in obtaining a complete structure solution.

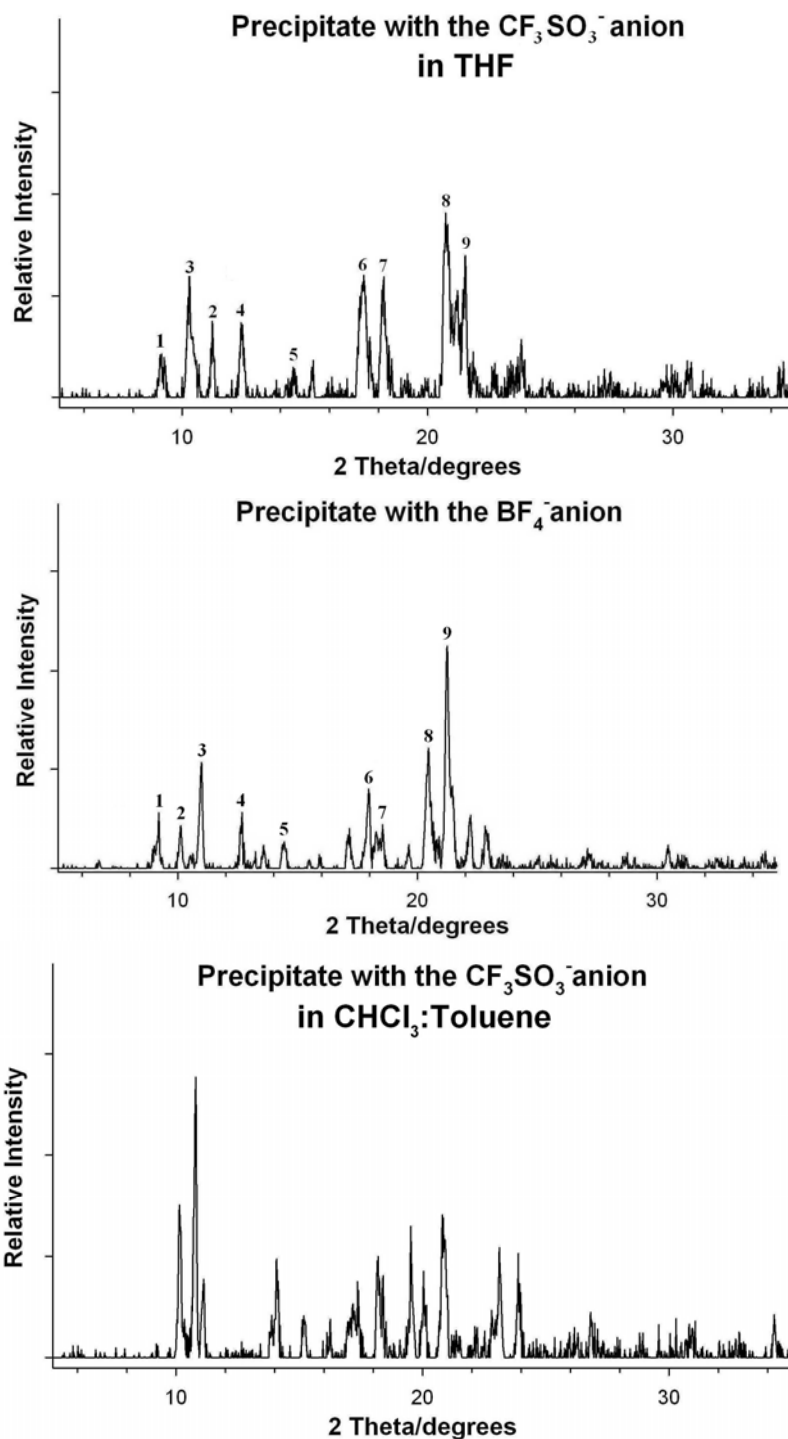
Nonetheless, we were still able to obtain a crude view of the structure's cationic network; though we were unable to locate either the triflate anion or any structural evidence of included solvent. There is enough of a solution available to allow us to see that the structure's network is much like that of the  $ClO_4^-$  hexagonal layered structure of **8**. Although we do not have a complete enough structure to determine whether or not these two crystalline solids are isostructural, from what evidence we have, they do appear to be fairly similar structures. The most important item to note is the unique structural invariance of **10** as it continues to appear in one solvent system after another. The cause of this invariance might be the key to answering many questions being brought up in this study.

As was first mentioned, there are instances of precipitate in some of the reactions. As the reactions with all the other anions would precipitate in a reaction solvent of pure THF, careful mixing of the triflate reactions in this solvent system usually results in a clear, yellow solution with the first traces of the crystals of **10** appearing several minutes later and full crystal growth after only 24 hours. It was found, however, that mixing these reactions too fast or agitation after mixing can lead to the production of a yellow polycrystalline precipitate instead; much like that with the other anions and one that resist the phase transformation as it did the with  $\text{PF}_6^-$  anion.

Analysis of this precipitate by  $^1\text{H}$  NMR shows that it has the typical 1.5:1.0 bpy:PPh<sub>3</sub> ligand ratio and, interestingly, XRPD reveals that the structure of the polycrystalline precipitate is somewhat similar but not as close a match as was found among the other three anion's precipitates. Figure 3.10 shows the powder pattern comparison of polycrystalline precipitate from the "crashing out" of reaction with the triflate anion with the precipitate produced in the reaction of the  $\text{BF}_4^-$  anion material with bpy in THF. Even with the visible differences, we can still locate several matching reflections and show how these two structures are fairly similar.

Again, as was with the  $\text{PF}_6^-$  case, we may be able to attribute lack of this precipitate's phase transformation to its reduced solubility because of the increase in molecular weight or because of a possible formation of a more stable precipitate when triflate is included. Just as was with the  $\text{PF}_6^-$  precipitate, we have never seen any sign of phase transformation in this system either, even after several months of the precipitate in contact with solution.





**Figure 3.10** Powder patterns of the precipitate with the triflate in THF reaction solvent with a comparison to the  $\text{BF}_4^-$  precipitates powder pattern showing several matches as with the other samples. We find no matches with the triflate's precipitate in the reactions performed in the  $\text{CHCl}_3$ :toluene solvent mixture.

Those reactions performed in CHCl<sub>3</sub>:toluene solvent mixtures also produce large single crystals of **10** in toluene concentrations >60%, at which point is the source of the second account of precipitate found in these reactions. Although the <sup>1</sup>H NMR analysis shows the precipitate has a 1.5:1.0 bpy:PPh<sub>3</sub> ligand ratio as found in the others, the XRPD analysis yields the multiple reflections of a crystalline compound, instead of the results found with the other three anions reactions in CHCl<sub>3</sub>:toluene reactions (of which no peaks were found). Unfortunately, these reflections (also shown in 3.10) do not match with any of the previous powder patterns from the polycrystalline precipitates produced from the THF reaction solvent, leaving it as an unknown phase with a 1.0:2.0 ligand ratio formula similar to a 1-D chain structure. This precipitate is also persistent and does not undergo any phase transformation, even after several months of being in contact with the reaction solvent solution.

### *3.3.5 Reactions With the HSO<sub>4</sub><sup>-</sup> Anion*

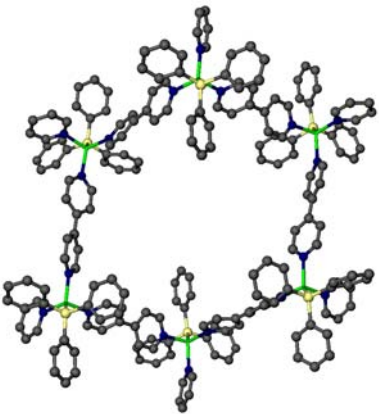
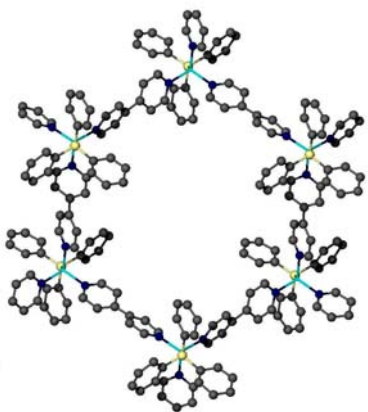
This final investigation was included much later in the study as we became more aware of the similarities and differences between each of the anions studied so far. It was, in fact, not until some of the evidence presented in the following chapter that led us to propose the viability of the hydrogensulfate, HSO<sub>4</sub><sup>-</sup> anion in these types of reactions. The results are presented at this time in order to facilitate the structural comparison of these results along with those results from the other four anions.

Although this study is still in its very early stages, we have already crystallized the first layered structure in reactions performed in CHCl<sub>3</sub> solvent alone. As we had suspected, the resulting structure of [Cu(C<sub>10</sub>H<sub>8</sub>N<sub>2</sub>)<sub>1.5</sub>(PPh<sub>3</sub>)]HSO<sub>4</sub>·(CHCl<sub>3</sub>)<sub>3</sub> **11** is

essentially isostructural to the hexagonal layered coordination solids found with the other oxoanions,  $\text{ClO}_4^-$  and triflate (**8** and **10**, respectively).

There are some subtle differences found in the geometry of the layers hexagonal cavities in each structure, which is probable what leads to the structures to be defined in two different space groups,  $P2_1/c$  for **8** and  $P1$  for **11**. This difference is seen in the bpy coordinated  $\text{Cu} - \text{Cu} - \text{Cu}$  angles that form the hexagons in each structure. Table 3.7 compares hexagons of the two structures pictorially and also list those angles found in each set of two unique hexagons per structure. From the representations alone, we can a somewhat warped hexagon being formed in **8**,

**Table 3.10** The angles found around the pairs of hexagons found in structures **8** and **11**. Structures shown as ball and stick representations with the hydrogens removed for clarity.  
(3 unique angles per hexagon)

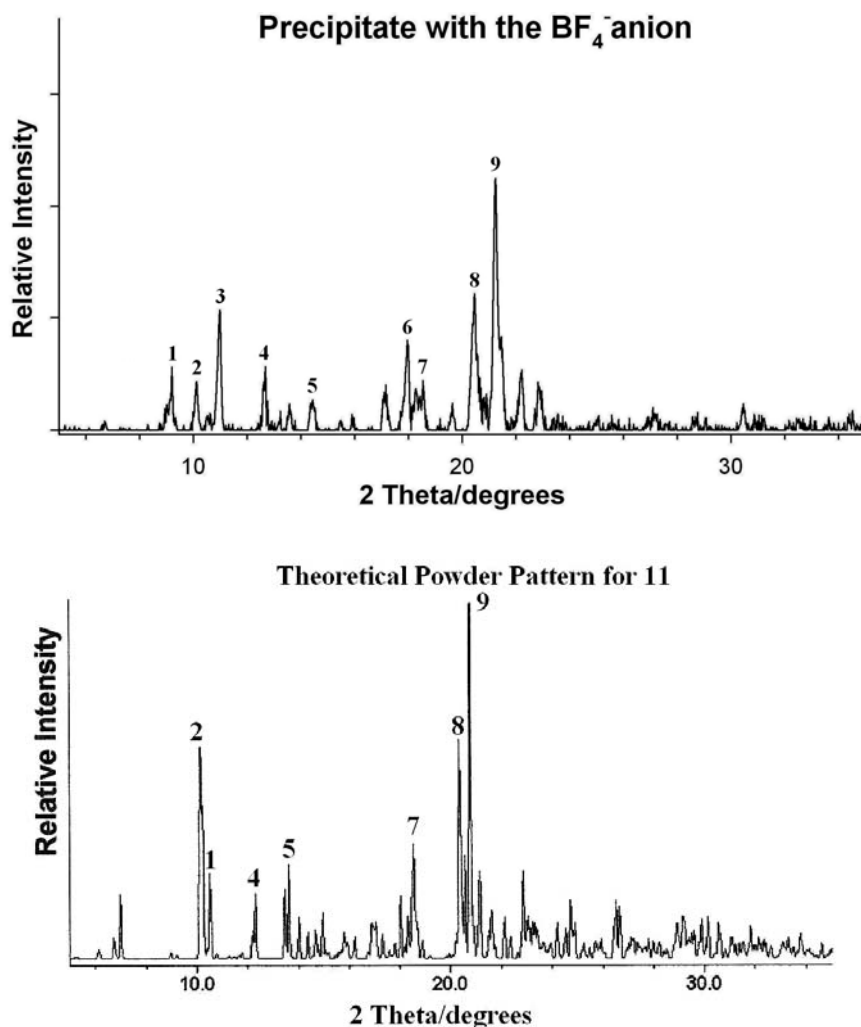
Structure <b>8</b>		
	Hexagon 1	Hexagon 2
	104.3°	105.1°
	92.8°	90.2°
	90.4°	94.1°
Structure <b>11</b>		
	Hexagon 1	Hexagon 2
	102.0°	102.0°
	101.2°	101.2°
	100.3°	100.2°

while the hexagon in **11** is much more ordered and symmetrical. This observation is then reflected by the angles listed, as there is a large variation between the three unique angles of **8** while those in **11** are very similar to each other. Each structure has the same copper(I) tetrahedral coordination environment and same general formula (aside from different anions); however, there are definite variations in the angles about the Cu(I) tetrahedron that make each structure unique in its own way. Comparison of the Cu(I) coordination spheres angles of these and the other structures mentioned will be listed towards the end of this chapter.

The theoretical powder pattern, shown in Figure 3.11, shows only a few (possible) matches with the powder pattern precipitate from the  $\text{BF}_4^-$  anion system. There appears to be much more shifting of the reflections providing only a small resemblance to those patterns from the precipitate of the other four anions. It is hard to make a definite determination from this crystallographic evidence but this study continues and further evidence may help to conclude whether or not this particular extended solid is related to the polycrystalline precipitate of the other four anions.

In all of the reaction solvent mixtures (with either THF or toluene in  $\text{CHCl}_3$ ) and at times even in pure  $\text{CHCl}_3$ , a heavy precipitate formed immediately upon mixing. The reason for this large amount of precipitate may be related to the  $\text{HSO}_4^-$  starting materials affinity towards water as will be explained in detail in the next chapter.

While we are still in the process of analyzing these resulting precipitates, the composition and color is quite similar those that found with the other anions. At this time we only have  $^1\text{H}$  NMR analysis available to confirm the precipitate as having the 1.5:1.0 bpy: $\text{PPh}_3$  ligand ratio required for the formation of the target layered extended solid.



**Figure 3.11** The spectra of XRPD data for (top) precipitate generated from the reaction of bpy with the starting materials with the  $\text{BF}_4^-$  and (bottom) the theoretical powder pattern for **11**. The matching peaks of the two spectra are numbered.

### 3.3.6 Examining the Distances and Angles: What it takes to make a square, pentagon, or hexagon network

With all the different structures we have shown, we will now explore what geometric requirements are needed to make a ladder chain of squares, and the pentagonal- and hexagonal-celled layers out of a single  $[\text{Cu}(\text{bpy})_{1.5}(\text{PPh}_3)]^+$  tetrahedral building block. In order to get a better understanding of what might be causing these

changes, we should get a closer look at the basic building blocks and examine any likes and differences between each of them.

Tables 3.11 and 3.12 list some select distances and angles in the Cu(I) coordination spheres in all of the structures presented in this chapter. Just by appearance alone, it is easy to pick out the differences in from one structure to the next just by looking at the degree of distortion each tetrahedron have. For ideal tetrahedral geometry, the each of the 6 angles formed by  $L_a - Cu - L_b$  are exactly  $120^\circ$ . The actual values of the angles representing the positioning of the ligands about the Cu coordination center give us an accurate account of how each tetrahedron vary from the ideal geometry in order to self-assembled into the different packing arrangements.

First, with the data given for the 1-D chains (only that from **5** pictured here), we attribute the distortion seen to the steric bulk of the  $PPh_3$  ligands, resulting in a wider  $P - Cu - P$  angle while the bpy ligands are compressed downward, away from the array of phenyl rings on each phosphine. The difference in the bond distances and ligand angles between the two tetrahedra does not seem that significant. Just looking at the  $N - Cu - N$  angle, we can only see a  $5^\circ$  difference, while the angle formed in the chain of **7** is almost  $18^\circ$  wider. The extra angle in **7** must then be the results of the ligand - Cu bond bending as was pointed out in 3.3.2. The data from **6** was not included since this structure is isostructural to **1**.

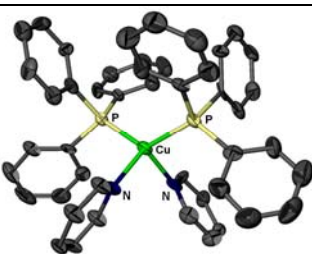
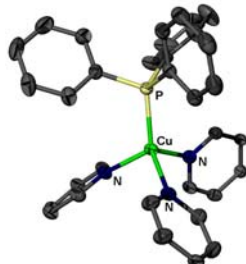
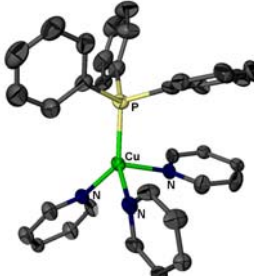
Next, with the two ladder structures we can see by the pictorial representation of **2** that, with the absence of one  $PPh_3$  ligand, this results in a fairly symmetric tetrahedron. The angles formed by bpy ligands appear somewhat compressed as they are directed away from the bulky remaining phosphine. The given  $N - Cu - N$  angles verify this

compression, having angles well below the ideal norm. One N – Cu – N angle seen in **2** is wider than the others and corresponds to the wider bpy coordinated Cu – Cu – Cu angle in the ladder chain of **2**, as was presented in the latter part of Section 3.3.1. Interestingly, phosphine ligands on all four tetrahedra appear to be tilted to one side, as is indicated by the lone 121 – 124° P – Cu – N angle. This could be the result of how the ladders are stacked, as  $\pi - \pi$  stacking between the phosphine phenyl rings and the bpy ligands influence the phosphines position on the Cu center.

As we look at the tetrahedra of pentagonal layered structure, there appears to be considerable ligand distortion about the Cu coordination center. Closer examination of the data indicates that this distortion observed is actually an exaggerated version of the same phosphine tilting as seen in the ladder chains. This time the P – Cu – N angle concerned is much wider at 124 – 135 °. Again, this phosphine tilting most likely the results of how these layers stack with the phenyl rings on the phosphines finding the best fit among the bpy and phosphine ligands of the adjacent layer. The data for structure **9** was not included since this structure is also isostructural to **3**.

Looking at the next two representations of hexagonal layered structures of **8** and **11**, we begin to see an improvement in the symmetry of the angles ligands. The data shows that while the tetrahedra found in **8** still have some distortion, it is considerably less than what was found in **3**. Although there is still some tilt to the phosphine on Cu(1), the phosphine on both Cu(2) and Cu(3) seem to be relatively normal to the ideal tetrahedral geometry. The angle symmetry is improved dramatically in **11** as we see very little

**Table 3.11** Selected Bond Lengths and Angles for Structures **1**, **2**, **3**, **5**, and **6**.

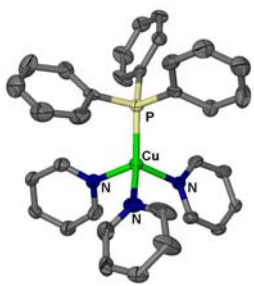
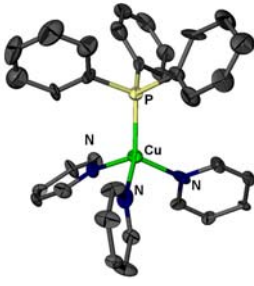
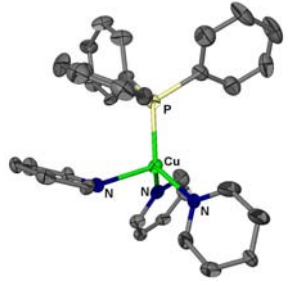
1-D Chain	Structures	<b>1</b>	<b>5</b>		
	Cu(1) – P(1) Å	2.271(1) Å	2.284(1) Å		
	Cu(1) – P(2) Å	2.270(1) Å	2.278(1) Å		
	Cu(1) – N(1) Å	2.092(3) Å	2.074(3) Å		
	Cu(1) – N(2) Å	2.089(3) Å	2.110(3) Å		
	P(1)–Cu(1)–P(2)	125.89(4)°	125.48(4)°		
	N(1)–Cu(1)–P(1)	102.00(9)°	104.60(9)°		
	N(2)–Cu(1)–P(1)	113.98(9)°	106.5(1)°		
	N(1)–Cu(1)–P(2)	110.90(9)°	113.30(9)°		
	N(2)–Cu(1)–P(2)	102.6(1)°	101.45(9)°		
	N(1)–Cu(1)–N(2)	98.2(1)°	103.1(1)°		
Ladder Chain	Structures	<b>2</b>	<b>6</b>		
	Cu center	Cu(1)	Cu(2)	Cu(1)	Cu(2)
	Cu – P	2.201(3) Å	2.199(3) Å	2.202(1) Å	2.206(2) Å
	Cu – N	2.058(9) Å	2.068(9) Å	2.090(5) Å	2.137(5) Å
	Cu – N	2.140(8) Å	2.092(9) Å	2.086(5) Å	2.085(5) Å
	Cu – N	2.073(9) Å	2.123(8) Å	2.154(5) Å	2.096(5) Å
	P – Cu – N	124.5(3)°	123.8(3)°	122.2(1)°	121.2(1)°
	P – Cu – N	110.7(2)°	111.3(3)°	113.6(2)°	113.98(1)°
	P – Cu – N	117.3(2)°	116.5(2)°	116.8(1)°	116.7(1)°
	N – Cu – N	97.7(4)°	109.2(4)°	101.8(2)°	101.5(2)°
	N – Cu – N	99.8(3)°	94.8(3)°	97.4(2)°	101.3(2)°
	N – Cu – N	102.6(3)°	96.8(3)°	101.3(2)°	97.3(2)°
	Fused Pentagon Layered	Structure	<b>3</b>		
	Cu Center	Cu(1)	Cu(2)	Cu(3)	
	Cu – P	2.213(2) Å	2.204(2) Å	2.200(2) Å	
	Cu – N	2.048(6) Å	2.059(7) Å	2.050(7) Å	
	Cu – N	2.095(7) Å	2.060(7) Å	2.102(7) Å	
	Cu – N	2.137(7) Å	2.090(6) Å	2.101(7) Å	
	P – Cu – N	102.7(2)°	109.8(2)°	108.8(2)°	
	P – Cu – N	115.3(2)°	114.7(2)°	115.1(2)°	
	P – Cu – N	135.1(2)°	124.2(2)°	135.3(2)°	
	N – Cu – N	97.3(2)°	97.5(1)°	98.5(3)°	
	N – Cu – N	98.0(3)°	102.7(3)°	100.5(3)°	
N – Cu – N	102.0(3)°	106.0(3)°	105.6(3)°		

variance in the P – Cu – N angles and the same with the N – Cu – N angles. This increase in symmetry is probably the result of how well a fit these honeycomb layers have as they stack on top of each other. Recall that the PPh<sub>3</sub> ligand of one layer fits neatly inside the hexagon of the adjacent layer. The improvement in angle ligand symmetry in **11** over that of **8** is most likely related to the different anions, since all the other components in the structure are the same. However, it could also be related to the presence of a small



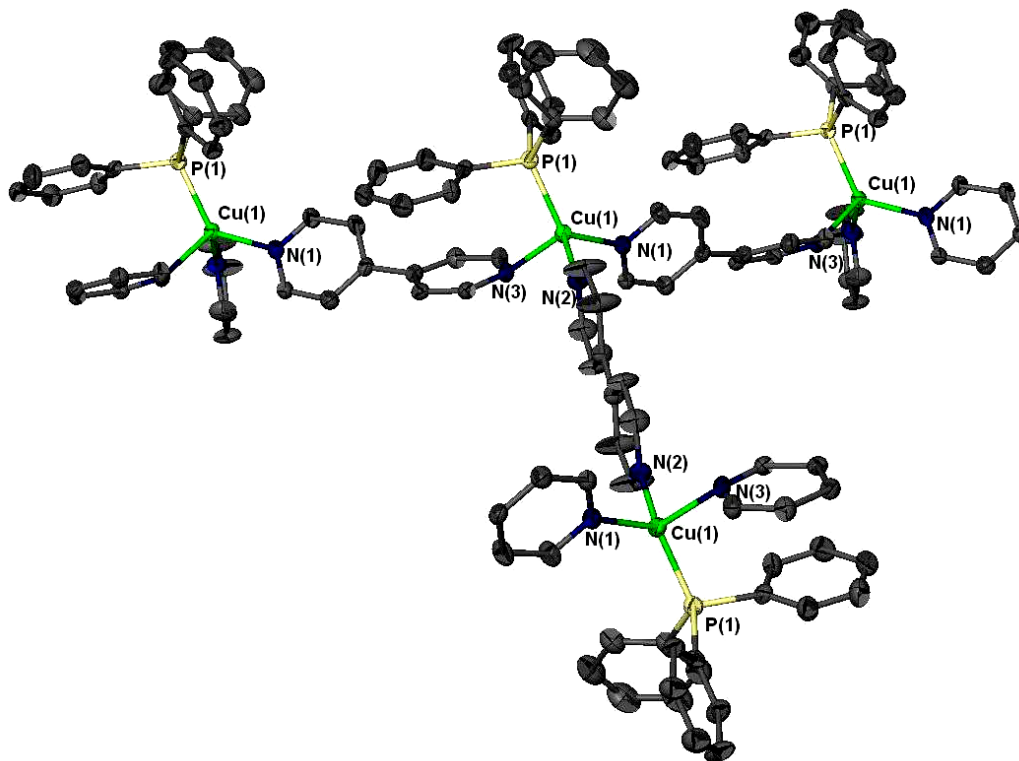
amount of THF in the reaction solvent used to make **8** while only  $\text{CHCl}_3$  was used in the synthesis **11**.

**Table 3.12** Selected Bond Lengths and Angles for Structures **4**, **8**, and **11**.

Hexagon Layered ( $\text{ClO}_4^-$ )	Structure		<b>8</b>			
	Cu center	Cu(1)	Cu(2)	Cu(3)	Cu(3)	
	Cu – P	2.187(2) Å	2.193(2) Å	2.180(2) Å		
	Cu – N	2.070(5) Å	2.086(5) Å	2.075(6) Å		
	Cu – N	2.074(5) Å	2.096(5) Å	2.069(6) Å		
	Cu – N	2.104(5) Å	2.069(5) Å	2.054(5) Å		
	P – Cu – N	98.9(2)°	120.2(2)°	115.1(2)°		
	P – Cu – N	114.1(2)°	117.8(2)°	118.7(2)°		
	P – Cu – N	120.6(2)°	115.5(2)°	119.7(2)°		
	N – Cu – N	98.4(2)°	98.8(2)°	98.1(2)°		
	N – Cu – N	98.9(2)°	96.1(2)°	101.2(2)°		
	N – Cu – N	102.5(2)°	104.4(2)°	100.3(2)°		
Hexagon Layered ( $\text{HSO}_4^-$ )	Structure		<b>11</b>			
	Cu center	Cu(1)	Cu(2)	Cu(3)	Cu(4)	
	Cu – P	2.188(4) Å	2.202(4) Å	2.209(4) Å	2.190(4) Å	
	Cu – N	2.03(1) Å	2.090(9) Å	2.11(1) Å	2.07(1) Å	
	Cu – N	2.08(1) Å	2.09(1) Å	2.094(8) Å	2.04(1) Å	
	Cu – N	2.04(1) Å	2.093(7) Å	2.09(1) Å	2.02(1) Å	
	P – Cu – N	117.5(3)°	116.3(3)°	113.8(3)°	119.2(3)°	
	P – Cu – N	117.6(3)°	114.3(3)°	117.2(3)°	117.6(3)°	
	P – Cu – N	114.2(3)°	116.2(3)°	117.5(3)°	113.6(3)°	
	N – Cu – N	101.8(4)°	101.4(4)°	102.2(4)°	102.3(4)°	
	N – Cu – N	102.7(4)°	102.3(4)°	101.4(4)°	101.9(4)°	
N – Cu – N	100.4(4)°	104.3(4)°	102.4(4)°	99.5(4)°		
Hexagonal Interpenetrated	Structure		<b>4</b>			
	Cu – P		2.189(2) Å			
	Cu – N		2.051(6) Å			
	Cu – N		2.031(6) Å			
	Cu – N		2.141(6) Å			
	P – Cu – N		121.4(2)°			
	P – Cu – N		123.2(2)°			
	P – Cu – N		102.8(2)°			
	N – Cu – N		102.5(3)°			
	N – Cu – N		101.5(3)°			
	N – Cu – N		101.6(2)°			

Finally, as we look at the interpenetrated hexagon layered solid, **4**, produced from the  $\text{CHCl}_3$ :toluene reaction solvent mixture, it is easy to see the dramatic distortion on one of the bipy ligands. From the data, the coordination bonding about the Cu center appears to be more symmetrical than both the ladder structure and the fused pentagon layers. However, visual inspection of this bent bipy ligand is undeniable and close

inspection reveals that the bpy ligand's Cu – L bond is bent at the nitrogen atom at a 143° angle. Figure 3.12 shows how, since there is only one single tetrahedron in the asymmetric unit of **4**, this ligand bowing affects two bpy positions on every tetrahedra



**Figure 3.12** Four tetrahedra shown in 50% thermal ellipsoids as they are bridged together in **4**. The extreme bowing of a bpy ligand Cu – L bond at N(3), while the N(2) – N(2) bpy ligand is relatively planar. The hydrogens, toluene molecules, and anion are omitted.

in the entire extended structure. The third position is occupied by a bpy ligand that is relatively straight as it bridges between the two copper atoms. As was pointed out in Chapter 1, this extreme L – Cu bond bending has been attributed to the  $\pi - \pi$  stacking between the bpy ligands and the aromatic toluene included in the structure.

## 3.7 Conclusion

In this chapter we have shown how subtle changes in either the anion or solvent used in the self-assembly of Cu(I) coordination solids have profound effects on the geometry of the resulting structure. Our studies of reactions performed in CHCl<sub>3</sub>:THF and CHCl<sub>3</sub>:toluene solvent mixtures have shown that there is not just a structural dependence on either the type of anion or solvent used, as was previously proposed, but a more complicated issue that involves both of these variables simultaneously in order to bring about these polymorphic networks. An isolated solvent-mediated reconstructive transformation event that is restricted to a particular anion, solvent, and structural isomer reinforces the anion-solvent-structure relationship. At the same time, the total structural invariance of a reaction, solely based on one particular anion indicates there is indeed a definite relationship going on between the anion and the reaction's self-assembly process. It appears, from the evidence presented, that there must be some sort of close relationship or interaction going on between the anion, solvent, and the copper center during the self-assembly process. In the next two chapters that follow, we will attempt to answer the questions as we further explore those particular relationships and interactions.

## References

1. (a) Vaccari, A.; *App. Clay Sci.* **1999**, *14*, 161. (b) Ball, P. *Made to Measure: New Materials for the 21st Century*, Princeton University Press, Princeton, 1997. (c) Lehn, J. -M.; *Acc. Chem. Res.* **1978**, *11*, 16. (d) Bruce, D. W.; O'Hare, D.; *Inorganic Materials*, John Wiley and Sons Ltd, West Sussex, 1992.
2. Lopez, S. *Ph.D. Thesis*, University of Missouri-Columbia, **2000**.
3. Barron, P. F.; Dyason, J. C.; Engelhardt, L. M.; Healy, P. C.; White, A. H. *Aust. J. Chem.* **1985**, *38*, 261.
4. Diez, J.; Falagan, S.; Gamasa, P.; Gimeno, J. *Polyhedron* **1988**, *7*, 37.
5. Green, J.; Sinn, E.; Woodward, S. *Polyhedron* **1993**, *12*, 991.
6. Leiva, A. M.; Rivera, L.; Loeb, B. *Polyhedron*, **1991**, *10*, 347.
7. Lopez, S.; Keller, S. W. *J. Am. Chem. Soc.* **1999**, *121*, 6306-6307.
8. A few examples. (a) Bu, X. -H.; Chen, W.; Hou, W. -F.; Du, M.; Zhang, R. -H.; Brisse, F. *Inorg. Chem.* **2002**, *41*, 3477-3482. (b) Blake, A. J.; Brooks, N. R.; Champness, N. R. Crew, M.; Deveson, A.; Fenske, D.; Gregory, D. H.; Hanton, L. R.; Hubberstey, P.; Schroder, M. *Chem. Commun.* **2001**, 1432-1433. (c) Lopez, S.; Keller, S. W. *Cryst. Engin.* **1999**, 101-114. Lopez, S.; Keller, S. W. *Inorg. Chem.* **1999**, *38*, 1883-1888. (d) Withersby, M. A.; Blake, A. J.; Champness, N. R.; Hubberstey, P.; Li, W. -S.; Schroder, M. *Angew. Chem. Int. Ed. Engl.* **1997**, *36*, No. 21, 2327-2329.
9. (a) Withersby M. A.; Blake, A. J.; Champness, N. R.; Cooke, P. A. Hubberstey, P.; Li, W. -S.; Schroder, M. *Inorg. Chem.* **1999**, *38*, 2259-2266. (b) Jung, O. -S.; Kim, Y. J.; Lee, Y. -A.; Park, K. -M.; Lee, S. S. *Inorg. Chem.* **2003**, *42*, 844-850. (c) Hannon, M. J.; Painting, C. L.; Plummer, E. A.; Childs, L. J.; Alcock, N. W. *Chem. Eur. J.* **2002**, *8*, (10) 2225-2238.
10. (a) Liesegang, R. E.; *Zeitschrift für Physikalische Chemie*, **1911**, *75*, 374. (b) Ostwald, W.; *Lehrbuch der Allgemeinen Chemie*, vol. 2, pg 444, Englemann, Leipzig, 1896. (c) Boistelle, R.; Astier, J.P.; *J Cryst. Growth* **1988**, *90*: 14.
11. Mullin, J. W.; *Crystallization*, 3<sup>rd</sup> ed. Butterworth-Heinemann Ltd., Oxford, 1993.
12. Ostwald, W.; *Zeitschrift für Physikalische Chemie* **1897**, *22*, 289.

13. Davey, R.; Garside, J.; *From Molecules to Crystallizers: An Introduction to Crystallization*, Oxford University Press, Oxford, 2000.
14. Mullin, J. W.; Teodossiev, N.; Söhnel, O.; *Chem. Engi. Proc.* **1989**, 26, 93.
15. (a) Wang, S. -L.; Lin, S. -Y.; Wei, Y. -S.; *Chem. & Pharm. Bul.* **2002**, 50, 153. (b) Elbary, A.; Nafadi, M. M.; El-Khateeb, M. A.; *Egyp. J. Pharm. Sci.* **2000**, 40, 49. (c) Maruyama, S.; Ooshima, H.; *Chem. Eng. J.* **2001**, 81, 1. (d) Otsuka, M.; Hasegawa, H.; Matsuda, Y.; *Chem. & Pharm. Bul.*, **1997**, 45, 894. (e) Kaneniwa, N.; Ichikawa, J.; Matsumoto, T.; *Chem. & Pharm. Bul.* **1988**, 36, 1063. (f) Pavtova, A. V.; *Pharmazie* **1984**, 39, 272. Chidambareswaran, P. K.; Sreenivasan, S.; Patil, N. B.; Lokhande, H. T.; *J. Appl. Poly. Sci.* **1882**, 27, 709.
16. G. M. Sheldrick, *SHELXS-90, program for Structure Solution*; University of Gottingen: Germany, **1991**.
17. (a) G. M. Sheldrick, *SHELXL-90, program for Structure Refinement*; University of Gottingen: Germany, **1991**. (b) L. Barbour, X-SEED, *Graphical Interface for SHEL-X*; University of Columbia, MO, **2000**.

## ANION AND SOLVENT INTERACTIONS

### 4.1 Introduction

The structural variations (or lack of the same) of the final products obtained from the synthesis of coordination polymers that we as well as others have observed indicate that there must be some influence that solvent or anion have over the self-assembly of the Cu(I) coordination networks.<sup>1,2</sup> Specifically, the results from the reaction of the  $[\text{Cu}(\text{MeCN})_2(\text{PPh}_3)_2]\text{X}$  salt with 4,4'-bipyridine we presented in the previous chapter suggests that there is a strong connection between the variations in the polymeric Cu(I) coordination networks formed and the type of anion and/or solvent used in the reaction. To better understand these influences, the effects that dissolution and recrystallization of a Cu(I) starting material,  $[\text{Cu}(\text{MeCN})_2(\text{PPh}_3)_2]\text{X}$  for  $\text{X} = \text{BF}_4^-$ ,  $\text{PF}_6^-$ ,  $\text{ClO}_4^-$ ,  $\text{CF}_3\text{SO}_3^-$ , and  $\text{HSO}_4^-$  in the solvents of  $\text{CHCl}_3$ , THF, and toluene were studied.

There are numerous examples of triflate-coordinated compounds with many being used as adducts in the formation of more complex compounds.<sup>3</sup> There has been no report however, on either the Cu(I) salt or the two neutral triflate coordinated solids. Although those salts of the  $\text{BF}_4^-$ ,  $\text{PF}_6^-$ , and  $\text{ClO}_4^-$  anion have previously studied,<sup>4</sup> no study has been mentioned of these compounds as they are recrystallized from various solvents. Neither is there any existing report on both the Cu(I) salt of  $\text{HSO}_4^-$  and the compounds resulting from any dissolution/crystallization reaction. This chapter examines these starting

materials and the resulting new compounds produced from the recrystallization reactions as characterized by both single crystal X-ray diffraction and thermogravimetric analysis.

## 4.2 Experimental

### 4.2.1 General Methods

Cu<sub>2</sub>O, HPF<sub>6</sub>, HBF<sub>4</sub>, HClO<sub>4</sub>, H<sub>2</sub>SO<sub>4</sub> (ACROS); acetonitrile, tetrahydrofuran, toluene, chloroform, dichloromethane, and diethyl ether (Fisher); triflic acid and triphenylphosphine (Aldrich), were used without further purification. All the [Cu(MeCN)<sub>2</sub>(PPh<sub>3</sub>)<sub>2</sub>]X salts for X = BF<sub>4</sub><sup>-</sup>, PF<sub>6</sub><sup>-</sup>, ClO<sub>4</sub><sup>-</sup>, CF<sub>3</sub>SO<sub>3</sub><sup>-</sup>, HSO<sub>4</sub><sup>-</sup>, were prepared as previously reported and described in Chapter 2.<sup>5,6</sup> For the reactions with the copper salt containing the HSO<sub>4</sub><sup>-</sup> anion, the THF used was dried first dried by refluxing (under nitrogen) a solution of THF with sodium metal and a benzophenone indicator for several hours until a dark purple solution is obtained. The dry THF is then isolated by distillation, placed into a clean, dry flask (still under nitrogen) and sealed for usage later.

### 4.2.2 Synthesis

#### *[Cu(MeCN)<sub>2</sub>(PPh<sub>3</sub>)<sub>2</sub>](CF<sub>3</sub>SO<sub>3</sub>), **12***

Initially, **12** was prepared by combining [Cu(MeCN)<sub>4</sub>](CF<sub>3</sub>SO<sub>3</sub>) with 2 equivalents of triphenylphosphine (PPh<sub>3</sub>) in dichloromethane.<sup>6</sup> Addition of diethyl ether (Et<sub>2</sub>O), produced a white polycrystalline precipitate which was collected via filtration, washed with small aliquots of Et<sub>2</sub>O, and dried under vacuum. To obtain single crystals suitable for X-ray diffraction, in a 4 mL vial 30 mg of **12** was dissolved in 2 mL of MeCN. This vial was then placed inside a 20 mL, screw top vial containing 5 mL of ethyl ether. The

large vial was sealed and the Et<sub>2</sub>O slowly diffused into the MeCN solution. After 24 hours, colorless, columnar crystals of **12** were harvested from the smaller vial.

*Cu(THF)(PPh<sub>3</sub>)<sub>2</sub>(CF<sub>3</sub>SO<sub>3</sub>), 13*

In a 20 mL vial, 90 mg of **12** was dissolved in 8 mL of THF and the vial was sealed with a screw-top lid. Crystal growth is observed after only 5 minutes, and colorless, prismatic crystals of **13** were harvested after 24 hours.

*Cu(MeCN)(PPh<sub>3</sub>)<sub>2</sub>(CF<sub>3</sub>SO<sub>3</sub>), 14*

In a 20 mL vial, 90 mg of **12** was dissolved in 8 mL of toluene and the vial was sealed with a screw-top lid. As was with the synthesis of **13**, crystals began to appear almost immediately and colorless, prismatic crystals of **14** were harvested after 24 hours.

*Cu(MeCN)(PPh<sub>3</sub>)<sub>2</sub>(CF<sub>3</sub>SO<sub>3</sub>), 15*

In a 20 mL vial, 90 mg of **12** was dissolved in 8 mL of CHCl<sub>3</sub>. This vial was then placed inside a larger (250 mL) glass container containing 10 mL of ethyl ether. The large vial was sealed and the Et<sub>2</sub>O slowly diffused into the MeCN solution. After 24 hours, colorless, prismatic crystals of **15** were harvested from the smaller vial.

*[Cu<sub>2</sub>(ClO<sub>4</sub>)(MeCN)(PPh<sub>3</sub>)<sub>4</sub>(THF)](ClO<sub>4</sub>), 16*

*Note: perchlorate salts are VERY strong oxidizers and potentially explosive. They should be handled with great care and always in small quantities.* In a 20 mL vial, 20 mg of [Cu(MeCN)<sub>2</sub>(PPh<sub>3</sub>)<sub>2</sub>](ClO<sub>4</sub>) was dissolved in 5 mL of THF and the vial was placed in



a 250 mL glass jar containing 5 mL of Et<sub>2</sub>O. The glass jar was sealed and the Et<sub>2</sub>O slowly diffused into the THF solution. After 24 hours, colorless, prismatic crystals of **16** were harvested from the smaller vial.

*[Cu(MeCN)<sub>2</sub>(PPh<sub>3</sub>)<sub>2</sub>](HSO<sub>4</sub>), **17***

Initially, **17** was prepared by combining [Cu(MeCN)<sub>4</sub>](HSO<sub>4</sub>) with 2 equivalents of triphenylphosphine (PPh<sub>3</sub>) in dichloromethane.<sup>6</sup> Addition of diethyl ether (Et<sub>2</sub>O), produced a white polycrystalline precipitate which was collected via filtration, washed with small aliquots of Et<sub>2</sub>O, and dried under vacuum. To obtain single crystals suitable for X-ray diffraction, in a 1-dram vial 30 mg of **17** was dissolved in 2 mL of MeCN. This vial was then placed inside a 20 mL, screw top vial containing 5 mL of ethyl ether. The large vial was sealed and the Et<sub>2</sub>O slowly diffused into the MeCN solution. After 24 hours, colorless, columnar crystals of **17** were harvested from the smaller vial.

*Cu(H<sub>2</sub>O)(PPh<sub>3</sub>)<sub>2</sub>(HSO<sub>4</sub>)·2THF, **18***

In a 20 mL vial, 100 mg of **17** was dissolved in 8 mL of THF and the vial was sealed with a screw-top lid. Slight crystal growth is observed after several minutes and colorless, prismatic crystals of **18** were harvested after 24 hours.

*Cu(MeCN)(PPh<sub>3</sub>)<sub>2</sub>(HSO<sub>4</sub>)·THF, **19***

In a 20 mL vial, 100 mg of **17** was dissolved in 8 mL of THF (with all water removed by the method described above) and the vial was sealed with a screw-top lid.

Slight crystal growth is observed after only 5 minutes, and colorless, prismatic crystals of **19** were harvested after 24 hours.

#### *Cu<sub>2</sub>(MeCN)(PPh<sub>3</sub>)<sub>4</sub>(HSO<sub>4</sub>)<sub>2</sub>, **20***

In a 4 mL vial, 20 mg of **17** was dissolved in 2 mL of THF. This vial was then placed inside a 20 mL, screw top vial containing 5 mL of ethyl ether. The large vial was sealed and the Et<sub>2</sub>O slowly diffused into the MeCN solution. After 24 hours, colorless, prismatic crystals of **20** were harvested from the smaller vial.

#### *4.2.3 Single Crystal X-Ray Diffraction*

In all cases, a single crystal of high quality (by uniform extinction of polarized light) was coated with light oil and then mounted on a tip of a glass fiber using small amount of silicon grease for adhesion. Crystallographic data was collected using a Siemens SMART system with a CCD area detector (Mo K<sub>α</sub> = 0.71070 Å).<sup>7</sup> During data collection, the crystals were cooled to 173 K. The initial space group was determined by indexing several hundred strong reflections and the structures were solved using Direct Methods.<sup>8</sup> The structure models were further refined using least-squares techniques.<sup>9</sup> Details of the data collection and structure solutions are given in Table 4.1 and 4.2.

For each structure, the majority of the heavier atoms were located with the initial solution. One phenyl-ring carbon atom and one triflate oxygen atom in **13** were located after the first least-squares refinement. Anisotropic thermal parameters were refined for all non-hydrogen atoms and the riding hydrogen atoms were included in calculated positions on the phenyl rings of the triphenylphosphine ligands and on the methyl carbon atoms of the acetonitrile ligands. There were a several different types of disorder that

were modeled in structure **16**. Firstly, the chlorine atoms of two of the perchlorate anions, Cl(2) and Cl(3), are located on two-fold axes, with the former also having one of its oxygen atoms, O(7) on the 2-fold axis. The other oxygen atoms on Cl(2) were modeled with a 180 rotational disorder with 50% occupancy at each orientation. While the Cl(1) perchlorate was present in full occupancy; this anion had the oxygen atoms disordered over three positions about the chloride atom center. The non-coordinated Cl(3) perchlorate exhibits high anisotropic thermal parameters, most likely brought on by the non-symmetric vibrational motion.

Secondly, the number of peaks having significant electron density near the both copper centers in **16** indicated that *both* MeCN and THF were coordinated to the same site of *both* Cu(1) and Cu(2). The final structure was modeled with both ligands in place as overlapping moieties with the THF and MeCN occupancies being ~ 80 and 20 %, respectively on Cu(1) and ~20 and 80 %, respectively on Cu(2); the atoms making up the overlapping MeCN and THF ligands were refined isotropically.

#### *4.2.4 Thermogravimetric Analysis*

All thermal analyses were performed using a TA Instruments TGA Q50 analyzer with a heating rate of 0.1 °C/min in a flowing nitrogen atmosphere.

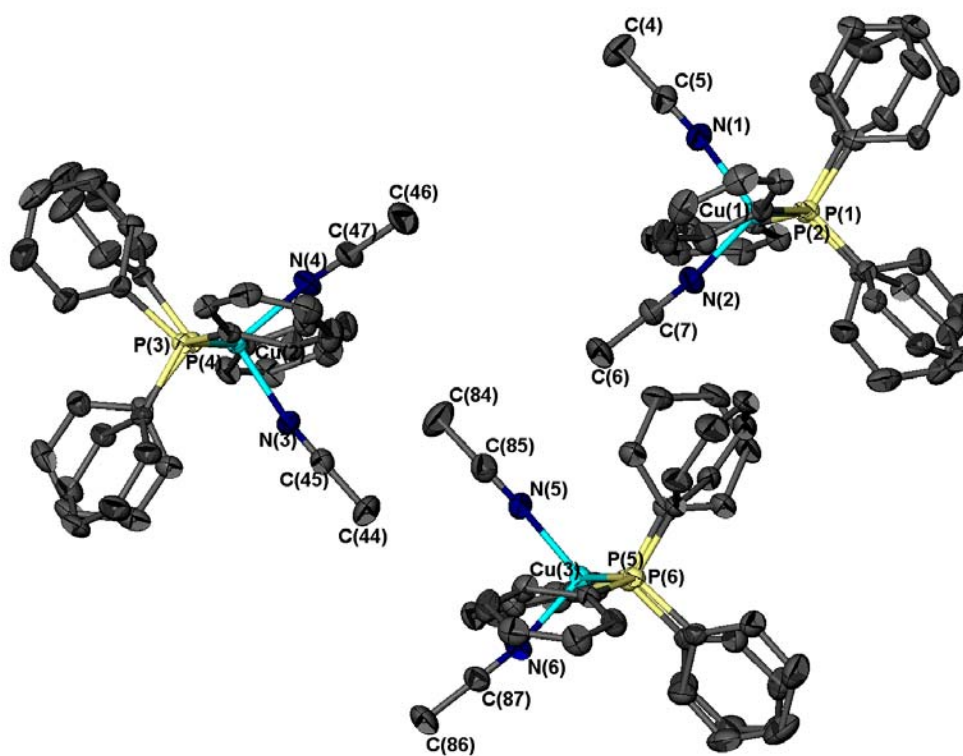
<b>Table 4.1 Crystallographic Details for 12 – 16</b>					
	<b>12</b>	<b>13</b>	<b>14</b>	<b>15</b>	<b>16</b>
Empirical formula	CuC <sub>41</sub> H <sub>36</sub> N <sub>2</sub> O <sub>3</sub> F <sub>3</sub> P <sub>2</sub> S	CuC <sub>41</sub> H <sub>38</sub> N <sub>2</sub> O <sub>4</sub> F <sub>3</sub> P <sub>2</sub> S	CuC <sub>39</sub> H <sub>33</sub> NO <sub>3</sub> F <sub>3</sub> P <sub>2</sub> S	CuC <sub>39</sub> H <sub>33</sub> NO <sub>3</sub> F <sub>3</sub> P <sub>2</sub> S	Cu <sub>2</sub> C <sub>78</sub> H <sub>71</sub> NO <sub>9</sub> Cl <sub>2</sub> P <sub>4</sub>
Formula weight (g·mol <sup>-1</sup> )	819.30	809.25	778.25	778.25	744.16
Temperature, K	173(2)	173(2)	173(2)	173(2)	173(2)
Space group	P2 <sub>1</sub> /c	Pca2 <sub>1</sub>	Pca2 <sub>1</sub>	C2/c	C2/c
Unit cell dimensions					
<i>a</i> (Å)	23.249(2)	22.533(1)	22.434(1)	18.3530(7)	27.308(1)
<i>b</i> (Å)	26.665(1)	9.0688(5)	8.9789(5)	19.8781(8)	28.064(1)
<i>c</i> (Å)	19.4201(9)	18.4689(9)	18.418(1)	21.1968(9)	21.448(1)
$\alpha$ , deg	90	90	90	90	90
$\beta$ , deg	102.614(1)	90	90	108.467(1)	120.342(1)
$\gamma$ , deg	90	90	90	90	90
<i>Z</i>	12	4	4	8	8
Volume, Å <sup>3</sup>	11748(2)	3774.1(3)	3710.0(4)	7334.9(5)	14185(2)
$\rho_{\text{calc}}$ , g·cm <sup>-3</sup>	1.3894	1.4241	1.3931	1.3409	1.392
Absorption coefficient, mm <sup>-1</sup>	0.747	0.775	0.784	0.793	0.842
F(000)	5064	1672	1600	3200	6156
Crystal size, mm	0.5 x 0.4 x 0.3	0.5 x 0.4 x 0.3	0.4 x 0.4 x 0.3	0.4 x 0.4 x 0.3	0.5 x 0.4 x 0.4
$\theta$ Range for data collection	1.46 to 27.10	1.81 to 20.81	1.82 to 27.15	1.44 to 16.52	1.45 to 27.11
Index ranges	-29 ≤ <i>h</i> ≤ 15 -34 ≤ <i>k</i> ≤ 33 -24 ≤ <i>l</i> ≤ 24	-21 ≤ <i>h</i> ≤ 22 -5 ≤ <i>k</i> ≤ 9 -18 ≤ <i>l</i> ≤ 18	-28 ≤ <i>h</i> ≤ 15 -11 ≤ <i>k</i> ≤ 11 -22 ≤ <i>l</i> ≤ 23	-14 ≤ <i>h</i> ≤ 14 -12 ≤ <i>k</i> ≤ 15 -16 ≤ <i>l</i> ≤ 16	-34 ≤ <i>h</i> ≤ 34 -35 ≤ <i>k</i> ≤ 32 -26 ≤ <i>l</i> ≤ 27
Reflections collected	72520	12647	22187	15005	44264
Unique reflections	25609 [R <sub>int</sub> = 0.0358]	3945 [R <sub>int</sub> = 0.0303]	8009 [R <sub>int</sub> = 0.0299]	3930 [R <sub>int</sub> = 0.0346]	15573 [R <sub>int</sub> = 0.0681]
Completeness to $\theta$	27.10 (98.7 %)	20.81 (100.0 %)	27.15 (99.7 %)	16.52 (100.0 %)	27.11 (99.6 %)
Max/min transmissions	1.00000/ 0.779765	0.928052/ 0.718772	1.00000/ 0.808055	1.00000/ 0.71912	1.00000/ 0.77687
Data/restraints/parameters	25609/0/1438	3945/1/469	8009/1/452	3930/0/903	15573/0/922
Goodness of fit F <sup>2</sup>	1.036	1.034	0.998	1.029	0.983
Final R indices [ <i>I</i> > 2 $\sigma$ ( <i>I</i> )] <sup>a,b</sup>	R <sub>1</sub> = 0.0584 wR <sub>2</sub> = 0.1578	R <sub>1</sub> = 0.0227 wR <sub>2</sub> = 0.0546	R <sub>1</sub> = 0.0299 wR <sub>2</sub> = 0.0665	R <sub>1</sub> = 0.0326 wR <sub>2</sub> = 0.0744	R <sub>1</sub> = 0.0699 wR <sub>2</sub> = 0.1662
R indices (all data)	R <sub>1</sub> = 0.0939 wR <sub>2</sub> = 0.1795	R <sub>1</sub> = 0.0249 wR <sub>2</sub> = 0.0556	R <sub>1</sub> = 0.0363 wR <sub>2</sub> = 0.0688	R <sub>1</sub> = 0.0444 wR <sub>2</sub> = 0.0804	R <sub>1</sub> = 0.1443 wR <sub>2</sub> = 0.2061
Largest difference peak and hole (e·Å <sup>-3</sup> )	1.80/-1.20	0.30/-0.14	0.36/-0.22	0.718/-0.336	1.408/-0.688
Structures were refined on F <sup>2</sup> for all data. <sup>a</sup> R(F <sub>o</sub> ) = $\sum   F_o  -  F_c   / \sum  F_o $ . <sup>b</sup> R <sub>w</sub> (F <sub>o</sub> ) = $(\sum w  F_o  -  F_c  ^2 / \sum  F_o ^2)^{1/2}$ , w = $[\sigma^2(F_o) + (0.002F_o)^2]^{-1}$ .					

<b>Table 4.2 Crystallographic Details for 17 – 20</b>				
	<b>17</b>	<b>18</b>	<b>19</b>	<b>20</b>
Empirical formula	CuC <sub>40</sub> H <sub>37</sub> N <sub>2</sub> O <sub>4</sub> P <sub>2</sub> S	CuC <sub>44</sub> H <sub>49</sub> O <sub>7</sub> P <sub>2</sub> S	CuC <sub>42</sub> H <sub>42</sub> NO <sub>5</sub> P <sub>2</sub> S	Cu <sub>2</sub> C <sub>74</sub> H <sub>65</sub> NO <sub>8</sub> P <sub>4</sub> S <sub>2</sub>
Formula weight (g·mol <sup>-1</sup> )	767.26	847.37	798.31	1411.34
Temperature, K	173(2)	173(2)	173(2)	173(2)
Crystal System, Space group	Monoclinic, P2 <sub>1</sub> /n	Triclinic, P-1	Triclinic, P1	Triclinic, P-1
Unit cell dimensions				
<i>a</i> (Å)	8.9236(4)	12.561(1)	22.321(2)	12.503(1)
<i>b</i> (Å)	16.4211(7)	13.380(2)	22.698(2)	13.022(1)
<i>c</i> (Å)	25.591(1)	13.697(2)	24.814(2)	23.975(2)
$\alpha$ , deg	90	111.204(2)	81.996(2)	92.374(2)
$\beta$ , deg	90.993(1)	101.202(2)	70.365(2)	103.913(2)
$\gamma$ , deg	90	93.097(2)	80.508(2)	116.786(1)
<i>Z</i>	4	2	12	4
Volume, Å <sup>3</sup>	3749.4(3)	2085.9(4)	11631(2)	3331.5(5)
$\rho_{\text{calc}}$ , g·cm <sup>-3</sup>	1.359	1.349	1.368	1.407
Absorption coefficient, mm <sup>-1</sup>	1.359	0.700	0.745	0.855
F(000)	1592	888	4992	1460
Crystal size, mm	0.5 x 0.3 x 0.05	0.4 x 0.3 x 0.3	0.4 x 0.3 x 0.2	0.5 x 0.3 x 0.3
$\theta$ Range for data collection	1.47 to 27.15	1.64 to 27.15	0.87 to 27.20	0.89 to 27.14
Index ranges	-11 ≤ <i>h</i> ≤ 11 -21 ≤ <i>k</i> ≤ 21 -32 ≤ <i>l</i> ≤ 32	-16 ≤ <i>h</i> ≤ 16 -16 ≤ <i>k</i> ≤ 17 -17 ≤ <i>l</i> ≤ 17	-28 ≤ <i>h</i> ≤ 28 -28 ≤ <i>k</i> ≤ 36 -31 ≤ <i>l</i> ≤ 31	-15 ≤ <i>h</i> ≤ 16 -16 ≤ <i>k</i> ≤ 16 -29 ≤ <i>l</i> ≤ 30
Reflections collected	32478	17916	102574	29191
Unique reflections	8277 [R <sub>int</sub> = 0.0376]	8992 [R <sub>int</sub> = 0.0221]	50615 [R <sub>int</sub> = 0.0665]	14430 [R <sub>int</sub> = 0.0445]
Completeness to $\theta$	27.15 (99.7 %)	27.15 (97.2 %)	27.20 (97.7 %)	27.14 (97.7 %)
Max/min transmissions	1.00000/ 0.746015	1.00000/ 0.818848	1.00000/0.813243	1.00000/ 0.735671
Data/restraints/ parameters	8277/0/454	8992/0/508	50615 /0/2821	14430/0/823
Goodness of fit F <sup>2</sup>	1.023	1.009	1.000	1.029
Final R indices [I > 2 $\sigma$ (I)] <sup>a,b</sup>	R <sub>1</sub> = 0.0362 wR <sub>2</sub> = 0.0943	R <sub>1</sub> = 0.0482 wR <sub>2</sub> = 0.1312	R <sub>1</sub> = 0.0786 wR <sub>2</sub> = 0.1659	R <sub>1</sub> = 0.0537 wR <sub>2</sub> = 0.1124
R indices (all data)	R <sub>1</sub> = 0.0520 wR <sub>2</sub> = 0.1001	R <sub>1</sub> = 0.0573 wR <sub>2</sub> = 0.1387	R <sub>1</sub> = 0.1697 wR <sub>2</sub> = 0.2020	R <sub>1</sub> = 0.0941 wR <sub>2</sub> = 0.1286
Largest difference peak and hole (e·Å <sup>-3</sup> )	0.716/-0.330	1.282/-0.783	0.883/-0.709	0.752/ -0.407
Structures were refined on F <sup>2</sup> for all data. <sup>a</sup> R(F <sub>o</sub> ) = $\sum   F_o  -  F_c   / \sum  F_o $ . <sup>b</sup> R <sub>w</sub> (F <sub>o</sub> ) = $(\sum w  F_o  -  F_c  ^2 / \sum  F_o ^2)^{1/2}$ , w = $1/\sigma^2(F_o) + (0.002F_o)^2$ .				

## 4.3 Results and Discussion

### 4.3.1 The Triflate Starting Material

Recrystallization of  $[\text{Cu}(\text{MeCN})_2(\text{PPh}_3)_2]\text{X}$  ( $\text{X} = \text{BF}_4^-$  and  $\text{PF}_6^-$ ) in  $\text{CHCl}_3$ , THF, or toluene did exactly that; the structures and composition of the complexes remained unchanged and identical to those previously reported.<sup>4</sup> The three independent Cu(I) complexes comprising the unit cell of the *triflate* salt  $[\text{Cu}(\text{MeCN})_2(\text{PPh}_3)_2]\text{CF}_3\text{SO}_3$ , **12**, are shown in Figure 4.1. Although the packing of **12** was essentially isostructural with  $[\text{Cu}(\text{MeCN})_2(\text{PPh}_3)_2]\text{X}$  for ( $\text{X} = \text{PF}_6^-$ ,  $\text{BF}_4^-$ , or  $\text{ClO}_4^-$ ),<sup>4</sup> the previously reported unit cells contain only a single Cu(I) unit. This type of packing arrangement was also found with the  $[\text{Cu}(\text{MeCN})_4]\text{X}$  system (for  $\text{X} = \text{CF}_3\text{SO}_3^-$ ,<sup>5</sup>  $\text{BF}_4^-$ ,<sup>10</sup>  $\text{ClO}_4^-$ ,<sup>11</sup> and  $\text{PF}_6^-$ ,<sup>12</sup>) and was



**Figure 4.1:** The three cation coordination spheres that comprise the asymmetric unit in **12** showing the eclipse conformation of the  $\text{PPh}_3$  ligands. Hydrogen atoms have been omitted and all other atoms are represented as 50% ellipsoids.

attributed to the need to pack the tetrahedra in the most efficient way.

Table 4.3 compares the Cu–P and Cu–N bond lengths (and angles) for the three independent complexes in **12**. As with the other  $[\text{Cu}(\text{MeCN})_2(\text{PPh}_3)_2]^+$  compounds, the  $\text{P}_2\text{CuN}_2$  copper coordination sphere has considerable angular distortions due to the bulky phosphine ligands.<sup>4</sup> Only subtle differences in the bend of a MeCN ligand or the torsion angle of a  $\text{PPh}_3$  phenyl ring distinguish one complex from the others in the asymmetric unit. Both the acetonitrile ligands on Cu(1) and Cu(3) are slightly bent to the same side of the  $\text{CuN}_2$  plane of symmetry, whereas each acetonitrile coordinated to Cu(2) are bent onto opposing sides of the plane.

**Table 4.3.** Selected bond lengths (Å) and angles (deg) for **12**

<i>Complex A</i>		<i>Complex B</i>		<i>Complex C</i>	
Cu(1) – P(1)	2.290(1)	Cu(2) – P(3)	2.2727(9)	Cu(3) – P(5)	2.270(1)
Cu(1) – P(2)	2.272(1)	Cu(2) – P(4)	2.267(1)	Cu(3) – P(6)	2.278(1)
Cu(1) – N(1)	2.037(3)	Cu(2) – N(3)	2.031(3)	Cu(3) – N(5)	2.046(3)
Cu(1) – N(2)	2.074(3)	Cu(2) – N(4)	2.072(3)	Cu(3) – N(6)	2.036(3)
P(1) – Cu(1) – P(2)	124.05(4)	P(3) – Cu(2) – P(4)	122.46(4)	P(5) – Cu(3) – P(6)	123.07(4)
N(1) – Cu(1) – N(2)	96.2(1)	N(3) – Cu(2) – N(4)	99.4(1)	N(5) – Cu(3) – N(6)	97.8(1)
P(1) – Cu(1) – N(1)	106.1(1)	P(3) – Cu(2) – N(3)	110.09(9)	P(5) – Cu(3) – N(5)	109.8(1)
P(1) – Cu(1) – N(2)	102.1(1)	P(3) – Cu(2) – N(4)	109.8(1)	P(5) – Cu(3) – N(6)	106.3(1)
P(2) – Cu(1) – N(1)	115.72(9)	P(4) – Cu(2) – N(3)	110.0(1)	P(6) – Cu(3) – N(5)	106.9(1)
P(2) – Cu(1) – N(2)	108.24(9)	P(4) – Cu(2) – N(4)	102.4(1)	P(6) – Cu(3) – N(6)	110.1(1)

In contrast to the other  $[\text{P}_2\text{CuN}_2]\text{X}$  analogs however, the two  $\text{PPh}_3$  ligands coordinated to each copper in **12** adopt an eclipsed conformation with a three-blade propeller conformation of the same chirality for both ligands (as opposed to staggered

and of opposite chirality for the analog compounds).<sup>4</sup> This type of arrangement is also found in a number of *anion coordinated*  $\text{Cu}(\text{PPh}_3)_2\text{X}$  compounds.<sup>13</sup> The triflate anion in **12**, however, is not coordinated but rather is located in the cleft formed between the acetonitrile ligands and one of the  $\text{PPh}_3$  ligands (as are  $\text{PF}_6^-$ ,  $\text{BF}_4^-$ , and  $\text{ClO}_4^-$  in the analogs) with the closest anion to Cu(I) contact being  $\sim 4.6$  Å. The Cu–P distances of 2.267(1) – 2.290(1) Å and P–Cu–P angles about  $123^\circ$  are also quite comparable to the analogs which, along with the similar anion positioning, accounts for the basically identical packing arrangement with respect to the other three  $[\text{Cu}(\text{MeCN})_2(\text{PPh}_3)_2]\text{X}$  structures.

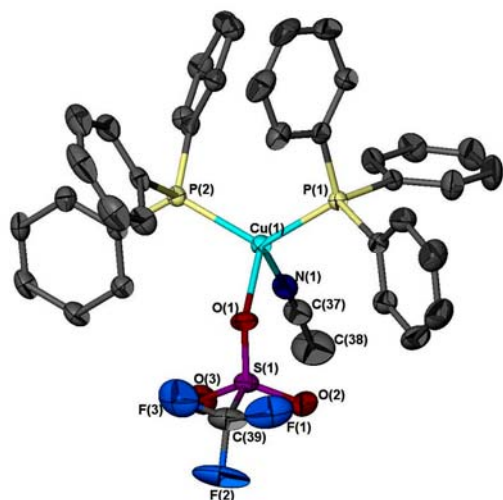
#### 4.3.2 Triflate and THF Coordination

Dissolution of **12** was rapid in MeCN, THF or toluene. Although recrystallization of **12** from MeCN required diffusion of ethyl ether vapor to promote crystal growth such treatment was not necessary for the other solvents. Soon after complete dissolution, and without the addition of another solvent, crystals began to appear in the vial. Specifically, crystals of two new, *neutral* Cu(I) species  $\text{Cu}(\text{THF})(\text{PPh}_3)_2(\text{CF}_3\text{SO}_3)$  **13**, and  $\text{Cu}(\text{MeCN})(\text{PPh}_3)_2(\text{CF}_3\text{SO}_3)$  **14**, from THF and toluene, respectively, became visible after only a few seconds. Each reaction produced a large collection of crystals with yields of 56% and 74%, respectively after 24 hours.

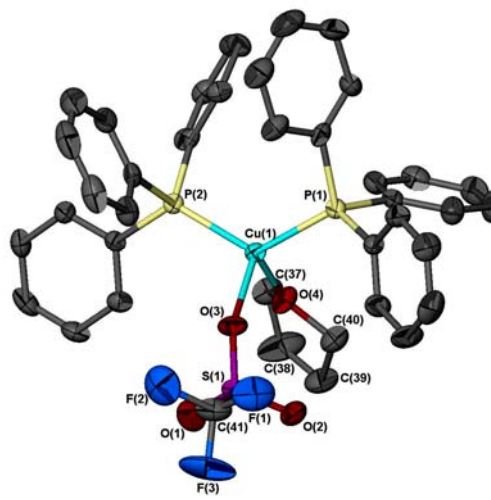
In both **13** and **14** anion coordination produced complexes clearly different from **12** but quite similar to each other as they share the same space group and identical packing motifs. They differ from each other only by a subtle increase in unit cell volume for **13**, likely due to the presence of the bulkier THF molecule. Unlike the starting material, **12**, the asymmetric unit of both of these structures consists of only a single Cu(I) tetrahedron.



There is considerably less distortion of the ligands outside of their plane of symmetry than was found in **12**. As shown in Fig. 4.2a, both the MeCN ligand and the coordinated triflate anion in **14** maintain positions directly on the N-Cu-O plane. This symmetry is somewhat lost for **13** (Fig. 4.2b) as the THF ligand is rotated by  $\sim 30^\circ$ .



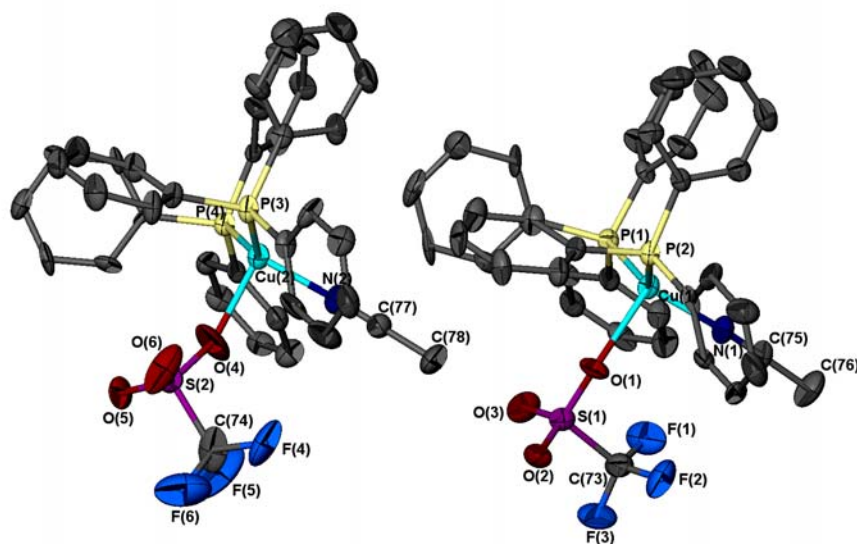
**Figure 4.2a**



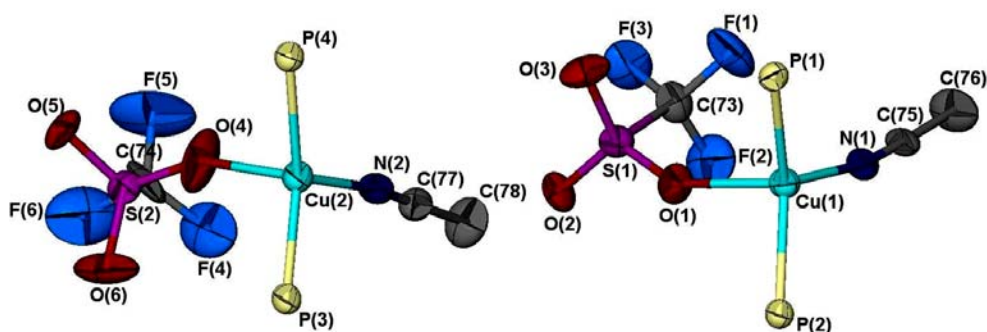
**Figure 4.2b**

**Figure 4.2:** Asymmetric units of the highly symmetric (a) **14** and somewhat less symmetric (b) **13** with the  $\sim 30^\circ$  rotated THF ligand. Both show the staggered conformation of the PPh<sub>3</sub> ligands. The hydrogen atoms have been omitted and the other atoms are represented as 50% thermal ellipsoids.

The final transformation of the triflate starting material as it is dissolved in CHCl<sub>3</sub> is presented by **15** shown in Figure 4.3a. Although **15** has the same formula as **14**, the asymmetric unit of **15** consists of two unique copper centers with each copper retaining one of the MeCN ligands while having a coordinated triflate anion. Along with this, subtle differences in the ligand arrangements set this molecule in its own unit cell. The most striking of these differences is how the triflate anion is directed inward toward the Cu center instead of outward as in **13** and **14**.



**Figure 4.3a**



**Figure 4.3b**

**Figure 4.3** (a) The two coordination spheres that comprise the asymmetric unit in **15**. (b) With the Phenyl groups removed, shifting of the triflate and MeCN ligands is shown for the two unique copper centers in **15**. Hydrogen atoms have been omitted and all other atoms are represented as 50% ellipsoids.

As shown in Figure 4.3b this is, for the most part, because of how both the triflate and MeCN ligands on Cu(1) are shifted to one side of the normal O – Cu – N plane of symmetry; while both ligands on Cu(2) are shifted to the other side. Interestingly, as the PPh<sub>3</sub> ligands in **12** took on an eclipsed conformation normally found in anion-coordinated species, **13**, **14**, and **15** have PPh<sub>3</sub> ligands that are *staggered* with respect to each other and adopt a three-blade propeller conformations with opposite chirality: as do the analog N<sub>2</sub>CuP<sub>2</sub> *salts*!

Bond distances and angles for **13** and **14** are summarized in Table 4.4 and the two complexes of **15** are summarized in Table 4.5. All values are within ranges expected for these types of complexes. The Cu–P distances around 2.24 Å are similar to those values found for other anion-coordinated Cu(PPh<sub>3</sub>)<sub>2</sub>X compounds.<sup>4, 13</sup> The Cu–N bond length of 2.012(2) Å in **14**, and 1.994(7) and 2.014(7) in **15** is slightly shorter than either of the Cu–N bonds in **12** and is indicative of relatively strong coordination of the acetonitrile ligand to the copper center. The ~2.2 Å Cu – O bonds of the triflate anion coordination found in all three complexes are a moderate example of a M–OSO<sub>2</sub>R

**Table 4.4** Selected bond lengths (Å) and angles (deg) for **13** & **14**

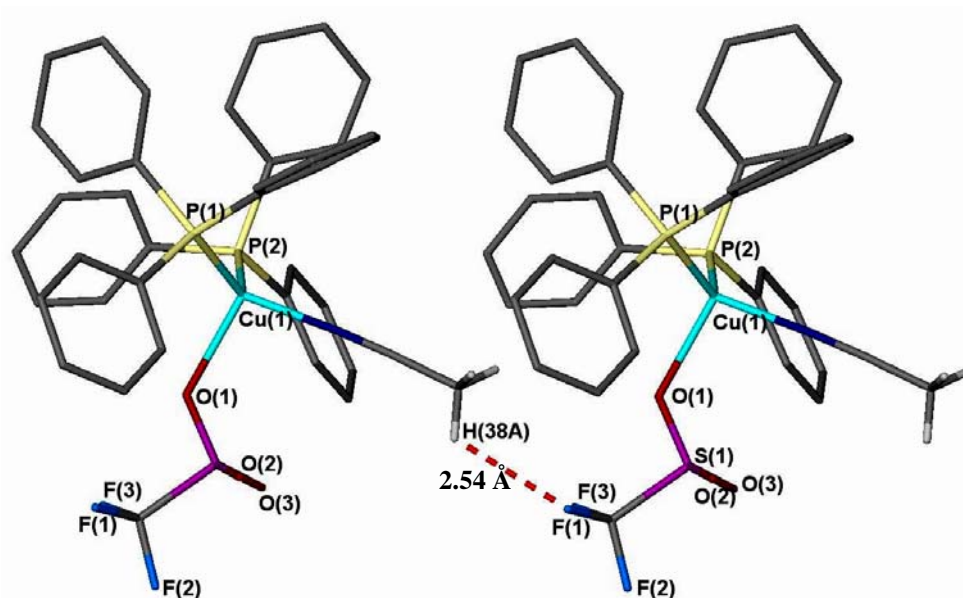
	<b>13</b>	<b>14</b>
Cu(1) – P(1)	2.242(1)	2.2546(6)
Cu(1) – P(2)	2.2353(9)	2.2448(6)
Cu(1) – O(4) <sub>triflate</sub>	2.168(2)	
Cu(1) – O(3) <sub>THF</sub>	2.125(2)	
Cu(1) – O(1) <sub>triflate</sub>		2.184(2)
Cu(1) – N(1) <sub>MeCN</sub>		2.012(2)
P(1) – Cu(1) – P(2)	122.91(4)	119.06(2)
O(3) – Cu(1) – O(4)	98.17(9)	
N(1) – Cu(1) – O(1)		98.25(7)
P(1) – Cu(1) – O(4)	106.68(7)	
P(1) – Cu(1) – O(1)		104.52(5)
P(1) – Cu(1) – O(3)	109.18(7)	
P(1) – Cu(1) – N(1)		111.51(6)
P(2) – Cu(1) – O(4)	107.56(6)	
P(2) – Cu(1) – O(1)		107.60(5)
P(2) – Cu(1) – O(3)	109.45(7)	
P(2) – Cu(1) – N(1)		113.24(6)

bond,<sup>14</sup> while the 2.125(2) Å Cu–O bond of the THF molecule is similar to other transition metal M–O bonds of this type. These bonds, however, are somewhat longer than a typical Cu–O bond indicative of the low degree of nucleophilicity of both the triflate anion and the THF molecule in this compound.<sup>5, 14</sup>

**Table 4.5** Selected bond lengths (Å) and angles (deg) for **15**

<i>Complex A</i>		<i>Complex B</i>	
Cu(1) – P(1)	2.257(2)	Cu(2) – P(3)	2.265(2)
Cu(1) – P(2)	2.264(2)	Cu(2) – P(4)	2.261(2)
Cu(1) – O(1) <sub>triflate</sub>	2.241(5)	Cu(2) – O(4) <sub>triflate</sub>	2.187(5)
Cu(1) – N(1) <sub>MeCN</sub>	1.994(7)	Cu(2) – N(2) <sub>MeCN</sub>	2.014(7)
P(1) – Cu(1) – P(2) 126.90(7)		P(3) – Cu(2) – P(4) 126.00(8)	
N(1) – Cu(1) – O(1) 95.8(2)		N(2) – Cu(2) – O(4) 89.6(2)	
P(1) – Cu(1) – N(1) 112.29(17)		P(3) – Cu(2) – N(2) 106.8(2)	
P(1) – Cu(1) – O(1) 107.02(13)		P(3) – Cu(2) – O(4) 109.6(2)	
P(2) – Cu(1) – N(1) 111.69(17)		P(4) – Cu(2) – N(2) 118.6(2)	
P(2) – Cu(1) – O(1) 96.58(12)		P(4) – Cu(2) – O(4) 98.9(1)	

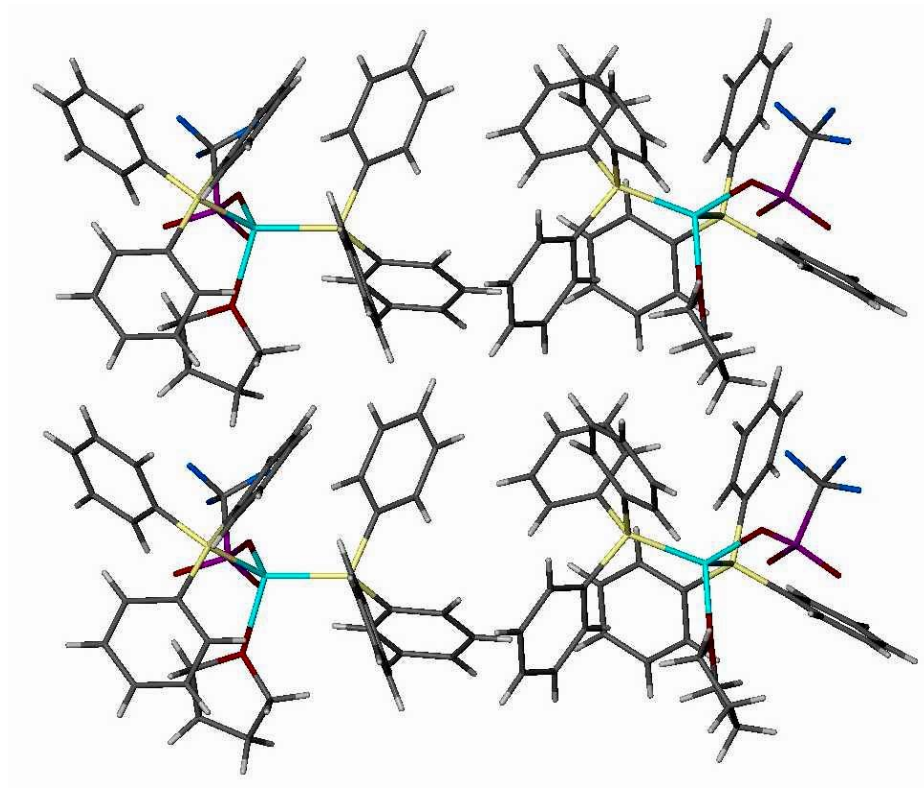
The individual complexes in both **13** and **14** pack with the Cu-centered tetrahedra forming stacks along the *b*-axis with adjacent stacks related by a  $2_1$  screw axis. As shown in Figure 4.4, the MeCN or THF ligand of one Cu complex is pointed toward a cleft



**Figure 4.4** Two units of **14** lock together with ligand-to-coordinated anion association. Hydrogen atoms have been omitted on the phenyl rings.

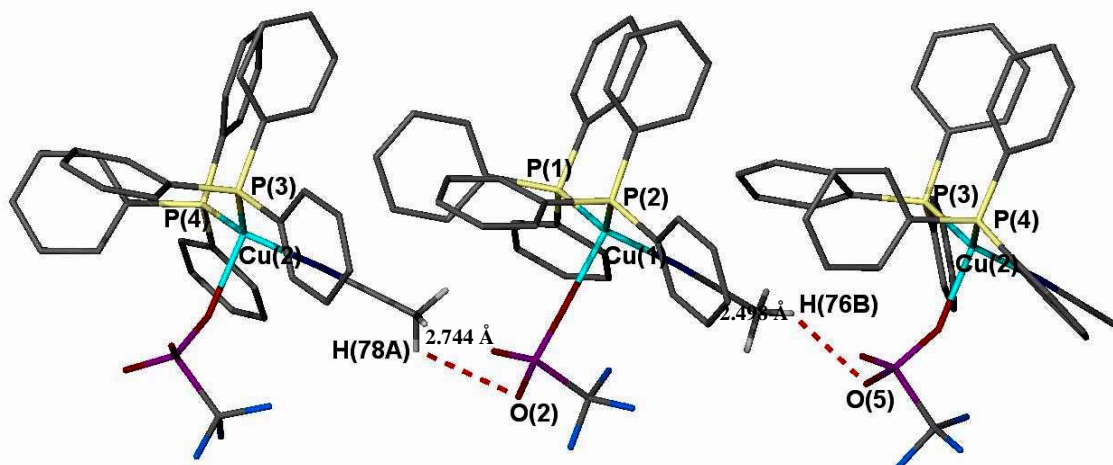
between the lower, fluorine end of the triflate anion and one phenyl ring PPh<sub>3</sub> ligand in an adjacent complex. Moderate to weak hydrogen bonding occurs between the triflate and the MeCN or THF ligand of the opposing Cu unit as indicated by distances of ~2.5 Å

(F $\cdots$ H<sub>MeCN</sub>) and  $\sim 2.9$  Å (F $\cdots$ H<sub>THF</sub>). A moderate to weak hydrogen-phenyl ring interaction is also shown by distances of  $\sim 2.8$  Å (Ph $\cdots$ H<sub>MeCN</sub>) and  $\sim 3.0$  Å (Ph $\cdots$ H<sub>THF</sub>). The rest of the structure is locked together by edge-to-face  $\pi$ - $\pi$  stacking (Figure 4.5) with H $\cdots$ Ph distances as close as  $\sim 2.8$  Å.



**Figure 4.5** PPh<sub>3</sub> ligands also contribute to lock crystalline solid together as they (shown for **13**) lock the in a series of edge-to-face  $\pi$ - $\pi$  stacking.

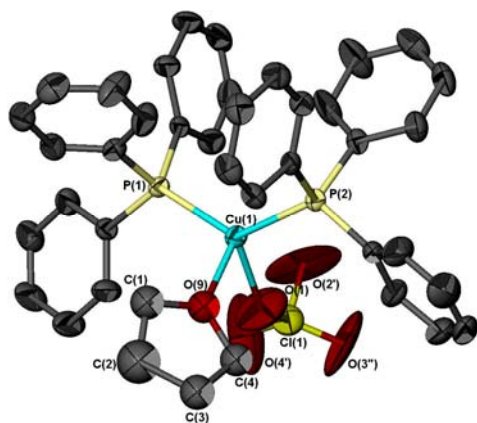
The complexes in **15** also have similar H-bonding and edge-to-face  $\pi$ - $\pi$  stacking. However, this in this case, the H-bonding occurs between the MeCN hydrogen and the oxygen in the triflate anion. Figure 4.6 shows the two closest H<sub>MeCN</sub> – O of 2.498 Å and 2.744 Å. As was the case in **13** and **14**, there is also edge-to-face  $\pi$ - $\pi$  stacking with H $\cdots$ Ph distances, again, as close as  $\sim 2.8$  Å and a moderate to hydrogen-phenyl ring interaction of  $\sim 2.8$  Å (Ph $\cdots$ H<sub>MeCN</sub>).



**Figure 4.6** The H-bonding in **15** between the MeCN ligands and the oxygen atom on the triflate anion.

### 4.3.3 Perchlorate Coordination

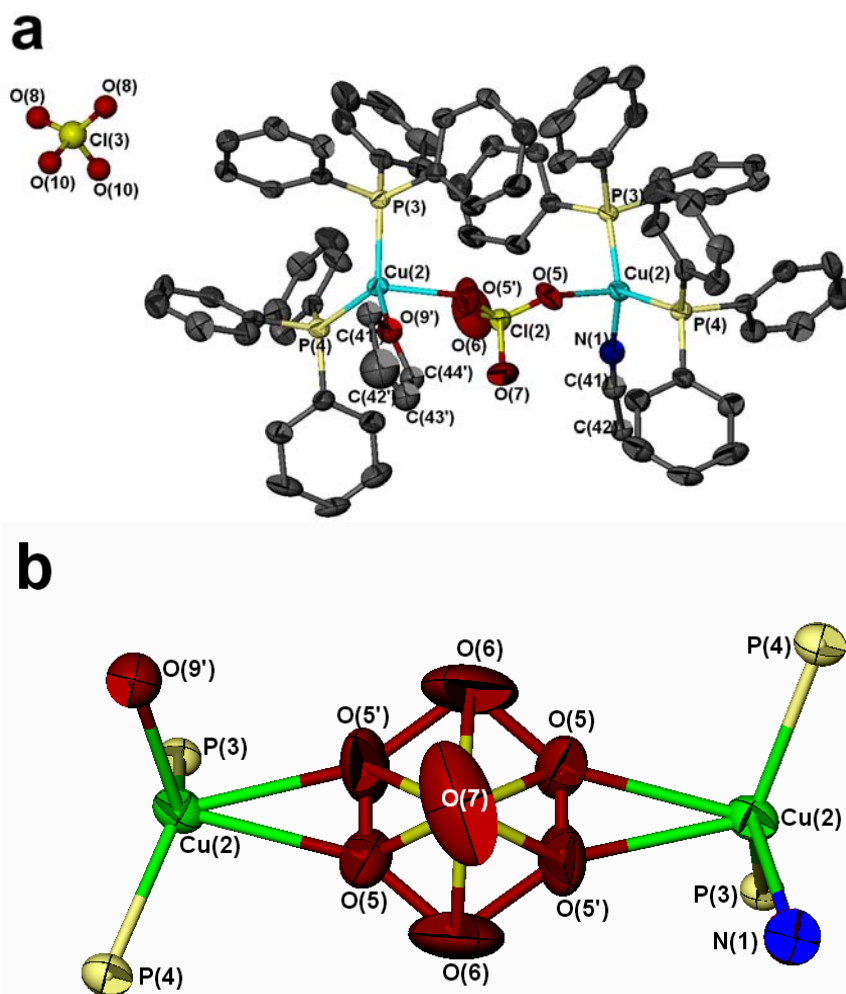
Analogous reactions to those above using  $[\text{Cu}(\text{MeCN})_2(\text{PPh}_3)_2]\text{ClO}_4$  resulted only in recrystallization of the original salt. However, vapor diffusion of diethyl ether into a THF solution of lower concentration of perchlorate salt produced a new compound,  $[\text{Cu}_2(\text{ClO}_4)(\text{MeCN})(\text{THF})(\text{PPh}_3)_4](\text{ClO}_4)$  **16**. There are two unique copper centers in the asymmetric unit. Cu(1) is coordinated by two triphenylphosphine ligands, and one



**Figure 4.7** The Cu(1) molecule of **16** with the terminally coordinated perchlorate anion (only THF molecule is shown in the THF/MeCN ligand overlap position). Hydrogen atoms have been omitted and all other atoms are represented as 50% ellipsoids.

perchlorate anion, with the final coordination site occupied by disordered THF and MeCN solvent molecules in approximately 80/20 ratio, respectively. This results in a neutral species analogous to **13** (Figure 4.7) with all of the bond distances and bond angles within expected norms.<sup>14</sup>

The coordination environment of Cu(2) is quite similar to that of Cu(1) including the disordered solvent molecules, albeit in opposite ratios (80%MeCN/20%THF), and a coordinated perchlorate anion. The difference in this case is that the perchlorate anion, Cl(2) sits on a 2-fold axis, and therefore generates (and bridges to) another Cu(2) center as shown in Figure 4.8a. The bridging perchlorate anion was also modeled with an additional 180° rotational disorder as shown in Figure 4.8b. As expected, the Cu – O



**Figure 4.8** (a) The dimer formed by the bridging perchlorate anion along with the third, non-coordinated perchlorate anion. Although both metal centers are from the same Cu(2) unit seen over a two-fold axis, one unit is shown with the THF ligand in place (left) and the other is shown with the MeCN ligand (right) to illustrate how these two ligands occupy the same position. (b) The complete 180° rotational disorder for the bridging perchlorate is shown (looking down the Cl – O(7) axis). All carbon and hydrogen atoms omitted).

distances to the disordered oxygen atoms (2.317(8) Å and 2.345(8) Å for Cu(2) – O(5) and Cu(2) – O(5'), respectively) are slightly elongated from the 2.171 Å for Cu(1) – O(1), the terminal perchlorate anion on Cu(1). Selected bond lengths and angles are listed in table 4.6.

**Table 4.6** Selected bond lengths (Å) and angles (deg) for **16**

<i>Complex A</i>		<i>Complex B</i>	
Cu(1) – P(1)	2.250(1)	Cu(2) – P(3)	2.268(1)
Cu(1) – P(2)	2.260(1)	Cu(2) – P(4)	2.271(2)
Cu(1) – O(1) <sub>perchlorate</sub>	2.171(5)	Cu(2) – O(5) <sub>perchlorate</sub>	2.345(8)
Cu(1) – O(9) <sub>THF</sub>	2.123(4)	Cu(2) – N(5') <sub>perchlorate</sub>	2.317(8)
		Cu(2) – N(1)	2.024(4)
P(1) – Cu(1) – P(2)	128.70(5)	P(3) – Cu(2) – P(4)	126.81(5)
		O(5) – Cu(2) – O(5')	27.0(3)
O(9) – Cu(1) – O(1)	83.2(2)	N(1) – Cu(2) – O(5)	107.4(2)
		N(1) – Cu(2) – O(5')	87.4(3)
P(1) – Cu(1) – O(9)	109.3(1)	P(3) – Cu(2) – N(1)	111.7(1)
P(1) – Cu(1) – O(1)	110.3(2)	P(3) – Cu(2) – O(5)	105.4(2)
		P(3) – Cu(2) – O(5')	97.2(2)
P(2) – Cu(1) – N(1)	111.7(1)	P(4) – Cu(2) – N(1)	108.4(1)
P(2) – Cu(1) – O(1)	110.8(2)	P(4) – Cu(2) – O(5)	94.1(2)
		P(4) – Cu(2) – O(5')	118.2(2)

Note that although the two Cu(2) centers shown in Figure 4.8a and 4.8b are crystallographically identical, we have shown one coordinated to THF (left) and the other coordinated to MeCN (right) to emphasize the coordinated solvent disorder. Though nothing definitive can be concluded regarding the specific ratios of THF and MeCN on each site, the model does provide evidence for the fairly equal competition between the coordination of the available ligands as the starting material is placed in the THF solvent.

The charge balance is achieved with an additional free perchlorate ion, Cl(3), which also resides on a 2-fold axis. The oxygen atoms bonded to Cl(3) exhibit high anisotropic thermal parameters, most likely brought on by the non-symmetric vibrational disorder



associated with these types of anions. The anion makes a series of long (and presumably weak) hydrogen bonds ( $\sim 2.685 - 3.126 \text{ \AA}$ ) to the phenyl groups and two shorter hydrogen bonds ( $2.095 \text{ \AA}$ ) to THF/MeCN molecules on adjacent sides.

#### 4.3.4 *The Hydrogen Sulfate Anion*

As was mentioned in Chapter 3, the Cu/bipy reactions using the hydrogen sulfate salt produced results strikingly similar to those using the triflate and perchlorate salts. Therefore it is of no surprise that the hydrogen sulfate salt, as well as the derivatives made from its dissolution and crystallization in THF also bears remarkably similar results. The synthesis and structure of  $[\text{Cu}(\text{MeCN})_2(\text{PPh}_3)_2]\text{HSO}_4$  starting material, in itself, has not been studied or published to the best of our knowledge. Therefore, the following section will cover both the  $\text{HSO}_4^-$  anions starting material as well as the derivatives that were developed as the salt was recrystallized in THF. To this date, there have not been any single crystals suitable for X-ray diffraction studies in those reactions involving the recrystallization of this material in either chloroform or toluene. These reactions, however, continue to be a subject of ongoing investigations.

The compound  $[\text{Cu}(\text{MeCN})_2(\text{PPh}_3)_2]\text{HSO}_4$ , **17** (or as **SM9** in Chapter 2), crystallizes in the monoclinic space group  $P2_1/n$  and its crystal packing is essentially isostructural to the other salts  $[\text{Cu}(\text{MeCN})_2(\text{PPh}_3)_2]\text{X}$  for ( $\text{X} = \text{ClO}_4^-$ ,  $\text{BF}_4^-$ , or  $\text{PF}_6^-$ ), **SM6-8**.<sup>4</sup> Even with this similarity in packing, the unit cell dimensions of **17** are significantly more different than that of the other three salts. As shown in Table 4.7, although the  $a$ ,  $b$ , and  $c$  indices are rearranged in **17**, they are fairly similar to those seen in the other three copper(I) salts. The almost  $90^\circ$  beta angle, however, almost hints to an increase in symmetry as the unit

**Table 4.7**

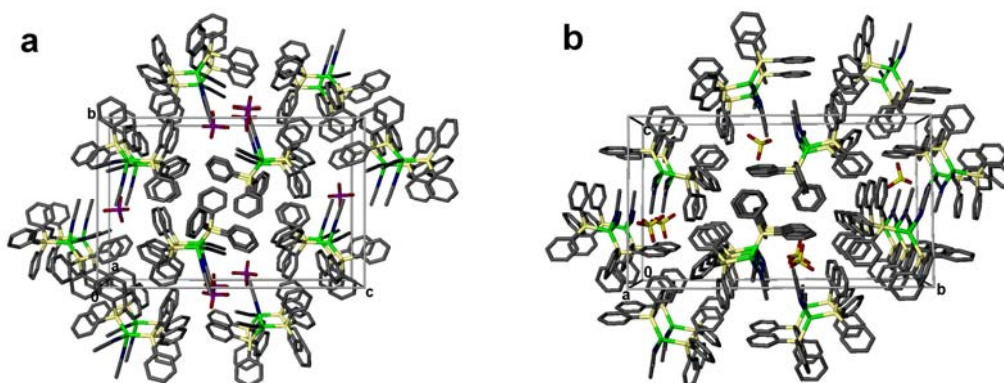
Unit cell dimensions for  $[\text{Cu}(\text{MeCN})_2(\text{PPh}_3)_2]\text{X}$ ,  
 ( $\text{X} = \text{ClO}_4^-$ ,  $\text{BF}_4^-$ ,  $\text{PF}_6^-$ , and  $\text{HSO}_4^-$ ), **SM6-8** and **17**

X	$\text{HSO}_4^-$	$\text{ClO}_4^-$	$\text{BF}_4^-$	$\text{PF}_6^-$
$a$ (Å)	8.9236(4)	15.434(2)	15.246(2)	15.616(3)
$b$ (Å)	16.4211(7)	26.958(3)	26.689(3)	27.38(1)
$c$ (Å)	25.591(1)	9.199(2)	9.16(1)	9.194(7)
$\alpha$ , deg	90	90	90	90
$\beta$ , deg	90.993(1)	94.68(5)	94.08	95.32(5)
$\gamma$ , deg	90	90	90	90

cell for **17** resembles comes close to being an orthorhombic cell rather than monoclinic.

In comparing the packing **17** with that of the perchlorate

salt, shown in Figure 4.9, the similarity is clear to see. Aside from the subtle differences found in the orientation of the ligands on each tetrahedron, these two structures appear to have identical packing.



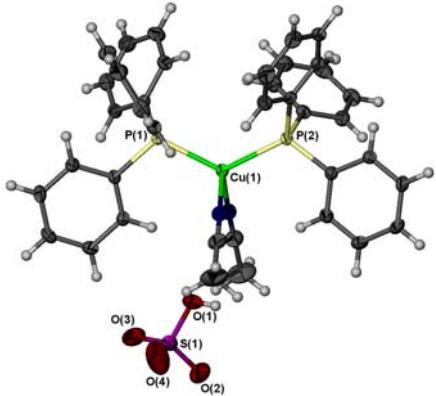
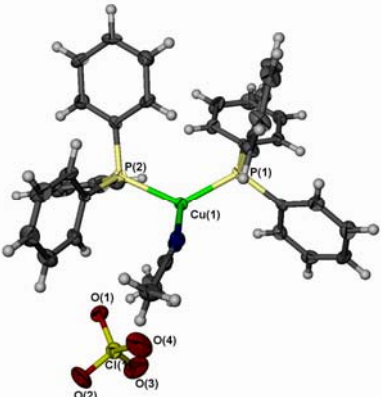
**Figure 4.9** Stick representations of the two *almost* identical packing arrangements for (a) structure **17** and (b) the perchlorate salt starting material  $[\text{Cu}(\text{MeCN})_2(\text{PPh}_3)_2]\text{ClO}_4$ . Color scheme: Cu green, P yellow, S purple, N blue, O red, C gray. The hydrogen atoms have been omitted for clarity.

A closer look at the individual tetrahedra found in the asymmetric unit of both compounds reveals that the ligand differences are not so subtle as the previous view suggests. The MeCN ligands seen in **SM6** have are bent to one side of the plane orthogonal to the  $\text{CuP}_2$  plane, as is the same with the other related salts, **SM7** and **SM8**. In **17**, however, the MeCN ligands appear to be bent to opposing sides of the same plane of symmetry, much as was found with the triflate salt.

In Table 4.7, select bond distances and ligand angles about the copper center for both **17** and **SM6** are presented for comparison. Examination of these angles shows how

even the direct Cu – N coordination bond is considerably distorted (bent to one side) in **SM6**. While the coordination angle distortion can also be seen in **17**, but at a much lesser extent as expected. Direct measurement of the bend in each ligand can also give us an idea of the extent of this ligand bending in each structure. Both of the MeCN ligands in **17** were found to have a Cu – N – C angle of 170°, while those two MeCN ligands in **SM6** are at a 164° and 166° angle. There does not appear to be any significant differences in any of the Cu – P or Cu – N bonds lengths between **17** and the other related salts.

**Table 4.8** Selected bond lengths (Å) and angles (deg) **17** and **SM6**

<b>17</b>		
	Cu(1) – P(1)	2.2789(6)
	Cu(1) – P(2)	2.2706(6)
	Cu(1) – N(1)	2.075(2)
	Cu(1) – N(2)	2.045(2)
	P(1)–Cu(1)–P(2)	126.58(2)
	N(1)–Cu(1)–P(1)	104.32(5)
	N(2)–Cu(1)–P(1)	113.16(5)
	N(1)–Cu(1)–P(2)	107.95(5)
	N(2)–Cu(1)–P(2)	103.23(5)
	N(1)–Cu(1)–N(2)	97.91(8)
<b>SM6</b>		
	Cu(1) – P(1)	2.260(1)
	Cu(1) – P(2)	2.277(1)
	Cu(1) – N(1)	2.026(4)
	Cu(1) – N(2)	2.036(4)
	P(1)–Cu(1)–P(2)	125.92(4)
	N(1)–Cu(1)–P(1)	111.92(9)
	N(2)–Cu(1)–P(1)	112.41(9)
	N(1)–Cu(1)–P(2)	102.63(9)
N(2)–Cu(1)–P(2)	100.18(9)	
N(1)–Cu(1)–N(2)	100.3(1)	

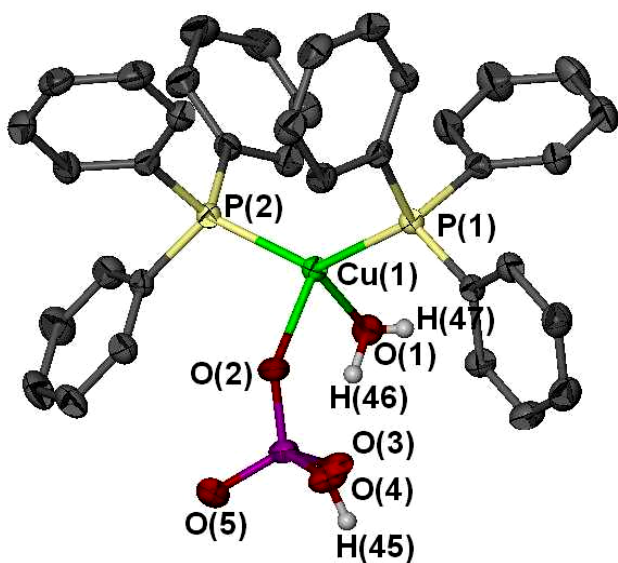
Further similarity of **17** to the triflate salt is seen in the positioning of the phosphines phenyl rings. As in the triflate salt, PPh<sub>3</sub> ligands adopt an eclipsed conformation with respect to each other. One difference, however, is that the three-blade propeller-like

phenyl rings on each phosphine are positioned in opposing chirality in respect to each other, as is for the analog compounds of **SM6-8**.<sup>4</sup>

#### 4.3.5 Reactions of **17** in THF

In our first attempts to recrystallize the hydrogen sulfate salt in THF in order to duplicate the results found with the triflate salt, we were presented with a bit of a surprise. While the  $\text{HSO}_4^-$  did indeed coordinate to the copper as expected, we also discovered that water had coordinated to the copper atom instead of the expected THF solvent. This resulted in the formation of the neutral compound of

$\text{Cu}(\text{H}_2\text{O})(\text{PPh}_3)_2(\text{HSO}_4) \cdot 2\text{THF}$ , **18**. Figure 4.10 shows the single tetrahedra found in the



**Figure 4.10** The water coordinated Cu(I) complex found in the asymmetric unit of **18** shown in 50% thermal ellipsoids. Hydrogen atoms on the phenyl rings and THF were omitted for clarity.

asymmetric unit of **18**. The two molecules of THF (not shown) in the structure are found only as included solvent.

The presence of water in our THF solvent is not too surprising since we make very little effort to dry our solvents (other than placing molecular sieves in the solvent bottle). However, the actual

coordination of water to our Cu(I) center was quite unexpected. In terms of the Pearson's Lewis acids and bases hard-soft classification, copper(I) is considered a soft anion while water is considered a hard base.<sup>15</sup> Given this, and according to Pearson's hard-soft acid-base (HSAB) principle,  $\text{Cu}^+$  is incompatible with water.<sup>15-17</sup> While water appears to be a

very common ligand in the chemistry of  $\text{Cu}^{2+}$ , the coordination of water to  $\text{Cu}^+$  is relatively unknown with only a few literature accounts available.<sup>18, 19</sup> In our studies alone, we have come across only two other instance involving the water coordination in our Cu/pyrimidine coordination polymers, as will be presented in detail in chapters 6 & 7.

The ligand orientation found with **18** is somewhat similar to that found with **17**, in which the phosphine ligands arrange in an eclipsed fashion with respect to each other.

<b>Table 4.9</b> Selected bond lengths (Å) and angles (deg) for <b>18</b>	
Cu(1) – P(1)	2.2395(7)
Cu(1) – P(2)	2.2504(7)
Cu(1) – O(1)	2.164(2)
Cu(1) – O(2)	2.180(2)
P(1)–Cu(1)–P(2)	132.70(3)
O(1)–Cu(1)–P(1)	106.33(7)
O(2)–Cu(1)–P(1)	105.74(6)
O(1)–Cu(1)–P(2)	104.61(7)
O(2)–Cu(1)–P(2)	105.20(6)
O(1)–Cu(1)–O(2)	96.65(8)

Now however, each propeller-like phenyl ring trio has an orientation with the same chirality.

Table 4.8 list select distances and angles for **18**, showing that the bond distances and angles are much like those of the other Cu-anion

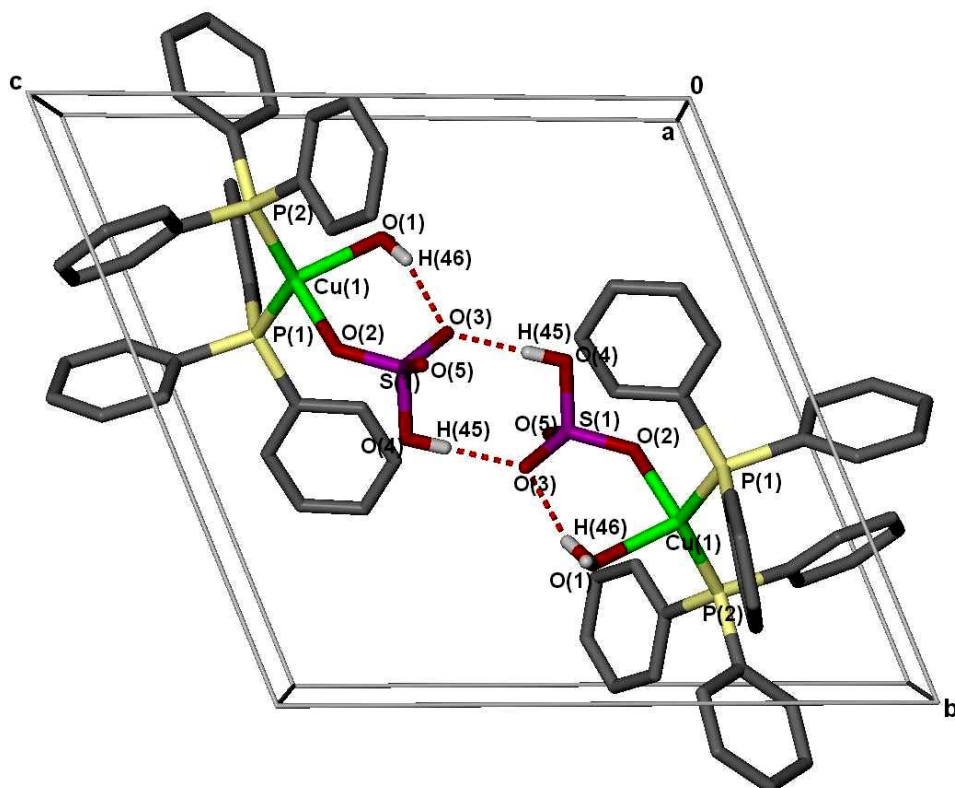
coordinated complexes we have presented in this

chapter. The Cu – O bond from both the coordinated water and anion are seem reasonable for M – O bonds compared to those examples given for both the M–OS<sub>2</sub>R and the few water coordinated Cu complexes.<sup>14, 19</sup>

One interesting feature in **18** is that this complex not only forms a *pair* of strong, 1.78 Å H-bonds between the anions of adjacent complexes, but **18** also forms a somewhat weaker, 2.00 Å H-bond between the water ligand and the HSO<sub>4</sub><sup>-</sup> anion, both of which are coordinated on the same copper(I) complex. This *intermolecular* hydrogen bonding could explain this compounds high affinity towards water. Figure 4.11 shows this hydrogen-bonded dimer as it appears in the unit cell.

The included THF solvent has considerably weaker forces that bind it into place. One THF appears to be held loosely in place by a very weak 2.2 Å H-bond between one

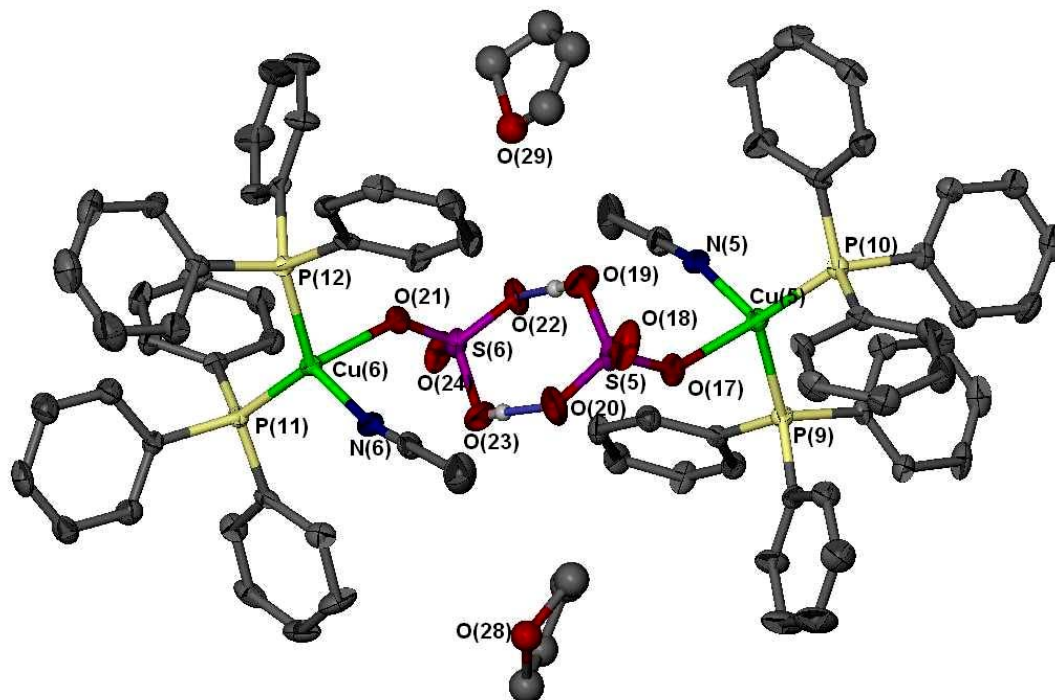
of its own hydrogen atoms and the oxygen on the water molecule. Some even weaker H- $\pi$  interactions may be what binds the other THF as it sits in a cavity bordered by the phenyl rings of eight surrounding Cu(I) complexes.



**Figure 4.11** A stick representation of the H – bonded dimer found in **18**. The hydrogen atoms on the phenyl rings and the THF have been omitted for clarity.

In yet another effort to duplicate the triflate results, this time without the coordination of water, the HSO<sub>4</sub> starting material was dissolved in THF that was dried by the procedure described in the experimental section. This did, indeed, result in a compound absent of water and still produced anion coordination as expected. However, instead of obtaining the THF coordination as well, we found that the compound retained the MeCN ligand and the THF was only included as before, resulting in the formation of Cu(MeCN)(PPh<sub>3</sub>)<sub>2</sub>(HSO<sub>4</sub>)·THF, **19**.

The asymmetric unit of **19** consists of six unique Cu(I) complexes. While these six complexes appear to be, for the most part, structurally identical to each other, subtle variances in the coordination sphere and bond lengths set them apart from each other. With the  $\text{HSO}_4^-$  anion in place, **19** exhibits hydrogen bonding between the coordinated anions much like is seen in **18**. Figure 4.12 shows the dimer formed by the two hydrogen-bonded Cu(I) complexes with the included THF as it sits in the cleft of this dimer. The entire is locked together by the various interactions between the phenyl rings on the phosphine ligands.



**Figure 4.12** Two hydrogen-bonded Cu(I) complexes in **19** shown as 50% thermal ellipsoids. The THF, shown as isotropic spheres, find a place in the cleft formed by the Cu(I) dimer. The two H-bonds located at O(20) and O(22) are colored in light blue. All unmarked carbon atoms are gray and hydrogen atoms, with the exception of those on the anion, have been omitted for clarity.

The selected bond lengths and angles for all six Cu(I) complexes of **19** are given in Table 4.9 and 4.10. As was mentioned above, each Cu(I) complex has subtle, yet significant differences that set them each apart from the other. As are with all the

complexes of this type, the two phosphine ligands are spread apart by their steric bulk, widening the angle slightly to 122.5 – 123.1°. In turn, both the MeCN ligand and coordinated HSO<sub>4</sub> anion are pushed downward the phosphines presence to a much smaller angle of 97.0 – 98.5°. There is nothing unusual about the anions coordination as well, with the 2.131(4) – 2.196(3) Å Cu – O bond well within the normal range seen for this particular anion and the other oxy-anions we have studied so far.

**Table 4.10** Selected bond lengths (Å) and angles (deg) for **19**

<i>Complex A</i>		<i>Complex B</i>		<i>Complex C</i>	
Cu(1) – P(1)	2.264(2)	Cu(2) – P(3)	2.276(1)	Cu(3) – P(5)	2.253(2)
Cu(1) – P(2)	2.281(1)	Cu(2) – P(4)	2.249(2)	Cu(3) – P(6)	2.266(1)
Cu(1) – N(1)	2.004(5)	Cu(2) – N(2)	2.031(5)	Cu(3) – N(3)	2.024(5)
Cu(1) – O(1)	2.188(3)	Cu(2) – O(5)	2.172(3)	Cu(3) – O(9)	2.131(4)
P(1) – Cu(1) – P(2)	122.49(5)	P(3) – Cu(2) – P(4)	122.96(5)	P(5) – Cu(3) – P(6)	123.96(6)
N(1) – Cu(1) – O(1)	97.6(2)	N(2) – Cu(2) – O(5)	97.2(2)	N(3) – Cu(3) – O(9)	98.5(2)
P(1) – Cu(1) – N(1)	116.8(1)	P(3) – Cu(2) – N(2)	104.7(1)	P(5) – Cu(3) – N(3)	116.0(1)
P(1) – Cu(1) – O(1)	108.6(1)	P(3) – Cu(2) – O(5)	97.5(1)	P(5) – Cu(3) – O(9)	107.6(2)
P(2) – Cu(1) – N(1)	108.8(2)	P(4) – Cu(2) – N(2)	119.1(1)	P(6) – Cu(3) – N(3)	106.2(1)
P(2) – Cu(1) – O(1)	97.5(1)	P(4) – Cu(2) – O(5)	110.4(1)	P(6) – Cu(3) – O(9)	100.5(1)



**Table 4.11** Selected bond lengths (Å) and angles (deg) for **19** cont.

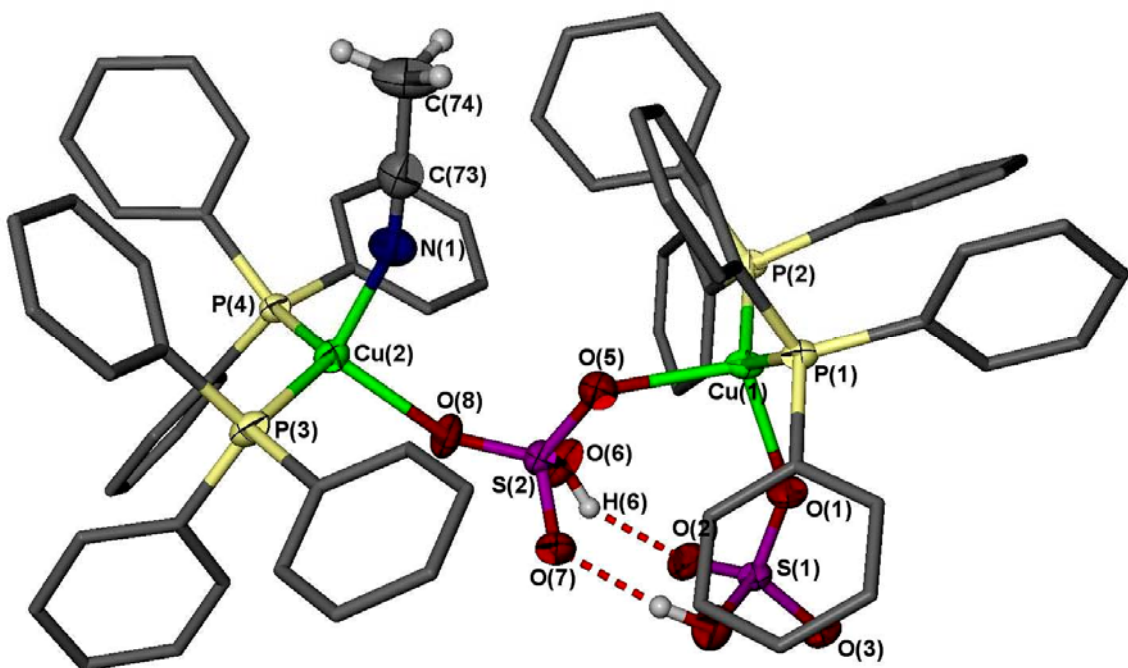
<i>Complex C</i>		<i>Complex D</i>		<i>Complex E</i>	
Cu(4) – P(7)	2.266(2)	Cu(5) – P(9)	2.279(1)	Cu(6) – P(11)	2.256(1)
Cu(4) – P(8)	2.298(1)	Cu(5) – P(10)	2.245(2)	Cu(6) – P(12)	2.278(1)
Cu(4) – N(4)	2.010(5)	Cu(5) – N(5)	2.024(4)	Cu(6) – N(6)	2.020(4)
Cu(4) – O(13)	2.196(3)	Cu(5) – O(17)	2.188(3)	Cu(6) – O(21)	2.186(3)
P(7) – Cu(4) – P(8)	123.42(5)	P(9) – Cu(5) – P(10)	122.45(5)	P(11) – Cu(6) – P(12)	124.10(5)
N(4) – Cu(4) – O(13)	97.4(2)	N(5) – Cu(5) – O(17)	97.5(2)	N(6) – Cu(6) – O(21)	97.0(2)
P(7) – Cu(4) – N(4)	106.7(1)	P(9) – Cu(5) – N(5)	104.5(1)	P(11) – Cu(6) – N(6)	120.6(1)
P(7) – Cu(4) – O(13)	95.2(1)	P(9) – Cu(5) – O(17)	95.1(1)	P(11) – Cu(6) – O(21)	107.6(1)
P(8) – Cu(4) – N(4)	119.7(1)	P(10) – Cu(5) – N(5)	119.6(1)	P(12) – Cu(6) – N(6)	104.8(1)
P(8) – Cu(4) – O(13)	108.2(1)	P(10) – Cu(5) – O(17)	112.3(1)	P(12) – Cu(6) – O(21)	96.4(1)

Perhaps the most interesting observation we have had with this material further illustrates the great affinity that the  $\text{HSO}_4^-$  salt apparently has towards water in THF. It was found that as crystals of **19** were placed in a watch glass along with the mother liquor (of dry THF) and exposed to air, over the span of only a few minutes the crystals of **19** dissolve as crystals of **18** begin to appear. This transformation is rapid and can be easily observed in real time under the microscope as the water-coordinated crystals of **18** quickly and completely replace the crystalline sample of **19**.

Since we still had not accomplished an exact duplication of the triflate reaction that produced THF coordinated **12** we preceded with one more reaction. This time, by reducing the amount of **17** dissolved in the dry THF, it was postulated that this would, in turn, increase the *relative* THF concentration over that of the Cu(I) starting material, in turn, favor the THF coordination over that of the MeCN ligand. It was found, however,

that spontaneous crystallization did not occur while at this lower salt concentration so we employed solvent vapor diffusion with diethyl ether as the crystallizing solvent. Since the solvent vapor diffusion would, instead, reduce the THF concentration, this produced results reminiscent of the perchlorate reaction in the formation of the  $\text{HSO}_4^-$  bridged dimer of  $\text{Cu}_2(\text{MeCN})(\text{PPh}_3)_4(\text{HSO}_4)_2$ , **20**, as shown below in Figure 4.13.

Each anion found in the asymmetric unit of **20** is coordinated to the two copper tetrahedra. One anion is coordinated as a terminal ligand while the other anion acts as a bridging ligand between the two Cu(I) centers. These two anions are also positioned within close proximity of each other allowing them to interact through a pair of strong (1.8 Å), intermolecular hydrogen bonds. There is no THF included in this structure and only one MeCN ligand remains coordinated along with of course along with the four phosphine ligands still in place.



**Figure 4.13** The  $\text{HSO}_4^-$  bridged dimer of **20** with all atoms except the phenyl rings shown as 50% thermal ellipsoids. The hydrogen bonds between the anions are shown as red dashed lines. The phenyl ring's hydrogen atoms have been removed for clarity.

The selected bond distances and angles are listed in Table 4.11. These results show, once again, that the bonds and coordination are within normal parameters; at least for those compounds others and we have observed for these types of compounds.<sup>14, 19</sup> The bridging anion's much longer Cu(1) – O(5) bond of 2.261 Å is perfectly understandable since Cu(I) is shared by both anions and the weaker and longer bond would be with the bridging anion.

**Table 4.12** Selected bond lengths (Å) and angles (deg) for **20**

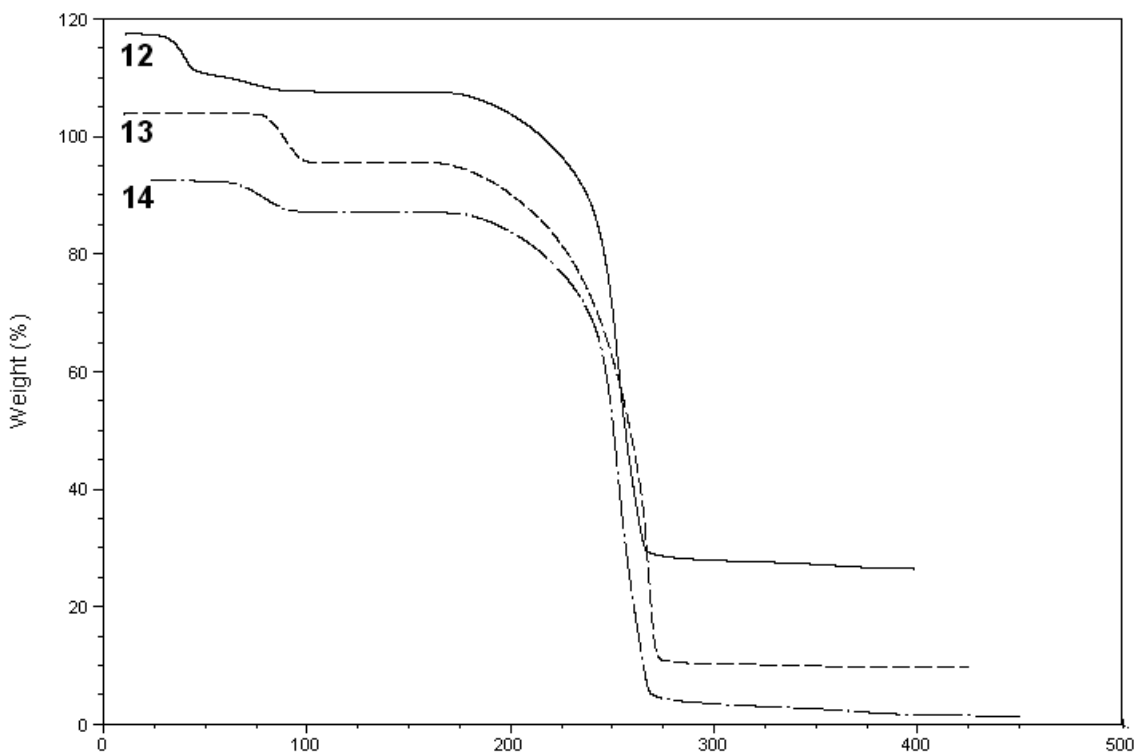
<i>Complex A</i>		<i>Complex B</i>	
Cu(1) – P(1)	2.2626(1)	Cu(2) – P(3)	2.268(1)
Cu(1) – P(2)	2.2493(1)	Cu(2) – P(4)	2.258(1)
Cu(1) – O(1)	2.128(2)	Cu(2) – N(1)	2.045(3)
Cu(1) – O(5)	2.261(3)	Cu(2) – O(8)	2.132(2)
P(1) – Cu(1) – P(2)	127.64(3)	P(3) – Cu(2) – P(4)	125.34(4)
O(1) – Cu(1) – O(5)	101.85(1)	N(1) – Cu(2) – O(8)	100.2(1)
P(1) – Cu(1) – O(1)	103.37(8)	P(3) – Cu(2) – N(1)	104.39(9)
P(1) – Cu(1) – O(5)	96.87(8)	P(3) – Cu(2) – O(8)	107.24(8)
P(2) – Cu(1) – O(1)	114.32(8)	P(4) – Cu(2) – N(1)	107.21(9)
P(2) – Cu(1) – O(5)	108.78(7)	P(4) – Cu(2) – O(8)	109.49(8)

#### 4.3.6 Thermogravimetric Analysis

The percent weight loss observed when compounds **12**, **13**, and **14** were heated to ~400° C under a flowing N<sub>2</sub> are shown in Figure 4.14. As expected, the results indicate that all three compounds undergo quite similar thermal decompositions, with the weakly bound solvent ligands being removed first (all below 100 °C), followed by a broad, featureless decomposition.

Specifically, the thermal behavior of **12** indicates that the two MeCN ligands in the compound are removed in two separate, yet overlapping events. The first MeCN loss

occurs at  $\sim 22^\circ\text{C}$  while the second MeCN loss begins at  $\sim 44^\circ\text{C}$ . A big difference is that this second loss is more gradual as it continues over  $\sim 50^\circ\text{C}$  range, after which results in 9.7 % weight loss and corresponds to both MeCN ligands (theoretical 10.0%).



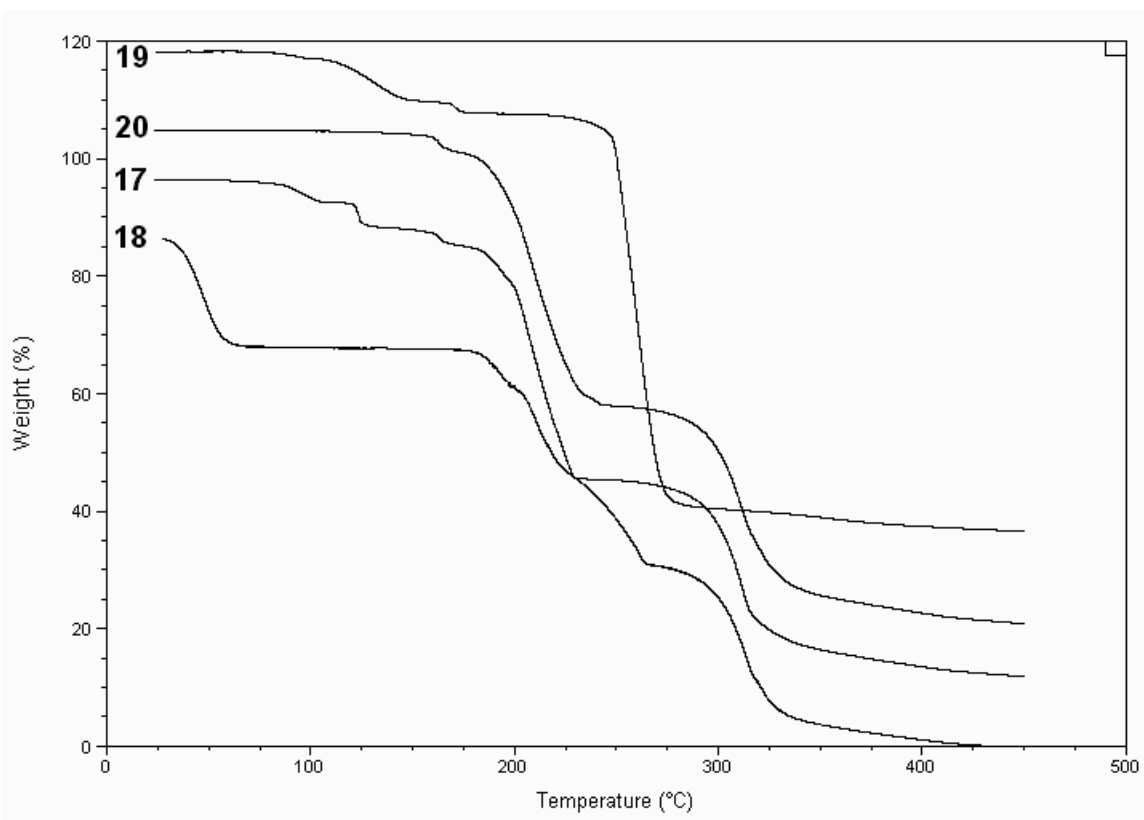
**Figure 4.14** Thermogravimetric analysis for **12**, **13**, and **14**.

There are only two distinct weight losses observed for both **13** and **14** with both showing (nearly) identical weight loss profiles. The first loss of 8.1 % at  $\sim 77^\circ\text{C}$  in **13** corresponds to the removal of the coordinated THF (theoretical 8.4 %) while the 5.1 % loss at  $62^\circ\text{C}$  in **14** represents the removal of the terminal MeCN ligand (theor. 5.3 %).

The final decomposition of all three compounds (i.e. loss of the remaining components about the Cu center) occurs at relatively the same temperature ( $>160^\circ\text{C}$ ) and rate. A black residue remained at the end of each run for **12**, **13** and **14** with a final weight of 8.7, 5.5 and 8.7 % the original mass, respectively. While this residue has not

been analyzed, it most likely consists of a mixture of CuO and Cu<sub>2</sub>O (theoretical 9.7% and 8.7% of the original mass, respectively).

As did with the triflate compounds, those compounds with hydrogen sulfate were also subjected to a thermal analysis in the same manner. In Figure 4.15 shows the weight change as a function of temperature for those compounds of **17**, **18**, **19**, and **20** as they were heated to ~400° C under flowing N<sub>2</sub> gas. As was with the triflate compounds, the included THF was the first species to be lost following with the weaker coordinated ligands. As the temperature reaches ~200° C, the compound begins to decompose by one or two large weight losses.



**Figure 4.15** Thermogravimetric analysis for **17**, **18**, **19**, and **20**.

For **17**, the loss of the two MeCN ligands again follows a two-step process as in above for **12**, but at a considerably higher temperature (~78 and 95° C) with the total loss

of 10.6% seen at  $\sim 182^\circ\text{C}$  which appears to correspond to the two MeCN ligands (theoretical 10.9%). Since the Cu – N bond lengths for both **12** and **17** are quite similar, there might be other variables such as to account for this difference such as the grain size of the material placed into the TGA. The span between each loss-step for both compounds is the similar at a  $\sim 20^\circ\text{C}$  difference so perhaps looking at these losses relative to the specific experiment is essential for analyses such as these.

In **18** and **19**, the immediate loss of the included THF is observed, with it somewhat more rapid with **18** at  $\sim 40 - 67^\circ\text{C}$ , than with **19** at  $\sim 107 - 150^\circ\text{C}$ . While we cannot seem to account for the water loss directly in **18**, combining the theoretical weight percents for both THF and water (17.0 and 2.1%, respectively) accounts for the observed 19.1% loss and indicates a simultaneous loss of THF and water. We can clearly isolate the loss of both the THF and MeCN ligand in **19**, with 11.3% in the first step for THF and 4.3% for the MeCN (theoretical 9.0 and 5.2%, respectively). The MeCN ligand in **19** remains until  $\sim 160^\circ\text{C}$ , which is comparable to what we saw for the second MeCN ligand in **17**.

In the dimer **20**, with the absence of any included solvent only the lone coordinated MeCN ligand is lost before the material decomposes. It is interesting that its loss of 2.6% (theoretical 2.9%) does not occur until  $\sim 164^\circ\text{C}$ . This mimics the higher temperature loss of the MeCN ligand in **18** and **19**.

The final decomposition for these four compounds varies somewhat, but for the compounds **17**, **18**, and **20**, this decomposition starts at around  $180^\circ\text{C}$  and occurs gradually in a series of steps. Analysis of these steps reveals no relationship with any of the components and could be a number of phenyl groups, carbon and sulfur compounds as the sample decomposes. The compound of **19** remains intact until  $\sim 250^\circ\text{C}$ , then

decomposes in one rapid step. A black residue remained at the end of each run for **17**, **18**, **19**, and **20** with a final weight of 15.4, 13.2, 18.6, and 16.2 % the original mass, respectively. While this residue has not been analyzed, it most likely consists of a mixture of CuO and Cu<sub>2</sub>O (theoretical ~10.5 % and 9.3 % of the original mass, respectively).

## 4.4 Conclusion

The rapid crystallization of **13** and **14** following the dissolution of **12** suggests an immediate metathesis reaction involving ligand displacement and anion coordination in either THF or toluene. It is interesting to note that in the absence of MeCN solvent, the triflate anion will displace one of the MeCN ligands but, while a high THF concentration can displace the other MeCN ligand, it still cannot overcome the triflate anion's coordination ability to the copper center. This is a clear indication that coordination strength increases in the order of THF < CF<sub>3</sub>SO<sub>3</sub> < MeCN. Though we do not have any mechanistic data, we infer that the anion coordination is key; the perfluorinated anions do not display the same kind of reactivity, even in a huge excess of THF. Once the anion is coordinated forming a neutral species, the solvent replacement seems to be facilitated. This may be the reason for the differences we have observed in the assembly of extended coordination solids containing these different anions. The lack of identical reactions conditions for the synthesis of **16** probably results from the decreased solubility of the perchlorate salts. Though triflate ions could act as bridging ligands through the —SO<sub>3</sub> end, the added steric requirements of the CF<sub>3</sub> group apparently precludes the formation of a triflate-bridged dimer.

Although  $[\text{Cu}(\text{MeCN})_2(\text{PPh}_3)_2](\text{CF}_3\text{SO}_3)$  is essentially isostructural to its  $\text{BF}_4^-$ ,  $\text{ClO}_4^-$ , and  $\text{PF}_6^-$  analogues, subtle differences in ligand positioning require three complexes in the asymmetric unit and therefore a threefold increase the unit cell volume. The increased coordinating ability of the triflate anion further differentiates this compound from the others as two new, neutral compounds are formed in the absence of acetonitrile solvent. The similarities in both structure and thermal decomposition of both **13** and **14** provide a rationalization for the invariance observed in the self-assembly of the coordination networks using Cu(I) triflate salts as starting materials.

The results found with the  $\text{HSO}_4^-$  system indicate its similarity with both the triflate and perchlorate systems. However, the continued lack of any THF coordination found with this system as well as this material's profound affinity toward water is an interesting and important difference. Such behavior seems to set the material with hydrogen sulfate anion into its own unique category relative to the other starting materials we have studied. It is possible that this material's activity towards water, and lack of the same with THF may be responsible for the difference we have encountered in its early-on use in the synthesis of the Cu-bpy coordination polymers and could become a crucial component in our understanding of these self-assembly mechanisms.



## References

1. (a) Lopez, S.; Keller, S. W.; *Cryst. Eng.* **1999**, *2*, 101, (b) Knaust, J. M.; Lopez, S.; Keller, S. W.; *Inorg. Chim. Acta*, **2001**, 81-89. (c) Blake, A. J.; Brooks, N. R.; Champness, N. R.; Crew, M.; Deveson, A.; Fenske, D.; Gregory, D. H.; Hanton, L. R.; Hubberstey, P.; Schroder, M.; *Chem. Commun.* **2001**, 1432. (d) Bu, X.; Chen, W.; Hou, W.; Du, M.; Zand, R.; Brisse, F., *Inorg. Chem.* **2002**, *41*, 3477-3482.
2. (a) Lopez, S.; Keller, S. W.; *J. Am. Chem. Soc.* **1999**, *121*, 6306. (b) Lopez, S.; *PhD Thesis*, University of Missouri, **2001**.
3. Lawrance, G. A.; *Chem. Rev.* **1986**, *86*, 17.
4. Hanna, J. V.; Hart, R. D.; Healy, P. C.; Skelton, B. W.; White, A. H.; *J. Chem. Soc., Dalton Trans.* **1998**, 2321.
5. Knaust, K. M.; Knight, D. A.; Keller, S. W.; *J. Chem. Cryst.* **2003**, *33*, 813.
6. Sinn, E.; Woodward, S.; *Polyhedron* **1993**, *12*, 991.
7. Bruker (1998). *SMART* and *SAINT*. Bruker AXS Inc.. Madison, Wisconsin, USA.
8. Sheldrick, G. M. *SHELXS-90, program for Structure Solution*; University of Gottingen: Germany, 1991.
9. (a) Sheldrick, G. M. *SHELXL-90, program for Structure Refinement*; University of Gottingen: Germany, 1991. (b) Barbour, L. X-SEED, *Graphical Interface for SHEL-X*; University of Columbia, MO, 2000.
10. Jones, P. G.; Crespo, O.; *Acta Cryst.* **1998**, *C54*, 18.
11. Csoregh, I; Kierkegaard, P.; Norrestam, R.; *Acta Cryst.* **1975**, *B31*, 314.
12. Black, J. R.; Levason, W.; Webster, M.; *Acta Cryst.* **1995**, *C51*, 623.
13. Hart, R. D.; Healy, P. C.; Peake, M. L.; White, A. H.; *Aust. J. Chem.* **1998**, *51*, 67.
14. Orpen A. G.; Brammer, L.; *J. Chem. Soc. Dalton Trans.* **1989**, S1.
15. Pearson, R. G.; *Inorg. Chim. Acta* **1995**, *240*, 93.
16. Douglas, B.; McDaniel, D.; Alexander, J.; *Concepts and Models of Inorganic Chemistry*, 3<sup>rd</sup> Ed., Wiley, New York, 1994.

17. Hati, S.; Datta, D.; *Proc. Indian Acad. Sci. (Chem. Sci.)*, **1997**, *108*, 143 and references therein.
18. (a) Datta, D.; *Indian J. Chem. Sec. A, (Chem. Sci.)*, **1987**, *26*, 605. (b) Hathaway, B. J.; in *Comprehensive Coordination Chemistry: The Synthesis, Reactions, Properties, and Applications of Coordination Compounds*, ed. Wilkinson, G.; Pergamon, Oxford, 1987, vol. 5, chap. 53.
19. (a) Naskar, J. P.; Hati, S.; Datta, D.; Tocher, D.; *Chem. Commun.* **1997**, 1319. (b) Naskar, J. P.; Chowdhurry, S.; Drew, M.; Micheal, G. B.; Datta, D.; *New J. Chem.*, **2002**, *26*, 170. (c) Munakata, M.; Kitagawa, S.; Ujjimaru, N.; Nakamura, M.; Maekawa, M.; Matsuda, H.; *Inorg. Chem.*; **1993**; *32*, 826. (d) Olmstead, M. M.; Musker W. K.; Kessler, R. M.; *Transition Met. Chem. (London)*, **1982**, *7*, 140.

# SELF-ASSEMBLY INTERMEDIATES

## 5.1 Introduction

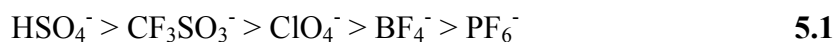
In Chapter 3 we showed how there is a strong relationship between the morphology of the Cu(I) coordination network that is obtained and the variances in either the anion or solvent system used in its synthesis. These results left us with several questions on how such a dramatic change can occur in the resulting coordination networks structure by simply making substitutions for either the anion or solvent in these self-assembly reactions; even when neither of these species is found to actually be part of the resulting coordination network.

We also showed in equation 3.2, that the transformation of the Cu(I) salt starting material from a *bis*- to a *mono*-PPh<sub>3</sub>, an important step in the layered coordination solid formation, could be accomplished by the introduction of small amounts of either THF or toluene to the chloroform reaction solvent. However, in reactions using triflate or hydrogen sulfate anion, this same important step is accomplished even without a trace of either THF or toluene.

The metathesis reactions presented in Chapter 4 provided valuable information regarding the reactivity of the anion and solvents used in our reactions. Some of these species present in our reactions seem to take on an active role and participate in the Cu(I) coordination, while other species are not so active and perform more like spectators than

participants. Nevertheless, we should not rush to classify these anions or solvents as being non-coordinating spectators. The fact that we had not yet come across an anion-coordinated structure with one particular anion does not imply that the anion itself is a non-coordinating anion or such a compound could not exist.

Some 30 years ago the term of *non-coordinating* anion was challenged and a more accurate term of *weakly coordinating anion* was suggested as a replacement.<sup>2, 3</sup> Among the anions used in our current study, those oxoanions and fluoroanions all have varying degrees of coordinating ability. Based on other studies and our own experience, we can rank these five anions in order of their degree of coordination ability as follows:<sup>2, 4, 5</sup>



This trend appears to follow the increasing amount of electronegativity in both the central and ligand atoms of each anion.

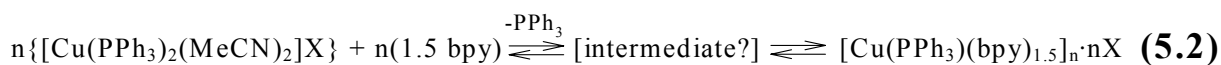
The same analogy can be presented for the so-called *non-coordinating solvents* such as chloroform and toluene. Although we have presented direct evidence that THF can indeed form a coordination bond with copper, we have failed to show any such coordination these the two other solvents mentioned. Just as with the anions, however, we cannot conclude that these chloroform or toluene coordinated copper complexes can not exist, simply because we could not isolate these complexes through any syntheses known to us at this time. The notion of toluene being non-coordinating can be easily discounted with several examples of cation –  $\pi$  bonding involving a variety of metal cations bonding to toluene with this weak, yet formidable intermolecular interaction we had presented in Chapter 1.<sup>6</sup> Although we have not come across any mention of coordinated chloroform, a

close second to this, dichloromethane is also generally considered non-coordinating; yet at least one CH<sub>2</sub>Cl<sub>2</sub> – coordinated structure is known to exist.<sup>2, 5a, 7, 8</sup>

As we had pointed out before in Chapter 1, self-assembly is a continual process involving various molecular components undergoing coordination, exchange, and recoordination of the reaction species present in the solution as the system strives to obtain the most thermodynamically favored structure possible with the given conditions. At some point during the self-assembly, there must be supramolecular species present that are *intermediate structures* that specifically lead to the specific polymorph that is developed as is dictated by the reaction components present.

The study of intermediate structures is nothing new it is an important part of many studies to gain an understanding of the processes and complex structures of proteins,<sup>9</sup> or to help map out elaborate organometallic reaction mechanisms.<sup>10</sup> This same type of intermediate structure investigation should also provide some answers regarding the type of forces or conditions that may or may not be involved in the self-assembly process leading to the various polymorphs we have previously mentioned.

Therefore, we need to modify our original reaction for the layered coordination solid (from equation 3.1) as we include a general form of an intermediate step in our equation as:



Although the identity of this intermediate is not immediately known (even the point of the PPh<sub>3</sub> loss is not exactly known), we can still speculate a number of different forms

it might take on. For example, if these are the anion-coordinated species we might find,  $\text{Cu}(\text{PPh}_3)_2(\text{MeCN})(\text{X})$ ,  $\text{Cu}(\text{PPh}_3)(\text{MeCN})_2(\text{X})$ , or even  $\text{Cu}(\text{PPh}_3)(\text{bpy})(\text{X})$  as intermediates.

If solvent coordination dominates the reaction, we might see intermediates in the form of  $[\text{Cu}(\text{PPh}_3)_2(\text{MeCN})(\text{L})](\text{X})$ ,  $[\text{Cu}(\text{PPh}_3)(\text{MeCN})_2(\text{L})](\text{X})$ , or as  $[\text{Cu}(\text{PPh}_3)(\text{bpy})(\text{L})](\text{X})$ . Of course the exact identity of the intermediate should depend upon the anion and solvent used in the reaction and whether or not the  $\text{PPh}_3$  ligand is lost before or after the intermediate formation. To complicate the issue, if the self-assembly follows a path as dictated in Chapter 1, we *could* expect to see any, if not ALL of the above compounds in a single reaction at some point in-between the initial mixing and the crystallization of the final product.

In this chapter, we present what might be considered the intermediate compounds of the Cu(I) coordination reactions. Since these self-assembly processes cannot simply be stopped in the middle, we simulated a partial self-assembly by limiting the amount of bpy used in the reaction. The structures shown here are those Cu(I) coordination polymers with the  $\text{CF}_3\text{SO}_3^-$ ,  $\text{ClO}_4^-$  and  $\text{BF}_4^-$  anions developed by reactions in THF solvent alone with less than the 1.5 equivalents of bpy required to produce a layered coordination solid. By analysis of these resulting structures, we hope to show the connection between the anion, solvent, and the resulting extended solids that are produced.

## 5.2 Experimental

### 5.2.1 General Methods

*Caution! Perchlorate salts are explosive and should be handled in small quantities and with extreme care at all times.*  $\text{Cu}_2\text{O}$ ,  $\text{HPF}_6$ ,  $\text{HBF}_4$ ,  $\text{HClO}_4$ ,  $\text{H}_2\text{SO}_4$  and 4,4'-bipyridine

(ACROS); acetonitrile, tetrahydrofuran, chloroform, dichloromethane, and diethyl ether (Fisher); triflic acid and triphenylphosphine (Aldrich), were used without further purification. All the  $[\text{Cu}(\text{MeCN})_2(\text{PPh}_3)_2]\text{X}$  salts for  $\text{X} = \text{BF}_4^-$ ,  $\text{PF}_6^-$ ,  $\text{ClO}_4^-$ ,  $\text{CF}_3\text{SO}_3^-$ ,  $\text{HSO}_4^-$ , were prepared using published methods and as described in Chapter 2.<sup>11, 12</sup>

### 5.2.2 Synthesis

#### *Cu(C<sub>10</sub>H<sub>8</sub>N<sub>2</sub>)(PPh<sub>3</sub>)(CF<sub>3</sub>SO<sub>3</sub>), 21*

In a 20 mL vial were combined  $[\text{Cu}(\text{PPh}_3)_2(\text{MeCN})_2]\text{CF}_3\text{SO}_3$  (0.030 g, 0.037 mmol) in 4 mL of THF and 4,4'-bipyridine (0.006 g, 0.037 mmol) in 4 mL of THF. The vial was sealed and left at room temperature. Yellow rhomboid crystals of **21** were harvested after 12 hours. This same compound was produced with 0.003 g (0.019 mmol) and 0.008 g (0.049 mmol) of bpy.

#### *Cu(C<sub>10</sub>H<sub>8</sub>N<sub>2</sub>)<sub>0.5</sub>(PPh<sub>3</sub>)<sub>2</sub>(ClO<sub>4</sub>)·(THF)<sub>3.5</sub>, 22*

In a 20 mL vial were combined  $[\text{Cu}(\text{PPh}_3)_2(\text{MeCN})_2]\text{ClO}_4$  (0.030 g, 0.039 mmol) in 4 mL of THF and 4,4'-bipyridine (0.003 g, 0.019 mmol) in 4 mL of THF. The vial was sealed and left at room temperature. Yellow crystal needles of **22** were harvested after 24 hours.

#### *Cu(C<sub>10</sub>H<sub>8</sub>N<sub>2</sub>)<sub>0.5</sub>(PPh<sub>3</sub>)(ClO<sub>4</sub>), 23*

In a 20 mL vial were combined  $[\text{Cu}(\text{PPh}_3)_2(\text{MeCN})_2]\text{ClO}_4$  (0.030 g, 0.039 mmol) in 4 mL of THF and 4,4'-bipyridine (0.006 g, 0.037 mmol) in 4 mL of THF. The vial was sealed and left at room temperature. Yellow crystal platelets of **23** were harvested after 24 hours.

*[Cu(C<sub>10</sub>H<sub>8</sub>N<sub>2</sub>)(PPh<sub>3</sub>)(THF)]BF<sub>4</sub>, **24***

In a 20 mL vial were combined [Cu(PPh<sub>3</sub>)<sub>2</sub>(MeCN)<sub>2</sub>]BF<sub>4</sub> (0.030 g, 0.039 mmol) in 4 mL of THF and 4,4'-bipyridine (0.006 g, 0.037 mmol) in 4 mL of THF. The vial was sealed and left at room temperature. Yellow prismatic crystals of **24** were harvested after 24 hours.

### *5.2.3 Single Crystal X-Ray Diffraction*

In all cases, a single crystal of high quality (by uniform extinction of polarized light) was coated with light oil and then mounted on a tip of a glass fiber using small amount of silicon grease for adhesion. Crystallographic data was collected using a Siemens SMART system with a CCD area detector (Mo K<sub>α</sub> = 0.71070 Å). During data collection, the crystal was cooled to 173 K. The initial space group was determined by indexing several hundred strong reflections and the structures were solved using Direct Methods.<sup>13</sup> The structure models were further refined using least-squares techniques.<sup>14</sup>

For each structure, the majority of the heavier atoms were located with the initial solution. Any remaining non-hydrogen atoms were usually located after the first or second refinements. Anisotropic thermal parameters were refined for all non-hydrogen atoms. The hydrogen atoms were included in calculated positions and refined as riding models with fixed U<sub>iso</sub> = 1.2U<sub>iso</sub> of the carbon atom for which they are bonded. Details of the data collection and structure solutions are given in Table 5.1.



	<b>21</b>	<b>22</b>	<b>23</b>	<b>24</b>
Empirical formula	CuC <sub>29</sub> H <sub>23</sub> F <sub>3</sub> N <sub>2</sub> O <sub>3</sub> PS	CuC <sub>55</sub> H <sub>62</sub> O <sub>8</sub> P <sub>2</sub> Cl	CuC <sub>28</sub> H <sub>23</sub> N <sub>2</sub> O <sub>4</sub> PCl	CuC <sub>32</sub> H <sub>31</sub> BF <sub>4</sub> N <sub>2</sub> OP
Formula weight (g·mol <sup>-1</sup> )	631.06	1025.99	581.44	640.91
Temperature, K	173(2)	173(2)	173(2)	173(2)
Crystal System, Space group	Monoclinic, P2 <sub>1</sub> /c	Monoclinic, P2 <sub>1</sub> /n	Orthorhombic, Pc21b	Monoclinic, Cc
Unit cell dimensions				
<i>a</i> (Å)	21.883(2)	9.184(1)	16.603(3)	22.191(2)
<i>b</i> (Å)	16.070(2)	22.989(3)	18.160(3)	9.9108(6)
<i>c</i> (Å)	17.910(2)	24.268(3)	18.390(3)	17.003(1)
$\alpha$ , deg	90	90	90	90
$\beta$ , deg	113.532(2)	92.166(3)	90	126.195(1)
$\gamma$ , deg	90	90	90	90
<i>Z</i>	8	4	8	4
Volume, Å <sup>3</sup>	5775(1)	5119.8(13)	5545(2)	3017.8(3)
$\rho_{\text{calc}}$ , g·cm <sup>-3</sup>	1.452	1.331	1.393	1.411
Absorption coefficient, mm <sup>-1</sup>	1.359	0.596	0.977	0.830
<i>F</i> (000)	2576	2156	2384	1320
Crystal size, mm	0.4 x 0.4 x 0.1	0.5 x 0.05 x 0.05	0.2 x 0.2 x 0.1	0.2 x 0.2 x 0.1
$\theta$ Range for data collection	1.01 to 17.22	1.22 to 27.14	1.23 to 27.15	2.27 to 20.81
Index ranges	-18 ≤ <i>h</i> ≤ 18 -12 ≤ <i>k</i> ≤ 13 -12 ≤ <i>l</i> ≤ 10	-11 ≤ <i>h</i> ≤ 11 -25 ≤ <i>k</i> ≤ 29 -27 ≤ <i>l</i> ≤ 31	-21 ≤ <i>h</i> ≤ 18 -23 ≤ <i>k</i> ≤ 23 -19 ≤ <i>l</i> ≤ 23	-22 ≤ <i>h</i> ≤ 22 -9 ≤ <i>k</i> ≤ 9 -14 ≤ <i>l</i> ≤ 16
Reflections collected	13020	30980	31774	5258
Unique reflections	3500 [ <i>R</i> <sub>int</sub> = 0.0295]	11268 [ <i>R</i> <sub>int</sub> = 0.1188]	11926 [ <i>R</i> <sub>int</sub> = 0.1034]	2632 [ <i>R</i> <sub>int</sub> = 0.0313]
Completeness to $\theta$	17.22 (100.0%)	27.14 (99.3 %)	27.15 (99.3 %)	20.81 (100.0 %)
Max/min transmissions	1.00000/ 0.768391	0.928052/ 0.623662	0.928052/0.557001	1.00000/ 0.840312
Data/restraints/ parameters	3500/0/721	11268/0/613	11926/1/658	2632/2/379
Goodness of fit <i>F</i> <sup>2</sup>	1.059	1.144	1.056	1.050
Final <i>R</i> indices [ <i>I</i> > 2 $\sigma$ ( <i>I</i> )] <sup>a,b</sup>	<i>R</i> <sub>1</sub> = 0.0317 <i>wR</i> <sub>2</sub> = 0.0692	<i>R</i> <sub>1</sub> = 0.1437 <i>wR</i> <sub>2</sub> = 0.3296	<i>R</i> <sub>1</sub> = 0.1217 <i>wR</i> <sub>2</sub> = 0.2910	<i>R</i> <sub>1</sub> = 0.0348 <i>wR</i> <sub>2</sub> = 0.0803
<i>R</i> indices (all data)	<i>R</i> <sub>1</sub> = 0.0394 <i>WR</i> <sub>2</sub> = 0.0728	<i>R</i> <sub>1</sub> = 0.2143 <i>WR</i> <sub>2</sub> = 0.3185	<i>R</i> <sub>1</sub> = 0.2040 <i>WR</i> <sub>2</sub> = 0.3579	<i>R</i> <sub>1</sub> = 0.0396 <i>WR</i> <sub>2</sub> = 0.0825
Largest difference peak and hole (e·Å <sup>-3</sup> )	0.403/-0.411	1.359/-1.152	2.217/-1.096	0.7311 -0.209
Structures were refined on <i>F</i> <sup>2</sup> for all data. <sup>a</sup> $R(F_o) = \frac{\sum   F_o  -  F_c  }{\sum  F_o }$ . <sup>b</sup> $R_w(F_o) = \frac{(\sum w  F_o  -  F_c  ^2)^{1/2}}{(\sum w F_o ^2)^{1/2}}$ , $w = \frac{1}{\sigma^2(F_o) + (0.002F_o)^2}$ .				

## 5.3 Results and Discussion

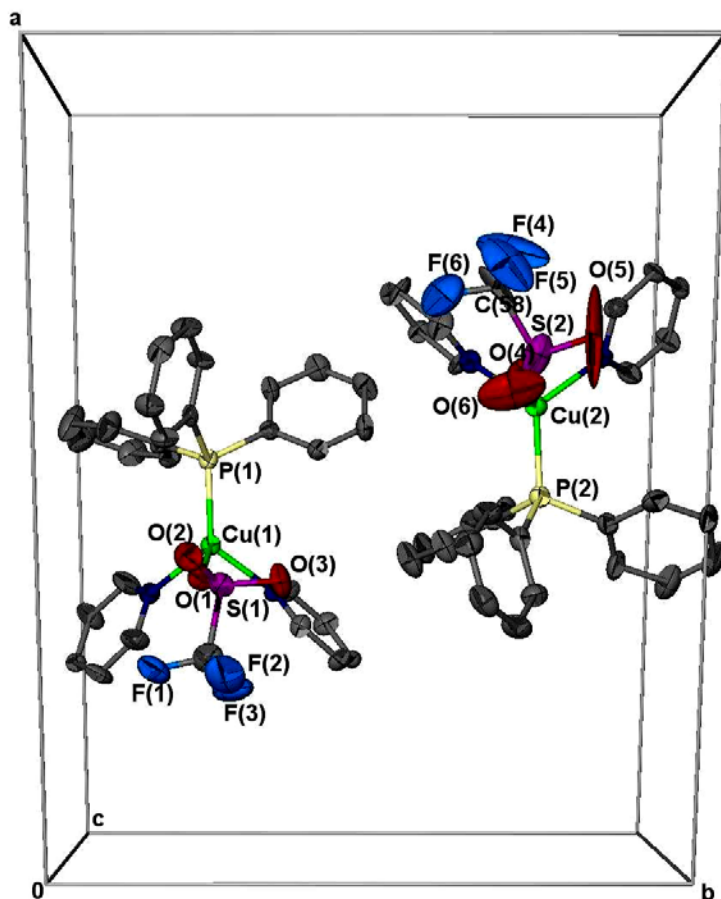
### 5.3.1 The Triflate 1-D Chain

In the reactions involving the  $\text{PF}_6^-$  and  $\text{HSO}_4^-$  anions, while these investigations are ongoing, there have been no significant results at this time. The compounds involving the  $\text{PF}_6^-$  anion continue to be troublesome, producing either precipitate or polycrystalline material. The reactions with  $\text{HSO}_4^-$  are still in progress, yet early results show that no crystallization has occurred with any of the reactions. These results may be related to this materials unique affinity towards water as we presented in Chapter 4.

The reactions involving the triflate anion resulted in the formation of an anion coordinated one-dimensional chain of  $[\text{Cu}(\text{bpy})(\text{PPh}_3)(\text{CF}_3\text{SO}_3)]_n$ , **21**. The discovery of this structure actually occurred by chance during the original layered coordination solid synthesis trials. It was this structures discovery that inspired the intermediate structure evaluation. Later observations found that **21** could be easily synthesized from reactions with slightly less than 1.5 equivalents of bpy and had continued to be produced even in reactions having less than the required 1.0 equivalents of bpy (as per the formula of **21**).

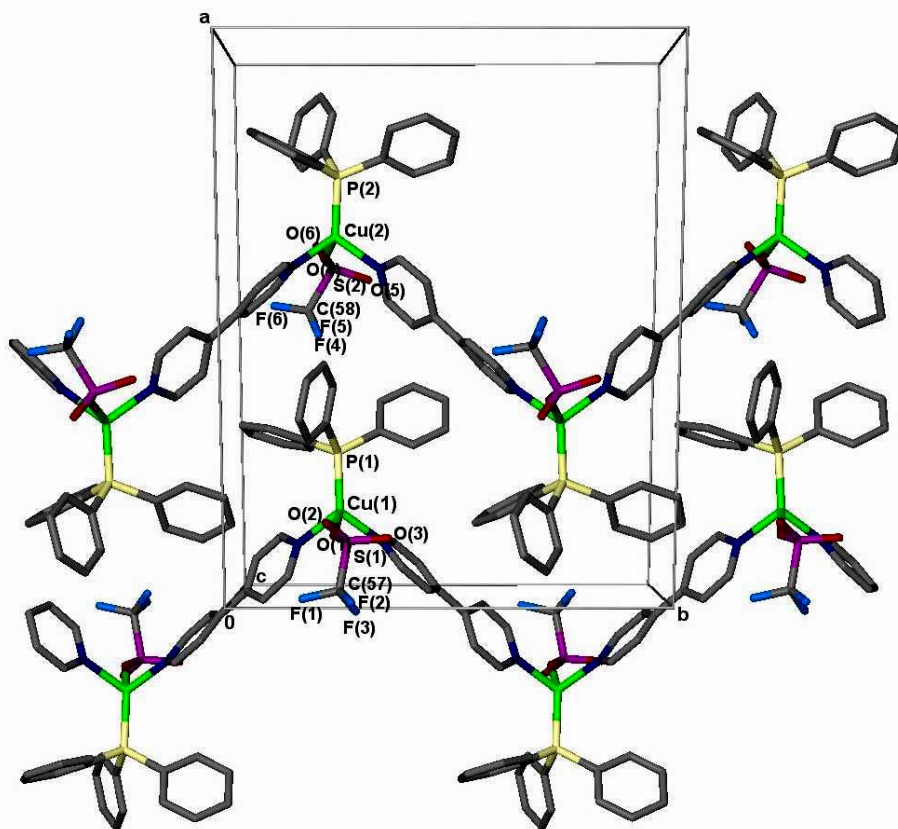
The structure of **21** is a 1-D chain of bpy bridged Cu(I) centers with one  $\text{PPh}_3$  ligand remaining and the forth coordination site being occupied by the triflate anion. The asymmetric unit, as shown in Figure 5.1, consist of two separate Cu(I) coordinated tetrahedra; each of which grow into their own unique one-dimensional chain.

Each of these two tetrahedra is then part of their own individual 1-D chain in the structure as is shown in Figure 5.2. The chains in the structure are locked together by a series of edge-to-face  $\pi$ - $\pi$  stacking interactions between the phenyl rings of the phosphine and bpy ligands at distances of  $\sim 2.9$  Å.



**Figure 5.1** The two tetrahedra of the asymmetric unit of **21** shown in 50% thermal ellipsoids. The hydrogen atoms have been omitted for clarity.

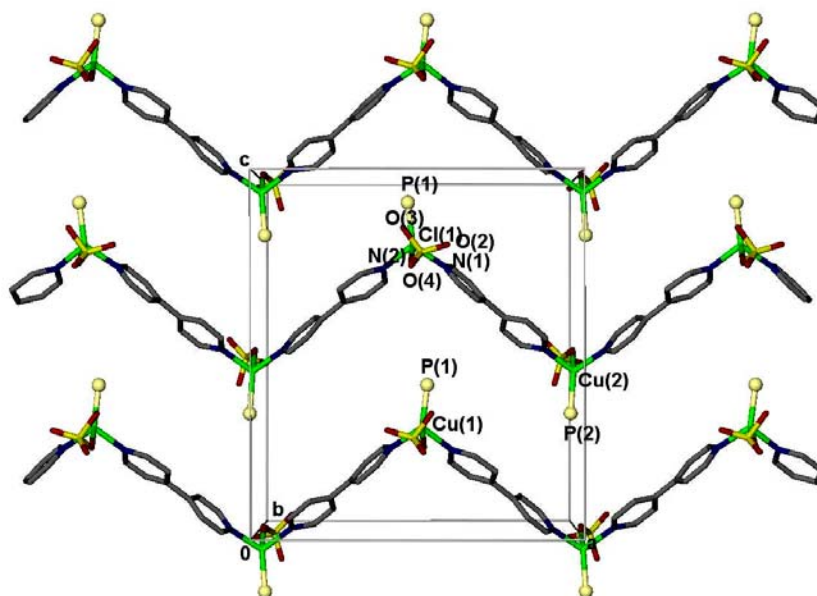
The triflate anions for both tetrahedra are directed out and down (shown in the end view), with the non-coordinated  $-\text{CF}_3$  end directed away from the phosphine ligand, The triflate anion fits into the cleft formed by the two Cu coordinated bpy ligands on the crystallographically identical tetrahedra (i.e. the Cu(1) triflate is directed toward an adjacent chain of Cu(1) tetrahedra, ect.) with a closest chain-to-chain O(2) – Cu(1) and O(6) – Cu(2) distance of  $\sim 4.63$  and  $4.71$  Å, respectively. No solvent, either coordinated or included is found in this structure. The selected distances and angles of the two tetrahedra will be discussed and compared with the other structures in a later section.



**Figure 5.2** (right) The two unique chains developed from the bpy coordination of both Cu(1) and Cu(2) in **21** shown in stick representation as is seen looking down the c-axis of the unit cell. The most apparent interaction between these chains are the edge-to- $\pi$  stacking between the phosphine phenyl rings and the bpy ligands. Hydrogen atoms have been omitted for clarity.

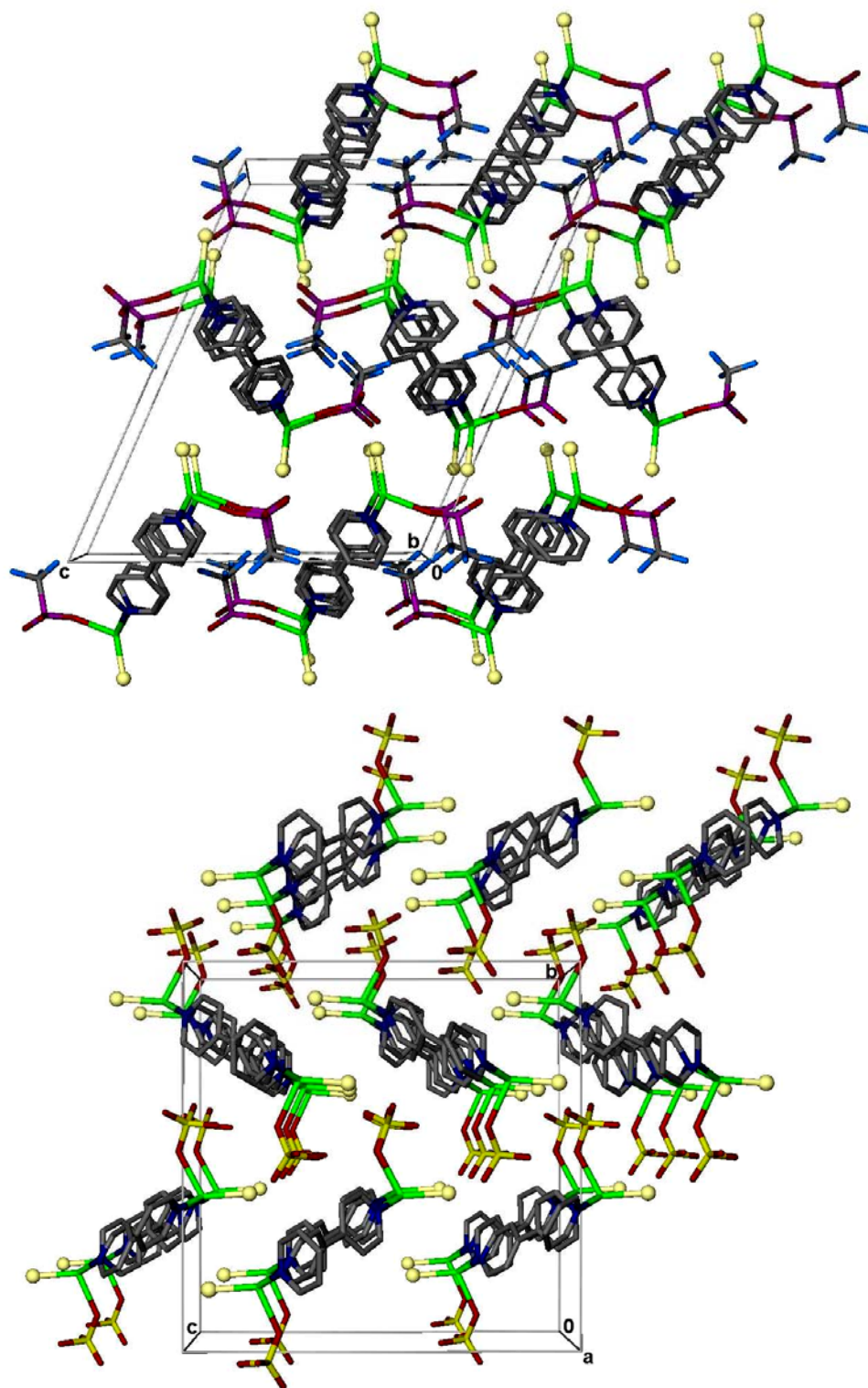
### 5.3.2 The Perchlorate 1-D Chain and Dimer

The reaction of the  $[\text{Cu}(\text{MeCN})_2(\text{PPh}_3)_2](\text{ClO}_4)$  with 1.0 equivalents of bpy resulted in a structure very much like **21**, as the  $\text{ClO}_4^-$  coordinated 1-D chain,  $[\text{Cu}(\text{bpy})(\text{PPh}_3)(\text{ClO}_4)]_n$ , **22**. Although **22** has the same basic components as is in **21**, a close examination reveals that these two structures have a slightly different orientation about the Cu(I) center. Figure 5.3 shows 3 chains as they stack in **22**, which look very similar to those seen in **21**. However, this views perspective is essentially the same given for **21** shown in Figure 5.2. It appears that the perchlorate and phosphine in **22** have switched positions relative to those in **21** in relation to the packing of the structure.



**Figure 5.3** Stick representation of **22** showing the reversed positioning (with respect to **21**) of the anion and phosphine ligands. The phenyl rings on the phosphine and hydrogen atoms have been omitted for clarity.

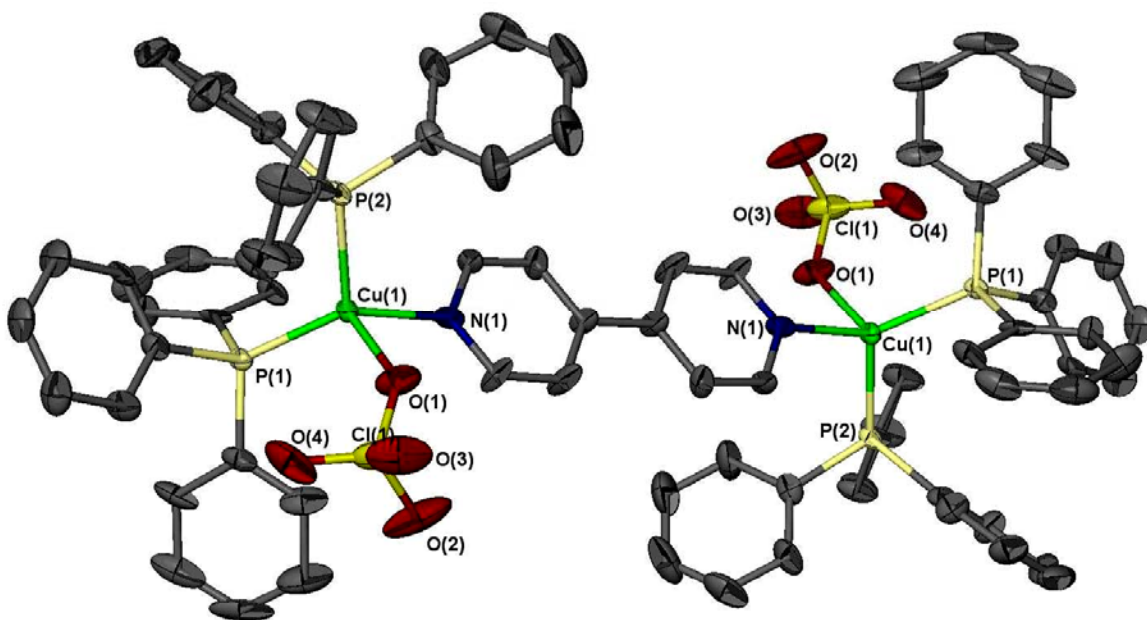
A view at the end of the chains in each structure, as shown in Figure 5.4, helps to confirm these findings. For each row of chains seen in (top) **21**, the phosphines are directed both downward and upward going along the chain, while the triflate anions are directed towards either side. Those same rows of chains shown for (bottom) **22** show the  $\text{ClO}_4^-$  anion now directed up and down while the phosphine point towards either side. From this view, we might be able to attribute this ligand switch to the smaller size of each anion as the larger triflate anion is forced away from the phosphine ring while the perchlorate is not. Even with this difference, the distance between each chain is comparable to that seen with the triflate anion with the closest distances of  $\text{O}(4) - \text{Cu}(1)$  and  $\text{O}(8) - \text{Cu}(2)$  at  $\sim 4.75$  and  $5.10 \text{ \AA}$ , respectively. As was with **21**, there is no THF solvent either coordinate or included in **22**.



**Figure 5.4** Stick representations of (top) **21** and (bottom) **22** showing how the anions and phosphines have switched positions relative to each other. The phenyl rings and hydrogen atoms have been omitted for clarity.

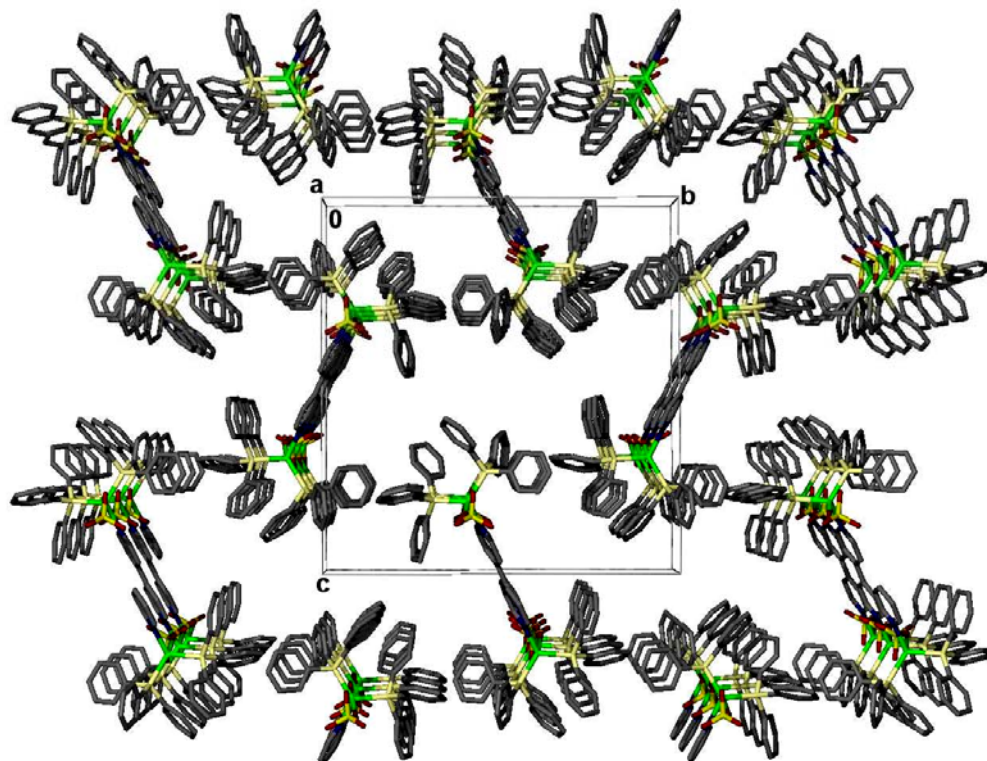
Another structure type with the perchlorate anion was crystallized, as the amount of bpy used is less than 0.5 equivalents. At around 0.25 equivalents, a new structure is obtained taking on the form of a dimer in the structure of  $\text{Cu}(\text{bpy})_{0.5}(\text{PPh}_3)_2(\text{ClO}_4) \cdot (\text{THF})_{3.5}$ , **23**.

The asymmetric unit in **23** consist of only one crystallographically independent Cu(I) tetrahedron, which grows into a  $\text{ClO}_4^-$  coordinated dimer as shown in Figure 5.5.



**Figure 5.5** The dimer found in the structure of **23** shown in 50% thermal ellipsoids. Each of the two tetrahedra shown are crystallographically identical, with only one found in the asymmetric unit. The hydrogen atoms and solvated THF have been omitted for clarity.

Probably the most striking feature of this structure is the presence of *both* triphenylphosphine ligands. While placing this structure in combination with that of **22**, we could be looking at examples of the step-by-step that leads to the formation of the layered coordination solid involving the  $\text{ClO}_4^-$  anion. Also seen different with **23** is the considerable amount (1.0:3.5 Cu:THF) of THF packed into this structure. This THF solvent is found within the cavities that are formed by the packing of the dimer units. The packing of **23** is shown in Figure 5.6 below.



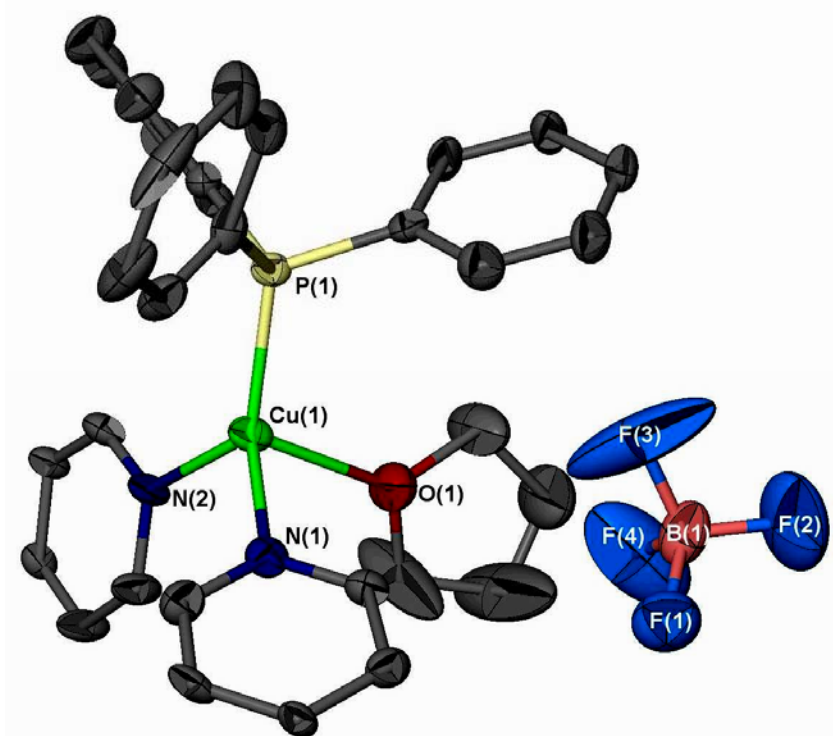
**Figure 5.6** A view in stick representation of the extended packing of the dimers in **23** showing as looking down the a-axis. The cavities shown here contain the 3.5 THF molecules per Cu (not shown) solvated in the structure. Hydrogen atoms are also omitted for clarity.

### 5.3.3 The Tetrafluoroborate (THF Coordinated) Chain

The final structure in this study was obtained from the reaction of the  $[\text{Cu}(\text{MeCN})_2(\text{PPh}_3)_2]\text{BF}_4^-$  with amounts  $>1.5$  equivalents of bpy in THF. Although a 1-D chain was also produced in this reaction, this time the THF solvent coordinated to the Cu(I) center, in place of the very weakly coordinating  $\text{BF}_4^-$  anion. The resulting structure,  $[\text{Cu}(\text{bpy})(\text{PPh}_3)(\text{THF})]_n \cdot n\text{BF}_4$ , **24**, has only one Cu(I) complex in the asymmetric unit as shown in Figure 5.7. The  $\text{BF}_4^-$  anion in this structure is disordered over two positions about the F(1)-B(1) axis resulting in unusually large anisotropic thermal parameters on F(3) and F(4). The coordinated THF also has a slight degree of non-symmetrical disorder resulting in two of its carbon atoms also having large anisotropic thermal parameters. The coordination about the Cu center is considerably distorted away from a normal tetrahedral



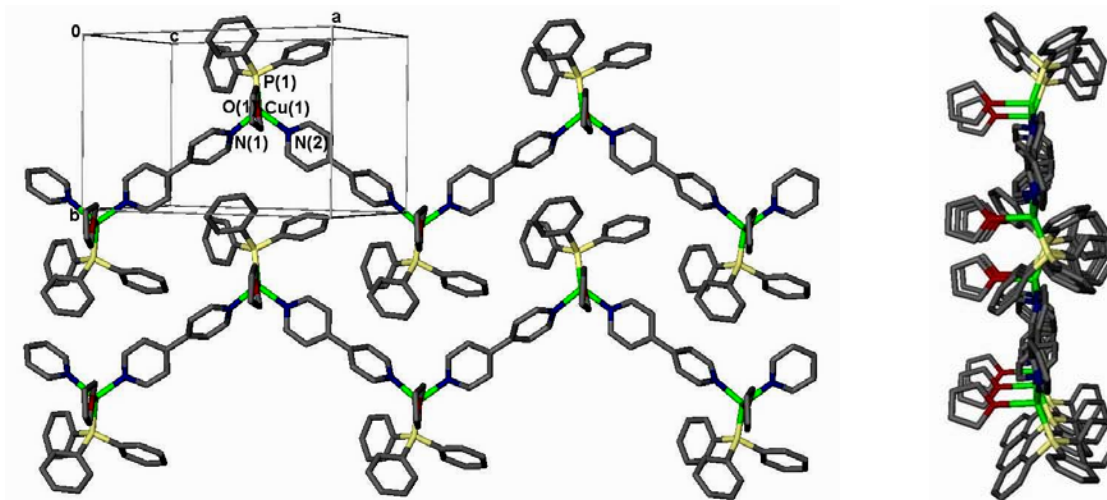
geometry. The distances and angles found in the tetrahedron will be presented in the following section along with the comparison with the other three structures.



**Figure 5.7** The asymmetric unit of **24** shown in 50% thermal ellipsoids. The hydrogen atoms have been omitted for clarity.

The resulting chain formed by the coordination of these distorted, THF coordinated Cu(I) tetrahedra is significantly different than either the triflate or perchlorate coordinated chains. The biggest difference is that the coordinated THF is positioned on only one side throughout the length of a chain. Recall that in **21** and **22**, the positioning of the coordinated anion alternates sides going from one copper center to the next. In addition, ALL the chains of the structure have the coordinated THF positioned on the same side. Figure 5.8 shows two chains as they are stacked together, as viewed (left) along the length of the chains and (right) looking down from the end of the same chains. The effect of the distorted tetrahedra is also seen in the way the PPh<sub>3</sub> ligands are directed straight up and down; instead of tilted to one side or the other as in **21** and **22**. As was with the other

chains, the phenyl rings on the phosphines lock the chains together in the stack and in-between the rows.



**Figure 5.8** Two chains from **24** shown in stick representation as viewed (left) lengthwise and a view (right) from the ends of the same two chains. Note how THF is always on one side and the phosphine ligands are more straight up and down other than tilted to the side as in **21** and **22**. The anions and hydrogen atoms have been omitted for clarity.

### 5.3.4 Coordination Spheres of the Intermediate Structures

This final section covers the selected distances and angles found in the Cu(I) coordination spheres of the intermediate structure presented in this chapter. Table 5.2 list all the selected distances and angles in the same manner as was for those extended solids we presented in Chapter 3. Along with the numerical analysis, we also show the tetrahedra as found in each structure listed. For those structures with two tetrahedra per asymmetric unit, only one will be presented as they are both essentially identical and any subtle differences between the two can be discussed sufficiently with the numerical listings.

At first glance, those tetrahedra with the triflate or perchlorate anion coordinated are fairly symmetrical and close to what a normal tetrahedral structure might look like. It appears that the angles of both the bpy ligands and the anions are approximately equal and, these three ligands are pushed away (downward) from the PPh<sub>3</sub> ligand, most likely

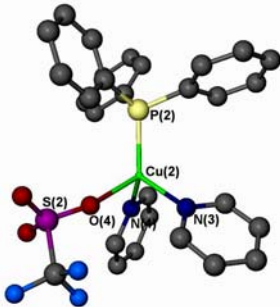

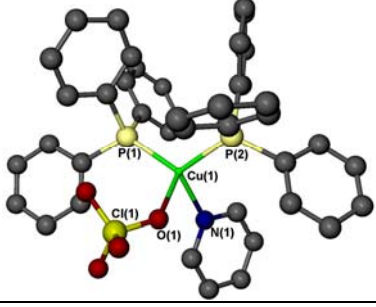
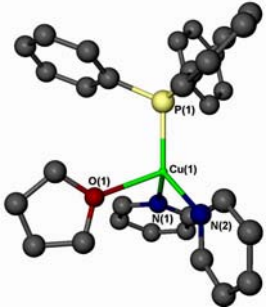
due to its steric bulk. It is hard to compare the tetrahedra in **23** to the rest of the structures since both PPh<sub>3</sub> are retained in this structure. However, this too looks symmetrical, with the bpy-to-anion angle appearing constricted as they are pushed away from the phosphine ligands. The last tetrahedron in the list has a distinctive non-symmetrical appearance. It is easy to see how this tetrahedron is tilted to one side, reminiscent of those tetrahedra found with the ladder chain or the pentagonal cavity layers.

The best analysis, of course is the comparison of the numerical values. As we look at those seen in **21**, we are reminded of how symmetrical the tetrahedron looks, as the angles themselves are relatively equal from the PPh<sub>3</sub> ligand to the other three ligands (two bpy and the triflate), along with the equality seen with the shared angles of those three ligands. A slight but notable difference is in reduction of both the bpy-to-phosphine angle in Cu(1) and the triflate-to-phosphine angle in Cu(2). This could be related to packing as the chains stack together with the triflate of one chain located in close proximity to the phenyl rings on the phosphine of another chain (closest F – H<sub>Ph</sub> = 2.5 Å).

Comparing these results with those for the tetrahedra with the coordinated perchlorate anion, we can again see similar symmetry in the angles about the Cu(I) center. However, the angle P – Cu – O angle formed by coordinated anion in this case is considerably smaller. This could be the results of the same packing effects as seen in **21** with greater results because of the longer, weaker bond for the coordinated perchlorate anion. This may account for the distortion we had noticed in the hexagon cavities in the honeycomb layers found in **8** as compared to the more symmetrical hexagon cavities found associated with the HSO<sub>4</sub><sup>-</sup> anion in **11**. Although results for the hydrogen sulfate

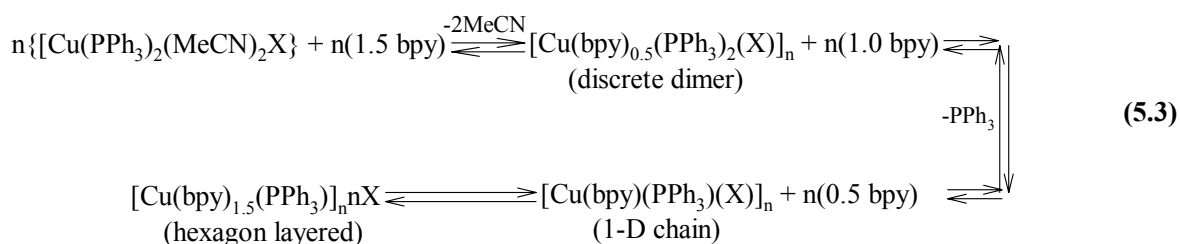
anion are still pending, we could imagine a trend that relates the stronger coordinating anion with the greatest symmetry of the resulting tetrahedron.

**Table 5.2** Selected Bond Lengths (Å) and Angles (deg.) for Structures **21**, **22**, **23**, and **24**

<b>21</b>			
Triflate 1-D Chain	Structures	Cu(1)	Cu(2)
	Cu – P	2.178(2)	2.177(2)
	Cu – O	2.223(4)	2.223(4)
	Cu – N	2.068(5)	2.048(5)
	Cu – N	2.042(5)	2.045(5)
	P – Cu – O	120.3(1)	116.2(1)
	N – Cu – P	120.2(2)	121.8(2)
	N – Cu – P	123.0(2)	120.6(2)
	N – Cu – O	90.3(2)	90.9(2)
	N – Cu – O	96.7(2)	99.5(2)
N – Cu – N	99.3(2)	102.2(2)	
<b>22</b>			
Perchlorate 1-D Chain	Structures	Cu(1)	Cu(2)
	Cu – P	2.172(4)	2.185(4)
	Cu – O	2.28(1)	2.34(1)
	Cu – N	2.04(2)	2.06(1)
	Cu – N	2.01(1)	2.04(1)
	P – Cu – O	92.9(5)	114.0(3)
	N – Cu – P	128.8(4)	126.9(4)
	N – Cu – P	119.9(4)	121.9(3)
	N – Cu – O	96.3(5)	92.0(4)
	N – Cu – O	110.4(4)	91.2(5)
N – Cu – N	100.6(6)	101.6(5)	
<b>23</b>			
Perchlorate Dimer	Structure		
	Cu – P(1)	2.238(3)	
	Cu – P(2)	2.265(3)	
	Cu – O	2.255(9)	
	Cu – N	2.067(8)	
	P(2)–Cu–P(2)	117.9(1)	
	N – Cu – P(1)	122.0(3)	
	O – Cu – P(1)	114.2(3)	
	N – Cu – P(2)	109.1(3)	
	O – Cu – P(2)	98.4(2)	
	O – Cu – N	89.1(3)	
<b>24</b>			
Tetrafluoroborate THF Coordinated 1-D Chain			
	Cu – P	2.195(2)	
	Cu – O	2.294(4)	
	Cu – N(1)	2.055(5)	
	Cu – N(2)	2.069(5)	
	O – Cu – P	109.3(1)	
	N(1) – Cu – P	121.1(2)	
	N(2) – Cu – P	126.8(2)	
	N(1) – Cu – O	91.3(2)	
	N(2) – Cu – O	95.0(2)	
	N(1)–Cu–N(2)	104.2(2)	

The tetrahedron found in the next structure, **23** is difficult to compare with the other two, since both the PPh<sub>3</sub> ligands are in place. However, we can at least see how, what might be considered an earlier step in these self-assembly reactions, appears and perhaps would help formulate an order of assembly of these extended solids, thus obtain an understanding of how each species influences the others in order to reach the final product.

It is interesting to see that the anion coordinates, along with one bpy ligand *prior* to the removal of the extra PPh<sub>3</sub> ligand, suggesting that the coordinating anion, itself, is the necessary component in this reaction that leads to the required mono-PPh<sub>3</sub> arrangement (equation 3.1). The next step should be that of the formation of **22**, as the second bpy ligand comes along and replaces one PPh<sub>3</sub> ligand. Then, of course, the final step to the formation of the layered coordination solid occurs as a third, bridging bpy ligand replaces the perchlorate as the extended solid takes form. If this is indeed the case, and if the other two oxoanions of HSO<sub>4</sub><sup>-</sup> and CF<sub>3</sub>SO<sub>3</sub><sup>-</sup> follow this same course, the former reaction can be modified as follows:



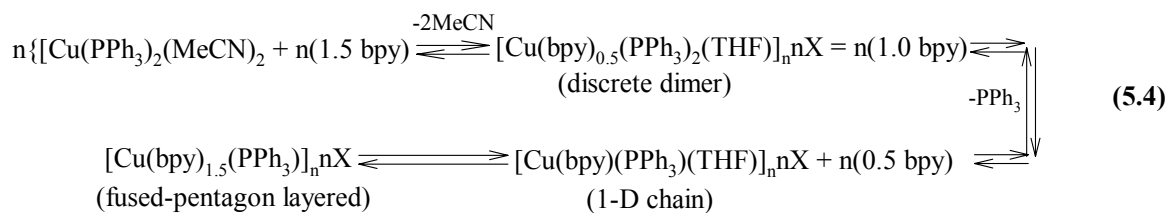
For the formation of the hexagon layered for X = HSO<sub>4</sub><sup>-</sup>, CF<sub>3</sub>SO<sub>3</sub><sup>-</sup>, and ClO<sub>4</sub><sup>-</sup>.

Finally, for the compound containing the BF<sub>4</sub><sup>-</sup> anion, we see that the angles do correspond to what we observe visually with the tetrahedron distortion. Essentially, the angle formed by the THF ligand with the PPh<sub>3</sub> ligand is significantly narrower than those

seen with the coordinated anions of **21** and **22**. This might be related to the packing that occurs as the THF is able to remain on one side throughout the length of the chains, or perhaps there is a  $H_{\text{THF}} - \pi$  between the THF and the phenyl rings on the phosphines. In any case, the distortion seen in this tetrahedron is remarkable similar to the distorted tetrahedra seen in both the ladder chains and the layered fused-pentagon coordination solids of **2** and **3**, respectively.

Although no intermediate dimer has been synthesized for this system so far, we can speculate that such a dimer would be similar to **23** and seen possibly as  $[\text{Cu}(\text{bpy})_{0.5}(\text{PPh}_3)_2(\text{THF})]\text{BF}_4$ , with the THF and one bpy coordinating before the release of the extra  $\text{PPh}_3$  ligand. This would make sense since we had found that, upon the addition of THF, the crucial step of removing one  $\text{PPh}_3$  ligand was accomplished. The angles formed during the intermediate stages are translated to the angles found in the final extended solid.

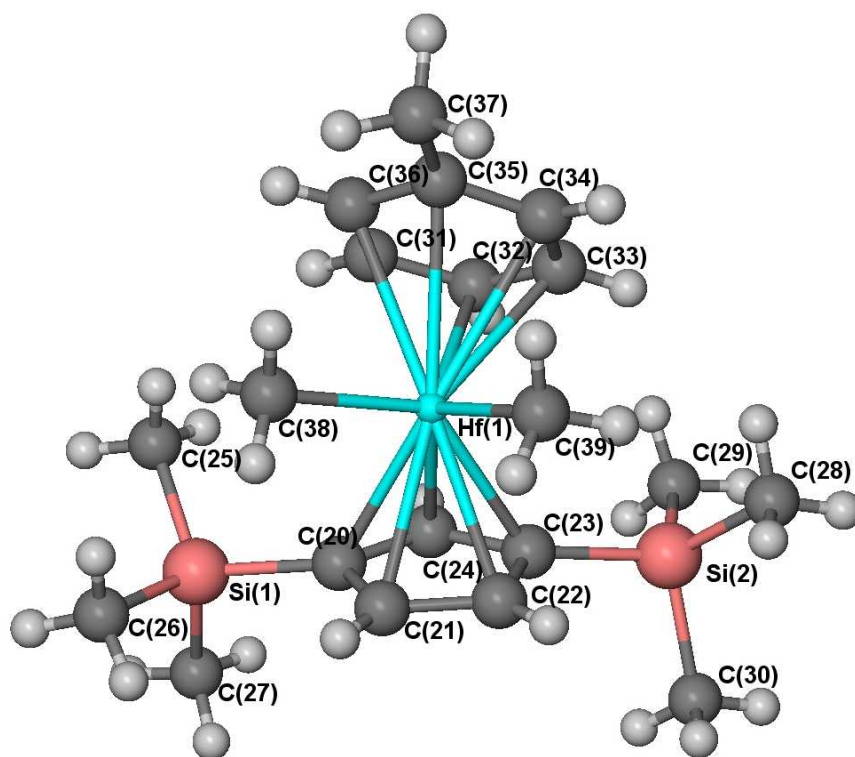
With the information given, and assuming that at high THF concentrations the perchlorate may act more like the  $\text{BF}_4^-$  anion than that of the other oxoanions, we can modify our reaction equation as:



For  $\text{X} = \text{BF}_4^-$  or  $\text{ClO}_4^-$  in the formation of the fused-pentagon layered coordination solid.

In the same light, if the toluene also becomes involved with such a coordination, as did the THF, then we might see a much more dramatic change in the distortion of the

tetrahedron. Figure 5.9 shows a representation of a toluene coordinated complex, as we first introduced early on in this chapter.<sup>6a</sup> If such a weak coordination of toluene does occur for or Cu(I) reactions in the  $\text{CHCl}_3$ :toluene mixture in the presence of a very weak coordinating anion like  $\text{BF}_4^-$ , then the toluene's coordination should be a dominate condition during the initial, intermediate steps in the self-assembly process. If this is the case, then we would expect an incredible influence on the angles of the tetrahedron as the toluene was attached, which could be responsible for the severe angle distortion found in the interpenetrated structure of **4**.



**Figure 5.9** A ball and stick representation of  $[\{\text{C}_5\text{H}_3(\text{SiMe}_3)_2\}\text{HfMe}_2(\eta^6\text{-toluene})][\text{Bme}(\text{C}_6\text{F}_5)_3]$  showing toluene coordination to Hf.<sup>6a</sup>

Although we expected the perchlorate anion to mimic the qualities seen with the  $\text{BF}_4^-$  anion in pure THF, keep in mind that the distortion found in the tetrahedra of this weakly coordinating anion is apparent in both the intermediate structures and the final extended layered solids. This could be an indication of a close competition occurring between the

perchlorate anion and the THF for Cu(I) coordination. In addition, the key step to producing the  $\text{BF}_4^-$  and  $\text{ClO}_4^-$  fused-pentagon layers is the initial formation of the precipitate phase followed by the solvent-mediated phase transition process to the final layered product. Every time there is no precipitate with the  $\text{ClO}_4^-$  anion reaction in low THF concentration, there is always the formation of the hexagon layers.

## 5.4 Conclusion

The results we have shown so far in Chapters 3-5 show how there is a definite relationship between the resulting particular polymorph of an extended Cu(I) coordination solid and the nature of the anion or solvent used in those reactions. By first observing the crucial elements of different polymorphs that are formed, followed by a step-by-step examination of the products formed we might consider as the intermediate structures, we can now see how each anion and/or solvent might influence the self-assembly process leading up to the variety of layered coordination solids and other extended solids that are produced. For those reactions involving the anion coordination, this might lead the self-assembly into producing the hexagon layered network, while those reactions with THF coordination might lead the formation of the pentagonal network. In all probability, it is the distortions of the tetrahedra brought on by either the coordination of the anion or solvent that dictates the morphology of the final extended solid.



## References

1. (a) Dassent, W. E.; *Non-existent Compounds*, Dekker, New York, 1965. (Yoon, K. B.; Kochi, J. K.; *Inorg. Chem.* **1990**, *29*, 869. (c) Appleman, E. H.; *Acc. Chem. Res.* **1973**, *6*, 113.
2. Strauss, S. H.; *Chem. Rev.* **1993**, *93*, 927.
3. Rosenthal, M. R.; *J. Chem. Educ.* **1973**, *50*, 331.
4. Lawrance, G. A.; *Chem. Rev.* **1986**, *86*, 17.
5. (a) Bond, A. M.; Ellis, S. R.; Hollenkamp, A. F.; *J. Am. Chem. Soc.* **1988**, *110*, 5293. (b) Todd, M. D.; Dong, Y.; Hupp, J. T.; *Inorg. Chem.* **1991**, *30*, 4687. (c) Xie, Z.; Liston, D. J.; Jelinek, T.; Mitro, V.; Bau, R.; Reed, C. A.; *J. Chem. Soc. Chem. Commun.* **1993**, 384.
6. (a) Lancaster, S. J.; Robinson, O. B.; Bochmann, M.; *Organomet.* **1995**, *14*, 2456. (b) Schaverien, C. J.; van Mechelen, J. B.; *Organomet.*, **1991**, *10*, 1704. (c) Klabunde, K. J.; Anderson, B. B.; Bader, M.; Radonovich, L. J.; *J. Am. Chem. Soc.* **1978**, *100*, 1313. (d) Benites, M.; Fronczek, F. R.; Maverick, F. R.; Andrew, W.; *J. of Organomet. Chem.* **1999**, *577*, 24. (e) Batsanov, A. S.; Bolesova, I. N.; Struchkov, Y.; Kravtsov, D. N.; *Metalloorganicheskaya Khimiya*, **1989**, *2*, 873.
7. Casa, M. D.; Fabbrizzi, L.; Mariani, M.; Seghi, B.; *J. Chem. Soc. Dalton Trans.* **1990**, 55.
8. Newbound, T. D.; Colman, M. R.; Miller, M. M.; Wulfsburg, G. P.; Anderson, O. P.; Strauss, S. H.; *J. Am. Chem. Soc.* **1989**, *111*, 3762.
9. (a) Stellbrink, J.; Willner, L.; Jucknischke, O.; Richter, D.; Lindner, P.; Fetters, L. J.; Huang, J. S.; *Macromolecules* **1998**, *31*, 4189. (b) Diaz, J. F.; Andrué, J. M.; Diakun, G.; Towns-Andrews, E.; Bordas, J.; *BioPhys. J.*, **1996**, *70*, 2408. (c) De Vocht, M. L.; Reviakine, I.; Ulrich, W. –P.; Bergsma-Schutter, W.; Wösten, H. A. B.; Vogel, H.; Brisson, A.; Wessels, J. G. H.; Robillard, G. T.; *Protein Science* **2002**, *11*, 1199. (d) Bohrmann, B.; Dobochoet, A. M.; Kuner, P.; Müller, F.; Huber, W.; Nordstedt, C.; Dobeli, H.; *J. Struct. Bio.* **2000**, *130*, 232. (e) Zhang, X.; Furutachi, H.; Fujinami, S.; Nagatomo, S.; Maeda, Y.; Watanabe, Y.; Kitagawa, T.; Suzuki, M.; *J. Am. Chem. Soc.* **2005**, *127*, 826. (f) Magnusson, O. T.; Toyama, H.; Saeki, M.; Schwarzenbacher, R.; Klinman, J. P.; *J. Am. Chem. Soc.* **2004**, *126*, 5342.
10. (a) Dosa, P. I.; Whitener, G. D.; Vollhardt, K. P. C.; Bond, A. D.; Teat, S. J.; *Org. Lett.* **2002**, *4*, 2075. (b) Jones, C.; Richards, A. F.; Fritzsche, S.; Hey-Hawkins, E.; *Organometallics*, **2002**, *21*, 438. (c) Tschan, M. J.-L.; Cherioux, F.; Karmazin-Brelot, L.; Suss-Fink, G.; *Organometallics*, **2005**, *24*, 1974.

11. Knaust, K. M.; Knight, D. A.; Keller, S. W.; *J. Chem. Cryst.* **2003**, *33*, 813.
12. Sinn, E.; Woodward, S.; *Polyhedron* **1993**, *12*, 991.
13. Sheldrick, G. M. *SHELXS-90, program for Structure Solution*; University of Gottingen: Germany, 1991.
14. (a) Sheldrick, G. M. *SHELXL-90, program for Structure Refinement*; University of Gottingen: Germany, 1991. (b) Barbour, L. X-SEED, *Graphical Interface for SHEL-X*; University of Columbia, MO, 2000.

# Cu(I)/Pyrimidine Discrete, One-, Two-, and Three-dimensional Solids

## 6.1 Introduction

Thus far we have shown how the Cu(I) coordination with 4,4'-bipyridine can lead to the formation of layered, materials given the proper conditions, including the type of anion and solvent used in the synthesis. We will now direct the attention to those reactions involving the tetrakis(acetonitrile)copper(I) salts with pyrimidine towards the formation of the zeolite-analog, as we first presented back in Section 1.5. In this study, we will not only show how both the anion and solvent influence the outcome of these reactions, but also how the stoichiometry of the bridging ligand can play an important role in the synthesis of these extended solids.

As one would expect, stoichiometry of reaction components is an important and easily varied factor in the synthesis of coordination polymers. Stoichiometric control of the structure and properties of materials is a popular method used in several areas of organometallic,<sup>1</sup> organic,<sup>2</sup> and inorganic synthesis.<sup>3</sup> Stoichiometric control is also widely used in the general synthesis of coordination polymers leading to the formation of discrete, one-, two, and three-dimensional structures.<sup>4</sup>

We described in Chapter 1 how the three-dimensional and two-dimensional coordination solids can find use as porous materials having properties similar to those

found in zeolites and clays. The same may be said for those one-dimensional chains and even the discrete coordinated macrocycles when you consider the possible porous solids that might develop from the normal crystal packing of these various species. A good example of this was just presented in the last chapter with the packing arrangement of the Cu(I) dimer,  $\text{Cu}(\text{bpy})_{0.5}(\text{PPh}_3)_2(\text{ClO}_4) \cdot (\text{THF})_{3.5}$ , **23**. The large pores this material exhibits could be useful for solvent exchange/extraction purposes or even serve as reaction sites, as is possible with both the clays and the zeolites.<sup>5</sup>

Other applications involve the discrete oligomers as they are still in solution. Several of these macrocycles have been shown to effectively bind other *target* molecules, such as planar aromatic species,<sup>6</sup> complex inorganic anions,<sup>7</sup> alkali metal cations,<sup>8</sup> and various porphyrin species.<sup>9</sup> Since many of these assemblies display considerable optical activity<sup>10</sup> and photoluminescence,<sup>7b, 9a</sup> they are beginning to be recognized for their use as chemical sensors.<sup>11</sup> Other potential applications involving the macrocycles can also be applied to the solid-state phase for uses as ultrafiltration, gated transport, and catalytic thin films.<sup>12</sup>

Several of these macrocycles with the above mentioned properties are found in the form of molecular squares. Still, others exist as molecular triangles,<sup>13</sup> pentagons,<sup>14</sup> hexagons,<sup>14</sup> and even molecular octahedra.<sup>15</sup> In light of the wide variety of possible macrocyclic forms, they have also been targeted as building blocks for even larger supramolecular assemblies leading to nanoscale molecular devices and nano-machines.<sup>16</sup>

In the first part of this study, we will present our own versions of discrete coordination solids, starting with a structure with the  $\text{BF}_4^-$  anion and relate this structure to the Cu(I) square tetramer,  $[\text{Cu}_4(\text{pyrimidine})_4(\text{MeCN})_8]4\text{PF}_6$ , which was first reported by Lopez.<sup>17</sup> Along with this study, and keeping within the overall theme, we will present

results obtained while using other anions (including the polyoxometalate,  $\text{PMo}_{12}\text{O}_{40}^{3-}$  anion) and then attempt to show the connection between the macrocycles and the higher dimensional structures resulting from the reaction of tetrakis(acetonitrile)copper(I) and tetrakis(benzonitrile)copper(I) salts with pyrimidine as a bridging Lewis base ligand. Once again, we will show the anion and solvent dependence observed in the synthesis of these structures, along with how the dimensionality of the materials is easily controlled by ligand stoichiometry.

## 6.2 Discrete Cu(I) Coordinated Oligomers

### 6.2.1 Experimental Section

#### 6.2.1.1 General Methods

*Caution! Perchlorate salts are explosive and should be handled in small quantities and with extreme care at all times.*  $\text{Cu}_2\text{O}$ ,  $\text{HBF}_4$ ,  $\text{HClO}_4$ ,  $\text{H}_3\text{PMo}_{12}\text{O}_{40}$ , nitrobenzene, nitromethane, and pyrimidine (ACROS); acetonitrile, tetrahydrofuran, and diethyl ether (Fisher); were used without further purification. The  $[\text{Cu}(\text{MeCN})_4]\text{X}$  salts for  $\text{X} = \text{BF}_4^-$ ,  $\text{ClO}_4^-$ , and  $\text{PMo}_{12}\text{O}_{40}^{3-}$  were prepared as described in *Chapter 2*.

#### 6.2.1.2 Synthesis

##### $[\text{Cu}_4(\text{C}_4\text{H}_4\text{N}_2)_4(\text{MeCN})_8]4\text{BF}_4$ , **25**

In a 1 dram vial were combined  $[\text{Cu}(\text{MeCN})_4]\text{BF}_4$  (0.054 g, 0.17 mmol) and pyrimidine (0.028 g, 0.34 mmol) in 0.5 mL of MeCN. This vial was then placed inside a 20 mL, screw top vial containing 5 mL of ethyl ether. The large vial was sealed and the

Et<sub>2</sub>O slowly diffused into the MeCN solution. After 24 hours, light yellow, prismatic crystals of **25** were harvested from the smaller vial.



In a 1 dram vial were combined [Cu(MeCN)<sub>4</sub>]ClO<sub>4</sub> (0.040 g, 0.122 mmol) and pyrimidine (0.028 g, 0.341 mmol) in 0.5 mL of MeCN and 0.2 mL of nitromethane (exposed to air for four days). This vial was then placed inside a 20 mL, screw top vial containing 5 mL of THF. The large vial was sealed and the THF slowly diffused into the MeCN solution. After 24 hours, blue-green, prismatic crystals of **26** were harvested from the smaller vial.



In a 1 dram vial were combined [Cu(MeCN)<sub>4</sub>]BF<sub>4</sub> (0.040 g, 0.13 mmol) and pyrimidine (0.028 g, 0.34 mmol) in 0.5 mL of MeCN and 2.0 mL of nitromethane (exposed to air for four days). This vial was then placed inside a 20 mL, screw top vial containing 5 mL of THF. The large vial was sealed and the THF slowly diffused into the MeCN solution. After 48 hours, blue-green, prismatic crystals of **27** were harvested from the smaller vial.



In a 1 dram vial were combined [Cu(MeCN)<sub>4</sub>]<sub>3</sub>Mo<sub>12</sub>O<sub>40</sub>P (0.020 g, 0.008 mmol) and pyrimidine (0.140 g, 1.71 mmol) in 0.5 mL of MeCN. This vial was then placed inside a 20 mL, screw top vial containing 5 mL of ethyl ether. The large vial was sealed and the

Et<sub>2</sub>O slowly diffused into the MeCN solution. After 24 hours, dark orange, prismatic crystals of **28** were harvested from the smaller vial.

### 6.2.1.3 Single Crystal X-Ray Diffraction

Single crystals of high quality (by uniform extinction of polarized light) were coated with light oil and then mounted on a tip of a glass fiber using small amount of silicon grease for adhesion. Crystallographic data was collected using a Siemens SMART system with a CCD area detector (Mo K<sub>α</sub> = 0.71070 Å). During data collection, the crystals were cooled to 173 K. The initial space group was determined by indexing several hundred strong reflections and the structures were solved using Direct Methods.<sup>18</sup> The structure models were further refined using least-squares techniques.<sup>19</sup>

For each structure, the majority of the heavier atoms were located with the initial solution. Any remaining non-hydrogen atoms were usually located after the first or second refinements. Anisotropic thermal parameters were refined for all non-hydrogen atoms. The hydrogen atoms were included in calculated positions and refined as riding models with fixed  $U_{\text{iso}} = 1.2U_{\text{iso}}$  of the carbon atom for which they are bonded. All other structure-specific crystallographic details will be explained in the *Results and Discussion* section. Details of the data collection and structure solutions are given in Table 6.1.

	<b>25</b>	<b>26</b>	<b>27</b>	<b>28</b>
Empirical formula	Cu <sub>4</sub> C <sub>32</sub> H <sub>40</sub> N <sub>16</sub> F <sub>16</sub> B <sub>4</sub>	Cu <sub>5</sub> C <sub>38</sub> H <sub>47</sub> N <sub>18</sub> Cl <sub>5</sub> O <sub>23</sub>	Cu <sub>5</sub> C <sub>38</sub> H <sub>47</sub> N <sub>18</sub> O <sub>2</sub> B <sub>5</sub> F <sub>20</sub>	Cu <sub>3</sub> C <sub>32.4</sub> H <sub>37.8</sub> N <sub>15</sub> O <sub>40.6</sub> PMo <sub>12</sub>
Formula weight (g·mol <sup>-1</sup> )	1250.19	1618.89	1538.64	2659.83
Temperature, K	173(2)	173(2)	173(2)	173(2)
Crystal System, Space group	Tetragonal, I4 <sub>1</sub> /a	Monoclinic, C2/m	Monoclinic, C2/m	Hexagonal, R-3c
Unit cell dimensions				
<i>a</i> (Å)	16.8689(8)	21.1511(9)	20.831(1)	18.7698(8)
<i>b</i> (Å)	16.8689(8)	16.6918(7)	16.5826(9)	18.7698(8)
<i>c</i> (Å)	18.230(1)	17.1612(7)	17.1009(9)	71.795(4)
$\alpha$ , deg	90	90	90	90
$\beta$ , deg	90	96.126(1)	95.4830(10)	90
$\gamma$ , deg	90	90	90	120
<i>Z</i>	12	12	8	9
Volume, Å <sup>3</sup>	5187.4(5)	6024.2(4)	5880.2(5)	21905(2)
$\rho_{\text{calc}}$ , g·cm <sup>-3</sup>	1.601	1.785	1.739	1.814
Absorption coefficient, mm <sup>-1</sup>	1.092	2.049	0.961	2.955
F(000)	2496	3260	3504	15144
Crystal size, mm	0.3 x 0.2 x 0.1	0.4 x 0.2 x 0.1	0.4 x 0.2 x 0.2	0.4 x 0.2 x 0.1
$\theta$ Range for data collection	1.64 to 27.09	1.56 to 27.13	1.57 to 27.16	1.38 to 27.14
Index ranges	-21 ≤ <i>h</i> ≤ 21 -21 ≤ <i>k</i> ≤ 20 -14 ≤ <i>l</i> ≤ 23	-23 ≤ <i>h</i> ≤ 27 -20 ≤ <i>k</i> ≤ 21 -21 ≤ <i>l</i> ≤ 22	-26 ≤ <i>h</i> ≤ 26 -16 ≤ <i>k</i> ≤ 21 -21 ≤ <i>l</i> ≤ 20	-24 ≤ <i>h</i> ≤ 23 -24 ≤ <i>k</i> ≤ 19 -91 ≤ <i>l</i> ≤ 92
Reflections collected	15945	21539	18822	44368
Unique reflections	2864 [R <sub>int</sub> = 0.0548]	6795 [R <sub>int</sub> = 0.0334]	6720 [R <sub>int</sub> = 0.0190]	5386 [R <sub>int</sub> = 0.0614]
Completeness to $\theta$	27.09 (100 %)	27.13 (98.5 %)	27.16 (99.5 %)	27.14 (99.9 %)
Max/min transmissions	1.00000/ 0.625620	1.00000/ 0.743344	1.00000/ 0.780163	1.00000/ 0.547969
Data/restraints/parameters	2864/0/165	6795/0/420	6720/0/432	5386/0/342
Goodness of fit F <sup>2</sup>	0.986	1.012	1.055	1.076
Final R indices [I > 2 $\sigma$ (I)] <sup>a,b</sup>	R <sub>1</sub> = 0.0419 wR <sub>2</sub> = 0.1088	R <sub>1</sub> = 0.0507 wR <sub>2</sub> = 0.1264	R <sub>1</sub> = 0.0575 wR <sub>2</sub> = 0.1757	R <sub>1</sub> = 0.0428 wR <sub>2</sub> = 0.1320
R indices (all data)	R <sub>1</sub> = 0.0946 wR <sub>2</sub> = 0.1305	R <sub>1</sub> = 0.0688 wR <sub>2</sub> = 0.1371	R <sub>1</sub> = 0.0688 wR <sub>2</sub> = 0.1916	R <sub>1</sub> = 0.697 wR <sub>2</sub> = 0.1466
Largest difference peak and hole (e·Å <sup>-3</sup> )	0.622/-0.499	1.184/-0.961	1.154/-1.370	1.826/-0.904
Structures were refined on F <sup>2</sup> for all data. <sup>a</sup> $R(F_o) = \sum   F_o  -  F_c   / \sum  F_o $ . <sup>b</sup> $R_w(F_o) = (\sum w  F_o  -  F_c  ^2 / \sum  F_o ^2)^{1/2}$ , $w = 1/(\sigma^2(F_o) + (0.002F_o)^2)^{-1}$ .				

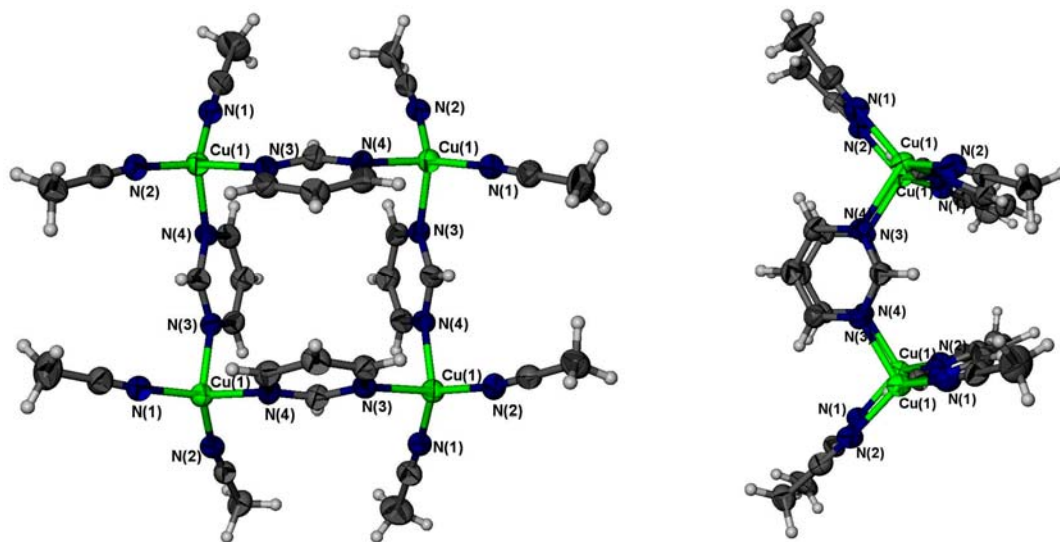


## 6.2.2 Results and Discussion

### 6.2.2.1 The Cu(I) Tetramer

The pyrimidine tetramer reported by Lopez was synthesized from the reaction of  $[\text{Cu}(\text{MeCN})_4]\text{PF}_6$  with pyrimidine (pyrim) in a 1:2 stoichiometry. Since then, we have found that a similar structure can be obtained with the  $\text{BF}_4^-$  anion as well, resulting in the tetramer structure of  $[\text{Cu}_4(\text{pyrim})_4(\text{MeCN})_8]4\text{BF}_4$ , **25**. The structure of **25** crystallizes in the same space group as the  $\text{PF}_6^-$  analog and the two structures are essentially isostructural. Reactions involving either the perchlorate or triflate anion have not resulted in these discrete tetramers. Possible reasons for this will be presented in Section 6.5.

The asymmetric unit of these discrete oligomers includes one pyrimidine, and two acetonitrile ligands coordinated to one Cu(I) tetrahedral center. Figure 6.1 shows a single tetramer in both face-on and side view.



**Figure 6.1** A single tetramer as seen in **25** with the non-hydrogen atoms shown in 50% thermal ellipsoids. Both the (left) face-on view and (right) side view illustrate how a square molecular unit can be constructed from tetrahedral building blocks. The  $\text{BF}_4^-$  anions have been omitted.

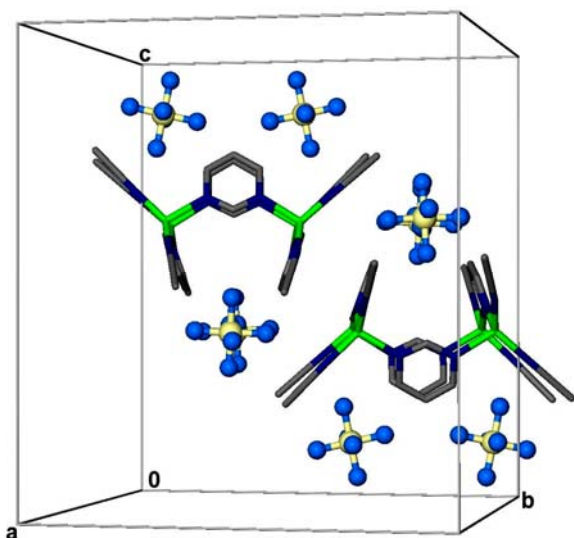
Even with this similarity, the unit cell of **25** is considerably smaller than the  $\text{PF}_6^-$  analog. Since these tetramers pack together by weak  $\pi - \pi$  stacking of adjacent pyrimidine ligands and even weaker intermolecular van der Waals forces, the structure can expand or contract, depending upon the size of the interstitial anion. From the parameters listed in Table 6.2 for the unit cell of each

**Table 6.2** Unit cells of the tetramers found in **24** and with the  $\text{PF}_6^-$  anion.

Structure	<b>25</b>	$\text{PF}_6^-$
Space group	$I4_1/a$	$I4_1/a$
$a$ and $b$ , Å	16.8689(8)	17.368(1)
$c$ , Å	18.230(1)	19.554(1)
Volume, Å <sup>3</sup>	5187.4(5)	5898.6(5)

structure, we can see that **25** has a volume that is ~12% smaller. This change in size is, of course, seen directly in the change in the  $a$ ,  $b$ , and  $c$  indices with a difference of 0.5 Å in sides  $a$  and  $b$  while the difference in  $c$  is almost 3x greater at 1.3 Å.

This uneven unit cell expansion is easily explained by observing how the tetramers pack in the crystalline state. Figure 6.2 shows how two tetramers from the  $\text{PF}_6^-$  structure



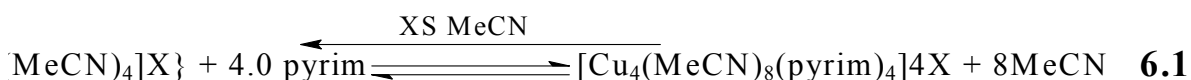
**Figure 6.2** Two tetramers of **25** in stick representation showing the anions (seen as isotropic spheres) in their positions along the  $c$ -axis. The hydrogen atoms have been omitted for clarity.

are arranged in the unit cell. Since the  $\text{PF}_6^-$  anions in positions on the top and bottom of the tetramers along the vertical  $c$  axis, the greater dimensional change is seen in this axis than in the other two as the size of the anion is changed.

The synthesis of these tetramers requires the addition of at least 1.5 equivalents of pyrimidine in the

reaction. The reason for this excess of pyrimidine is because the MeCN used as the

reaction solvent competes with the pyrimidine for the Cu(I) coordination. As shown in eq. 6.1:

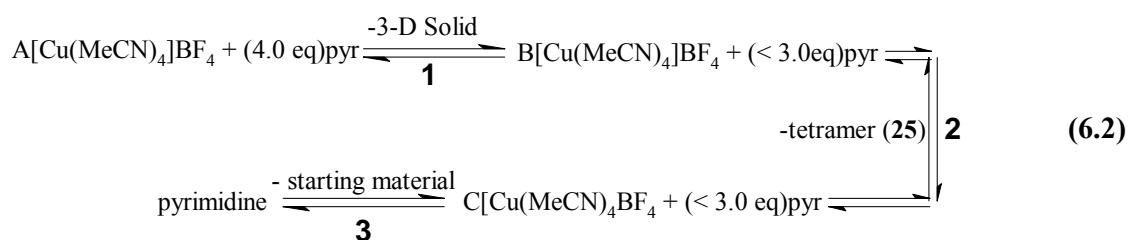


Although the pyrimidine ligand is a considerably much stronger Lewis base than MeCN, the reaction is performed in an excess of MeCN (almost 10 fold with 0.5 mL MeCN,  $\delta = 0.786 \text{ g/mL}$ ), which should shift the equilibrium to the left, as is dictated by Le Châtelier's principle. Solvent vapor diffusion with either THF or Et<sub>2</sub>O effectively crystallizes out the product and, if this pyrimidine concentration is too low, the MeCN coordination will dominate the reaction and only the tetrakis(acetonitrile)copper(I) starting material will crystallize.

Experimentation has shown us that the ideal conditions for producing **25** involves using 2.0 – 3.0 equivalents of pyrimidine, with the reaction carried out in only MeCN with solvent vapor diffusion using THF. Using Et<sub>2</sub>O as the crystallizing solvent is also an option that has little, if any, negative effects on the outcome. Reactions containing an amount of nitrobenzene (along with the usual amount and MeCN) can still result in the synthesis of this tetramer. However, in many cases, these types of reactions are less predictable and many times result in either the starting material or a 3-D coordination solid, depending on pyrimidine concentration. We will further discuss these reactions dependence involving nitrobenzene later in the Section 6.5 on three-dimensional structures.

As stated above, reactions carried out at very low pyrimidine concentrations (<2.0 equivalents) usually results in only the crystallization of the tetrakis(acetonitrile)copper(I)

salt. In the same light, reactions carried out with a larger excess of pyrimidine (>3.0 equivalents) leads to the formation one of two 3-D solids, depending on the nature of the reaction solvent (see Section 6.5). It is interesting to note that even in reactions that do produce the 3-D structures, we observe the tetramers co-crystallize as the pyrimidine is used up during the reaction. Since the 3-D solids use pyrimidine on a 2:1, pyr:Cu basis, as the 3-D solid forms, the pyrimidine concentration continuously decreases. This is best illustrated in the step-wise reaction equation as follows:



The first step in this reaction scheme produces the 3-D coordination solid as the pyrimidine concentration is >3.0 equivalents. When the pyrimidine concentration drops below 3.0 equivalents (step 2), the discrete tetramer begins to form as the crystalline product. Although there is a one-to-one stoichiometric relationship in the reaction forming the tetramer, the actual molar concentration of the pyrimidine eventually drops to a level to where it is overwhelmed by the amount of MeCN present and (step 3) the reaction in equation 6.1 shifts to the left resulting in the crystallization of only the starting material. Any unused pyrimidine remains in the reaction solution.

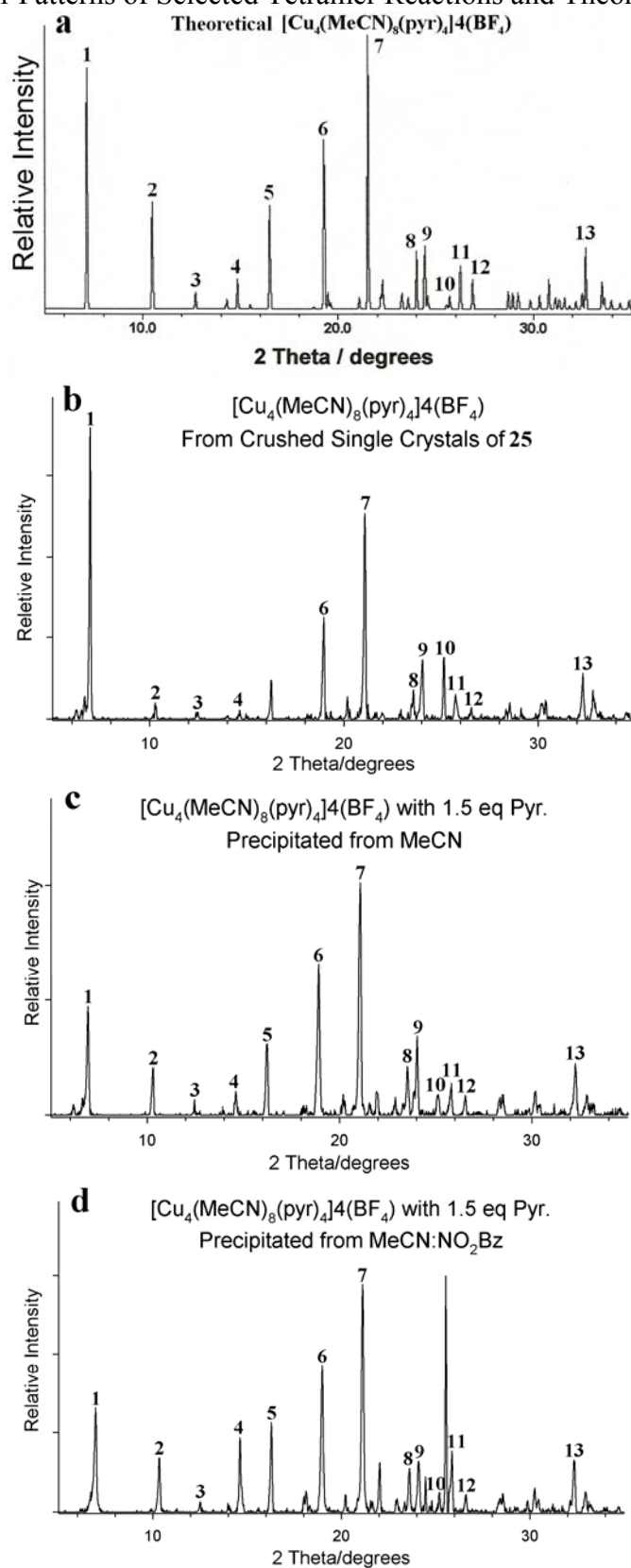
Although the synthesis of these tetramers has become relatively easy, the detection of the discrete molecules in solution has proved to be a considerable challenge. Lopez showed that individual tetramers might have been detected by electrospray mass

spectroscopy but she admitted that the results was subject to scrutiny since the tetrakis(acetonitrile)copper(I) starting material had a similar m/z value as the tetramer.<sup>17</sup>

Efforts in this study to use <sup>1</sup>H NMR analysis to identify the tetramer while still in solution had mixed results. An earlier study had indicated that a reaction with 1.0 equivalent of pyrimidine with the Cu(MeCN)<sub>4</sub>PF<sub>6</sub> resulted in an initial broadening of the pyrimidine proton peaks, which then sharpened up over a three-day period. We hypothesized these broad peaks are associated with the continual pyrimidine ligand exchange on the Cu(I) coordination sites. The sharpening of these peaks might indicate the eventual assembly of the tetramer, which should effectively lock the pyrimidine ligands in place. Unfortunately, reproduction of similar results with the BF<sub>4</sub><sup>-</sup> anion has not been successful; this area of study remains an ongoing investigation.

Perhaps the most promising evidence for the presence of solution bound tetramers was obtained by the XRPD analysis of the precipitates generated by *crashing out* of the tetramer reactions in diethyl ether. Figure 6.3 shows the XRPD data of the precipitates collected from reactions of the BF<sub>4</sub><sup>-</sup> starting material with 1.5 equivalents of pyrimidine in reaction solvents of either (c) MeCN or (d) a MeCN:NO<sub>2</sub>Ph (nitrobenzene) mixture. For comparison, (a) the theoretical powder pattern and (b) the powder pattern collected from crushed single crystals of **25** are included in the table. Each powder pattern matches with the theoretical pattern quite well indicating that they are all the tetramer structure. Most interesting is that these reactions were crashed out within minutes of their initiation; somewhat contrary to the <sup>1</sup>H NMR results mentioned above which suggested a three day period was required for the complete tetramer formation.

**Figure 6.3** Powder Patterns of Selected Tetramer Reactions and Theoretical Comparison

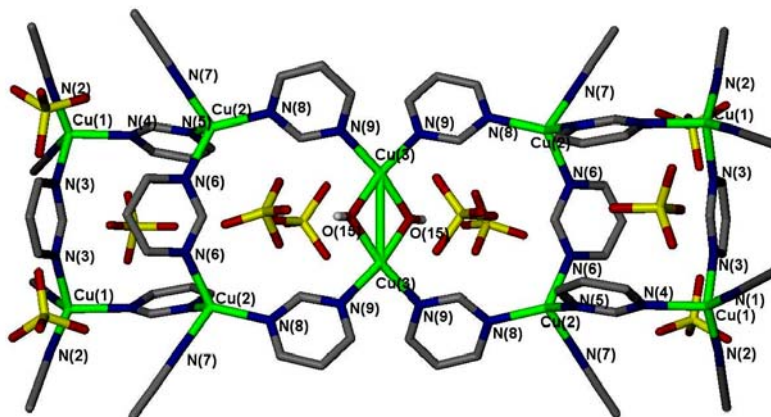


### 6.2.2.2 The Cu(I/II) Tetramer Dimer

During the course of our studies with this system, we came across some interesting copper oxidation which occurred during the self-assembly process of these Cu(I) materials. One particular reaction with either the  $\text{BF}_4^-$  or the  $\text{ClO}_4^-$  anion resulted in the formation of the discrete, mixed-valence copper coordination dimers of  $[\text{Cu}_{2.5}(\text{C}_4\text{H}_4\text{N}_2)_3(\text{OH})_{0.5}(\text{MeCN})_3](\text{ClO}_4)_{2.5} \cdot (\text{THF})_{0.25}$ , **26** and the isostructural  $[\text{Cu}_{2.5}(\text{C}_4\text{H}_4\text{N}_2)_3(\text{OH})_{0.5}(\text{MeCN})_3](\text{BF}_4)_{2.5} \cdot (\text{THF})_{0.25}$ , **27**.

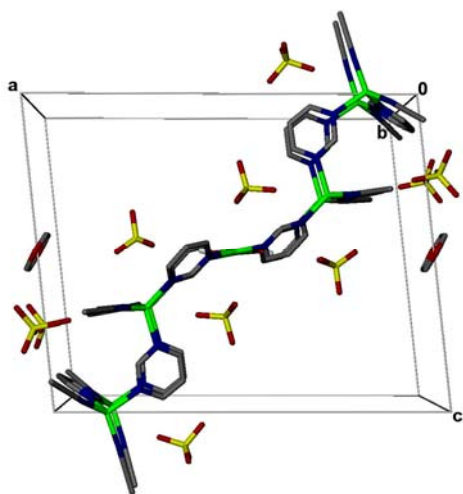
Both **26** and **27** crystallize in monoclinic  $C2/m$  space group. The asymmetric unit consists of two Cu(I) tetrahedra bridged by a pyrimidine ligand with each copper also coordinated to one MeCN ligand and one-half of a pyrimidine ligand; two of its carbons are one-half occupied as they sit on a mirror plane. Also found in the asymmetric unit is a one-half occupied copper(II) atom on a two-fold rotation axis with an attached, one-half occupied OH ligand found on a mirror plane. Three of the four crystallographically unique anions (of either  $\text{ClO}_4^-$  or  $\text{BF}_4^-$ ) have the central atom and two ligands are located on a mirror plane and one half occupied. The fourth anion is completely occupied. Each structure also has included THF solvent of which only a carbon (with hydrogens) and one-half oxygen (sitting on a mirror plane) is present in the asymmetric unit as the THF is then disordered over a two-fold perpendicular rotation axis.

Figure 6.4 shows that the structure in **26** is a dimer formed by two Cu(I) tetramers that are linked by a copper(II)  $[\text{Cu}_2(\text{OH})_2(\text{pyr})_4]$  bridge. The positioning of the anions about the dimer is reminiscent of the way the anions set within the discrete tetramer, **25**.



**Figure 6.4** The Cu(I/II) dimer shown in stick representation. Unmarked atoms are gray for carbon, red for oxygen and yellow for chlorine. All the hydrogen atoms except on the hydroxides have been omitted.

A side view of this dimer is shown in Figure 6.5, not only providing more detail on the anion positioning but also showing the location of the included THF. Seen here, only two THF molecules are associated with the entire dimer unit and are located on adjacent far end corners of the dimer. The packing of both **26** and **27** are identical with only a slight 2.4% larger in unit cell volume in **26** to accommodate the larger perchlorate anion.



**Figure 6.5** A side view of **26** showing the anion and THF positioning. The hydrogen atoms are omitted for clarity.

Most interesting with this structure is the presence of the tetramer *within* this structure, as if the tetramer seen in **25** might be a building block for the higher-dimensional structure.

The reaction leading to the formation of these mixed-valence materials is undoubtedly due to Cu(I)'s oxidation by the dioxygen present in the nitromethane solvent. The sensitivity of copper(I) compounds toward dioxygen that is absorbed into solvents has been known for some time.<sup>20</sup> These reactions were first noticed in our lab as the result of using nitromethane that was exposed to air for several



days. The normally yellow reaction solutions quickly turned a blue-green color when this air-exposed nitromethane was used. The solvent vapor diffusion brought about the crystallization of the blue-green crystals of **26** and **27** after only 24 hours. Reactions performed in the same solvent, which was first flushed with nitrogen, did not exhibit any copper oxidation.

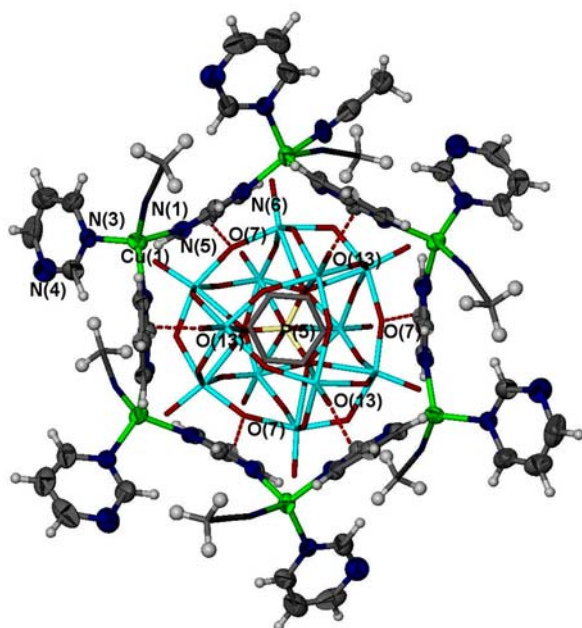
This same type of copper oxidation has also been seen in reactions involving the nitrobenzene solvent. However, actual control over these reactions seems to be limited and several attempts to induce this mixed-valence oxidation (by first bubbling the solvent with O<sub>2</sub> for example) results in the formation of Cu(II) *molecular* solids only. The recent investigation using nitromethane has proven much more reliable and predictable as those structures of both **26** and **27** have been reproduced several times. Further reactions in this system are pending as is the study of the magnetic properties of the mixed-valent solids.

### 6.2.2.3 Anion Templatation of a Discrete Hexagon

In an effort to mimic the anion-templation used to develop the large cavity zeolites as was introduced in Chapter 1, we employed the use of a large, weakly coordinating polyoxometalate (POM), PMo<sub>14</sub>O<sub>40</sub><sup>3-</sup> anion. Our group has already seen success in this endeavor in the synthesis of [Cu<sub>3</sub>(μ<sub>2</sub>-bpy)<sub>4</sub>(MeCN)<sub>4</sub>]PW<sub>12</sub>O<sub>40</sub> layered structure with expanded cavities to accommodate this incredibly much larger anion.<sup>21</sup> This same anion has also shown templation-like attributes in a few other coordination structures resulting from these same studies.<sup>21, 22</sup> In this study, we developed another anion templation-like synthesis produced in unusually high pyrimidine concentration, which resulted in the discrete hexagon structure of [Cu<sub>6</sub>(C<sub>4</sub>H<sub>4</sub>N<sub>2</sub>)<sub>9</sub>(MeCN)<sub>6</sub>]2PMo<sub>12</sub>O<sub>40</sub>, **28**.

For the most part, this particular synthesis defies all logic as this zero-dimensional, discrete hexagon is produced from reactions using an incredibly high, 75 equivalents of pyrimidine! To add to the novelty of this compound, the hexagonal R-3c unit cell of this structure has an incredibly long (71 Å) *c*-axis. The synthesis of this structure has been reproduced only with the equivalents of pyrimidine at or around those reported and analysis of the structure confirms the correct choice of the unit cell.

The asymmetric unit of **28** consists of only one copper center with two pyrimidine ligands attached (one of which is terminal) and also has an acetonitrile ligand which is disordered in two non-symmetric positions on the same coordination site. Only one-third of a POM anion is present with the central, phosphorous atom only one-third occupied and sitting on a three-fold rotation axis. Also, only single carbon atom of the included THF solvent is present, which grows into a THF molecule that is disordered over two

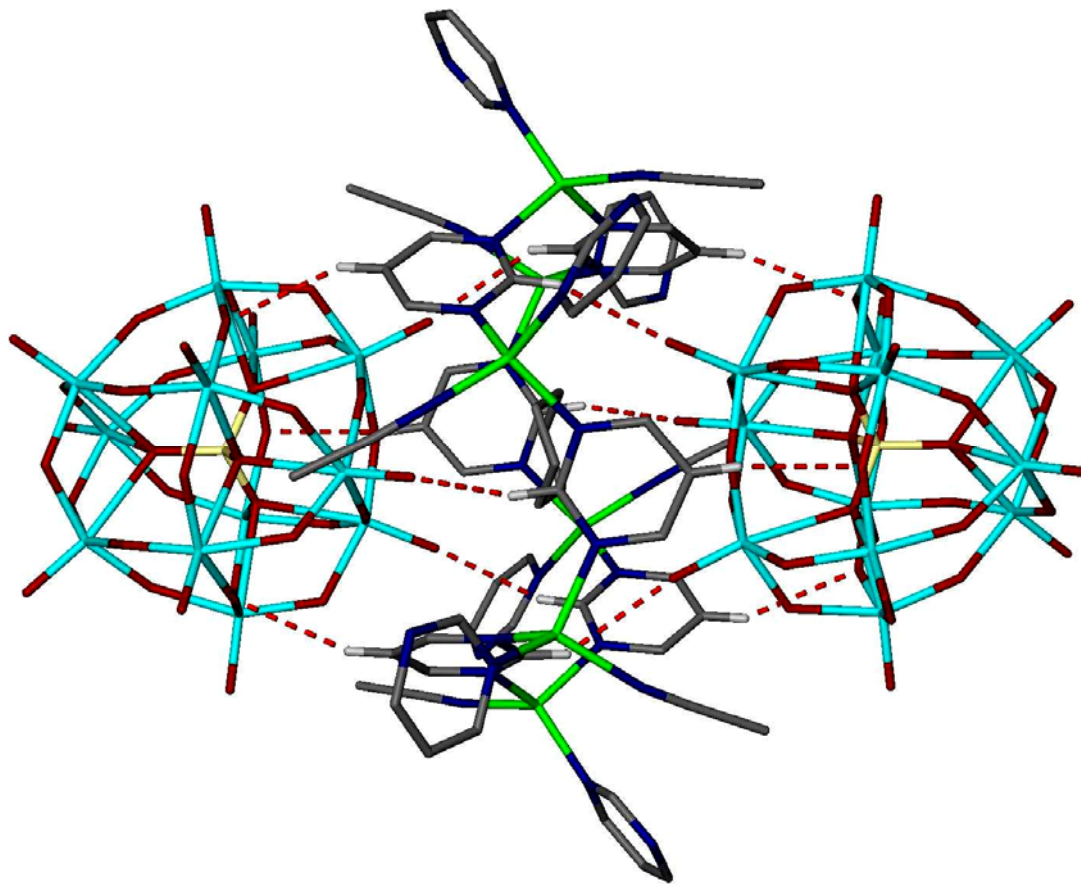


**Figure 6.6** The discrete hexagon found in **28** shown as 50% thermal ellipsoid, with the anion and THF (center) shown in stick representation. Each of the O(13) and O(7) labeled indicates a weak H-bond location. Carbon are gray and Mo are blue.

positions about a vertical two-fold rotation axis. Figure 6.6 shows a single hexagonal unit of **28** with only one of two POM anions in place.

The templation effect from the POM anion is the likely cause for this discrete hexagon formation at such high levels of pyrimidine concentration. Close examination of the structure shown in Figure 6.6

reveals the six, weak (2.8 Å) hydrogen bonds; three more formed between terminal O(13) atoms and pyrimidine's H(12) atom and three formed between the POM's bridging O(7) atoms and the pyrimidine's H(10) atoms. As shown in Figure 6.7 below, another POM anion sits directly on the other side of the hexagon, thus forming six more hydrogen bonds to tie this supramolecular complex together.



**Figure 6.7** A side view of **28** showing the 12 H-bonds formed between the hydrogen atoms on the pyrimidine ligands and the oxygen atoms of the two POM anions. All other hydrogen atoms have been omitted for clarity.

## 6.3 One-Dimensional Chains

### 6.3.1 Experimental Section

#### 6.3.1.1 General Methods

*Caution! Perchlorate salts are explosive and should be handled in small quantities and with extreme care at all times.*  $\text{Cu}_2\text{O}$ ,  $\text{HClO}_4$ ,  $\text{H}_3\text{PMo}_{12}\text{O}_{40}$ , pyrimidine (ACROS); acetonitrile, tetrahydrofuran, and diethyl ether (Fisher); were used without further purification. All the  $[\text{Cu}(\text{MeCN})_4]\text{X}$  salts for  $\text{X} = \text{ClO}_4^-$  and  $\text{PMo}_{12}\text{O}_{40}^{3-}$  were prepared as described in *Chapter 2*.

#### 6.3.1.2 Synthesis

##### $[\text{Cu}_3(\text{C}_4\text{H}_4\text{N}_2)_5(\text{MeCN})_5]\text{PMo}_{12}\text{O}_{40}$ , **29**

In a 5 dram vial were combined  $[\text{Cu}(\text{MeCN})_4]_3\text{PMo}_{12}\text{O}_{40}$  (0.157 g, 0.063 mmol) and pyrimidine (0.014 g, 0.171 mmol) in 5.0 mL of MeCN. This vial was then placed inside a 20-dram, screw top vial containing 10 mL of THF. The large vial was sealed and the THF slowly diffused into the MeCN solution. After 24 hours, dark orange, prismatic crystals of **29** were harvested from the smaller vial.

##### $\text{Cu}(\text{C}_4\text{H}_4\text{N}_2)_2(\text{ClO}_4) \cdot \text{THF}$ , **30**

In a 1 dram vial were combined  $[\text{Cu}(\text{MeCN})_4]\text{ClO}_4$  (0.040 g, 0.123 mmol) and pyrimidine (0.20 g, 2.44 mmol) in 0.5 mL of MeCN. This vial was then placed inside a 20 mL, screw top vial containing 5 mL of THF. The large vial was sealed and the THF slowly diffused into the MeCN solution. After 72 hours, yellow prismatic crystals of **30** were harvested from the smaller vial. This structure will also appear in reactions with

greater equivalents of pyrimidine (i.e., >20 eq.) up to and including reactions performed in *neat* pyrimidine. Et<sub>2</sub>O can also be substituted for THF in these reactions as the crystallizing solvent.

### 6.3.1.3 Single Crystal X-Ray Diffraction

Single crystals of high quality (by uniform extinction of polarized light) were coated with light oil and then mounted on a tip of a glass fiber using small amount of silicon grease for adhesion. Crystallographic data was collected using a Siemens SMART system with a CCD area detector (Mo K<sub>α</sub> = 0.71070 Å). During data collection, the crystals were cooled to 173 K. The initial space group was determined by indexing several hundred strong reflections and the structures were solved using Direct Methods.<sup>18</sup> The structure models were further refined using least-squares techniques.<sup>19</sup>

For each structure, the majority of the heavier atoms were located with the initial solution. Any remaining non-hydrogen atoms were usually located after the first or second refinements. Anisotropic thermal parameters were refined for all non-hydrogen atoms. The hydrogen atoms were included in calculated positions and refined as riding models with fixed  $U_{\text{iso}} = 1.2U_{\text{iso}}$  of the carbon atom for which they are bonded. All other structure-specific crystallographic details will be explained in the *Results and Discussion* section. Details of the data collection and structure solutions are given in Table 6.3.

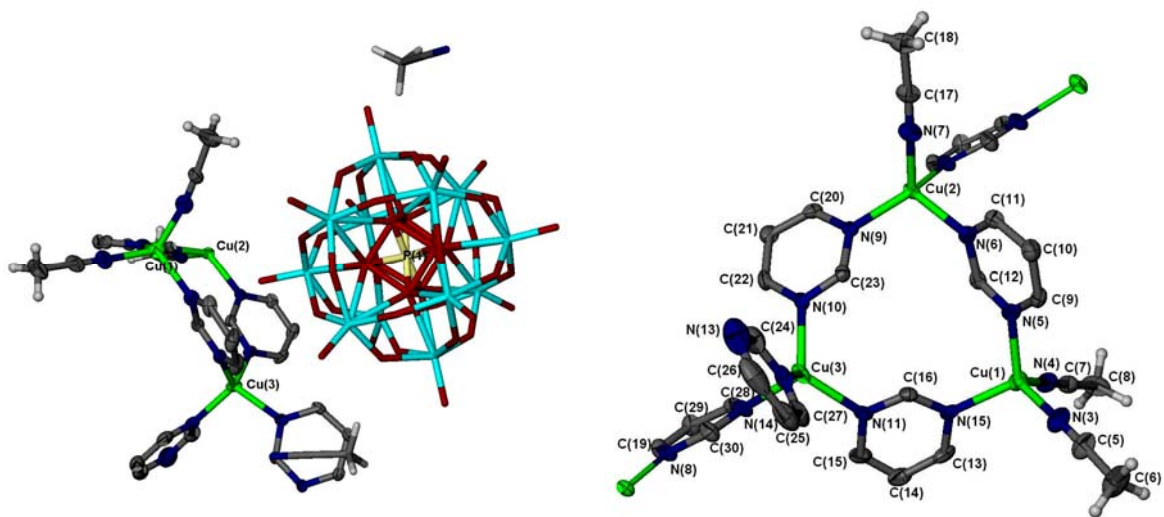
<b>Table 6.3 Crystallographic Details for 29 and 30</b>		
	<b>29</b>	<b>30</b>
Empirical formula	Cu <sub>3</sub> C <sub>30</sub> H <sub>35</sub> N <sub>15</sub> O <sub>40</sub> Mo <sub>12</sub> P	CuC <sub>12</sub> H <sub>12</sub> N <sub>6</sub> O <sub>4</sub> Cl
Formula weight (g·mol <sup>-1</sup> )	2618.60	403.27
Crystal System, Space group	Triclinic, P-1	Monoclinic, C2/c
Unit cell dimensions		
<i>a</i> (Å)	11.1180(3)	22.009(1)
<i>b</i> (Å)	15.3382(5)	8.0174(5)
<i>c</i> (Å)	19.3795(6)	17.913(1)
<i>α</i> , deg	88.4430(10)	90
<i>β</i> , deg	77.2890(10)	97.4810(10)
<i>γ</i> , deg	85.8410(10)	90
Z	2	8
Volume, Å <sup>3</sup>	3215.1(2)	3133.9(3)
ρ <sub>calc</sub> , g·cm <sup>-3</sup>	2.705	1.709
Absorption coefficient, mm <sup>-1</sup>	3.354	0.596
F(000)	2492	1632
Crystal size, mm	0.4 x 0.2 x 0.03	0.5 x 0.3 x 0.3
θ Range for data collection	1.08 to 27.13	1.87 to 27.16
Index ranges	-14 ≤ <i>h</i> ≤ 14 -19 ≤ <i>k</i> ≤ 19 -24 ≤ <i>l</i> ≤ 24	-28 ≤ <i>h</i> ≤ 14 -9 ≤ <i>k</i> ≤ 10 -23 ≤ <i>l</i> ≤ 21
Reflections collected	28327	9476
Unique reflections	13961 [R <sub>int</sub> = 0.0299]	3444 [R <sub>int</sub> = 0.0329]
Completeness to θ	27.13 (98.1 %)	27.16 (99.2 %)
Max/min transmissions	1.00000/0.732181	1.00000/0.696311
Data/restraints/ parameters	13961/0/951	3444/0/217
Goodness of fit F <sup>2</sup>	1.022	1.011
Final R indices [ <i>I</i> > 2σ( <i>I</i> )] <sup>a,b</sup>	R <sub>1</sub> = 0.0372 wR <sub>2</sub> = 0.0911	R <sub>1</sub> = 0.0454 wR <sub>2</sub> = 0.1238
R indices (all data)	R <sub>1</sub> = 0.0598 WR <sub>2</sub> = 0.1052	R <sub>1</sub> = 0.0697 WR <sub>2</sub> = 0.1338
Largest difference peak and hole (e·Å <sup>-3</sup> )	1.329/-1.310	0.817/-0.456
Structures were refined on F <sup>2</sup> for all data. <sup>a</sup> R(F <sub>o</sub> ) = Σ  F <sub>o</sub>   -  F <sub>c</sub>   /Σ F <sub>o</sub>  . <sup>b</sup> R <sub>w</sub> (F <sub>o</sub> ) = (Σw  F <sub>o</sub>   -  F <sub>c</sub>    <sup>2</sup> /Σ F <sub>o</sub>   <sup>2</sup> ) <sup>1/2</sup> , w = [σ <sup>2</sup> (F <sub>o</sub> ) + (0.002F <sub>o</sub> ) <sup>2</sup> ] <sup>-1</sup> .		

## 6.3.2 Results and Discussion

### 6.3.2.1 An Anion Templated One-Dimensional Chain

In the previous section we described how an incredibly high pyrimidine concentration can lead to the formation of an anion templated, discrete hexagon. Further investigation into this system revealed that using a much lower amount of pyrimidine resulted in yet another anion templation. Lowering the amount of pyrimidine used to only 2.5 equivalents resulted in the formation of the anion templated, one-dimensional chain of  $[\text{Cu}_3(\text{C}_4\text{H}_4\text{N}_2)_5(\text{MeCN})_5]\text{PMO}_{12}\text{O}_{40}$ , **29**.

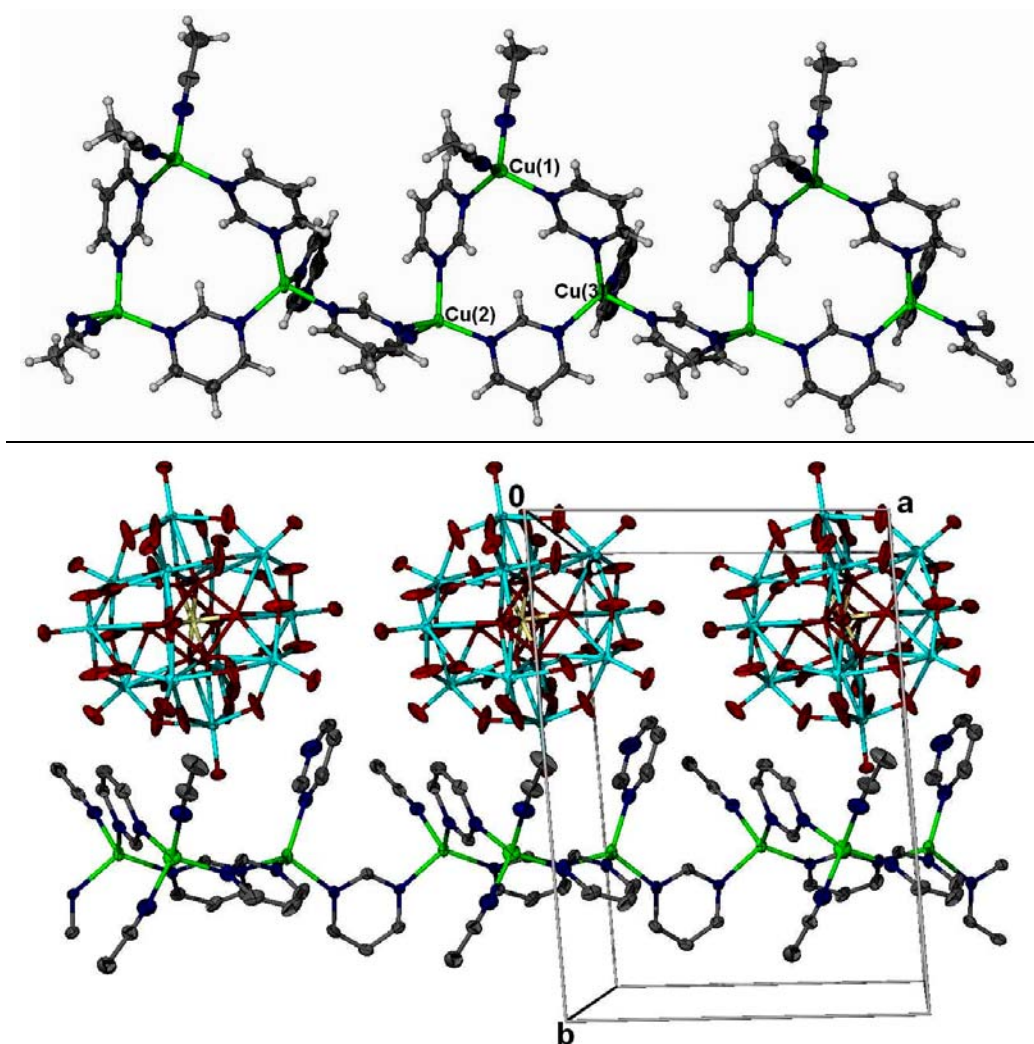
The asymmetric unit of **29**, shown in Figure 6.8, is composed of three unique Cu(I) centers, each with a different set of coordinated components and forming a Cu(I) coordinated triangular arrangement. While Cu(1) has two MeCN and two bridging pyrimidine ligands coordinated to it, Cu(2) has only one MeCN ligand and three bridging



**Figure 6.8** (left) The asymmetric unit of **29** with the cation shown as 50% thermal ellipsoids and all other atoms in stick representation. In this figure, Mo is light blue, C gray, H light gray, N blue, and O red. The three unique Cu(I) centers, each with different coordinated components is shown on the right. In this figure, all non-hydrogen atoms belonging to the asymmetric unit are labeled.

pyrimidine ligands. The Cu(3) center has no MeCN ligands coordinated. Instead, there are three bridging pyrimidine ligands and one more pyrimidine as a terminal ligand.

Included in this asymmetric unit is one POM anion, which is disordered over two positions about a two-fold center of rotation located at the central phosphorous atom. The anion is situated in the triangular bowl formed by the three coordinated Cu(I) complexes. Also included are two solvated MeCN molecules, situated about the POM anion. These triangles of copper centers are then linked together (linking bridges shown at upper-right and lower-left of the right figure in Figure 6.8) to form one-dimensional chains as shown in Figure 6.9.



**Figure 6.9** A single chain (top) of linked Cu(I) coordinated triangles and a side view (bottom) with the POM anions in place as is found in **29**. Both are shown as 50% thermal ellipsoids. Hydrogen atoms and the included MeCN solvent have been omitted.



Some selected angles of the three Cu(I) complexes are shown below in Table 6.4. It appears that the Cu(I)/pyrimidine tetrahedra are well suited to form these triangles as the angles about each tetrahedron show only minimal distortion with no major constriction or expansion of these angles as the seemingly tight angles of the triangle is formed. This is

**Table 6.4** Selected bond lengths (Å) and angles (deg) for **29**

<i>Complex A</i>		<i>Complex B</i>		<i>Complex C</i>	
Cu(1) – N(1)	1.956(6)	Cu(2) – N(5)	2.085(5)	Cu(3) – N(9)	2.053(5)
Cu(1) – N(2)	1.978(6)	Cu(2) – N(6)	1.990(5)	Cu(3) – N(10)	2.061(5)
Cu(1) – N(3)	2.037(5)	Cu(2) – N(7)	2.047(5)	Cu(3) – N(11)	2.083(5)
Cu(1) – N(4)	2.039(5)	Cu(2) – N(8)	1.987(5)	Cu(3) – N(12)	2.054(6)
N(1) – Cu(1) – N(2)	111.4(2)	N(5) – Cu(2) – N(6)	101.1(2)	N(9) – Cu(3) – N(10)	114.4(2)
N(1) – Cu(1) – N(3)	107.5(2)	N(5) – Cu(2) – N(7)	103.0(2)	N(9) – Cu(3) – N(11)	107.2(2)
N(1) – Cu(1) – N(4)	116.3(2)	N(5) – Cu(2) – N(8)	111.1(2)	N(9) – Cu(3) – N(12)	110.3(2)
N(2) – Cu(1) – N(3)	108.7(2)	N(6) – Cu(2) – N(7)	101.9(2)	N(10) – Cu(3) – N(11)	113.3(2)
N(2) – Cu(1) – N(4)	103.9(2)	N(6) – Cu(2) – N(8)	117.7(2)	N(10) – Cu(3) – N(12)	105.2(2)
N(3) – Cu(1) – N(4)	108.8(2)	N(7) – Cu(2) – N(8)	119.6(2)	N(11) – Cu(3) – N(12)	105.7(2)

most likely due to how the pyrimidine ligand forms a bent bridge (~117 ° between the two coppers as well as the ability of this ligand to adopt various positions as these assemblies come together. Looking back at the asymmetric unit in Figure 6.7, it can be seen how two of the pyrimidine ligands are tilted in the same direction out of the plane defining the triangle bonding while the third pyrimidine ligand tilts in the opposite direction. This type of tilting of the pyrimidine was also seen in the tetramer of **25** (Figure 6.1), in which the positioning of the pyrimidines alternates going from one side of the square to the others.

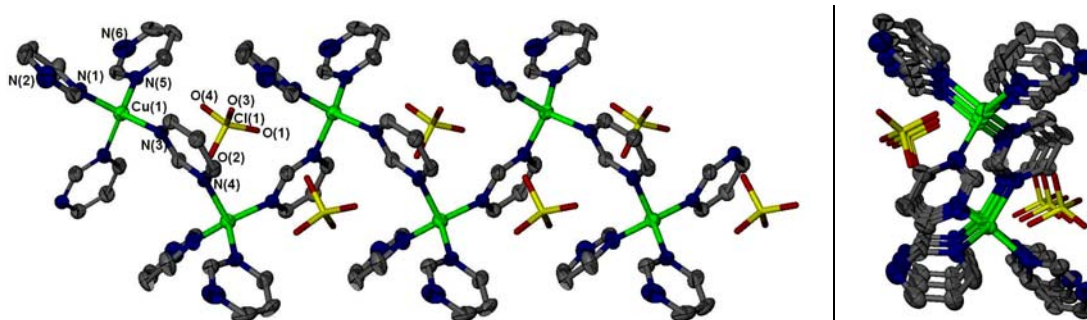
Interestingly, under the same conditions but with either the BF<sub>4</sub><sup>-</sup> or PF<sub>6</sub><sup>-</sup> anions, the discrete square tetramer is formed. Also under the same conditions and using the stronger coordinating ClO<sub>4</sub><sup>-</sup> and CF<sub>3</sub>SO<sub>3</sub><sup>-</sup> anions two unique three-dimensional extended solids (covered in detail in Section 6.5 and Chapter 7, respectively) were crystallized.

The positioning of the POM anion in this structure strongly suggests that this structure also could be formed by the anion templation brought on the spherical POM anion, just as was seen in the discrete hexagon of **28**. Again we find  $O_{\text{POM}} - H_{\text{pyr}}$  distances of 2.6 Å between the anion and the bridging ligands of the Cu(I) coordinated triangle. The positioning of the terminal pyrimidine ligand helps to complete a bowl-like formation that wraps about the POM anion. The POM anion templation seen in this structure as well as that in **28** offer hope that a large cavity porous solid can be templated by these large, non-coordinating anions, much like in the synthesis of the large cavity ZMS-5 zeolite as was presented in Chapter 1.

### 6.3.2.2 The 1-D Chain of $[Cu(\text{pyrim})_3]ClO_4$

The results obtained from the reaction the perchlorate tetrakis(acetonitrile)copper(I) starting material with 20+ equivalents of pyrimidine reminds us of the results leading to the formation of the discrete hexagon. With this reaction, instead of an expected high-dimensional solid being produced, we obtained a one-dimensional chain of  $Cu(C_4H_4N_2)_2(ClO_4) \cdot THF$ , **30**.

The symmetric unit of **30** contains one unique copper with three pyrimidine ligands coordinated along with one non-coordinated anion. As shown in Figure 6.10, two of the



**Figure 6.10** The 1-D chain from **30** shown (left) lengthwise and (right) as viewed from the end in 50% thermal ellipsoids (anion in stick representation). The unique Cu and the associated nitrogen atoms and anion in the asymmetric unit are labeled and carbons unlabeled in gray. Hydrogen atoms have been omitted for clarity.

pyrimidine ligands are actually terminal ligands while the third pyrimidine bridges from one copper to another, completing the tetrahedral coordination geometry as it progresses into a one dimensional chain. As is shown in Figure 6.10, the coppers linked by pyrimidine (left) in a zigzag fashion while aligned on the same plane as is seen (right) viewing from the end of a chain. The terminal pyrimidines are positioned to either side of the chain.

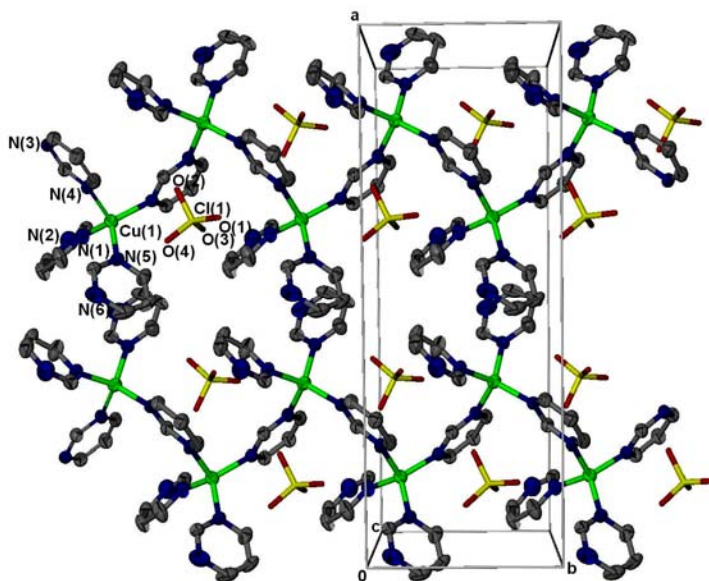
Selected angles of the found in **30** are listed in Table 6.5. Once again we can see that the pyrimidine is tilted to one side or the other to make the ligand fit the tetrahedral

**Table 6.5** Selected bond lengths (Å) and angles (deg) for **30**

Cu(1) – N(1)	2.035(3)
Cu(1) – N(3)	2.028(3)
Cu(1) – N(4)	2.085(3)
Cu(1) – N(5)	2.039(3)
N(3) – Cu(1) – N(1)	114.47(12)
N(1) – Cu(1) – N(5)	106.70(12)
N(5) – Cu(1) – N(3)	115.65(11)

geometry, instead of distorting the tetrahedron to fit the pyrimidine, as we have shown happens using the linear, rod-shaped bpy ligand.

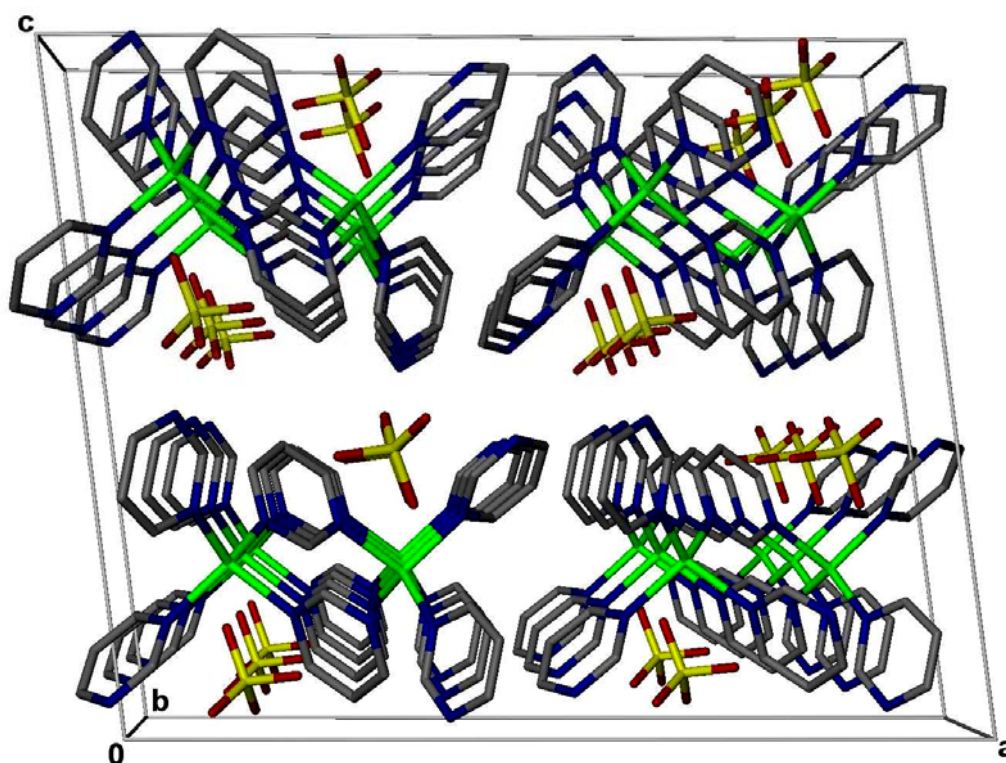
So far, we have shown how other 1-D chains (**21**, **22**, and **24**) pack fairly close as one chain fits into the grooves of the adjacent chain. As is shown in Figure 6.11, the 1-D chains of **30**



**Figure 6.11** Two chains as they stack together in **30** shown in 50% thermal ellipsoids. The anions are shown in stick representation and the hydrogen atoms have been omitted for clarity.

have adopted a somewhat different packing arrangement as the terminal pyrimidine ligands of one chain are paired with the terminal ligands of the adjacent chain, with each pair of ligands meeting the other at  $\sim 90^\circ$  angle to each other. They are then locked into place in this fashion by what might be a set of rather long distant (some 4.0 Å closest distance)  $\pi - \pi$  interactions between the terminal pyrimidine ligands. The  $\text{ClO}_4^-$  Anions are found well within the confines of the cavities formed by each individual chain network with a non-coordinated Cu – O distance of 4.3 Å and the perchlorates closest encounter being with the pyrimidine ligands at an O – H of  $\sim 2.9$  Å.

The complete packing of these chains, as seen in Figure 6.12, then takes on the all too familiar appearance of a layered clay-analog we have been searching for all along.



**Figure 6.12** A stick representation of the chains in **30** as they take on the appearance of a layered solid.

The spaces between the layers are about 2.4 Å wide and are devoid of any included solvent. Even the anion is tucked away within the chain's cavities. Even with the seemingly loosely bonded packing seen in **30**, the crystals have a fairly solid texture and are also relatively air-stable and can remain intact while out of solvent for an extended length of time. Such stability is important trait in solids to be considered for applications such as anion exchange and selective solvent extraction.

Most interesting with the synthesis of this structure is how it forms with such large amounts of pyrimidine. At just slightly less than 20 equivalents of pyrimidine, this same reaction results in the synthesis of three-dimensional solid, which persists as the only product even at pyrimidine concentrations below the stoichiometry found in the structure itself. Further discussion on this matter and details of these results for the 3-D structures will be presented in Section 6.5.

## **6.4 Two-Dimensional Bilayered Extended Solids**

### *6.4.1 Experimental Section*

#### *6.4.1.1 General Methods*

*Caution! Perchlorate salts are explosive and should be handled in small quantities and with extreme care at all times.* Cu<sub>2</sub>O, HBF<sub>4</sub>, HClO<sub>4</sub>, pyrimidine (ACROS); acetonitrile, dichloromethane, and diethyl ether (Fisher), were used without further purification. The [Cu(MeCN)<sub>4</sub>]X salts for X = BF<sub>4</sub><sup>-</sup> and ClO<sub>4</sub><sup>-</sup> were prepared as described in *Chapter 2*.

### 6.4.1.2 Synthesis

#### $[Cu_2(C_4H_4N_2)_3(MeCN)](ClO_4)_2$ , **31**

In a 5 dram vial were combined  $[Cu(MeCN)_4]ClO_4$  (0.040 g, 0.122 mmol) and pyrimidine (0.014 g, 0.171 mmol) in a solvent mixture of 4.0 mL of  $CH_2Cl_2$  and 1.0 mL MeCN. The vial was sealed and left at room temperature. Yellow prismatic crystals of **31** were harvested after 72 hours.

#### $[Cu_2(C_4H_4N_2)_3(MeCN)](BF_4)_2$ , **32**

In a 5 dram vial were combined  $[Cu(MeCN)_4]BF_4$  (0.040 g, 0.127 mmol) and pyrimidine (0.014 g, 0.171 mmol) in a solvent mixture of 4.0 mL of  $CH_2Cl_2$  and 1.0 mL MeCN. The vial was sealed and left at room temperature. Yellow prismatic crystals of **32** were harvested after 72 hours.

### 6.4.1.3 Single Crystal X-Ray Diffraction

Single crystals of high quality (by uniform extinction of polarized light) were coated with light oil and then mounted on a tip of a glass fiber using small amount of silicon grease for adhesion. Crystallographic data was collected using a Siemens SMART system with a CCD area detector ( $Mo K_{\alpha} = 0.71070 \text{ \AA}$ ). During data collection, the crystals were cooled to 173 K. The initial space group was determined by indexing several hundred strong reflections and the structures were solved using Direct Methods.<sup>7</sup> The structure models were further refined using least-squares techniques.<sup>8</sup>

For each structure, the majority of the heavier atoms were located with the initial solution. Any remaining non-hydrogen atoms were usually located after the first or second refinements. Anisotropic thermal parameters were refined for all non-hydrogen

atoms. The hydrogen atoms were included in calculated positions and refined as riding models with fixed  $U_{\text{iso}} = 1.2U_{\text{iso}}$  of the carbon atom for which they are bonded. All other structure-specific crystallographic details will be explained in the *Results and Discussion* section. Details of the data collection and structure solutions are given in Table 6.6.

<b>Table 6.6 Crystallographic Details for 31 and 32</b>		
	<b>31</b>	<b>32</b>
Empirical formula	Cu <sub>2</sub> C <sub>14</sub> H <sub>15</sub> N <sub>7</sub> O <sub>8</sub> Cl <sub>2</sub>	Cu <sub>2</sub> C <sub>14</sub> H <sub>15</sub> N <sub>7</sub> F <sub>8</sub> B <sub>2</sub>
Formula weight (g·mol <sup>-1</sup> )	607.31	582.03
Temperature, K	173(2)	173(2)
Crystal System, Space group	Monoclinic, P2 <sub>1</sub> /c	Monoclinic, P2 <sub>1</sub> /c
Unit cell dimensions		
<i>a</i> (Å)	15.268(2)	15.3474(7)
<i>b</i> (Å)	10.360(1)	10.2542(5)
<i>c</i> (Å)	14.876(2)	14.7363(7)
$\alpha$ , deg	90	90
$\beta$ , deg	114.824(2)	114.667(1)
$\gamma$ , deg	90	90
Z	4	4
Volume, Å <sup>3</sup>	2135.6(4)	2107.5(2)
$\rho_{\text{calc}}$ , g·cm <sup>-3</sup>	1.889	1.834
Absorption coefficient, mm <sup>-1</sup>	2.301	2.105
F(000)	1216	1152
Crystal size, mm	0.4 x 0.2 x 0.2	0.5 x 0.3 x 0.1
$\theta$ Range for data collection	2.45 to 27.14	1.46 to 27.11
Index ranges	-9 ≤ <i>h</i> ≤ 19 -13 ≤ <i>k</i> ≤ 13 -19 ≤ <i>l</i> ≤ 18	-18 ≤ <i>h</i> ≤ 19 -12 ≤ <i>k</i> ≤ 13 -18 ≤ <i>l</i> ≤ 18
Reflections collected	13171	12827
Unique reflections	4733 [R <sub>int</sub> = 0.0345]	4639 [R <sub>int</sub> = 0.0258]
Completeness to $\theta$	27.14 (99.8 %)	27.11 (99.8 %)
Max/min transmissions	1.00000/0.694415	1.00000/0.596443
Data/restraints/ parameters	4733/0/299	4639/0/299
Goodness of fit F <sup>2</sup>	1.010	0.963
Final R indices [ <i>I</i> > 2 $\sigma$ ( <i>I</i> )] <sup>a,b</sup>	R <sub>1</sub> = 0.0360 wR <sub>2</sub> = 0.0820	R <sub>1</sub> = 0.0340 wR <sub>2</sub> = 0.0924
R indices (all data)	R <sub>1</sub> = 0.0526 WR <sub>2</sub> = 0.0874	R <sub>1</sub> = 0.0445 WR <sub>2</sub> = 0.0961
Largest difference peak and hole (e·Å <sup>-3</sup> )	0.547/-0.323	0.916/-0.418
Structures were refined on F <sup>2</sup> for all data. <sup>a</sup> $R(F_o) = \frac{\sum   F_o  -  F_c  }{\sum  F_o }$ . <sup>b</sup> $R_w(F_o) = \frac{(\sum w   F_o  -  F_c  ^2)^{1/2}}{\sum  F_o }$ , $w = \frac{1}{\sigma^2(F_o) + (0.002F_o)^2}$ .		

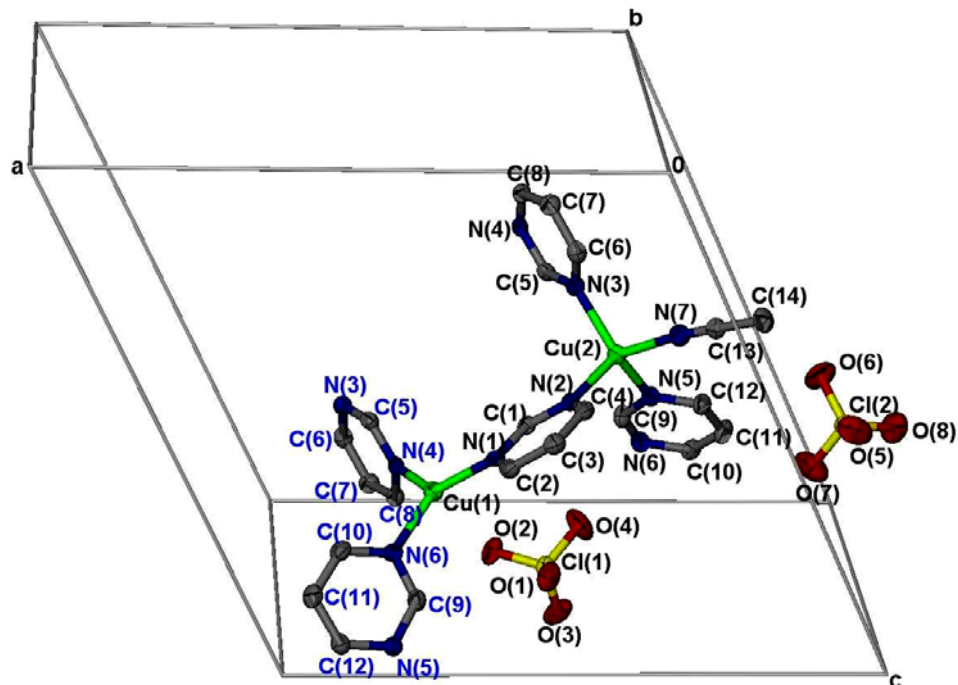


### 6.4.2 Results and Discussion

In the course of our study involving an investigation of other reaction solvent systems, we crystallized a novel two-dimensional Cu/pyrimidine coordinated layered structure. It was found that the reaction of either the perchlorate or the tetrafluoroborate starting materials with measured amounts of pyrimidine in a CH<sub>2</sub>Cl<sub>2</sub>:MeCN reaction solvent mixture would result in the self-assembly of the bilayered, two-dimensional extended solids of [Cu<sub>2</sub>(C<sub>4</sub>H<sub>4</sub>N<sub>2</sub>)<sub>3</sub>(MeCN)]X where X = (ClO<sub>4</sub>)<sub>2</sub>, **31** and X = (BF<sub>4</sub>)<sub>2</sub>, **32**.

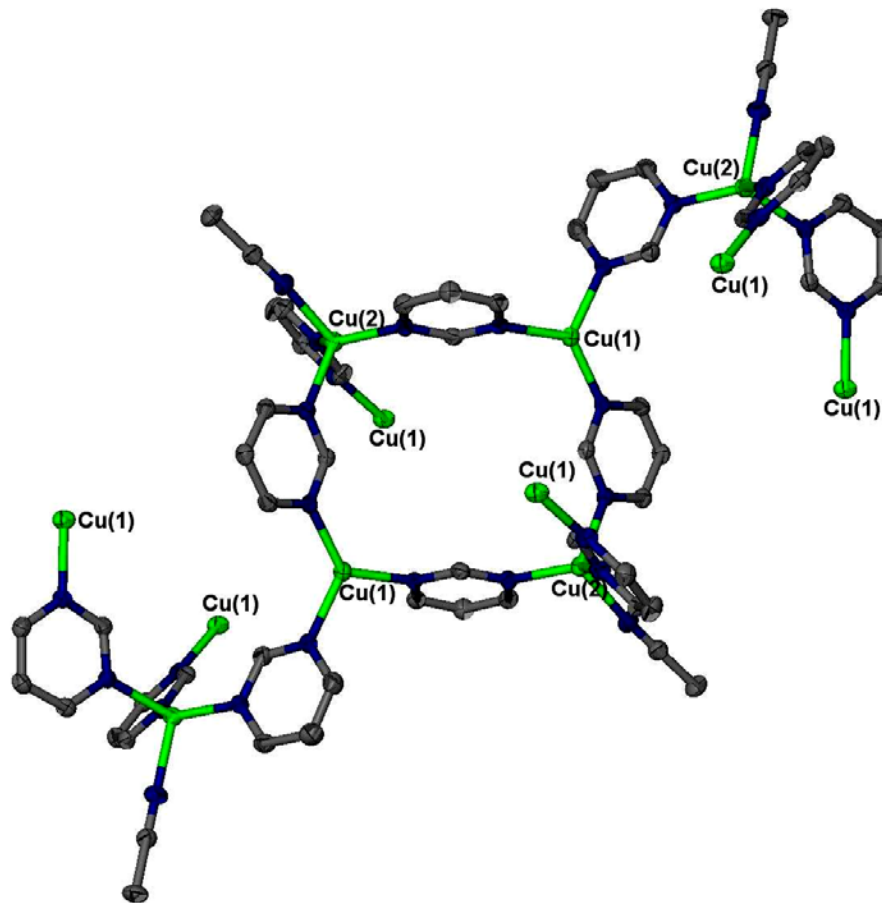
As shown in Table 6.6, both of these isostructural compounds crystallize in the monoclinic, P2<sub>1</sub>/c space group. Even the volumes of each of these structures show little change as the size of the anion changes (as in BF<sub>4</sub><sup>-</sup> and ClO<sub>4</sub><sup>-</sup>), since these anions reside among a rigid bilayer Cu(I) coordinated network. The asymmetric unit of these two structures contains two unique copper atoms; one of which is tetrahedrally coordinated to one MeCN and three bridging pyrimidine ligands while the other is coordinated to only three bridging pyrimidines in a trigonal planar coordination.

Figure 6.13 shows the coordination environments for both copper(I) centers in **31**. The atoms found in the asymmetric unit are labeled in black with additional atoms labeled in blue as are repeated on Cu(1) to illustrate how each of the three pyrimidine ligands on Cu(1) bridge to the Cu(2) tetrahedron. Although the trigonal planar coordination for Cu(I) is not very common, it has still been observed in a few structures. Lopez has identified a couple of these in her related studies,<sup>17, 23</sup> while three-coordinated Cu(I) polymers can be found in a limited amount of results from others as well.<sup>24</sup>



**Figure 6.13** The unit cell of **31** with the atoms belonging to the asymmetric unit labeled in black and additional atoms labeled in blue. Two additional pyrimidine ligands are included to illustrate the trigonal coordination of Cu(2). All atoms are shown as 50% thermal ellipsoids with hydrogen atoms omitted for clarity.

A somewhat familiar shape takes form as the asymmetric unit is grown out by a few units. As seen in Figure 6.14, the trigonal and tetrahedral Cu(I) centers bridge together to form a Cu-coordinated square. The trigonal and tetrahedral Cu units each form opposite diagonal corners of a square, which is then linked to the corner of another square (at each corner) in a flip-flop fashion, resulting in a sort of bilayered coordination network. One of the two anions [with Cl(1)] is closely associated with the trigonal copper with a Cu – O or Cu – F distance of  $\sim 2.5$  Å or 2.6 Å respectively and resides within the ‘bilayer’ network. The other anion [of Cl(2)] is rather distantly associated with the tetrahedral copper center with the closest Cu – O and Cu – F distances at  $\sim 3.9$  Å for both as it sits on either side on the surface of the bilayer.



**Figure 6.14** The two Cu(I) centers in **31** combine to form a square building block unit. Shown as 50% thermal ellipsoids with hydrogen atoms omitted for clarity.

Some selected distances and angles found in both **31** and **32** are listed in Table 6.7.

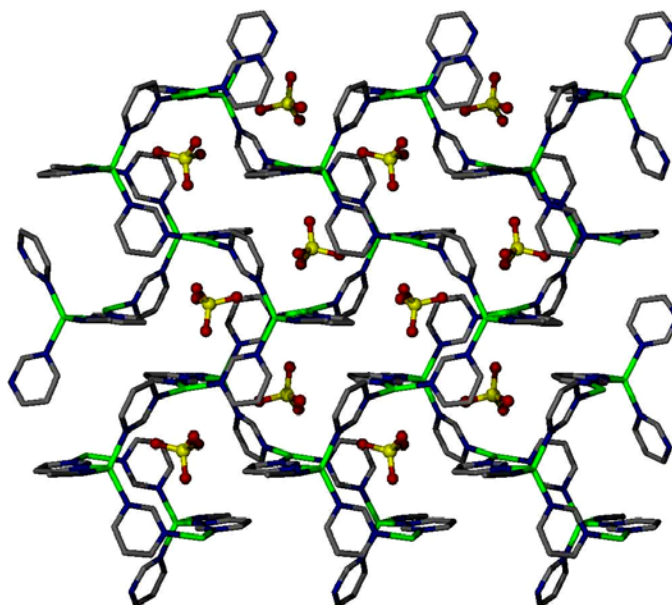
One big difference seen here are the shorter Cu – N coordination bonds around the trigonal Cu. This is most probably caused by the greater attraction the copper atom has

**Table 6.7** Selected bond lengths (Å) and angles (deg) for **31** and **32**.

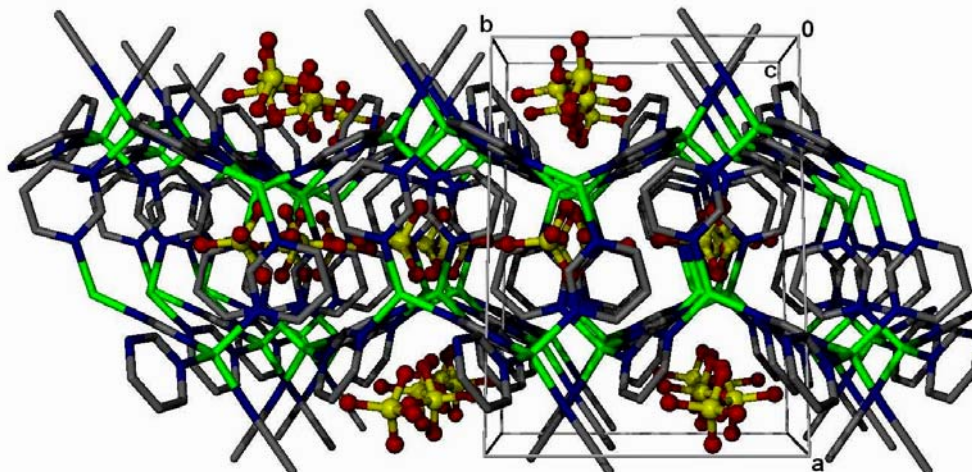
	<i>Cu(1) Complex</i>		<i>Cu(2) Complex</i>		
	<b>31</b>	<b>32</b>	<b>31</b>	<b>32</b>	
Cu(1) – N(1)	1.964(2)	1.964(2)	Cu(2) – N(2)	2.057(2)	2.057(2)
Cu(1) – N(4)	1.990(2)	1.986(2)	Cu(2) – N(3)	2.026(2)	2.037(3)
Cu(1) – N(6)	2.022(2)	2.019(2)	Cu(2) – N(5)	2.010(2)	2.015(2)
			Cu(2) – N(7)	2.038(3)	2.052(3)
N(1)-Cu(1)-N(4)	127.41(9)	128.17(9)	N(3)-Cu(2)-N(2)	103.94(9)	104.40(9)
N(1)-Cu(1)-N(6)	121.04(9)	120.55(9)	N(5)-Cu(2)-N(2)	112.06(9)	114.06(9)
N(4)-Cu(1)-N(6)	110.97(9)	111.29(9)	N(7)-Cu(2)-N(2)	102.4(1)	102.72(9)
			N(5)-Cu(2)-N(3)	128.64(9)	126.35(9)
			N(7)-Cu(2)-N(3)	103.48(9)	103.5(1)
			N(5)-Cu(2)-N(7)	103.1(1)	102.90(9)

for only three lone pairs of electrons than for four pairs as in the tetrahedral coordination. In the angles of the tetrahedra in **31** and **32** there once again seems to be only a little distortion as the adjustments provided by the pyrimidine ligands account for a lot of the changes in the angles of the coordination network. The single wide,  $128^\circ$  and  $126^\circ$  N – Cu – N angle in **31** and **32** respectively is at the site where one square is bridged to another square and the resulting wider angle is most likely due to the steric effects between these two Cu(I) coordinated squares. In the trigonal coordination, there is also some distortion out of the normal  $120^\circ$  for each angle. The widest N – Cu – N angle of  $127^\circ$  and  $128^\circ$  for **31** and **32** respectively is related to the strain caused by the formation of the corner of the square by this particular angle.

The top figure in Figure 6.15 shows face view of the bilayer as each square cell is linked to four other cells. The resulting layer has a series of peanut shaped cavities in which the anions found within the layer reside. The outer anion was omitted to help with the view of the cavities and the positioning of the interlayer anions.



**Figure 6.15** Stick representation of (top) a face view of a single layer in **31** showing only the anion inside the payer in the peanut shaped cavities.

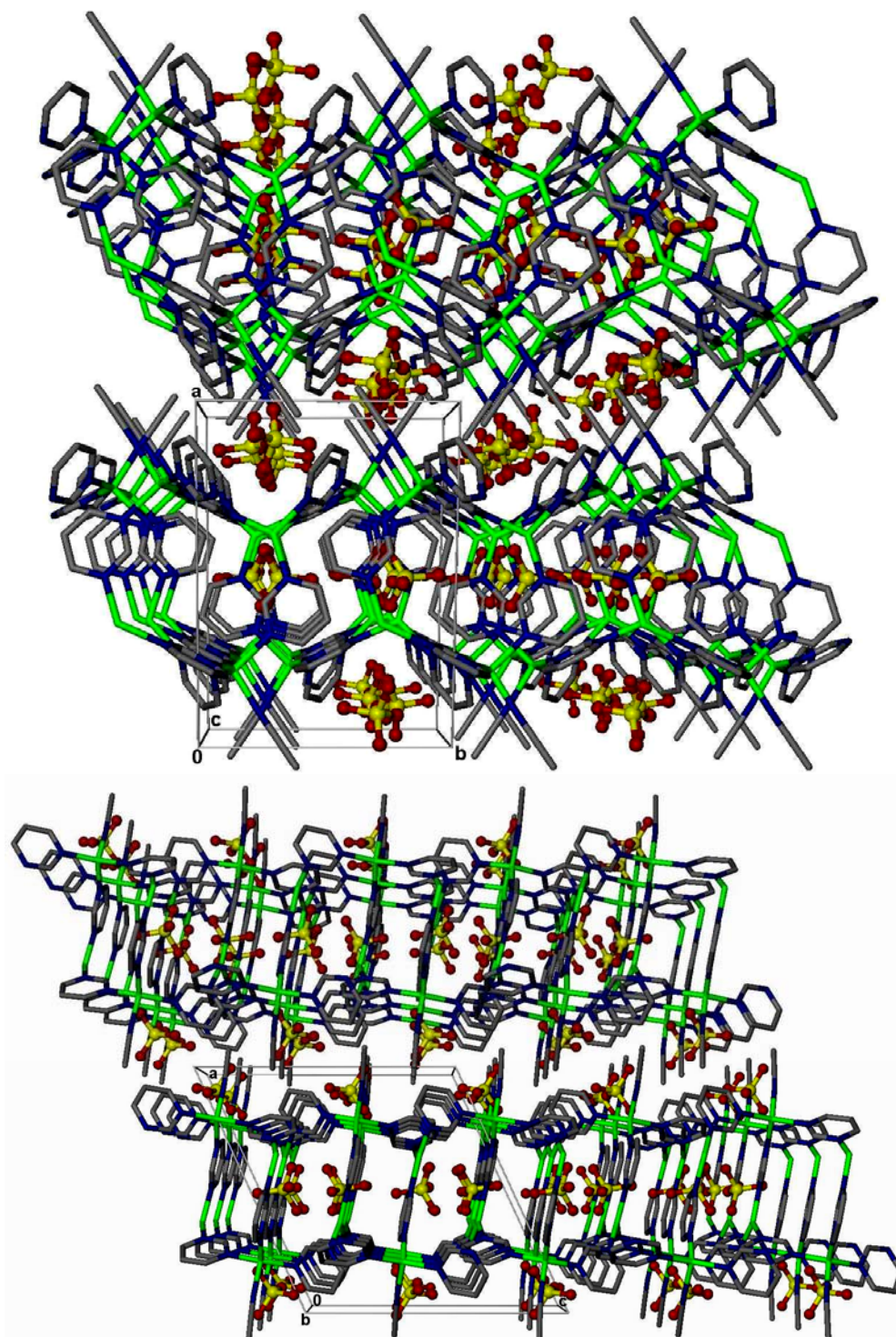


**Figure 6.16** That same layer as shown in Figure 6.15 as seen from the side (bottom) showing the positioning of the outer anion. Anions are shown as spheres and the hydrogen atoms are omitted.

In Figure 6.16, a single layer is shown looking down the *c*-axis, with both anions included. These bilayers stack with the extended MeCN ligands in one layer fitting into the trough of the adjacent layer. Figure 6.17 shows two layers (top) as they are looking down the *c*-axis and (bottom) looking down the *b*-axis of the unit cell. What appears to be a close encounter between the MeCN ligands and the anion in-between the layers is somewhat misleading. However, the anion actually does sit in-between two MeCN ligands with a H – O or H – F distance of  $\sim 2.5$  Å on one side and  $\sim 2.7$  Å on the other.

It is interesting that this structure might appear as bilayer composed of linked squares. Once again we see that the basic tetramer shape is incorporated into a higher dimensional solid. This suggests this simpler, four-copper unit is a basic building block for these structures. The formation of this structure only in the  $\text{CH}_2\text{Cl}_2$ :MeCN mixture might be simply due to different solubility afforded in this particular solvent system. Both **31** and **32** also appear somewhat stable when removed from the reaction solvent and appear to meet the structural requirements for being considered as a clay-analog. Future

studies with this material are ongoing to uncover any interesting and useful functionality that these materials might have.



**Figure 6.17** Stick representation of two layers in **31** as they are stack together. The perchlorate anion is shown as spheres and the hydrogen atoms have been omitted for clarity.

## 6.5 Three-Dimensional Extended Solids

### 6.5.1 Experimental Section

#### 6.5.1.1 General Methods

*Caution! Perchlorate salts are explosive and should be handled in small quantities and with extreme care at all times.* Cu<sub>2</sub>O, HBF<sub>4</sub>, HClO<sub>4</sub>, HPF<sub>6</sub> and pyrimidine (ACROS); acetonitrile (MeCN), benzonitrile (PhCN), tetrahydrofuran (THF), benzene (Bz), nitrobenzene (NO<sub>2</sub>Ph), nitromethane (NO<sub>2</sub>Me), dichloromethane (CH<sub>2</sub>Cl<sub>2</sub>), and diethyl ether (Fisher); and triflic acid (Aldrich), were used without further purification. The [Cu(MeCN)<sub>4</sub>]X salts for X = BF<sub>4</sub><sup>-</sup> and ClO<sub>4</sub><sup>-</sup>, and the [Cu(PhCN)<sub>4</sub>]X salts for CF<sub>3</sub>SO<sub>3</sub><sup>-</sup> and PF<sub>6</sub><sup>-</sup>, were prepared as described in *Chapter 2*.

#### 6.5.1.2 Synthesis

Since this study shows how various structures can be made in a variety of solvents and solvent mixtures, each synthesis presented below will be specific to one particular solvent system while the variations of these syntheses, as they exist, will be dealt with in totality in the *Results and Discussion* section. A few select structures (structures **38 – 41**) previously reported by Lopez and Keller have been included in the synthesis section (with the most current and reliable synthesis method stated) since they are also included in this study. In each relevant case, the ownership has been duly noted and reference sited.

*[Cu(C<sub>4</sub>H<sub>4</sub>N<sub>2</sub>)<sub>2.3</sub>](ClO<sub>4</sub>), **33***

As previously reported by Lopez.<sup>6</sup> In a 1 dram vial were combined [Cu(MeCN)<sub>4</sub>]ClO<sub>4</sub> (0.040 g, 0.122 mmol) and pyrimidine (0.042 g, 0.512 mmol) in 0.5 mL of MeCN and 2.0 mL nitrobenzene. This vial was then placed inside a 20 mL, screw-top vial containing 5 mL of THF. The large vial was sealed and the THF slowly diffused into the reaction solution. After 72 hours, yellow, prismatic crystals of **33** were harvested from the smaller vial.

*[Cu(C<sub>4</sub>H<sub>4</sub>N<sub>2</sub>)<sub>2</sub>]BF<sub>4</sub> · *n* solvent, **34***

As previously reported by Lopez and Keller.<sup>6,7</sup> In a 1 dram vial were combined [Cu(MeCN)<sub>4</sub>]BF<sub>4</sub> (0.040 g, 0.127 mmol) and pyrimidine (0.042 g, 0.512 mmol) in 0.5 mL of MeCN and 2.0 mL nitrobenzene. This vial was then placed inside a 20 mL, screw-top vial containing 5 mL of THF. The large vial was sealed and the THF slowly diffused into the reaction solution. After 72 hours, yellow, columnar crystals of **34** were harvested from the smaller vial.

*[Cu(C<sub>4</sub>H<sub>4</sub>N<sub>2</sub>)<sub>2.3</sub>]BF<sub>4</sub>, **35***

In a 1 dram vial were combined [Cu(MeCN)<sub>4</sub>]BF<sub>4</sub> (0.040 g, 0.127 mmol) and pyrimidine (0.042 g, 0.512 mmol) in 0.5 mL of MeCN. This vial was then placed inside a 20 mL, screw-top vial containing 5 mL of THF. The large vial was sealed and the THF slowly diffused into the MeCN. After 72 hours, yellow, columnar crystals of **35** were harvested from the smaller vial.



*[Cu<sub>3</sub>(C<sub>4</sub>H<sub>4</sub>N<sub>2</sub>)<sub>7.5</sub>(PhCN)](PF<sub>6</sub>)<sub>3</sub>, **36***

In a 1 dram vial were combined [Cu(PhCN)<sub>4</sub>]PF<sub>6</sub> (0.040 g, 0.065 mmol) and pyrimidine (0.14 g, 0.171 mmol) in 0.5 mL of PhCN. This vial was then placed inside a 20 mL, screw-top vial containing 5 mL of THF. The large vial was sealed and the THF slowly diffused into the PhCN solution. After 72 hours, yellow prismatic crystals of **36** were harvested from the smaller vial.

*6.5.1.3 Single Crystal X-Ray Diffraction*

In all cases, a single crystal of high quality (by uniform extinction of polarized light) was coated with light oil and then mounted on a tip of a glass fiber using small amount of silicon grease for adhesion. Crystallographic data was collected using a Siemens SMART system with a CCD area detector (Mo K<sub>α</sub> = 0.71070 Å). During data collection, the crystal was cooled to 173 K. The initial space group was determined by indexing several strong reflections and the structures were solved using Direct Methods.<sup>8</sup> The structure models were further refined using least-squares techniques.<sup>9</sup>

For each structure, the majority of the heavier atoms were located with the initial solution. Any remaining non-hydrogen atoms were usually located after the first or second refinements. Anisotropic thermal parameters were refined for all non-hydrogen atoms. The hydrogen atoms were included in calculated positions and refined as riding models with fixed U<sub>iso</sub> = 1.2U<sub>iso</sub> of the carbon atom for which they are bonded. All other structure-specific crystallographic details will be explained in the *Results and Discussion* section. Details of the data collection and structure solutions are given in Table 6.8.

<b>Table 6.8 Crystallographic Details for 33 – 36</b>				
	<b>33</b>	<b>34</b>	<b>35</b>	<b>36</b>
Empirical formula	Cu <sub>1.3</sub> C <sub>12</sub> H <sub>12</sub> N <sub>6.2</sub> O <sub>5.4</sub> Cl <sub>1.3</sub>	CuC <sub>21</sub> H <sub>22</sub> F <sub>4</sub> N <sub>4</sub> O <sub>2</sub> B	Cu <sub>1.3</sub> C <sub>12</sub> H <sub>12</sub> N <sub>6.2</sub> F <sub>5.4</sub> B <sub>1.3</sub>	CuC <sub>9.23</sub> H <sub>8.31</sub> N <sub>4.15</sub> F <sub>6</sub> P
Formula weight (g·mol <sup>-1</sup> )	458.16	596.03	440.93	385.94
Crystal System, Space group	Hexagonal, R-3	Orthorhombic, Pmc2 <sub>1</sub>	Hexagonal, R-3	Hexagonal, R-3
Unit cell dimensions				
<i>a</i> (Å)	33.749(2)	20.342(2)	33.557(3)	33.889(1)
<i>b</i> (Å)	33.749(2)	16.365(2)	33.557(3)	33.889(1)
<i>c</i> (Å)	12.8981(8)	15.794(2)	12.7192(16)	13.3064(7)
$\alpha$ , deg	90	90	90	90
$\beta$ , deg	90	90	90	90
$\gamma$ , deg	120	90	120	120
Z	30	12	30	39
Volume, Å <sup>3</sup>	12723(1)	5258(1)	12404(2)	13234.3(10)
$\rho_{\text{calc}}$ , g·cm <sup>-3</sup>	1.794	1.521	1.771	1.892
Absorption coefficient, mm <sup>-1</sup>	1.900	1.686	1.762	1.803
F(000)	6912	2392	6585	7449
Crystal size, mm	0.3 x 0.1 x 0.05	0.3 x 0.1 x 0.1	0.4 x 0.3 x 0.2	0.3 x 0.3 x 0.2
$\theta$ Range for data collection	1.21 to 27.10	1.60 to 27.18	1.21 to 27.27	1.20 to 27.13
Index ranges	-43 ≤ <i>h</i> ≤ 34 -34 ≤ <i>k</i> ≤ 43 -16 ≤ <i>l</i> ≤ 16	-26 ≤ <i>h</i> ≤ 26 -18 ≤ <i>k</i> ≤ 20 -20 ≤ <i>l</i> ≤ 17	-40 ≤ <i>h</i> ≤ 43 -41 ≤ <i>k</i> ≤ 43 -16 ≤ <i>l</i> ≤ 16	-43 ≤ <i>h</i> ≤ 34 -43 ≤ <i>k</i> ≤ 43 -12 ≤ <i>l</i> ≤ 17
Reflections collected	26640	16338	25901	27901
Unique reflections	6243 [R <sub>int</sub> = 0.1102]	5626 [R <sub>int</sub> = 0.1209]	6180 [R <sub>int</sub> = 0.0753]	6510 [R <sub>int</sub> = 0.0752]
Completeness to $\theta$	27.10 (100.0 %)	27.18 (99.6 %)	27.27 (99.6 %)	27.13 (100 %)
Max/min transmissions	1.00000/0.691366	1.00000/0.651609	1.00000/0.808055	1.00000/0.637099
Data/restraints/parameters	6243/0/397	5626/1/320	6180/0/423	6510/0/421
Goodness of fit F <sup>2</sup>	1.040	1.028	1.114	1.029
Final R indices [I > 2 $\sigma$ (I)] <sup>a,b</sup>	R <sub>1</sub> = 0.0620 wR <sub>2</sub> = 0.1554	R <sub>1</sub> = 0.1085 wR <sub>2</sub> = 0.2628	R <sub>1</sub> = 0.0717 wR <sub>2</sub> = 0.1470	R <sub>1</sub> = 0.0656 wR <sub>2</sub> = 0.1567
R indices (all data)	R <sub>1</sub> = 0.0897 WR <sub>2</sub> = 0.1779	R <sub>1</sub> = 0.2012 WR <sub>2</sub> = 0.3165	R <sub>1</sub> = 0.1189 WR <sub>2</sub> = 0.1619	R <sub>1</sub> = 0.1322 WR <sub>2</sub> = 0.1886
Largest difference peak and hole (e·Å <sup>-3</sup> )	1.019/-0.671	1.397/-0.880	0.722/-0.856	1.958/-0.748
Structures were refined on F <sup>2</sup> for all data. <sup>a</sup> $R(F_o) = \sum   F_o  -  F_c   / \sum  F_o $ . <sup>b</sup> $R_w(F_o) = (\sum w  F_o  -  F_c  ^2 / \sum  F_o ^2)^{1/2}$ , $w = [\sigma^2(F_o) + (0.002F_o)^2]^{-1}$ .				

## 6.5.2 Results and Discussion

### 6.5.2.1 Three-Dimensional Extended Solids With the $\text{ClO}_4^-$ and $\text{BF}_4^-$ Anions

The three-dimensional Cu(I)/pyrimidine extended solids were actually the first structures to be synthesized by the reaction between the tetrakis(acetonitrile)copper(I) salt and pyrimidine. The first of these, as  $[\text{Cu}(\text{C}_4\text{H}_4\text{N}_2)_2]\text{BF}_4 \cdot n$  solvent (noted in this report as structure **34**) was described as being a prime example of how these materials can mimic the silicates; its structure was compared to the likeness of the silicate mineral *feldspar*.<sup>25</sup> Following this discovery, Lopez had discovered yet another three-dimensional structure with this system, this time involving the  $\text{ClO}_4^-$  anion in the structure of  $[\text{Cu}(\text{C}_4\text{H}_4\text{N}_2)_{2.3}](\text{ClO}_4)$  **33**.

The occurrence of both of these structures appears to be dependent upon the identity of the anion included in each reaction. In fact, the earlier conclusion made by Lopez was that these type of structures were indeed anion-dependant, much as what we have seen with the reactions with the 4,4'-bipyridine ligand.<sup>17</sup> In this section we will support, modify, and/or improve on the former conclusions by presenting the findings of this study. In the course of our investigation into these reactions with the perchlorate anion, we had uncovered some interesting finds in regards to the synthesis of **33**. It appears that **33** can, in fact, be produced in a wide variety of solvents as well as with a wide range of pyrimidine equivalence.

Those reaction solvents that produced **33** include: the original 1:4 MeCN:NO<sub>2</sub>Ph, MeCN alone, 1:4 MeCN:NO<sub>2</sub>Me, all followed by vapor diffusion with either THF or Et<sub>2</sub>O. It was also found that the reaction solvents of 1:4 MeCN:CH<sub>2</sub>Cl<sub>2</sub>, 1:4

MeCN:Benzenes, and even Benzene or THF alone produce **33** without the aid of solvent vapor diffusion. These later group of reaction solvents would generally produce a precipitate at first which would then transform slowly into the single crystals of **33**; much like we had seen with the Cu(I)/bpy reactions but at a much slower rate, typically several weeks instead of only a couple days. Also with 2-3 equivalents of pyrimidine, the 2-D bilayered **31** co-crystallized with **33** in the MeCN:CH<sub>2</sub>Cl<sub>2</sub> reaction solvents.

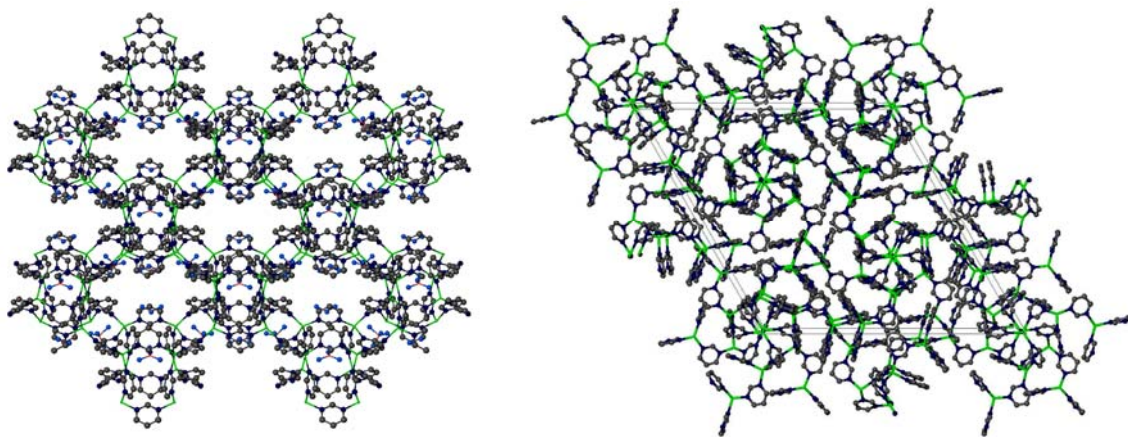
Along with this lack of solvent dependence, **33** appears to be the dominant structure of this system as it appeared in a wide range of pyrimidine concentrations. **33** is seen in reactions using just less than the 20 equivalents used to make the linear chain of **30** and is the sole product in reaction all the way until just below 2.0 equivalents of pyrimidine used. At this stoichiometric level of pyrimidine, as **33** continues to appear, the starting material also begins to crystallize. These two products appear in a step-wise fashion, much as was indicated happens for the BF<sub>4</sub><sup>-</sup> anion's system (equation 6.2), in which **33** forms first with the starting material appearing as the pyrimidine concentration is reduced. At no time, however, is a similar tetramer with the ClO<sub>4</sub><sup>-</sup> produced.

Although these results seem to confirm the anion dependence of **33**, results obtained in the investigation of the BF<sub>4</sub><sup>-</sup> system contradicted this conclusion. During the course of our study of the reactions with BF<sub>4</sub><sup>-</sup> anion, we found that as the reaction solvent was changed to using *only* MeCN, resulted in the synthesis of [Cu(C<sub>4</sub>H<sub>4</sub>N<sub>2</sub>)<sub>2.3</sub>]BF<sub>4</sub> **35**, which was found to be surprisingly isostructural to **33**. Subsequent reactions carried out in the same variety of solvents used with the reactions involving the perchlorate anion (listed above) also produced **35**; with the exception of those reactions having either nitrobenzene or nitromethane included in the solvent, of which both produced the feldspar-analog of

**34**. Also, just as with  $\text{ClO}_4^-$ , the 2-D bilayered **32** co-crystallized with **35** in the  $\text{MeCN}:\text{CH}_2\text{Cl}_2$  reaction solvents.

These results suggested that there was a  $\text{NO}_2\text{Ph}$  and  $\text{NO}_2\text{Me}$  solvent dependence with the formation of the original, feldspar-analog structure of **34** all along. In the absence of either of these nitro-bearing solvents, these reactions follow the path laid out by the perchlorate reactions. Examination of both **34** and **35** might provide explanation as to what might be the directing factor in these reactions.

Figure 6.18 shows a side-by-side view of structures **34** and **35**. From this view alone it can be seen how the structure of **34** has spacious cavities within the structure while **35** is a tightly woven Cu(I) coordination network with very little open space visible. The extensive cavity formation in **34** is expansive; both the  $\text{BF}_4^-$  anion and  $\text{NO}_2\text{Ph}$  solvent are



**Figure 6.18** A side-by-side comparison of (left) **34** and **35**. The unit cell is doubled for **34** so a view of the porous network can be seen and compare to the tightly woven network of **35**. The anions have been omitted in **35** while both structures hydrogen atoms are omitted for clarity.

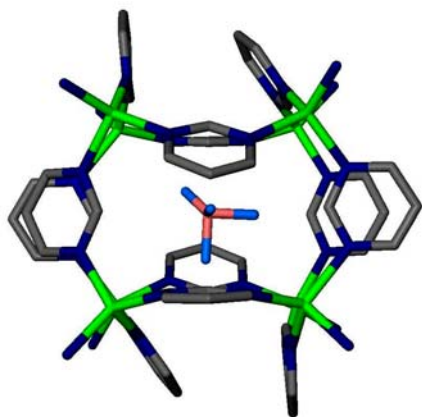
highly disordered throughout the structure. The nitrobenzene is so disordered, that the exact position cannot be determined from the crystallographic data and its actual presence in the structure only confirmed by  $^1\text{H}$  NMR analysis.<sup>25</sup> The structure of **35** has no included solvent within the structure (as is also the case with **33**) as the Cu(I) coordination provides little room for anything else besides the non-coordinated anion.

A closer examination of the differences of these two structures can be done by observing the differences in the Cu(I) tetrahedral coordination spheres. Table 6.9 list those select distances and angles of each tetrahedron found in both **34** and **35**. There

<b>Table 6.9</b> Selected bond lengths (Å) and angles (deg) for <b>34</b> and <b>35</b> .					
<b>34</b>					
<i>Complex A</i>			<i>Complex B</i>		
Cu(1) – N(1)	2.076(11)		Cu(2) – N(5)	2.075(11)	
Cu(1) – N(2)	2.036(12)		Cu(2) – N(6)	2.004(13)	
Cu(1) – N(3)	2.078(12)		Cu(2) – N(7)	2.084(13)	
Cu(1) – N(4)	2.022(12)		Cu(2) – N(8)	2.150(12)	
N(1) – Cu(1) – N(2)	113.1(5)		N(5) – Cu(2) – N(6)	118.3(5)	
N(1) – Cu(1) – N(3)	102.0(5)		N(5) – Cu(2) – N(7)	109.9(5)	
N(1) – Cu(1) – N(4)	107.3(4)		N(5) – Cu(2) – N(8)	109.4(5)	
N(2) – Cu(1) – N(3)	111.4(4)		N(6) – Cu(2) – N(7)	111.3(5)	
N(2) – Cu(1) – N(4)	110.1(5)		N(6) – Cu(2) – N(8)	94.7(5)	
N(3) – Cu(1) – N(4)	112.6(5)		N(7) – Cu(2) – N(8)	112.4(5)	
<b>35</b>					
<i>Complex A</i>		<i>Complex B</i>		<i>Complex C</i>	
Cu(1) – N(1)	2.053(5)	Cu(2) – N(6)	2.010(5)	Cu(3) – N(10)	2.20(1)
Cu(1) – N(2)	2.047(5)	Cu(2) – N(7)	2.091(5)	Cu(3) – N(11)	2.08(2)
Cu(1) – N(3)	2.055(6)	Cu(2) – N(8)	2.036(5)		
Cu(1) – N(5)	2.029(5)	Cu(2) – N(9)	2.027(5)		
N(1) – Cu(1) – N(2)	106.1(2)	N(6) – Cu(2) – N(7)	105.6(2)	N(10) – Cu(3) – N(10)	117.3(2)
N(1) – Cu(1) – N(3)	102.8(2)	N(6) – Cu(2) – N(8)	112.2(2)	N(10) – Cu(3) – N(11)	99.5(3)
N(1) – Cu(1) – N(5)	114.0(2)	N(6) – Cu(2) – N(9)	114.2(2)		
N(2) – Cu(1) – N(3)	113.1(2)	N(7) – Cu(2) – N(8)	105.5(2)		
N(2) – Cu(1) – N(5)	107.2(2)	N(7) – Cu(2) – N(9)	104.9(2)		
N(3) – Cu(1) – N(5)	113.5(2)	N(8) – Cu(2) – N(9)	113.5(2)		

seems to be nothing too unusual about most of the tetrahedron with the exception of complex B in **34** and complex c in **35**. The most prominent distortion is seen in one N – Cu – N angle in complex B of **35**. The occurrence of this 94° may be the key factor that directs this coordination assembly to form its own unique structure. The identical distances and angles seen in complex C for **35** is due to how the Cu is only one-sixth occupied at that position as it is disordered over a three bar axis. The unusually long Cu – N distances here may be due to the strain placed on this structure as it forms a tight cage about one of the BF<sub>4</sub><sup>-</sup> anions.

Figure 6.19 shows a stick representation of one of those *anion cages* that is found in **35** and in the perchlorate's structure of **33**, as well as in three other structures we will present in the later part of this chapter. These cages are constructed of two tetramers



**Figure 6.19** The anion cage found in **34**. Hydrogen atoms are omitted for clarity.

bridged together as the self-assembly process continued. The way this anion sits within this coordinated cage indicates that anion-templation could have been responsible for its formation. As Lopez had first proposed this anion templation effect by the  $\text{ClO}_4^-$  anion in **33**, this should also apply than for  $\text{BF}_4^-$  in the formation of a similar cage in **34**.<sup>17</sup> It would seem more probable that these cages formed around the anion rather than the anion finding its way into the cage during the final crystallization of the solid from solution.

This anion templation proposal can be supported as we look back to the feldspar-analog solvent dependence question. In order to form the feldspar-analog, one must have either nitrobenzene or nitromethane present in the reaction solvent. What is it about these two solvents that might bring about a certain route of self-assembly? In order to answer this question, we can apply what we have learned in from the study of the Cu/bpy reactions with regards to anion and solvent influences on the self-assembly.

In Chapters 4 and 5 we showed how the coordination ability of either the solvent or the anion might be a controlling factor in the self-assembly of these coordination solids. We have also provided evidence that even the most non-coordinating anion or solvent can and will coordinate, if only temporarily, under certain conditions. It was then

proposed that this temporary coordination by either the anion or solvent produces intermediate structures, which then lead to the formation of the final product.

Now we see, in structures **33** and **34**, evidence that suggests anion templation is involved with the formation of these structures. However, if anion templation is indeed the case here, we would expect this effect to occur at a much lesser degree for the very weak coordinating  $\text{BF}_4^-$  anion over that of the much stronger coordinating  $\text{ClO}_4^-$  anion. Since we see a definite change in the self-assembly as either  $\text{NO}_2\text{Ph}$  or  $\text{NO}_2\text{Me}$  is present, than perhaps these weakly coordinating solvents do, in fact, interfere with the weak templation effect of the  $\text{BF}_4^-$  anion.

Although we have not yet succeeded to isolate any structures (intermediate or otherwise) that have either  $\text{NO}_2\text{Ph}$  or  $\text{NO}_2\text{Me}$  as a coordinated ligand, such a coordination should be possible considering the lone pairs that are available on the two oxygen atoms on the nitro group. There is a small collection of coordination compounds that do exist with either of these solvent molecules coordinated.<sup>26</sup> Although these two solvents are described as being notoriously non-coordinating, they still have managed to isolate both monodentate and bidentate,  $\text{M} - \text{O}$  coordinated species.

Even though these two nitro solvents are such weak coordinators, they can still offer competition with the weakly coordinating anions when present in such large volumes as



**Table 6.10** Selected Donor Numbers [kcal. mol<sup>-1</sup>]

	DN
Anion	
BF <sub>4</sub> <sup>-</sup>	6.03
ClO <sub>4</sub> <sup>-</sup>	8.44
CF <sub>3</sub> SO <sub>3</sub> <sup>-</sup>	16.9
Solvent	
Bz	0.1
NO <sub>2</sub> Me	2.7
NO <sub>2</sub> Ph	4.4
PhCN	11.9
MeCN	14.1
THF	20.0

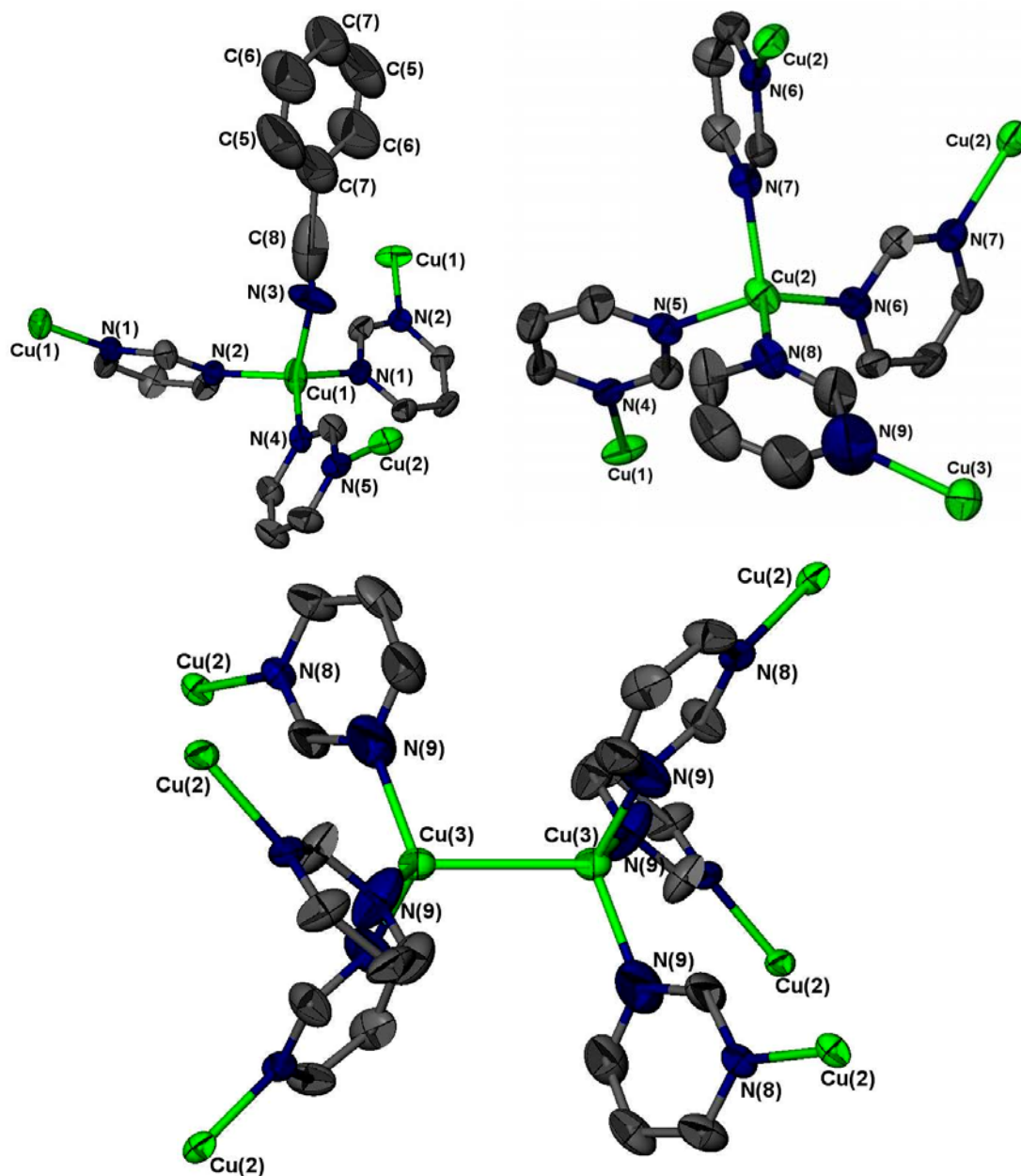
they are in these reactions. Table 6.10 list some calculated donor numbers for some of the anions<sup>27</sup> and solvents<sup>28</sup> as were available. From this data we can understand why some of these solvents, like acetonitrile and THF are such active participants in many of the reactions we have shown so far. The same holds true for the anions, showing the triflate anion's high DN of 16.9 is only rivaled in this group by the THF solvent. As expected, benzene turns out to be the poorest Lewis base while second and third runners up are the two nitro solvents in question. Still, these two solvents DN are quite comparable to that of the BF<sub>4</sub><sup>-</sup> anion and should be a formidable match for Cu(I) coordination dominance during the self-assembly since either solvent is present at well over 100 fold concentrations to that of the anions in solution in a standard reaction.

#### 6.5.2.2 Three-Dimensional Extended Solid With the PF<sub>6</sub><sup>-</sup> Anion

One final structure in this section is similar to another 3-D structure Lopez had presented. The reaction with the tetrakis(benzonitrile)copper(I) salt of the PF<sub>6</sub><sup>-</sup> anion with the pyrimidine ligand in PhCN resulted in the three-dimensional structure of [Cu<sub>3</sub>(C<sub>4</sub>H<sub>4</sub>N<sub>2</sub>)<sub>7.5</sub>(PhCN)](PF<sub>6</sub>)<sub>3</sub> **36**.

The structure of **36** is fairly similar those of both **33** and **36** as what could best be described as a pseudopolymorph of [Cu<sub>3</sub>(C<sub>4</sub>H<sub>4</sub>N<sub>2</sub>)<sub>7.5</sub>(MeCN)](PF<sub>6</sub>)<sub>3</sub> reported by Lopez.<sup>17</sup> Although the structure found by Lopez crystallized in the trigonal R-3 space group, **36** was found to best fit in the hexagonal R-3 space group. Of course, both these space groups are closely related and these structures are strikingly similar, almost isostructural to each other.

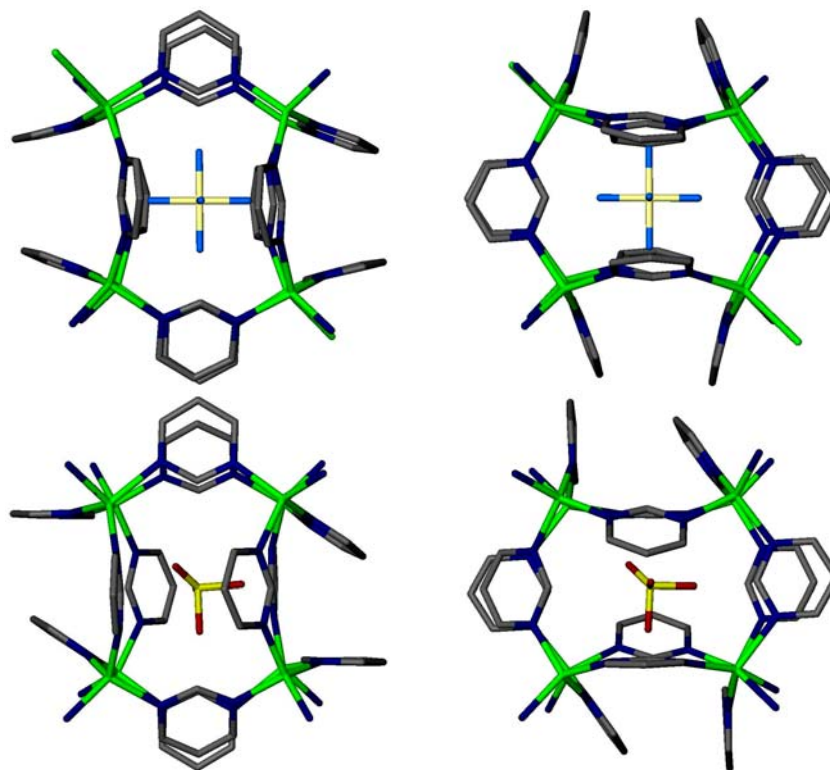
The asymmetric unit of **36** is also similar to those found in **33** and **34** in having two fully occupied, tetradedrally coordinated coppers and one, one-sixth occupied copper sitting on a three bar axis. Figure 6.20 shows the three different copper units found in **36**. The Cu(1) unit (upper left) has three coordinated pyrimidine ligands; two of which bridge onto another Cu(1) center while the third pyrimidine bridges to Cu(2). The fourth position



**Table 6.20** The three copper units found in **36** shown as 50% thermal ellipsoids. Hydrogen atoms and anions have been omitted.

on Cu(1) is occupied by a terminal PhCN ligand. This would be likened to the terminal pyrimidine found in both **33** and **34** as well as the terminal MeCN ligand found in  $[\text{Cu}_3(\text{C}_4\text{H}_4\text{N}_2)_{7.5}(\text{MeCN})](\text{PF}_6)_3$ . The Cu(2) unit (upper right) has four bridging pyrimidines, two linking to other Cu(2) centers while the other two go to Cu(1) and Cu(3). Lastly, Cu(3) is shown on the bottom as it appears with another Cu(3) bridged together over the three bar axis. The final packing is similar to those seen with **33** and **35** as is also seen by the similar unit cell parameters for each structure shown in Table 6.

As was seen in structures **33** and **35**, the one of the  $\text{PF}_6^-$  anions in **36** is found within an eight-copper coordinated cage. Again, it appears as if a possible anion templation effect has brought together two tetramers during the assembly of **36**. In Figure 6.21 we show the cage as it appears in **36** and also compare this cage with that of structure **33**.



**Figure 6.21** Two views of the cages from both (top) **36** and (bottom) **33**. Hydrogen atoms have been omitted for clarity.

From this comparison, it can be seen just how more orderly the cage from **36** compared to the misshaped sides seen in the cage from **33**. The most likely cause of this may stem from the way the anions fit into this cage. The  $\text{PF}_6^-$  anion seems to be a perfect fit, with each of the six fluoride atoms directed towards the center of each of the six sides of the cage. This may also contribute to how the  $\text{PF}_6^-$  anion might resist any interference from the nitrobenzene solvent (as with the  $\text{BF}_4^-$  anion) since this better fit should greatly enhance the anion templation effect, resisting any change even when another weakly coordinating solvent is present.

## 6.6 Conclusion

This study of the reaction of the tetrakis(acetonitrile)copper(I) and tetrakis(benzonitrile)copper(I) salts with the pyrimidine ligand has shown, once again, that both anion and solvent play an important role in the self-assembly of these coordination solids. In addition to this, it was also shown how the stoichiometry adds additional control to the variations that may exist with these extended solids, opening up new routes for the rational design of functional porous solids. In some cases, we have seen strong indications that anion templation might be responsible for the various polymorphs being formed, while in other cases only a subtle hint tells us of a solvent's involvement in these self-assembly processes.

## References

1. (a) Klausmeyer, K. K.; Beckles, F. R.; *Inorg. Chim. Acta* **2005**, *358*, 1050. (b) Iyoda, M.; Ogura, E.; Hara, K.; Kuwatani, Y.; Nishikawa, H.; Sato, T.; kikuchi, K.; Ikemoto, I.; Mori, T.; *J. Mater. Chem.* **1999**, *9*, 335. (c) Zhang, Z. F.; Kennish, R. A.; Blohowiak, K. A.; Hoppe, M. L.; Laine, R. M.; *J. Mater. Res.* **1993**, *8*, 1777. (d) Ossola, F.; Rossetto, G.; Zanella, P.; Paolucci, G.; Fisher, R. D.; *J. Organ. Chem.* **1986**, *309*, 55. (e) Brown, H. C.; Liotta, R.; Kramer, G. W.; *J. Am. Chem. Soc.* **1979**, *101*, 2966.
2. (a) Wiznycia, A. V.; Rush, J. R.; Baures, P. W.; *J. Organ. Chem.* **2004**, *69*, 8489. (b) Kisak, E. T.; Kennedy, M. T.; Trommeshauser, D.; Zasadzinski, J. A.; *Langmuir* **2000** *16*, 2825. (c) Donaldson, W. A.; *Current Org. Chem.* **2000** *4*, 837. (d) Kawahata, M.; Yamaguchi, K.; Ishakawa, T.; *Cryst. Growth Des.ign* **2005**, *5*, 373.
3. (a) Timoshkin, A. Y.; *Phosphorous, Sulfur, Silicon and the Related Elements* **2004**, *179*, 707. (b) Kitamura, K.; Furukawa, Y.; Hatano, H.; MacFarlane, R.; Guenther, H.; *Prog. Photoref. Nonlin. Op.* **2002**, *79*. (c) El-fadli, Z.; Coret, E.; Sapina, F.; Martinez, E.; Beltran, A, Beltran, D.; Lloret, F.; *J. Mater. Chem.* **1999**, *9*, 1793. (d) Bendiab, N.; Anglaret, E.; Bantignies, J. -L.; Zahab, H.; Sauvajol, J. L.; Patit, P.; Mathis, C.; Lefrant, S.; *Phys. Rev. B: Cond. Mat. Mater. Phys.* **2001** *64*, 245424/1. (e) Mercier, L.; Pinnavaia, T. J.; *Chem. Mater.* **2000**, *12*, 188. (f) Partin, D. L.; Pelczynski, M.; Cooke, P.; Geen, L.; Heremans, J.; Thrush, C. M.; *J. Cryst. Growth* **1998**, *195*, 378.
4. (a) Coronado, E.; Gimenez-saiz, C.; Nuez, A.; Sanchez, V.; Romero F. M.; *Eur. J. Inorg. Chem.* **2003**, *24*, 4289. (b) Lu, J. Y.; Cabrera, B. R.; Wang, R, -J.; Li, J.; *Inorg. Chem.* **1999**, *38*, 4608. (c) Oh, M. Stern, C. L.; Mirkin, C. A.; *Inorg. Chem.* **2005**, *44*, 2647. (d) Zaworotko, M. J.; *NATO ASI Series, Series C: Math. Phys. Sci.* **1999**, *539*, 383. (e) Caeson, C. E.; Klausmeyer, K. K.; *Eur. J. Inorg. Chem.* **2005** *16*, 1434. (f) Yu, Z.; Yu, K.; Lai, L.; Udachin, K.A.; Zhu, H.; Tao, J.; You, X.; Stroebel, M.; Meyer, H.; Ripmeester, J. A.; *Chem. Commun.* **2004**, *6*, 648.
5. (a) Slone, R. V.; Hupp, J. T.; Stern, C. L.; Albrecht-Schmitt, T. E.; *Inorg. Chem.* **1996**, *35*, 4096. (b) Belanger, S.; Hupp, J. T.; Stern, C. L.; Slone, R. V.; Watson, D. F.; Carrel, T. G.; *J. Am. Chem. Soc.* **1999**, *121*, 557.
6. (a) Fujita, M.; Yakazi, J.; Ogura, K.; *J. Am. Chem. Soc.* **1990**, *112*, 5645. (b) Fujita, M.; Nagao, S.; Iida, M.; Ogata, K.; Ogura, K.; *J. Am. Chem. Soc.* **1993**, *115*, 1574. (c) Fujita, M. Yakazi, J.; Ogura, K. *Tetrahedron Lett.* **1991**, *32*, 5589.
7. (a) Beer, P. D. J.; *J. Chem. Soc. Chem. Commun.* **1996**, 689. (b) Slone, R. V.; Yoon, D. L.; Calhoun, R. M.; Hupp, J. T.; *J. Am. Chem. Soc.* **1995**, *117*, 11813.

8. (a) Stang, P. J.; Olenyuk, B.; *Acc. Chem. Res.* **1997**, *30*, 504. (b) Stang, P. J.; Cao, D. H.; Chen, K.; Gray, G. M.; Muddiman, D. C.; Smith, R. D.; *J. Am. Chem. Soc.* **1997**, *119*, 5163.
9. (a) Slone, R. V.; Hupp, J. T.; *Inorg. Chem.* **1997**, *36*, 5422. (b) Lehn, J. –M, Drain, C. M.; *J. Chem. Soc. Chem. Commun.* **1994**, 2313. (c) Anderson, S.; Anderson, H. L.; Bashall, A.; McPartlin, M.; Sanders, J. K. M.; *Angew, Chem., Int. Ed. Engl.* **1996**, *35*, 1936.
10. Olenyuk, B.; Whiteford, J. A.; Stang, P. J.; *J. Am. Chem. Soc.* **1996**, *118*, 8221.
11. Slone, R. V.; Benkstein, K. D.; Belanger, S.; Hupp, J. T.; Guzei, I. A.; Rheingold, A. L.; *Coord. Chem. Rev.* **1998**, *171*, 221.
12. (a) Nishizawa, M.; Menon, V. P.; Martin, C. R.; *Science* **1995**, *268*, 700. (b) Jirage, K. B.; Hulteen, J. C.; Martin, C. R.; *Science* **1997**, *278*, 655. (c) Burgmayer, P.; Murray, R. W.; *J. Am. Chem. Soc.* **1982**, *104*, 6139. (d) Burgmayer, P.; Murray, R. W.; *J. Electroanal. Chem.* **1983**, *147*, 339. (e) Burgmayer, P.; Murray, R. W.; *J. Phys. Chem.* **1984**, *88*, 2515. (f) Campbell, D.; Herr, B. R.; Hulteen, J. T.; VanDuyne, R. P.; Mirkin, C. a.; *J. Am. Chem. Soc.* **1996**, *118*, 10211.
13. (a) Fujita, M.; *J. Synth. Org. Chem. Jpn.* **1996**, *54*, 953. (b) Fujita, M.; Sasaki, O.; Mitsunashi, T.; Fujita, T.; Yazaki, J.; Yamaguchi, K.; Ogura, K.; *J. Chem. Soc. Chem. Commun.* **1996**, 1535.
14. Stang, P. J.; Persky, N. Manna, J.; *J. Am. Chem. Soc.* **1997**, *119*, 4777.
15. (a) Fujita, M.; Ogura, D.; Miyazawa, M.; Oka, H.; Yamaguchi, K.; Ogura, K.; *Nature* **1995**, *378*, 469. (b) Stang, P. J.; Olenyuk, B.; Muddiman, D. C.; Wunschel, D. S.; Smith, R. D.; *Organomet.* **1997**, *16*, 3094.
16. (a) Ball, P.; *Designing the Molecular World*; Princeton University Press, Princeton, 1994. (b) Drexler, K. E.; *Nanosystems: Molecular Machinery, Manufacturing, and Computation*; Wiley Pub., New York, 1992.
17. Lopez, S.; *PhD Thesis*, University of Missouri, **2000**.
18. Sheldrick, G. M. *SHELXS-90, program for Structure Solution*; University of Gottingen: Germany, 1991.
19. (a) Sheldrick, G. M. *SHELXL-90, program for Structure Refinement*; University of Gottingen: Germany, 1991. (b) Barbour, L. X-SEED, *Graphical Interface for SHEL-X*; University of Columbia, MO, 2000.

20. (a) Gray, R. D.; *J. Am. Chem. Soc.*; **1969**, *91*, 56. (b) Zagel, J.; Spodine, E.; Zamudio, W.; *J. Chem. Soc., Dalton Trans.* **1974**, (c) Henry, P. M.; *Inorg. Chem.*, **1966**, *5*, 688. (d) El-Sayed, M. A.; Davies, G.; *Inorg. Chem.* **1990**, *29*, 4891.
21. Knaust, J. M.; *PhD Thesis*, University of Missouri, **2003**.
22. (a) Knaust, J. M.; Inman, C.; Keller, S. W.; *Chem. Commun.* **2004**, 492. (b) Knaust, J. M.; Inman, C.; Keller, S. W.; *Chem. Commun.* **2002**, 156.
23. (a) Lopez, S.; Keller, S. W.; *Inorg. Chem.* **1999**, *38*, 1883. (b) Lopez, S.; Keller, S. W.; *Cryst. Engin.* **1999**, *2*, 101.
24. (a) Lobana, T. S.; Castineiras, A.; Turner, P.; *Inorg. Chem.*; **2003b**, *47*, 4731. (b) Brooks, N. R.; Blake, A. J.; Champness, N. R.; Cooke, P. A.; Hubberstey, P.; Proserpio, D. M.; Wilson, C.; Schroder, M.; *J. Chem. Soc., Dalton Trans.* **2001**, 456. (c) Kappenstein, C.; Hugel, R. P.; *Inorg. Chem.* **1977**, *16*, 250. (d) Kappenstein, C.; Hugel, R. P.; *Inorg. Chem.* **1978**, *17*, 1945. (e) Potts, K. T.; Horwitz, C. P.; Fessak, A.; Keshavarz-K, M.; Nash, K. E.; Toscano, P. J.; *J. Am. Chem. Soc.* **1993**, *115*, 10444.
25. Keller, S. W.; *Angew. Chem. Int. Ed.* **1997**, *36*, 247.
26. (a) Rack J. J.; Hurlburt, P. K.; Kellet, P. J.; Luck, J. S.; Anderson, O. P.; Struass, H. S.; *Inorg. Chim. Acta* **1996**, *242*, 71. (b) Hurlburt, P. K.; Kellettt, P. J.; Anderson, O. P.; Strauss, S. H.; *J. Chem. Soc. Chem. Commun.* **1990**, 576. (c) Lanfranchi, M.; Pellinghelli, M. A.; Predieri, G.; Bigi, F.; Maggi, R.; Sartori, G.; *J. Chem. Soc., Dalton Trans.* **1993**, 1463.
27. Linert, W.; Jameson, R. F.; Taha, A.; *J. Chem. Soc., Dalton Trans.* **1993**, 3181.
28. Gutmann, V.; *Coord. Chem. Rev.* **1976**, *18*, 225.

# Anion Exchange Using a Large Cavity, Functional Porous Solid

## 7.1 Introduction

In previous chapters, we showed several ways in which the copper(I) coordination polymers can develop into a variety of porous solids. Some of these materials bore striking resemblance to the clays and zeolites we hope to copy and improve upon. The rational design of these materials continues to pose a significant challenge, due to the many variables present in these reactions. The ultimate goal of these studies, of course, is to produce viable, porous materials for use in applications such as molecular electronics,<sup>1a</sup> catalysis,<sup>1b</sup> solvent extraction,<sup>1c, d</sup> and anion exchange.<sup>1d</sup> Selective guest binding in the 3-D porous Zn(II)-benzenetricarboxylate network<sup>2a</sup> and reversible anion exchange performed within the porous framework of Ag(4, 4'-bpy)·NO<sub>3</sub><sup>2b</sup> are just a couple of examples of the many applications possible with coordination solids.

Another practical application that is gaining considerable importance is the remediation and general management of radioactive waste. Technetium-99 (<sup>99</sup>Tc) is one of the largest components of nuclear waste<sup>3</sup>, which not only has a rather lengthy half-life of  $2.15 \times 10^5$  years, but it is also predominately found as the pertechnetate (<sup>99</sup>TcO<sub>4</sub><sup>-</sup>) anion. This highly water-soluble oxoanion could easily contaminate water tables and pose a considerable radiological threat to entire ecosystems.<sup>4</sup>



Current methods of extracting pertechnetate from waste streams include solvent extraction,<sup>5</sup> selective binding in host-guest complexes,<sup>3a,6</sup> and ion-pairing mechanisms.<sup>7</sup> Although the bulk of the methods show success in the binding and removal of technetium, many of them rely on the use of environmentally hazardous solvents, which exacerbates the disposal problem. Organic polymer-based resins have been employed as anion exchange materials; however, they lack both stability and surface area to be efficient.<sup>8</sup>

The selective removal of  $^{99}\text{TcO}_4^-$  in the presence of other anions (such as  $\text{ClO}_4^-$ ,  $\text{NO}_3^-$ ,  $\text{SO}_4^{2-}$ , and  $\text{PO}_4^{3-}$ ) is also somewhat problematic, as these species tend to compete with pertechnetate in the extraction process. Study of the anion binding in proteins have shown that anion discrimination results from both hydrogen-bonding interactions and size-exclusion, which offers a great degree of selectivity as a guest anion fits into a host molecule.<sup>9,10</sup>

This chapter describes the use of  $[\text{Cu}_3(\text{C}_4\text{H}_4\text{N}_2)_{7.5}(\text{H}_2\text{O})](\text{CF}_3\text{SO}_3)_3 \cdot 3(\text{C}_4\text{H}_8\text{O})$  **37** to conduct anion exchange between the material's triflate anion ( $\text{CF}_3\text{SO}_3^-$ ) with  $^{99}\text{TcO}_4^-$  anion in solution. This Cu(I) coordination solid exhibits a three-dimensional, large cavity *cationic* matrix that remarkably resembles the *anionic* framework found in zeolite structures.<sup>12,13</sup> Not only do the large cavities of this polymeric matrix allows anion exchange to freely take place, it also provides a degree of size-selectivity that, in conjunction with the hydrogen bonding sites available, plays a significant role in selective exchange with pertechnetate over the other anions found in solution. We will describe the results found in the exchange study of **37** by first comparing exchange studies involving both the  $\text{PF}_6^-$  and  $\text{BF}_4^-$  anions followed by a selectivity study as anion

exchange performed using  $\text{ReO}_4^-$  (as a surrogate for  $^{99}\text{TcO}_4^-$ ) with a variety of competing oxoanions as monitored by using  $^{99\text{m}}\text{TcO}_4^-$  as a radiotracer. Further characterization of **37** was performed by both single crystal and powder X-ray diffraction, and FT-IR analysis.

## 7.2 Experimental Section

### 7.2.1 General Methods

*Caution!*  $^{99\text{m}}\text{Tc}$  emits a 140 keV  $\gamma$ -ray with a half-life of 6.0 hours. This material should be handled only in a controlled environment by qualified personnel trained in radiation safety. The  $^{99\text{m}}\text{Tc}$  was eluted with saline as sodium pertechnetate from a  $^{99}\text{Mo}/^{99\text{m}}\text{Tc}$  generator (Mallinckrodt, St. Louis, MO).  $\text{Cu}_2\text{O}$ ,  $\text{HPF}_6$ , pyrimidine (ACROS); acetonitrile (MeCN), benzonitrile (PhCN), nitrobenzene ( $\text{NO}_2\text{Ph}$ ), tetrahydrofuran (THF), acetone, and diethyl ether, (Fisher); triflic acid,  $\text{TBAHSO}_4$ , and  $\text{TBAH}_2\text{PO}_4$ , (Aldrich), were used without further purification. The  $[\text{Cu}(\text{MeCN})_4]\text{PF}_6^-$  and  $\text{Cu}(\text{PhCN})_4[\text{CF}_3\text{SO}_3]^-$  salts were prepared as described in *Chapter 2*. The TBA salts with the  $\text{BF}_4^-$ ,  $\text{PF}_6^-$ ,  $\text{ClO}_4^-$ ,  $\text{ReO}_4^-$ , and  $\text{NO}_3^-$  anions were made by anion metathesis of  $\text{TBABr}$  with equal molar amounts of the sodium salts of the corresponding anion ( $\text{AgNO}_3$  used for  $\text{NO}_3^-$ ), in 100 mL of DI water. The precipitate was filtered and washed with water, then with diethyl ether and the resulting white crystalline solid was dried by vacuum for 24 hours.

### 7.2.2 Instrumentation Details.

X-ray powder diffraction (XRPD) data were recorded on a Scintag X<sub>2</sub> diffractometer at 40 kV and 20 mA for Cu K $\alpha$  ( $\lambda = 1.54050 \text{ \AA}$ ). A Bruker 250 MHz NMR was used and set to observe the simultaneous  $^{19}\text{F}$  signal of both the  $\text{BF}_4^-$  (or  $\text{PF}_6^-$ ) and  $\text{CF}_3\text{SO}_3^-$  anions

in solution. IR analysis was performed on a Thermo Nicolet, Nexus 670 FT-IR spectrometer. The radiotracer study was performed using a NaI(Tl) solid scintillation detector with Ortec electronics. Windows were set as per the current calibration of that instrument to detect the  $\gamma$ -emitting  $^{99m}\text{Tc}$  radionuclide. Energy and efficiency calculations were based on  $^{137}\text{Cs}$ .

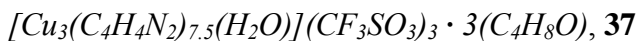
*Ion Exchange Reactions.* In all cases, **37** was washed with two, 1.0 mL aliquots of THF and again with  $\text{Et}_2\text{O}$ , following which the solid was dried under vacuum. Although the crystals lose transparency during this process, their crystalline, cubic morphology remains intact.

*NMR analysis of  $\text{CF}_3\text{SO}_3^-$  anion exchange with  $\text{BF}_4^-$  and  $\text{PF}_6^-$ .* In each trial, 0.020 g (0.037 mmol) of **37** was placed in a standard NMR tube along with 1.5 mL of a 0.5 M THF solution of either  $\text{TBABF}_4$  or  $\text{TBAPF}_6$ . The sample was placed into a 250 MHz NMR unit which was set to perform subsequent  $^{19}\text{F}$  scans at 15 minute intervals over a 12 hour period, with an additional  $^{19}\text{F}$  scan after 48, 72, and 96 hours. A single  $^1\text{H}$  scan was performed along with the last three  $^{19}\text{F}$  scans to determine if any of **37** had dissolved into the THF solution during the exchange process.

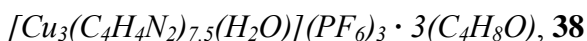
*Radiotracer analysis of  $\text{CF}_3\text{SO}_3^-$  anion exchange with  $\text{ReO}_4^-$ .* A 2.0 mL 5 to 1 THF : acetone solution containing 0.037 mmol of  $\text{TBAREO}_4$  to three 1-dram vials containing 0.02 g (0.037 mmol) of **37**. A 100  $\mu\text{L}$  aqueous solution containing 30  $\mu\text{Ci}$  of  $^{99m}\text{Tc}$  as  $\text{NaTcO}_4$  was added to each vial and the vial was sealed with a screw top cap. This procedure was repeated using anion combinations of 0.037 mmol each of  $\text{ReO}_4^-$  with either  $\text{ClO}_4^-$ ,  $\text{HSO}_4^-$ ,  $\text{H}_2\text{PO}_4^-$ , or  $\text{NO}_3^-$  competing anion. An initial activity count was

performed for each vial in entirety and a final count was taken ~22 hours later on three separate 200  $\mu\text{L}$  of the solution from each vial.

### 7.2.3 Synthesis



In a 1 dram vial were combined  $[\text{Cu}(\text{PhCN})_4]\text{CF}_3\text{SO}_3$  (0.090 g, 0.014 mmol) and pyrimidine (0.014 g, 0.171 mmol) in 1.0 mL of PhCN. This vial was then placed inside a 5-dram, screw top vial containing 5 mL of THF. The large vial was sealed and the THF slowly diffused into the PhCN solution. After 12 hours, yellow cubic crystals of **37** were harvested from the smaller vial.



In a 1 dram vial were combined  $[\text{Cu}(\text{MeCN})_4]\text{PF}_6$  (0.040 g, 0.065 mmol) and pyrimidine (0.014 g, 0.171 mmol) in 0.5 mL of MeCN: $\text{NO}_2\text{Ph}$ . This vial was then placed inside a 5-dram, screw top vial containing 5 mL of THF. The large vial was sealed and the THF slowly diffused into the MeCN: $\text{NO}_2\text{Ph}$  reaction solution. After 72 hours, yellow cubic crystals of **38** were harvested from the smaller vial.

### 7.2.4 Single Crystal X-Ray Diffraction

In all cases, a single crystal of high quality (by uniform extinction of polarized light) was coated with light oil and then mounted on a tip of a glass fiber using small amount of silicon grease for adhesion. Crystallographic data was collected using a Siemens SMART system with a CCD area detector ( $\text{Mo K}\alpha = 0.71070 \text{ \AA}$ ). During data collection, the crystal was cooled to 173 K. The initial space group was determined by indexing several

strong reflections and the structures were solved using Direct Methods.<sup>14</sup> The structure models were further refined using least-squares techniques.<sup>15</sup>

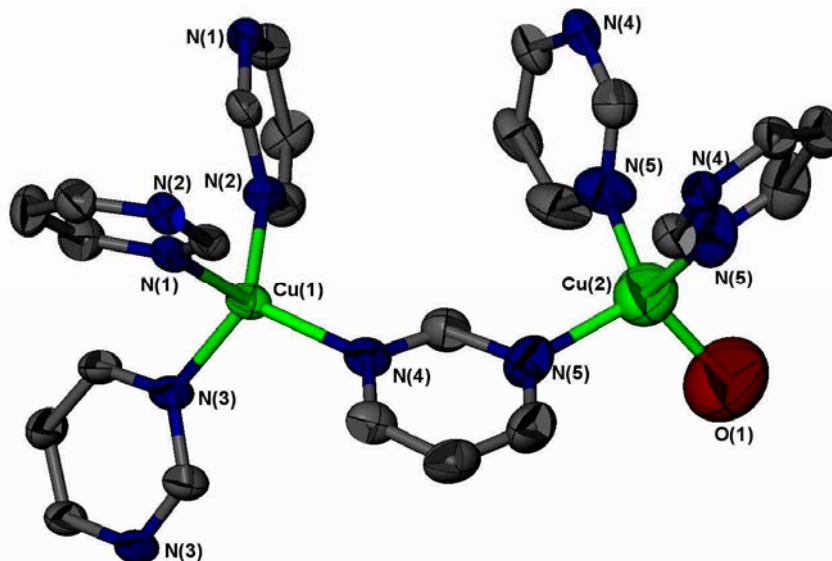
For each structure, the majority of the heavier atoms were located with the initial solution. For both structures presented, several large Fourier peaks remain, as the result of considerable solvent disorder within the large cavities formed in the extended solid. Anisotropic thermal parameters were refined for all non-hydrogen atoms identified. The hydrogen atoms were included in calculated positions and refined as riding models with fixed  $U_{\text{iso}} = 1.2U_{\text{iso}}$  of the carbon atom for which they are bonded. All other structure-specific crystallographic details will be explained in the *Results and Discussion* section. Details of the data collection and structure solutions are given in Table 7.1

<b>Table 7.1 Crystallographic Details for 37 and 38</b>		
	<b>37</b>	<b>38</b>
Empirical formula	Cu <sub>1.33</sub> C <sub>15.33</sub> H <sub>18.67</sub> N <sub>5</sub> O <sub>4.67</sub> F <sub>3.33</sub> S <sub>1.33</sub>	Cu <sub>1.33</sub> C <sub>15.33</sub> H <sub>18.67</sub> N <sub>5</sub> O <sub>4.67</sub> F <sub>3.33</sub> P <sub>1.33</sub>
Formula weight (g·mol <sup>-1</sup> )	538.12	534.95
Crystal System, Space group	Cubic Im-3	Cubic Im-3
Unit cell dimensions		
<i>a</i> (Å)	29.4359(8)	29.6973(4)
<i>b</i> (Å)	29.4359(8)	29.6973(4)
<i>c</i> (Å)	29.4359(8)	29.6973(4)
$\alpha$ , deg	90	90
$\beta$ , deg	90	90
$\gamma$ , deg	90	90
<i>Z</i>	36	4
Volume, Å <sup>3</sup>	25505(1)	26190.9(6)
$\rho_{\text{calc}}$ , g·cm <sup>-3</sup>	1.261	1.220
Absorption coefficient, mm <sup>-1</sup>	1.158	1.477
F(000)	9822	12916
Crystal size, mm	0.3 x 0.3 x 0.3	0.2 x 0.2 x 0.2
$\theta$ Range for data collection	0.98 to 28.78	0.97 to 27.11
Index ranges	-34 ≤ <i>h</i> ≤ 39 -37 ≤ <i>k</i> ≤ 38 -38 ≤ <i>l</i> ≤ 39	-37 ≤ <i>h</i> ≤ 34 -38 ≤ <i>k</i> ≤ 38 -38 ≤ <i>l</i> ≤ 35
Reflections collected	85883	94189
Unique reflections	5716 [R <sub>int</sub> = 0.0924]	5109 [R(int) = 0.0519]
Completeness to $\theta$	27.16 (97.5 %)	27.11 (100.0 %)
Max/min transmissions	1.00000/0.773250	1.00000/0.874015
Data/restraints/ parameters	5716/0/280	5109/0/270
Goodness of fit F <sup>2</sup>	1.495 <sup>†</sup>	1.937 <sup>†</sup>
Final R indices [ <i>I</i> > 2 $\sigma$ ( <i>I</i> )] <sup>a,b</sup>	R <sub>1</sub> = 0.1257 <sup>†</sup> wR <sub>2</sub> = 0.3520 <sup>†</sup>	R <sub>1</sub> = 0.1216 <sup>†</sup> wR <sub>2</sub> = 0.3749 <sup>†</sup>
R indices (all data)	R <sub>1</sub> = 0.2242 <sup>†</sup> WR <sub>2</sub> = 0.4390 <sup>†</sup>	R <sub>1</sub> = 0.1738 <sup>†</sup> WR <sub>2</sub> = 0.4531 <sup>†</sup>
Largest difference peak and hole (e·Å <sup>-3</sup> )	2.300/-2.459 <sup>†</sup>	2.089/-2.279 <sup>†</sup>
Structures were refined on F <sup>2</sup> for all data. <sup>a</sup> R(F <sub>o</sub> ) = $\sum   F_o  -  F_c   / \sum  F_o $ . <sup>b</sup> R <sub>w</sub> (F <sub>o</sub> ) = $(\sum w  F_o  -  F_c  ^2 / \sum w F_o ^2)^{1/2}$ , w = $[\sigma^2(F_o) + (0.002F_o)^2]^{-1}$ .		
<sup>†</sup> High GOF, R indices, and remaining Fourier peaks are the result of considerable amount of disordered solvent and difficulty in refining an anion's position, as will be pointed out in greater detail in the discussion section.		

## 7.3 Results and Discussion

### 7.3.1 Crystal Structure of **37** and **38**

The asymmetric unit of **37** and **38** consists of only two crystallographically unique copper atoms with one copper displaying tetrahedral coordination while the other copper is located on a three bar axis as shown in Figure 7.1. The fully occupied copper is coordinated with four bridging pyrimidines, while the one-third occupied copper is coordinated to three bridging pyrimidines and what appears to be a terminal water ligand. Analysis of **37** and **38** by FT-IR reveals a large, broad peak at  $\sim 3500\text{ cm}^{-1}$  supporting the supposition that



**Figure 7.1** The two unique copper coordination tetrahedra of **37** and **38**. Hydrogen atoms have been omitted and the non-hydrogen atoms are represented as 50% ellipsoids.

water is in the structure. There was a great deal of difficulty refining one of the triflate anion's position in **37**. This, along with considerable disorder associated solvated THF in the structure resulted in a high  $R_1$  of 0.12. This disorder is also problematic with **37** with possibly both acetonitrile and THF solvate disordered within the structure. However, all

three of the  $\text{PF}_6^-$  anions seen in **38**, are fairly ordered with their positions within the structure similar to that of the triflate anions in **37**. In any case, the disorder found in both **37** and **38** prevents us from obtaining a complete solution for each structure resulting in high  $R_1$ , GOF and other related values.

A similar situation with coordination solid reported by Robson several years ago,<sup>16</sup> the exceptionally large cavity allows non-coordinated molecules (the triflate and solvated THF) to flow more freely in the structure. Similarly to Robson's structure, the interatomic distances, bond angles, and the entire three-dimensional network of both

**Table 7.2** Selected bond lengths (Å) and angles (deg) for **37** & **38**

	<b>37</b>	<b>38</b>
Cu(1) - N(1)	2.071(7)	2.051(7)
Cu(1) - N(2)	2.057(7)	2.057(8)
Cu(1) - N(3)	2.055(6)	2.064(8)
Cu(1) - N(4)	2.031(8)	2.047(8)
Cu(2) - N(5)	2.10(1)	2.057(9)
Cu(2) - O(1)	2.14(5)	1.97(3)
N(1) - Cu(1) - N(2)	106.4(3)	108.8(3)
N(1) - Cu(1) - N(3)	109.0(3)	111.1(3)
N(1) - Cu(1) - N(4)	111.8(3)	115.7(3)
N(2) - Cu(1) - N(4)	114.6(3)	107.0(3)
N(3) - Cu(1) - N(4)	111.3(3)	111.8(3)
N(5) - Cu(2) - N(5)	108.3(3)	106.6(3)
N(5) - Cu(1) - O(1)	110.7(3)	112.2(3)

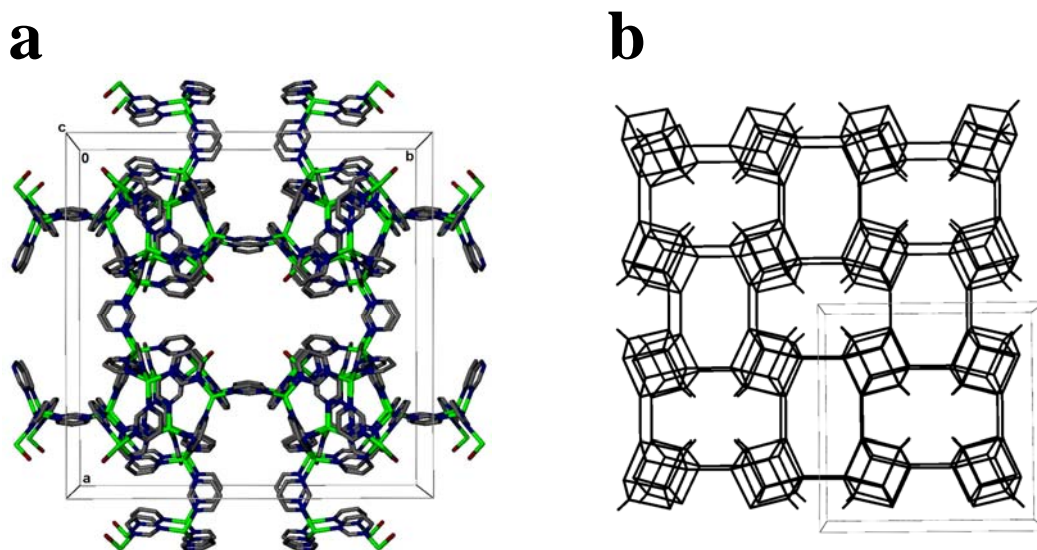
**37** and **38** are in accord to chemical common sense, leaving little doubt that the framework is anything but what is presented here. Selected bond lengths and angles for **37** and **38** are given in Table 7.2.

Figure 7.2a shows how the network is assembled in the unit cell. The asymmetric units are linked together by bridging

pyrimidine molecules forming a  $\text{Cu}_8$  cube, just as was seen in **33**, **35**, and **36**. In turn, each Cu corner of the cube link to adjacent cubes as the structure takes on its three-dimension form. The result is a large cavity cubic framework with the terminal water molecules directed towards the interior of the cavity. A schematic view of the structure is shown in Figure 7.2b, in which single lines connect the Cu-centers and all other atoms are deleted. This view of the network reveals a structure that appears to be assembled from cubic secondary building units (SBU), much like what was seen with the zeolites in



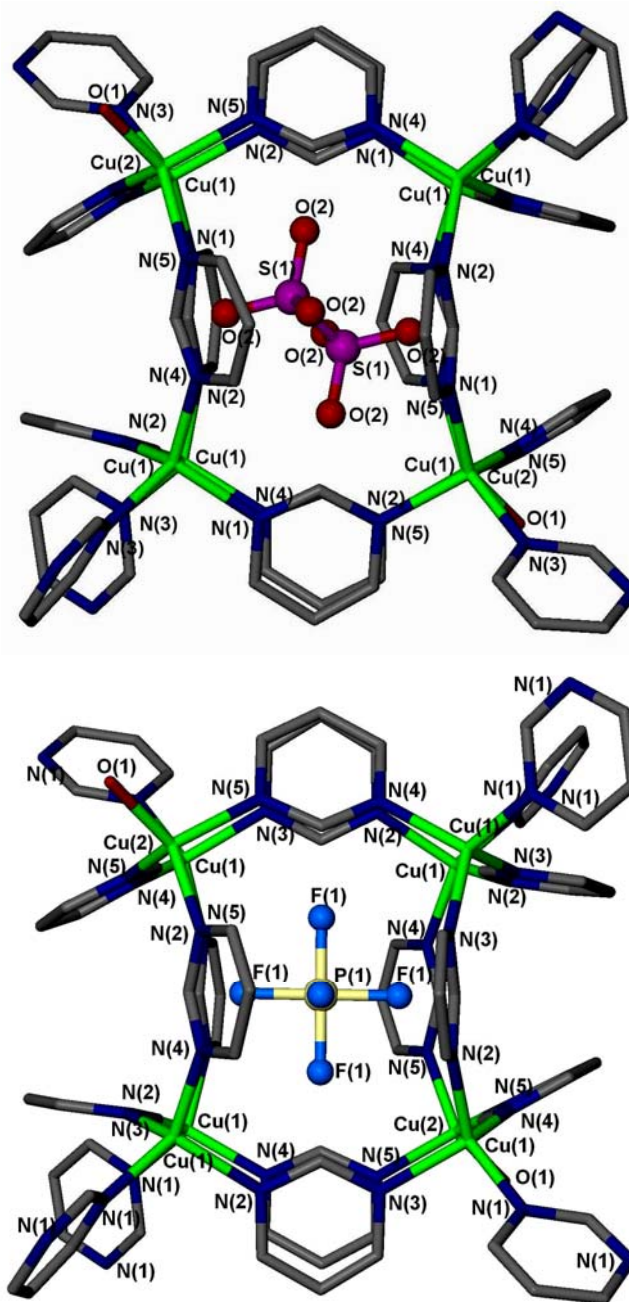
Section 1.3. The inner cavity, or *supercage*, measures  $\sim 18 \text{ \AA} \times 11 \text{ \AA}$ , as measured from the closest hydrogens on each adjacent pyrimidine that form the cavity sides. These supercages are arranged to form continuous channels throughout the structure.



**Table 7.2** Stick representation of the cationic framework comprising the unit cell of **37** and **38**. The triflate cations are shown as ball and stick figures while the hydrogens have been omitted for clarity. (b) An expanded, four unit cell view of **37** and **38**. The Cu – Cu bonds replace the bridging pyrimidines revealing a zeolite analog formed from the cationic network.

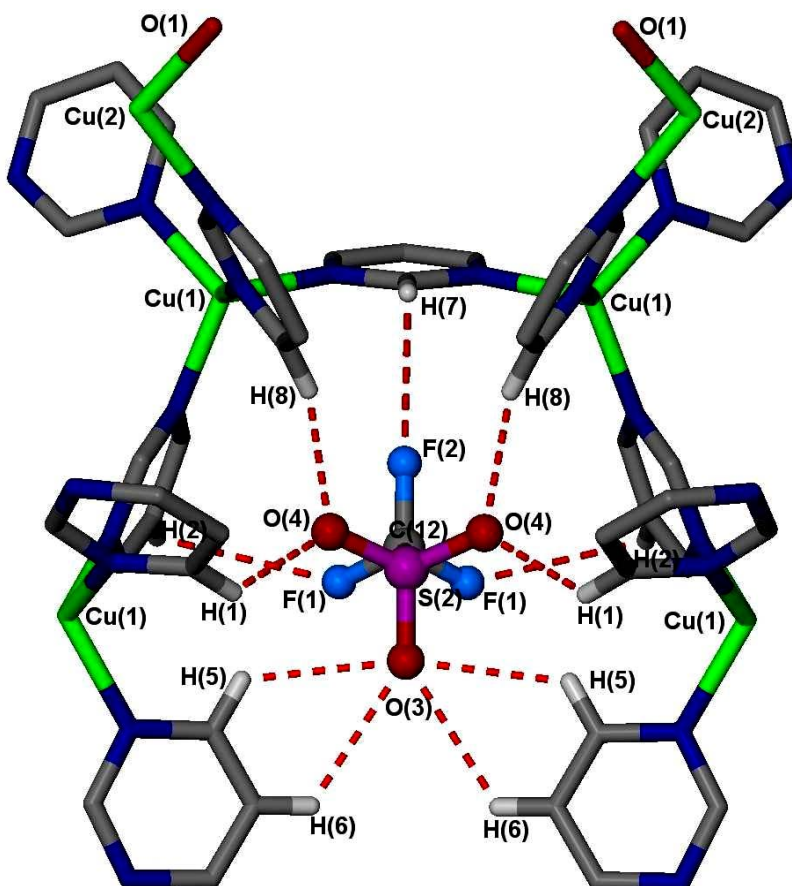
As shown in the top of Figure 7.3, of the two more crystallographically stable triflate anions, one is completely enclosed by a  $\text{Cu}_8$  cube. This same arrangement holds true for (bottom) **38** as well. Since this triflate anion appears in the asymmetric unit as only a sulfur and oxygen atom sitting on a six-fold rotation position, attempts to grow the complete triflate ( $\text{CF}_3\text{SO}_3^-$ ) anion only generates another sulfur where the carbon should be as well as placing oxygen atoms where the fluoride atoms would normally be. Although the resulting molecule looks much like a triflate anion, we were unable to model the actual  $\text{CF}_3\text{SO}_3^-$  formula due to limitations of the crystallographic software. Even still, this gives us a good idea of how the triflate anion sits within the small cage; however, the F – H distances between the anion and pyrimidine sides can only be estimated. Although the hydrogen bond to the triflate are fairly large ( $\sim 2.80 - 3.27 \text{ \AA}$ )

and the (bottom)  $\text{PF}_6^-$  anion as well ( $\sim 2.70 - 3.20 \text{ \AA}$ ), there is added stability as each of the six ligands on either the triflate or  $\text{PF}_6^-$  anion are directed to each of the six sides of the Cu/pyrimidine enclosure; much like the other cage formed with the  $\text{PF}_6^-$  anion in **36**.



**Figure 7.3** The Cu(I) coordinated cage with anion in place for (top) **37** and (bottom) **38**. The hydrogen atoms have been omitted.

Figure 7.4 provides a view of one of the two anions that are located in the larger, supercage of the structure. As is shown by the dotted bonds, each fluoride atom has weak hydrogen bonds with two F(1) – H(2) distances of 3.14 Å and one F(2) – H(7) distance of

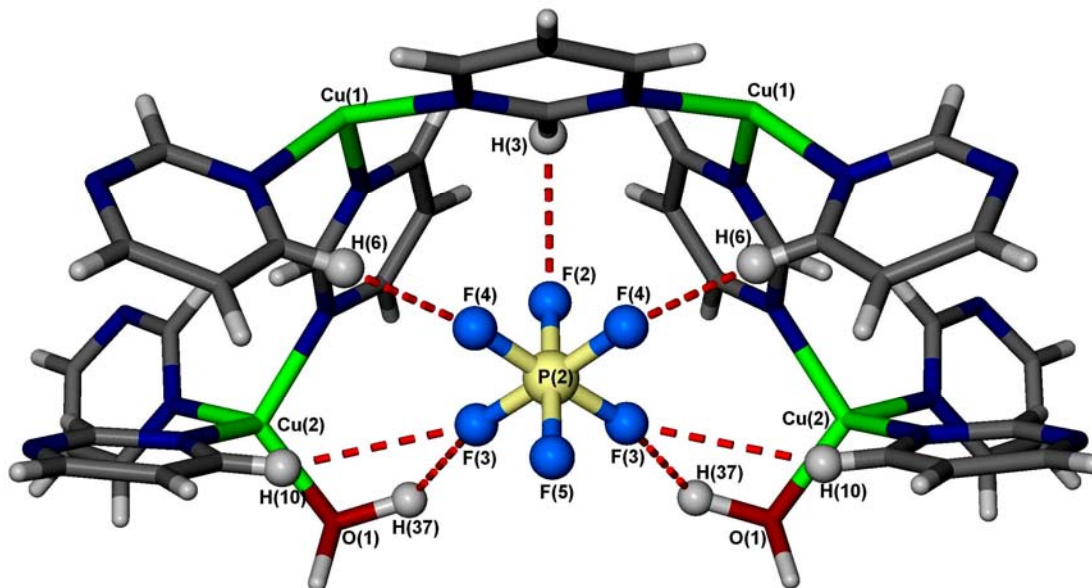


**Figure 7.4** One of the triflate anions as it sets into a corner in the *supercage* found in **37**. The anion and the hydrogen atoms associated with the H-bonding are shown as spheres while the rest of the structure is in stick representation.

3.15 Å, the oxygen ligands encounter multiple H – bonding with O – H distances of 2.46 Å, 2.61 Å, and 3.36 Å on one ligand and two of both 2.74 Å and 2.60 Å H – bond distances on the two equivalent oxygen atoms. The third triflate anion is highly disordered as it is located within the expanse of the network in a sort of open-faced saucer formed by only a few of the Cu/pyrimidine units. The amount of H – bonding to

this anion is limited and an accurate account of the distances is not possible because of the great disorder encountered.

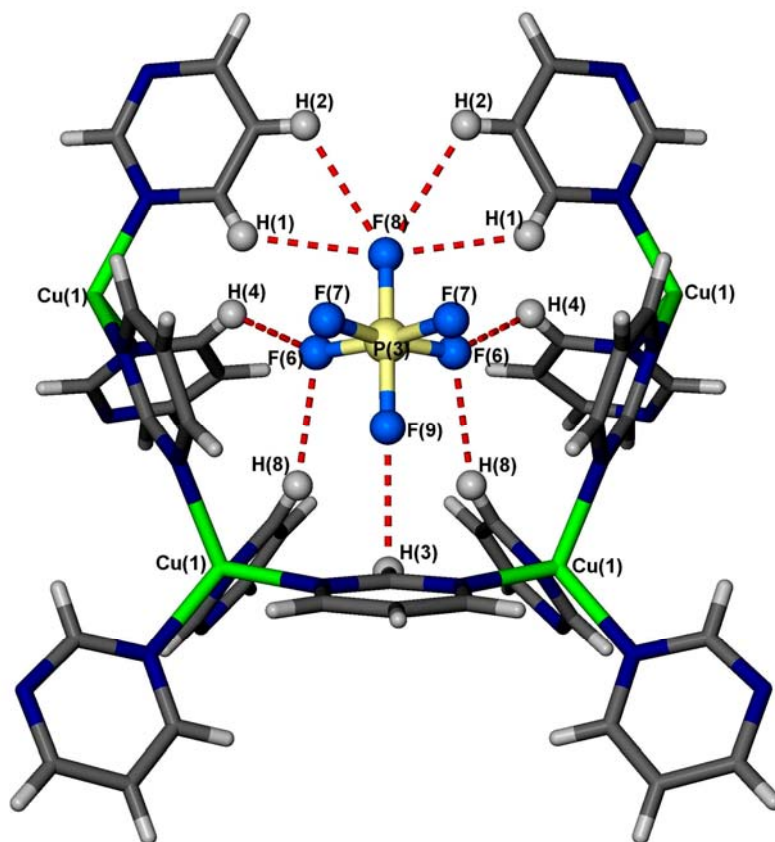
Figure 7.5 below and Figure 7.6 on the next page shows the two  $\text{PF}_6^-$  anions in their positions within the supercage of **38**. Several H-bonds hold each anion in place with the F – H distances ranging 2.6 – 2.9 Å. The anion seen in Figure 7.5 is at the same positioning that the third, disordered triflate anion is positioned. Even though this position seems slightly more open up than the position shown in the left figure, there are still several H-bonds, including two from the coordinated water.



**Figure 7.5** One of the two  $\text{PF}_6^-$  anions that sit in the supercage in **38** shown as spheres along with their H-bonded hydrogen atoms. The rest of the structure is in stick representation.

It should be noted that for the reactions with the triflate anion produced large, well-formed crystals, while the reaction with the  $\text{PF}_6^-$  anion produced small crystals that mostly appeared as crystal clusters. Much of this might be due to the difference of solubility of the different anion's starting material and product, with the more insoluble  $\text{PF}_6^-$  analog crystallizing more quickly, resulting in poor crystal formation. Many times, the reactions with the  $\text{PF}_6^-$  anion would even produce little to no single crystalline

product (producing precipitate instead) while those with the triflate anion would produce large, well formed single crystals of the product 100 % of the time.



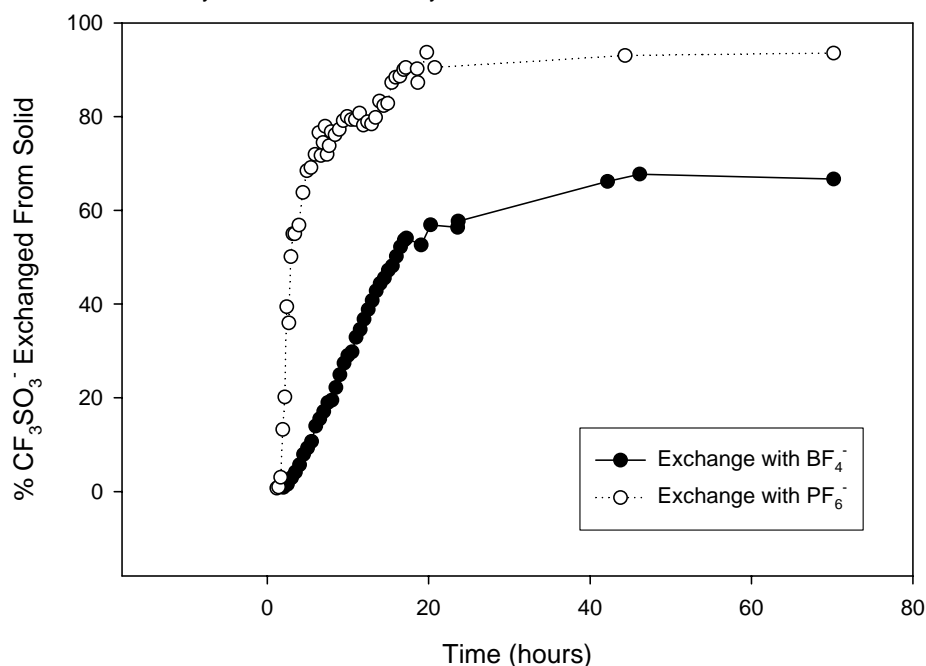
**Figure 7.6** The third  $\text{PF}_6^-$  anion found in the supercage in **38** shown as spheres along with their H-bonded hydrogen atoms. The rest of the structure is in stick representation.

It is interesting to note as well, that the reactions with the triflate anion would produce this 3-D porous solid, even at very low amounts of pyrimidine. It was observed that even at only 1.0 equivalents of pyrimidine, **37** would still form as the only product. The high solubility of the triflate starting material might account for this occurrence, since the triflate starting material, itself, has never been successfully crystallized into single crystals. Therefore, it is for the reasons stated above that only **37** was used in the following anion exchange.

### 7.3.2 $\text{BF}_4^-$ and $\text{PF}_6^-$ Anion Exchange

The graph in Figure 7.7 shows the results of the exchange between  $\text{BF}_4^-$  and  $\text{PF}_6^-$  with triflate. The data shows that the exchange of the triflate anion with either  $\text{BF}_4^-$  or  $\text{PF}_6^-$  was nearly complete after only ~12 hours, with the exchange continuing after that time at a much slower rate to a point of completion after 2 days.

**Figure 7.7** The solid state anion exchange of triflate with  $\text{PF}_6^-$  and  $\text{BF}_4^-$  as observed by  $^{19}\text{F}$  NMR over a 3 day time scale.



Although both of the  $\text{BF}_4^-$  anion exchanged with ~67% of triflate, the  $\text{PF}_6^-$  anion greatly surpassed this by replacing over 93% of the triflate in the solid. Since the porous solid used for these exchange studies can also be produced *with* the  $\text{PF}_6^-$  anion, it is of little surprise that there is an increased extent of exchange involving the  $\text{PF}_6^-$  anion over that of the  $\text{BF}_4^-$  anion. While the octahedral geometry of the  $\text{PF}_6^-$  anion might make a better fit in the  $\text{Cu}_8$  cube of the structure, the larger size of this anion (over that of the

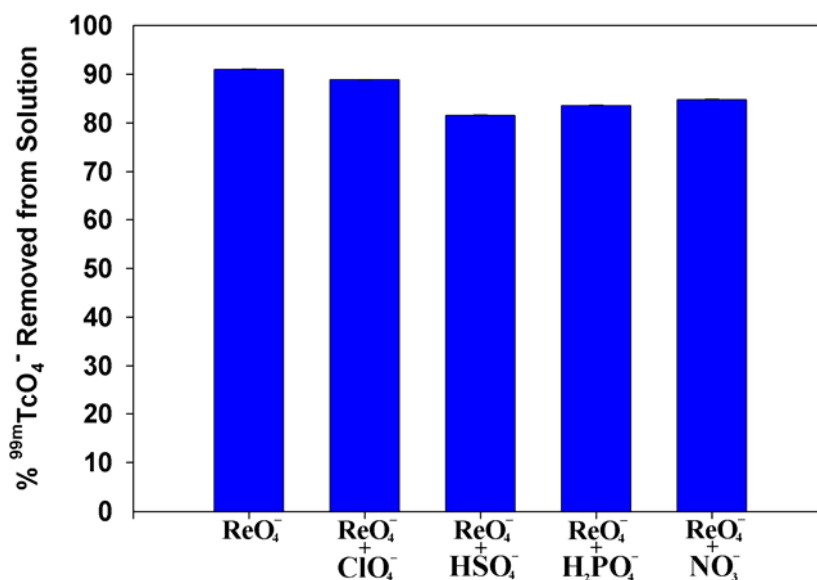
BF<sub>4</sub><sup>-</sup> anion) may also provide more effective use of the hydrogen bonding that is available in the supercage of the structure.

### 7.3.3 Competition Exchange Study With ReO<sub>4</sub><sup>-</sup>

Figure 7.8 shows the four anion exchanges between the ReO<sub>4</sub><sup>-</sup> anion and the triflate anion found in **37** while in competition with the ClO<sub>4</sub><sup>-</sup>, HSO<sub>4</sub><sup>-</sup>, H<sub>2</sub>PO<sub>4</sub><sup>-</sup>, and NO<sub>3</sub><sup>-</sup> oxoanions. While the ReO<sub>4</sub><sup>-</sup> anion served as a suitable surrogate for the hazardous <sup>99m</sup>TcO<sub>4</sub><sup>-</sup> anion, the pertechnetate anion with the <sup>99m</sup>Tc isotope (t<sub>1/2</sub> = 6 hr) was used as a radiotracer to monitor the exchange.

The results show that **37** has a high affinity towards the <sup>99m</sup>TcO<sub>4</sub><sup>-</sup> anion (in turn for the ReO<sub>4</sub><sup>-</sup>), even in the presence of other competitive oxoanions. The results show that **37** removes <sup>99m</sup>TcO<sub>4</sub><sup>-</sup> selectively and efficiently from the THF/acetone solution while in competition with ClO<sub>4</sub><sup>-</sup>, HSO<sub>4</sub><sup>-</sup>, H<sub>2</sub>PO<sub>4</sub><sup>-</sup>, and NO<sub>3</sub><sup>-</sup>. This exchange is comparable to the PF<sub>6</sub><sup>-</sup> results as, after only 22 hours, 91.00 ± 0.07 % of the <sup>99m</sup>TcO<sub>4</sub><sup>-</sup> was effectively removed from solution when in the presence of only the ReO<sub>4</sub><sup>-</sup> anion, with only a slight decrease when in the presence of the competing anions. The 88.86 ± 0.08 % exchange of pertechnetate in the presence of the ClO<sub>4</sub><sup>-</sup> anion is most impressive.

Because the perchlorate anion is known to be a suppressor of MO<sub>4</sub><sup>-</sup> (M = Tc, Re) binding in certain cyclotrimeratrylenes, the lack of this suppression in the presence of perchlorate indicates that **37** must have a very high selectivity towards pertechnetate.<sup>3a, 17</sup> Judging from the amount of suppression on the pertechnetate – triflate exchange each competing anion exhibits, it can be concluded that **37** has a varying degree of selectivity in the sequence of TcO<sub>4</sub><sup>-</sup> >> HSO<sub>4</sub><sup>-</sup> > H<sub>2</sub>PO<sub>4</sub><sup>-</sup> > NO<sub>3</sub><sup>-</sup> > ClO<sub>4</sub><sup>-</sup>.



**Figure 7.8** The removal of the  $^{99m}\text{TcO}_4^-$  radioanion in competition with other oxoanions. Each anion exchange was labeled with 30  $\mu\text{Ci}$  of  $^{99m}\text{TcO}_4^-$  and monitored over a 22 hour period.  $\text{ReO}_4^-$  used as a surrogate for the long half lived, ( $^{99}\text{Tc}$ ) pertechnetate anion.

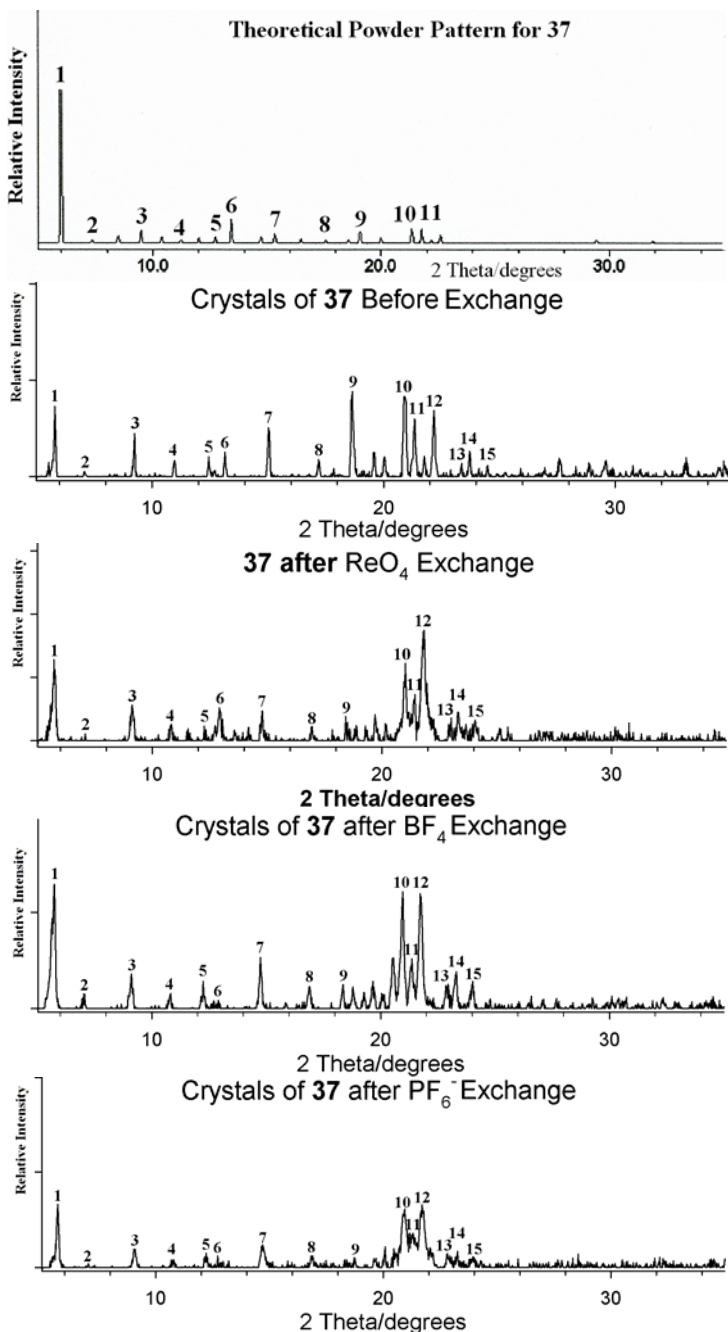
This high degree of selectivity towards pertechnetate could be a simple matter of size exclusion as the larger  $^{99m}\text{TcO}_4^-$  anion is able to make better use of the hydrogen bonds available in the matrix of **37** while the slightly larger suppression ability of the hydrogensulfate anion could be due to the presence of a small amount of the completely disassociated, divalent  $\text{SO}_4^{2-}$ . The degree of selectivity towards perrhenate seen in this study should be comparable to pertechnetate, given that rhenium is commonly believed to be an excellent analog for technetium along with the results of the previous anion binding studies.<sup>3a, 17</sup>

*Post Exchange Material Characterization.* For all the anion exchange studies, **37** has remained solid and intact, even after several weeks in the anion exchange solvent. Post exchange  $^1\text{H}$  NMR examinations on the solvents have detected no traces of dissolved **37**. After washing with THF and  $\text{Et}_2\text{O}$  and vacuum drying, it is clear that the solid has retained its cubic, crystalline morphology. Analysis of these post exchanged



samples of **37** by FT-IR showed strong peaks at 1051, 905, and 835  $\text{cm}^{-1}$  corresponding to  $\text{BF}_4^-$ ,  $\text{ReO}_4^-$ , and  $\text{PF}_6^-$  respectively.

Figure 7.8 shows before and after XRPD patterns along with the theoretical powder pattern for **37**. The reflection peaks for each anion exchange powder pattern matched



**Figure 7.9** The XRPD patterns for **37**, before and after selected anion exchanges.

those peaks found from the XRPD of the crushed sample of **37**. These peaks also matched the theoretical powder pattern of **37**. From these results we concluded that the sample retained much of the structural integrity as it underwent anion exchange.

## 7.4 Conclusion

The reactions involving both the triflate and  $\text{PF}_6^-$  anions with pyrimidine show a accessible route to obtain zeolite-analog materials using Cu(I) coordination. The large cavity copper(I) coordination solid produced from these reactions appears to be an excellent candidate as anion exchange material for use in the efficient and selective removal of pertechnetate from wastewater streams. As an added bonus, the structural relationship with the octahedral triflate and hexafluorophosphate anions suggest anion templating is involved in its synthesis, providing valuable knowledge for the further development of functional solids. This spacious, hydrogen-bond laden cavities of this Cu(I) matrix provide a perfect haven for the larger perrhenate and pertechnetate anions and offers a definite solution to our growing nuclear waste management problem.

## References

1. (a) Miyasaka, H.; Matsumoto, N.; Okawa, H.; Re, N.; Gallo, E. Floriani, C. *J. Am. Chem. Soc.* **1996**, *118*, 881 (b) K. P. Reis, V. K. Joshi, M. E. Thompson, *J. Catal.* **1996**, 161, 62. (c) Yaghi, O. M.; Li, G.; Li, H.; *Nature* **1995**, 378, 703-706. (d) Hamilton, B. H.; Kelly, K. A.; Wagler, T. A.; Espe, M. P.; Ziegler, C. J. *Inorg. Chem.* **2004**, 50-56.
2. (a) Yaghi, O. M.; Davis, C. E.; Li, G.; Li, H. *J. Am. Chem. Soc.* **1997**, *119*, 2861-2868. (b) Yaghi, O. M.; Li, H.; Davis, C.; Richardson, D.; Groy, T. L. *Acc. Chem. Res.* **1998**, *31*, 474-484.
3. (a) Gawanis, J. A.; Holman, T.; Atwood, J. L.; Jurisson, S. S. *Inorg. Chem.* **2002**, 6028-6031. (b) Lieser, K. H. *Radiochim. Acta* **1993**, *63*, 5.
4. (a) Schroeder, N. C.; Morgan, D. Rokop, D. J.; Fabryka-Martin, J. *Radiochem. Acta*, **1993**, *60*, 203. (b) Deutsch, E.; Libson, K.; Vanderhyden, J. -L.; *Technicium and Rhenium in Chemistry and Nuclear Medicine*, **1990**, 13-22. (c) Amano, R.; Ando, A. Hiraki, T. Mori, H.; Matsuda, H. Hisada, K. *Radioisotopes* **1990**, *39*, 583-586.
5. Rohal, K. M.; Strauss, S. H.; Schroeder, N. C. *Solvent Extr. Ion Exch.* **1996**, *14*, 401-416.
6. Steed, J. W.; Juneja, R. K.; Atwood, J. L. *Angew. Chem., Int. Ed. Engl.* **1994**, *33*, 2456.
7. Michel, H.; Barci-Funel, G.; Dalmaso, J. Ardisson, G. *Radiochim. Acta* **1997**, *78*, 153-157.
8. (a) Marsh, S. F.; Jarvinen, G. D.; Kim, J. S.; Nam, J.; Bartsch, R. A. *React. Func. Polym.* **1997**, *35*, 75. (b) Marsh, S. F.; Jarvinen, G. D.; Bartsch, R. A.; Nam, J.; Barr, M. E. *J. Radioanal. Nucl. Chem.* **1998**, 235, 37. (c) Ju, Y. H.; Webb, O. F.; Dai, S.; Lin, J. S.; Barnes, C. E. *Ind. Eng. Chem. Res.* **2000**, *39*, 550-553.
9. Atwood, J. L.; Steed, J. W. *Supramolecular Chem.* **2000**, 231.
10. (a) He, J. J.; Quioco, F. A. *Science* **1991**, *251*, 1497. (b) Luecke, H.; Quioco, F. A. *Nature* **1990**, *347*, 402.
11. Atwood, J. L.; Steed, J. W. *Supramolecular Chem.* **2000**, 258-256.
12. Baerlocher, Ch.; Meier, W. M.; Olson, D. H.; *Atlas of Zeolite Framework Types 2<sup>nd</sup> Ed.*, Elsevier Science B. V.; Amsterdam, 2001.

13. (a) Ball, P; *Designing the Molecular World: Chemistry at the Frontier*, Princeton University Press, Princeton, 1994. (b) Ball, P. *Made to Measure: New Materials for the 21st Century*, Princeton University Press, Princeton, 1997.
14. Sheldrick, G. M. *SHELXS-90, program for Structure Solution*; University of Gottingen: Germany, 1991.
15. (a) Sheldrick, G. M. *SHELXL-90, program for Structure Refinement*; University of Gottingen: Germany, 1991. (b) Barbour, L. X-SEED, *Graphical Interface for SHEL-X*; University of Columbia, MO, 2000.
16. Hoskins, B. F.; Robson, R. *J. Am. Chem. Soc.* **1989**, *111*, 5962-5964.
17. (a) Holman, H. T.; Halihan, M. M.; Jurisson, S. S.; Atwood, J. L.; Burkhalter, R. S.; Mitchell, A. R.; Steed, J. L. *J. Am. Chem. Soc.*, 1996, *118*, 9567 – 9576. (b) Halihan, M. M., *PhD Thesis*, University of Missouri-Columbia, 1996.

# CONCLUSION

In the past several chapters, we presented evidence to support the assumption that both the anion and solvent play incredibly important roles in the self assembly of copper(I) coordination solids. Previous studies of reactions of the copper(I) salts with both the 4,4'-bipyridine and pyrimidine bridging ligands laid the ground-work and presented the first of the many structural variations in Cu(I) coordination networks. We have taken that study even further, investigating these reactions in greater detail as we attempted to discover all possible structural isomers and identifying the conditions necessary to crystallize them.

Those close observations of the resulting products in relation to a specific reaction were supplemented by an even closer look at those structures we deemed *intermediate* structures for the Cu(I)/bpy reactions. With this investigation, we attempted to understand the self-assembly process, and to provide us with possible mechanisms leading to the formation of the observed final products. We discovered basic structural similarities between the discrete square tetramer,  $[\text{Cu}_4(\text{pyr})_4(\text{MeCN})_8]4(\text{BF}_4)$  and the two- and three-dimensional coordination networks suggesting that this tetramer might be the intermediate structure of these higher dimensional, coordination solids.

Observations of the POM anion nestled within a Cu(I) coordinated hexagon or triangle, or the discovery of anions residing within an eight copper coordinate cage indicate the ability of these anions to template these self-assembly reactions. Even subtle

coordination events seen with the solvents, both with the intermediate structures and from the published work of others, hints that these species are much more than a medium to aid in the crystallization of our product; they are an active participant in the self-assembly reaction leading to the wide variations of structure presented in this study.

This study provided a wealth of information with regards to both the role of anion and solvent in the self-assembly of a coordination solid. Studies such as these are an important part of our understanding of the reactions leading to these various extended solids. With the knowledge gained from this study compiled with that of others, “discovery” can then be replaced with “rational design” when we speak of our current efforts towards the development of functional porous solids.

## VITA

Douglas Knight was born in September 1, 1957, in Clinton, Iowa. He attended the public schools in Clinton, Iowa until his mid-junior year in high school at which time he enlisted in the United States Army and served as an infantryman in the 3<sup>rd</sup> Armored Cavalry, Ft. Bliss, El Paso, Texas. After his tour of duty and upon receiving an honorable discharge from the armed services he returned to Clinton, Iowa and worked in the plastics molding industry in which he held the position of Leadman and was in charge of the manufacturing processes and personnel management. During this time, he married and became a father of a two children. His separation from both job and marriage in 1982 began several years of professional stagnation. As part of a reorganization effort, Douglas returned to school in 1995 to pursue a degree in chemistry. He achieved his educational goal upon receiving a B.A. in chemistry from Iowa State University, Ames, Iowa (May 1999), and then his Ph.D. in chemistry from the University of Missouri, Columbia, Missouri (December 2005). He is currently remarried, expecting the arrival of a baby boy in February 2006, and plans to have a career in research in the area of supramolecular chemistry study involving the development of inorganic/organic materials.